PHYSIK-DEPARTMENT

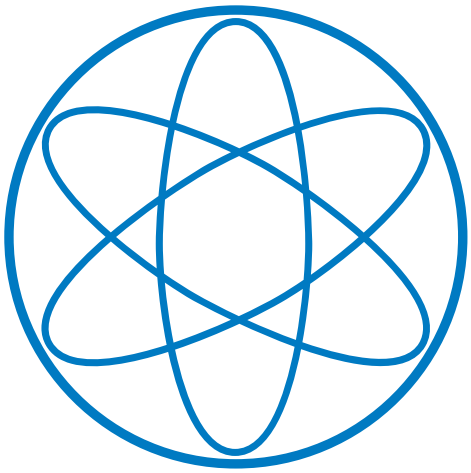

The n–Si(111):H Surface in Contact with an Aqueous Electrolyte: Surface States, Electrochemical Charge Transfer, and Nanoscale Structuring

Dissertation

von

Sebastian Bernhard Ludwig Jakob

TECHNISCHE UNIVERSITÄT
MÜNCHEN

TECHNISCHE UNIVERSITÄT MÜNCHEN

Lehrstuhl E20

-

Molekulare Nanowissenschaften & Chemische Physik von Grenzflächen

The n – Si (111):H Surface in Contact with an Aqueous Electrolyte: Surface States, Electrochemical Charge Transfer, and Nanoscale Structuring

Sebastian Bernhard Ludwig Jakob

Vollständiger Abdruck der von der Fakultät für Physik
der Technischen Universität München zur Erlangung des akademischen Grades eines

Doktors der Naturwissenschaften (Dr. rer. nat.)

genehmigten Dissertation.

Vorsitzender: Univ.-Prof. Dr. P. Vogl
Prüfer der Dissertation:

1. Priv.-Doz. Dr. W. Schindler
2. Univ.-Prof. Dr. K. Krischer

Die Dissertation wurde am 19.03.2013 bei der
Technischen Universität München eingereicht und
durch die Fakultät für Physik am 31.07.2013 angenommen.

Abstract

H-terminated n – Si (111) surfaces (n – Si (111):H) in contact with an aqueous electrolyte (0.1 M H_2SO_4) have been studied in view of charge transfer processes at the solid / liquid interface with a focus set on processes involving small amounts of charge.

Impedance measurements were utilised for electronic characterisation of the n – Si (111):H surface in contact with the electrolyte. In addition to the working electrode potential dependent space charge region at the n – Si (111):H surface, the experiments revealed electronically active "surface states" in the Si band gap as a further actor determining charge transfer processes at the solid / liquid interface. These states have been related to hydrogen incorporated in the n – Si (111):H subsurface region.

Charge transfer via states in the n – Si (111):H band gap was investigated at electron depleted n – Si (111):H surfaces exemplarily for Cu electrodeposition / -dissolution. In scanning tunneling microscopy, cyclic voltammetry and impedance measurements Cu clusters were detected on the n – Si (111):H surface in the working electrode potential range, where the states are electronically active and, where due to electron depletion of the n – Si (111):H surface usually no electrodeposition is expected. The Cu cluster size could be controlled by the n – Si (111):H working electrode potential in the potential range of electronically active states and did not change, while the electrode potential was kept constant.

Experiments on Co electrodeposition onto n – Si (111):H under electron accumulation, did not show a surface state related deviation from the known behaviour of this system. However, electric fields generated at the n – Si (111):H surface utilising a STM tunneling contact have been found to allow for localised Co electrodeposition onto the n – Si (111):H surface at the position of the STM tip, while without electric field Co is not electrodeposited at otherwise identical experimental parameters. This effect allows to localise electrochemical metal deposition processes to a nanometer length scale and can be exploited for the creation of complex nanostructures.

Evaluating the role of electric fields in localised Co electrodeposition required determination of the tip–sample separation and the influence of the STM tip apex radius on the STM imaging process. For this purpose simulations of a STM tunneling contact taking into account its three-dimensional geometry and the exponential current–distance dependence, have been carried out and related to experimentally obtained STM images. The simulations have demonstrated, that for an accurate imaging of nanoscale structures tips with radii comparable to or smaller than the size of the nanostructures under investigation are mandatory. Larger tip radii generate artificial shapes of such structures in STM images together with a loss of detail of the imaged structure and may only give reasonable image quality on scales larger than the tip radius.

Zusammenfassung

H-terminierte n – Si (111) Oberflächen (n – Si (111):H) in Kontakt mit einem wässrigen Elektrolyten (0.1 M H_2SO_4) wurden in Hinsicht auf Ladungstransferprozesse an der fest / flüssig Grenzfläche untersucht, wobei der Fokus auf Prozesse gerichtet war, an denen nur kleine Ladungsmengen beteiligt sind.

Sich in Kontakt mit dem Elektrolyten befindliche n – Si (111):H Oberflächen wurden mittels Impedanzmessung elektronisch charakterisiert. Zusätzlich zu der vom Arbeitselektrodenpotential abhängenden Raumladungszone an der n – Si (111):H Oberfläche, enthüllten die Experimente elektronisch aktive „Oberflächenzustände" in der Si Bandlücke, die ebenfalls eine Rolle in Ladungstransferprozessen an der fest / flüssig Grenzfläche spielen. Diese Zustände konnten auf oberflächennahem Wasserstoff in n – Si (111):H zurückgeführt werden.

Ladungstransfer über Zustände in der n – Si (111):H Bandlücke an n – Si (111):H Oberflächen im Bereich der Elektronenverarmung beispielhaft für elektrochemische Cu Abscheidung und Auflösung untersucht. Mittels Rastertunnelmikroskopie (RTM), Zyklischer Voltammetrie und Impedanzmessung wurden Cu Cluster auf der n – Si (111):H Oberfläche in einem Potentialbereich nachgewiesen, in dem diese Zustände elektronisch aktiv sind und, in dem aufgrund von Elektronenverarmung an der n – Si (111):H Oberfläche, üblicherweise keine Elektrodeposition erwartet wird. Die Größe der Cu Cluster konnte im Potentialbereich, in dem die Oberflächenzustände elektronisch aktiv sind, durch das
n – Si (111):H Arbeitselektrodenpotential eingestellt werden, und veränderte sich nicht, wenn das Elektrodenpotential konstant gehalten wurde.

Experimente zur Elektrodeposition von Co auf n – Si (111):H im Bereich der Elektronenanreicherung zeigten keine Abweichungen vom bekannten Verhalten dieses Systems, welche auf Oberflächenzustände hätten zurückgeführt werden können. Allerdings hat sich gezeigt, daß elektrische Felder, die unter Verwendung eines RTM Kontaktes an der n – Si (111):H Oberfläche erzeugt wurden, lokalisierte Co Elektrodeposition auf die n – Si (111):H Oberfläche erlauben und zwar an der Stelle, an der sich die RTM Spitze befindet, während ohne elektrisches Feld, unter sonst identischen Bedingungen, Co nicht abgeschieden werden kann. Dieser Effekt erlaubt lokalisierte elektrochemische Metallabscheidung auf der Nanoskala und kann zur Erzeugung komplexer Nanostrukturen herangezogen werden.

Um die Rolle, die elektrische Felder bei der lokalisierten Co Metallabscheidung spielen, auswerten zu können, war es notwending den Abstand Spitze–Probe bestimmen zu können, sowie den Einfluß des RTM Spitzenradius auf den Abbildungsprozess. Zu diesem Zweck wurden, unter berücksichtigung seiner dreidimensionalen Geometrie und der exponentiellen Strom–Spannungs Abhängigkeit, Simulationen eines Tunnelkontaktes durchge-

führt, und in Beziehung zu RTM Bildern aus Experimenten gesetzt. Die Simulationen haben gezeigt, daß für die präzise Abbildung von Strukturen auf der Nanometerskala zwingend Spitzen erforderlich sind, deren Radien vergleichbar oder kleiner sind als die Abmessungen der Nanostrukturen, die untersucht werden. Spitzen, die größere Radien aufweisen, geben solche Strukturen nur verfälscht wider, wobei Details der abgebildeten Struktur verloren gehen, und bieten Bilder annehmbarer Qualität nur auf Längenskalen, die größer als der Spitzenradius sind.

Contents

Chapter 1

Introduction

The result of metal electrodeposition or electroplating can be found in daily life in the form of various surfaces, one of the most prominent representatives being chrome finished surfaces. Besides for an aesthetical aspect, these coatings are usually employed for increasing durability and resistance against wear of the respective object [1].

However, metal electrodeposition is not limited to such a "macroscopic" application, but also employed at much smaller length scales. In semiconductor technology electroplating for the creation of Cu interconnects has been pursued through the 1990s and established by IBM end of the 1990s as a replacement of CVD or PVD techniques, which with decreasing structure size showed shortcomings in the creation of defect free and reliable interconnects [2–6]. Following this success, further advance in the field was aspired: *"Copper interconnect technology is an exciting area for the electrochemical community in particular, as it invites the pursuit of new applications for electrochemical processes and related understanding, in the fabrication of advanced IC chips."* [2]

The ongoing trend towards further miniaturisation of integrated circuits (IC) to boost their performance, as evident from *Moore's law* [1] [7–9], is accompanied by more and more sophisticated nanostructuring methods, as e.g. extreme ultra violet (EUV) lithography [10, 11], electron beam lithography [12–14], x-ray lithography [15, 16], or ion-beam lithography [17, 18] and research on new materials in ICs as, e.g., metal silicides, which may find an application in ohmic silicide–nanowires interconnects for transistors [19, 20] or in higher performing gates in CMOS devices [21, 22].

Integrated circuits of shrinking structure size require higher precision and less material in their fabrication process. A smaller amount of material in metal electrodeposition is associated with a correspondingly smaller amount of charge transferred at the solid / liquid interface. Therefore, when aiming at structure sizes of a few nanometer, a detailed understanding of charge transfer processes at the solid / liquid interface is mandatory for a precise control of metal electrodeposition.

[1] Moore's law predicts an approximate annual doubling of components on a chip.

There have been previous investigations on nanoscale structures at the solid / liquid interface. However, these studies were attributed to nucleation and growth of low dimensional systems and in particular focused on metal clusters on metal [23–37] and semiconductor electrodes surfaces [36–38], rather than to an investigation of the underlying charge transfer processes.

In view of experimental techniques, these studies employed scanning tunneling microscopy (STM) for characterising the solid / liquid interface in real space and as a tool for generating nanoscale clusters. Besides in the electrochemical environment, where it gave insights into electrochemical processes and phenomena at an atomic view [25, 30, 39–45], the STM is frequently encountered in various areas of physics, where it is employed for studying or manipulating surfaces their electronic properties [46–85]

In the present thesis the STM operated at the solid / liquid interface is used as a complementary technique to "classical" electrochemical techniques as cyclic voltametry or impedance measurements in the investigation of hydrogen terminated n – Si (111) surfaces (n – Si (111):H). The combinations of these methods allows for characterising the topology and the electronic structure of the n – Si (111):H surface in view of charge transfer processes at the nanoscale.

The metals chosen for the present investigation of electrochemical charge transfer processes at the solid / liquid interface and electrochemical nanostructuring are Cu and Co, respectively. Both metals exhibit properties relevant for applications in (future) integrated circuits. Cu is a well conduction material and, as mentioned before, is already used in interconnects in semiconductor devices. Co, on the other hand, due to its magnetic properties, appears interesting in view of magnetic storage utilising nanoscale structures, or spintronic devices based on spin polarised current transport in semiconductors [86–91].

In view of electrodeposition, the two metals behave quite different, with the equilibrium potential of Co being negative and the equilibrium potential of Cu being positive of the n – Si (111):H flatband potential and, thus, sitting in the potential range of electron accumulation and electron depletion at the n – Si (111):H surface, respectively.

A further characteristic of the n – Si (111):H surface is its H-termination saturating dangling bonds and making it robust against contamination, thus guaranteeing "clean" surfaces in the experiments [92–96], which makes n – Si (111):H surfaces well suited for electrochemistry at the nanoscale [36–38, 97, 98]. Electric fields, however, interact with such bonds and are therefore another parameter having impact on electrochemical processes at solid / liquid interfaces. spatially localised electric fields at n – Si (111):H surfaces may, thus, allow for control of electrochemical charge transfer processes on a distinct area of the the electrode surface. Supposing sufficient precision in applying an electric field, such effects could be exploited in electrochemical nanostructuring processes.

Chapter 2

Basic principles & theory

This chapter briefly introduces the physical phenomena and processes encountered within the framework of the present thesis and the corresponding theoretical approaches used in their interpretation.

In the first part of this chapter, fundamental aspects of electrochemical metal deposition are addressed and related to parameters, which can be controlled in experiments

Next, the tunneling effect and its application in the scanning tunneling microscope (STM) is reviewed. A sketch of the working principle of the scanning tunneling microscope and its operation modes is given.

In the end of this chapter a look is taken at semiconductors, in particular Silicon (Si), in view of their behaviour as electrodes in the electrochemical environment are.

Within this thesis only a coarse overview of these topics can be given. A more detailed review the reader is referred to, e.g., [99–103] on STM, [104–122] on electrochemistry, and [106–108, 123–131] on semiconductors and semiconductors in electrochemistry. Well-established relations or equations and well-known phenomena presented in the following text without an explicit indication of source are taken from and found in these references.

2.1 Electrochemistry

Electrochemical deposition and dissolution of metals are the processes of attaching metal ions to and respectively detaching them from a surface (phase 1) that is in contact with a solution (phase 2), while simultaneously electric charge is transferred between surface and metal ion. Such electrochemical reactions can be described by Equation (2.1), the double arrow implying the "dual direction" character of the process:

$$M \rightleftarrows M^z + ze \tag{2.1}$$

Here M^{z+} denotes the metal ion in solution, that becomes a neutral ion (atom) M on the sample surface when receiving z electrons of charge e from the sample surface.

The driving force behind the respective processes of electrochemical deposition and dissolution is the difference in electrochemical potentials of the two phases in contact. The electrochemical potential $\tilde{\mu}_i$ of a phase i is defined by Equation (2.2).

$$\tilde{\mu}_i = \mu_i + zF\varphi_i \tag{2.2}$$

Here μ_i and φ_i are the chemical potential and Galvani potential of phase i, respectively. The Galvani potential of a single phase can not be determined directly, but only with respect to a second (reference) potential (Figure 2.1). The difference in Galvani potentials of two phases is referred to as Galvani voltage. When the two phases are in equilibrium, the difference in Galvani potentials takes a certain equilibrium value E^0. In equilibrium

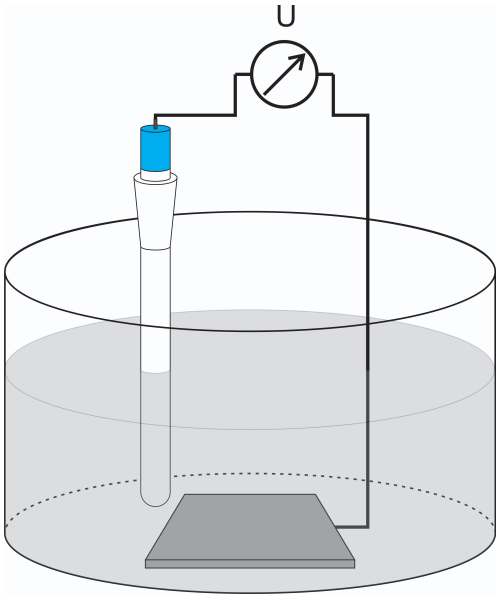

Figure 2.1: The Galvani potential of a working electrode (grey square) in contact with an electrolyte can be measured with respect to a reference electrode in contact with the electrolyte.

there is no net transfer of ions (and associated charge) between the two phases, but always a certain amount of fluctuation: some atoms will go on, while others will go off the surface. Those particle streams are correlated with charge transfer and thus, with an electrical current (density). In equilibrium those two currents compensate each other and their magnitude is referred to as exchange current density j_0. When the system is brought out of equilibrium, one of the two opposing particle streams is becoming larger than the other and the larger one is the process determining the overall direction.

The sample on the surface of which the electrochemical processes are run is referred to as "working electrode" (WE) or "electrode".

The "basis" for the solution in electrochemical experiments is the supporting electrolyte. Aqueous electrolytes consists of anion and cation species dissolved in pure water and are necessary to establish a diluted phase (of metal ions) on the one hand and to screen the electric field between the different electrodes to avoid electromigration processes within the electrolyte on the other hand. By use of the supporting electrolyte the potential in the solution can be assumed constant, with a steep potential change at the electrode / solution interface (see 2.1.1). In the further text "electrolyte" and "solution" will be used synonymously.

The potentials of the working electrodes can be influenced by integrating them in an electrical circuit: A reference electrode (RE) is brought in contact with the solution and acts as a terminal for connecting the solution to the circuit. The potential of the working electrode in contact with the solution is measured with respect to this reference electrode. When applying a potential difference between WE and RE, the resulting current in the working electrode is not delivered from the RE, as this would falsify the measurement of the potentials in the setup, but is obtained from the counter electrode (CE). Technically potentials control and corresponding current flow are realised by a potentiostat device.

A schematic illustrating the arrangement of the electrodes in an electrochemical cell ("three electrode arrangement") is given in Figure 2.2.

As already mentioned, a single (Galvani) potential can not be measured on an absolute scale, but only with respect to second potential as a reference. Potentials quoted with respect to a reference (electrode) are denoted E_{index}, where the index specifies the potential, e.g. E_{WE} denotes the working electrode (WE) potential. There are various references available in electrochemistry, but, usually, potentials are quoted with respect to the standard hydrogen electrode (SHE), which is defined as "zero". This electrode is used because of its equilibrium potential can be set fast, reproducible and with high temporal constance. The equilibrium potentials (Galvani voltage in equilibrium) E^{00} for various electrochemical reactions are available in tables, see e.g. [132–134]. In electrochemistry no "absolute" reference scale is available, since the definition of "zero" by the standard

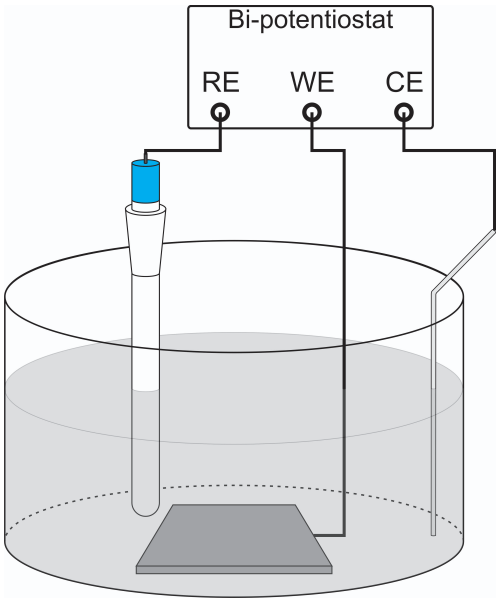

Figure 2.2: Three electrode setup commonly used in electrochemical experiments. The working electrode (WE) potential is measured and set with respect to the reference electrode (RE) in contact with the solution, while the counter electrode (CE) delivers a current to establish the working electrode potential.

hydrogen electrode is an arbitrary choice. In surface science the energy scale is usually given on the vacuum scale of energy, where "zero" is defined by an electron at infinity distance, i.e. not interacting with the object (surface) under investigation.

These two scales can be related to each other and "zero" of the SHE is found at approximately 4.5 eV below the vacuum energy scale "zero". Different approaches giving this result are listed e.g. in [104, 106, 135] and references therein, where also the following well accepted derivation [136] is quoted from. It is based on the change in free energy ("freie Enthalpie" in reference [136]) associated with the reduction of an silver ion. The characters in brackets indicate the respective phase: g – gaseous, aq – in aqueous solution, s – solid, "zero" in the potential scale is the electron at infinity. The values in electron Volts give the respective change in (Gibbs) free energy.

$$
\begin{aligned}
\mathrm{Ag^+(g) + e^-} &= \mathrm{Ag(g)} && -7.64\,\mathrm{eV} \\
\mathrm{Ag(g)} &= \mathrm{Ag(s)} && -2.60\,\mathrm{eV} \\
\mathrm{Ag^+(aq)} &= \mathrm{Ag^+(g)} && +4.96\,\mathrm{eV} \\
\mathrm{H^+(aq) + Ag(s)} &= \mathrm{Ag^+(aq) + {}^1\!/_2\,H_2} && +0.80\,\mathrm{eV} \\
\hline
\mathrm{H^+ + e^-} &= \mathrm{{}^1\!/_2\,H_2} && -4.48\,\mathrm{eV}
\end{aligned}
$$

2.1.1 The electrode / electrolyte interface

The interface of a piece of condensed matter (electrode) in contact with an aqueous electrolyte does not consist of an abrupt change from one to another bulk like phase at

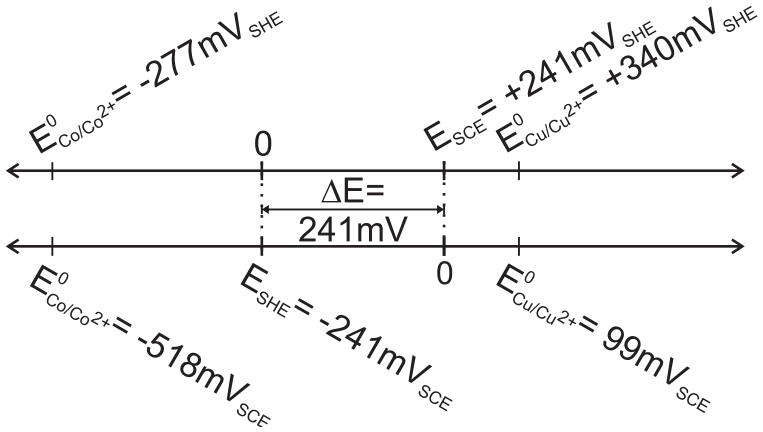

Figure 2.3: Schematic illustrating different reference electrode potential scales: standard equilibrium potentials for several metal / metal ion systems are given with respect to the Standard Hydrogen Electrode (SHE) and Saturated Calomel Electrode (SCE).

the solid / liquid interface, but can be described as series of different regions. Starting from the bulk of the electrode and going towards the solid / liquid interface there evolves a space charge region next to the interfacial area, that is opposed by the double layer in the electrolyte. Within the space charge region and the double layer the potential difference of the two bulk phases is equalised, where in the electrode electrons or holes and in the double layer ions represent the charge carrying species, which compensate each other in total charge.

The model accepted to represent the double layer characteristics in an adequate way [137–144] is sketched in Figure 2.4. The inner Helmholtz plane is indicated by the range "I". It has a width in the order of Ångström [144,145] and is characterised by partially solvated ions at the minimum attainable distance to the surface. The outer Helmholtz plane is indicated by the range "II". It is characterised by fully solvated ions next to the inner Helmholtz plane. The diffuse Gouy-Chapman layer is indicated by the range "III". It is characterised by fully solvated ions with a negative gradient in ion concentration towards the "bulk" electrolyte, due to increasing screening of the space charge at the electrode surface by the solvated ions with increasing distance from the solid / liquid interface. The gradient increases with increasing ion concentration of the supporting electrolyte. The width of the diffuse layer for aqueous electrolytes of concentrations $\gtrapprox 0.1\,\mathrm{M}$ is of the order of 10 Å.

The potential drop across the double layer is proportional to the distance d from the electrode surface in the range of the Helmholtz layer ("I" and "II") and proportional e^{-d} in the diffuse layer ("III"). Without the sharp potential drop at the solid / liquid interface, a significant electric field gradient would exist between the electrodes and electrochemical processes would not be diffusion limited but be subject to electromigration due to the electric field.

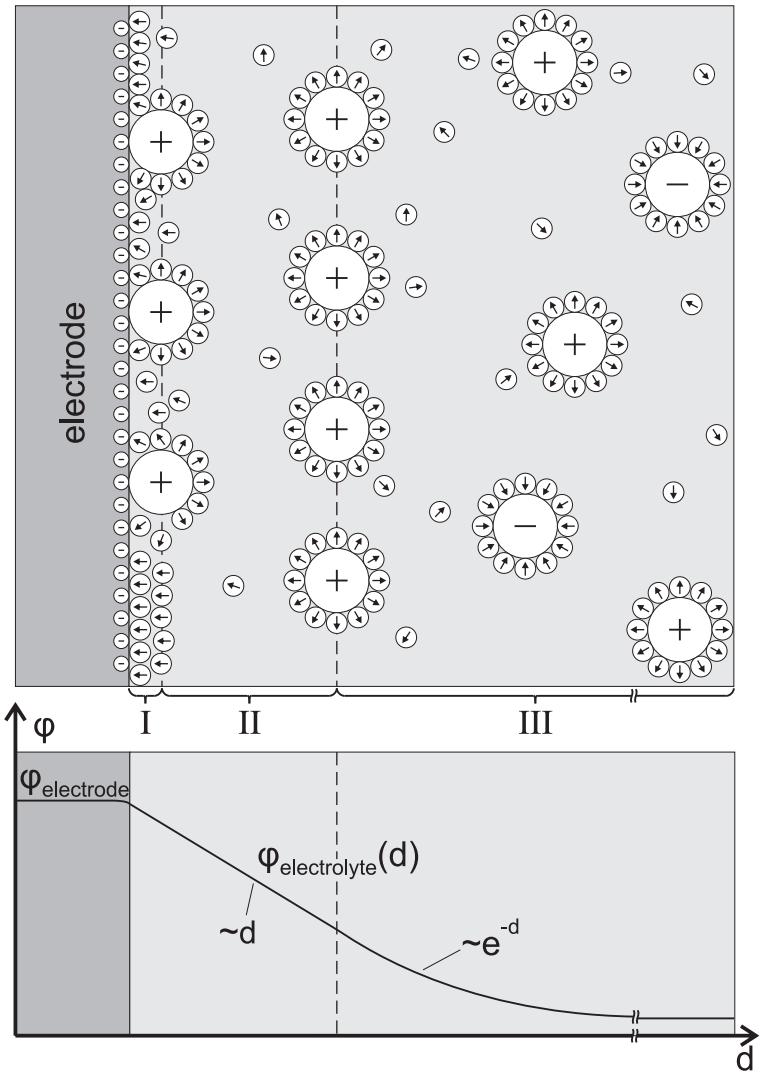

Figure 2.4: Upper part: schematic of the solid / liquid interface. The space charge at the working electrode surface is compensated by adsorbed "layers" (I to III) of ions in the electrolyte. Large spheres represent ions, small spheres solvent molecules. Lower part: schematic of the potential drop across the solid / liquid interface.

2.1.2 Concentration dependent processes – Nernst equation

The actual equilibrium potential E^0 of a specific metal / metal ion system depends on Temperature and the activity of the two phases in contact. The deviation from the standard potential E^{00} of a system is given by the Nernst equation (Equation (2.3)):

$$E^0_{M/M^{z+}} = E^{00}_{M/M^{z+}} + \frac{RT}{zF} \ln \frac{a_{M^{z+}}}{a_M} \tag{2.3}$$

Here a is the activity, T is the absolute Temperature in Kelvin, $R = 8.314\,\mathrm{J\,mol^{-1}\,K^{-1}}$ the universal gas constant, $F = N_A \cdot e = 9.649 \cdot 10^{-4}\,\mathrm{C\,mol^{-1}}$ and $E^{00}_{M/M^{z+}}$ the equilibrium potential at standard conditions. Activity in this context means effective concentration

of the phases, which includes e.g. interactions between the ions within a solution. It holds the relation $a = f \cdot c$, where c is the nominal concentration of the phase and f is the coefficient of activity, which includes the interactions between the ions. For dilute phases, i.e. low concentrations and weak interactions, $f \approx 1$. For a solid metal phase, e.g. a metal electrode, holds the definition $a_M = 1$. According to Equation (2.3), in such a system a variation of $a_{M^{z+}}$ by one order of magnitude leads to a a shift of E^0 by $59/z\,mV$.

$$\Delta E^0_{M/M^{z+}} = \frac{RT}{zF} \ln \frac{10^m}{1} = \frac{m}{z} \cdot 59\,\mathrm{mV} \tag{2.4}$$

Therefore, increasing/ lowering the concentration of the ions in the electrolyte, shifts the equilibrium potential E^0 to more positive/ negative potential values with respect to E^{00}.

2.1.3 Potential dependent processes – Butler-Volmer equation

Applying a potential to a working electrode exposed to a solution of metal ions will cause electrochemical deposition or dissolution of metal to take place at the WE surface, depending on the working potential E_{WE} being negative or positive of the equilibrium potential E^0 of this particular system, respectively. A difference $\eta = E_{WE} - E^0 < 0$ is defined as "overpotential", a difference $\Delta E = E_{WE} - E^0 > 0$ is defined as "underpotential".

The current density j^- related to the cathodic branch $M^{z+} + ze \rightarrow M$ (deposition) and the current density j^+ related to the anodic branch $M \rightarrow M^{z+} + ze$ (dissolution) depend on the working electrode potential E_{WE} with respect to the equilibrium potential $E^0_{M\,/\,M^{z+}}$ according to equations (2.5) and (2.6).

$$j^-(E_{WE} - E^0) = -j_0 exp\left[-\frac{(1-\alpha)zF}{RT}\left(E_{WE} - E^0\right)\right] \tag{2.5}$$

$$j^+(E_{WE} - E^0) = j_0 exp\left[-\frac{\alpha zF}{RT}\left(E_{WE} - E^0\right)\right] \tag{2.6}$$

The superposition of equations (2.5) and (2.6) gives the total current density.

$$\begin{aligned} j(E_{WE} - E^0) &= j^+(E_{WE} - E^0) + j^-(E_{WE} - E^0) = \\ &= j_0 \left\{ \exp\left[-\frac{\alpha zF}{RT}\left(E_{WE} - E^0\right)\right] - \exp\left[-\frac{(1-\alpha)zF}{RT}\left(E_{WE} - E^0\right)\right] \right\} \end{aligned} \tag{2.7}$$

Equation (2.7) is known as "Butler-Volmer Equation". In equations (2.5) to (2.7) α denotes the transfer coefficient and j_0 the exchange current density. j_0 is determined by the equality

of j^+ and $|j^-|$ at $E_{WE} = E^0$.

$$j^-(E^0) = -j_0 = -zFc_{ox}k_0^- exp\left[-\frac{(1-\alpha)zFE_0}{RT}\right] \tag{2.8}$$

$$j^+(E^0) = j_0 = zFc_{red}k_0^+ exp\left[\frac{\alpha zFE_0}{RT}\right] \tag{2.9}$$

k_0^- and k_0^+ in equations (2.8) and (2.9) denote kinetic parameters of the respective reaction.

j_0 can be determined from experimental $j(E_{WE} - E^0)$ curves. For large cathodic/ anodic potentials with respect to E^0 the respective counter reaction can be neglected in Equation (2.7) and logarithmising gives the relations (2.10) and (2.11), while $E_{WE} < E^0$ and $E_{WE} > E^0$, respectively.

$$\lg|j| = \lg j_0 + \frac{(1-\alpha)zF}{2.3RT}|E_{WE} - E^0| \tag{2.10}$$

$$\lg j = \lg j_0 + \frac{\alpha zF}{2.3RT}(E_{WE} - E^0) \tag{2.11}$$

In a semi-logarithmic plot of $j(E_{WE})$, j_0 can be determined from the intersection of the extrapolated linear part of the graph with the ordinate at E^0. The slope of this linear part is determined by $(1-\alpha)zF / 2.3RT$ and $\alpha zF / 2.3RT$, respectively.

The amount n and the direction of metal transfer with respect to the working electrode surface can be determined by integrating the measured current I_{WE} including its sign over time, considering the valency z of the metal ions involved: $n = \int I_{WE}\,dt / zF$.

2.2 The scanning tunneling microscope

The scanning tunneling microscope (STM) is based on the quantum mechanical phenomenon of electron tunneling. In contradiction to the understanding in classical physics electron tunneling allows an electron to cross an energy barrier of finite height, even if the electron has an energy lower than the barrier height. Tunneling is possible as long as the quantum mechanical particle wave function of an electron extends beyond the barrier and the probability of presence takes a finite value there. The associated charge transfer can be measured as a (tunneling) current "through" the barrier.

Scanning tunneling microscopes emerged in the late 1970s/ early 1980s [46–48, 60–62, 99, 146, 147] and allow for the "imaging" of surfaces at the nanoscale in real space.

In a STM setup a sharp tip is positioned next to a substrate surface and a bias voltage U_{bias} is applied between the sample and the tip. The distance in between tip and surface is reduced until a (tunneling) current is measured, while the tip and the surface are not in physical contact. Maintaining this "tunneling contact" and scanning the tip across the sample surface allows to obtain an image of the surface by evaluation of the tunneling current as function of the tip position.

In the following, the quantum mechanical foundation of electron tunneling is illustrated and the working principle of STM is introduced.

2.2.1 Quantum mechanical description

Electrons, obey the wave-particle dualism and therefore can be described by a wave function Ψ. This wave function is a solution to the Schrödinger equation, which is further on used to describe the tunneling effect.

On the basis of the situation illustrated in Figure 2.5 electron tunneling through a barrier and a derivation of the associated tunneling current are discussed. An electron shall be at energy E, traveling freely along the x-axis of a cartesian coordinate system. Perpendicular to this axis exists potential a barrier of constant (energetic) height W in the range $x_a < x < x_b$.

The Schrödinger equation (for this electron) reads:

$$-\frac{\hbar^2}{2m}\frac{d^2}{dx^2}\Psi(x) + W(x)\Psi(x) = E\Psi(x) \tag{2.12}$$

Depending on the relation of E and W there are two possible scenarios for the electron–barrier interaction.

For an electron with E > W the conception of classical physics allows the electron to overcome the barrier, since its energy is higher than the barrier height. Also the quantum mechanical approach gives an electron freely propagating along x at constant momentum, described by a time independent solution for Equation (2.12):

$$\Psi(x) = \Psi(0)e^{\pm ikx};\ k = i\frac{\sqrt{2m(E-W)}}{\hbar} \tag{2.13}$$

For an electron with E < W in classical physics it is forbidden to enter the potential barrier at $x_a < x < x_b$, while from a quantum mechanical point of view the situation is different. Here a time independent solution of Equation (2.12) exists for the range $x_a < x < x_b$.

$$\Psi(x) = \Psi(0)e^{-\kappa x};\ \kappa = \frac{\sqrt{2m(W-E)}}{\hbar} \tag{2.14}$$

The existence of this solution gives a probability P to find the electron within dx.

$$P = |\Psi(0)|^2 e^{-2\kappa x}\mathrm{d}x, \text{ where } \int_{-\infty}^{\infty} P\mathrm{d}x = 1 \tag{2.15}$$

Thus, the probability to find an electron at a position x within the barrier decreases exponentially into the barrier.

$$P(x - x_a) \propto e^{-2\kappa(x-x_a)};\ \kappa = \frac{\sqrt{2m(W-E)}}{\hbar} \tag{2.16}$$

For an infinitely wide barrier the probability becomes 0.

$$\lim_{(x_b - x_a)\to\infty} P(x - x_a) = 0 \tag{2.17}$$

Equation (2.16) and Equation (2.17) state, that there is a finite probability for an electron to pass the potential barrier W, as long as the barrier has a finite width (see Figure 2.5). The electron is either seen on the one or the other side of the classically insuperable barrier. The passing process "through" the barrier is referred to as "tunneling", the associated charge transfer per time interval correspondingly is referred to as "tunneling current".

Based on these considerations, in the following the parameters acting on the tunneling current are examined. For this purpose consider a modification of our Gedankenexperiment above by replacing the free electron by an electron bound in a piece of matter. The potential barrier W is replaced by the potential barrier Φ with respect to the energy of

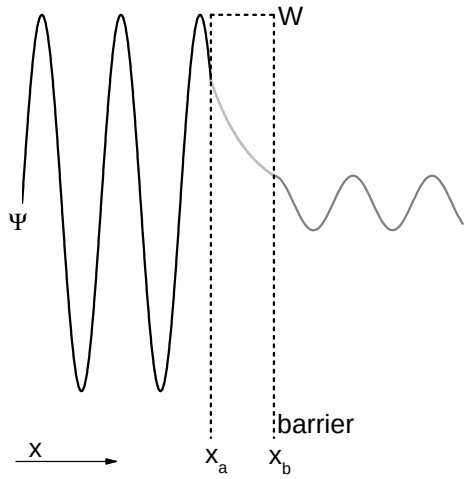

Figure 2.5: In a quantum mechanical description, its wave nature (Ψ) allows an electron at energy E to pass a barrier of height W and finite width, even at $E < W$. In classical mechanics this process is forbidden. The probability to pass the barrier is $\propto |\Psi|^2$ and, thus, finite.

the electron.

An electron can only tunnel (elastically) from one side of a potential barrier to the other, if there is an empty state to occupy. Therefore next to the sample we place a STM tip of the same material and Fermi level at a distance d. The Fermi levels of tip and sample are aligned, as long as no potential difference U_{bias} is applied between sample and tip. When $U_{bias} \neq 0$, we assume the barrier Φ not to be influenced by U_{bias} for $\Phi \gg eU_{bias}$.

At $U_{bias} \neq 0$ all electrons on the STM tip sitting above the Fermi level of the sample can potentially tunnel into empty states in the sample. Thus, the tunneling current is the sum over all of these electrons in the energy interval $(E_F - eU_{bias})$ to E_F in the STM tip. Including the local density of states in the sample $D_{sample}(E)$, only considering elastic electron tunneling, and including the step function shape of the Fermi distribution, the tunneling current is characterised by

$$I_{tunnel} \propto e \cdot \sum_{E_F - eU_{bias}}^{E_F} |\Psi_n(x)|^2 \tag{2.18}$$

$$\propto e \cdot \sum_{E_F - eU_{bias}}^{E_F} E \cdot D_{sample}(E) \cdot e^{-2\kappa(E)d};\ \kappa = \frac{\sqrt{2m\Phi(E)}}{\hbar} \tag{2.19}$$

$$\propto e \cdot U_{bias} \cdot D_{sample} \cdot e^{-2\kappa d} \tag{2.20}$$

Here D_{sample} is the respective local density of states (LDOS), E the energy of a specific electron, E_F the Fermi level, d the tip sample distance and U_{bias} the bias voltage applied between sample and STM tip. In the last step $D_{sample}(E)$ and $\Phi(E)$ are assumed constant

in the energy range $(E_F - eU_{bias})$ to E_F.

A more sophisticated treatment of the electron transfer process between sample and STM tip is based on the overlap of the corresponding independent wavefunctions of sample Ψ_{sample} and tip Ψ_{tip} states [148]. This is represented in the transfer matrix element M, the integration is carried out over a surface S lying completely within the tunneling barrier between sample and tip.

$$M = \frac{\hbar}{2m} \int_S (\Psi_s^* \nabla \Psi_t - \Psi_t^* \nabla \Psi_s) \, \mathrm{d}S \tag{2.21}$$

Evaluating M, according to *Tersoff* and *Hamann* [149] an expression for the tunneling current is derived

$$I_{tunnel} = \frac{2\pi e}{\hbar} \sum_{s,t} f(E_t) \left[(1 - f(E_s + eU_{bias}) \right] |M|^2 \, \delta(E_t - E_s) \tag{2.22}$$

Here $f(E_t)$ and $f(E_s + eU_{bias})$ are the Fermi functions in the STM tip and sample, respectively.
For small bias voltages U_{bias} and room temperature conditions Equation (2.22) simplifies and further, modeling the tip apex as a spherical potential well centered at r_0 and only taking s-wave functions into account gives a expression for the tunneling current [149]:

$$I_{tunnel} = \frac{32\pi^3}{\hbar} e^2 U_{bias} \Phi^2 D_{tip}(E_F) R^2 \kappa^{-4} e^{2\kappa R} \cdot \sum_s |\Psi_s(\mathbf{r}_0)|^2 \, \delta(E_s - E_F) \tag{2.23}$$

Here R is the tip radius, $\kappa = \sqrt{2m\phi\hbar^{-1}}$ is the minimum inverse decay length for wave functions in the vacuum gap with tip workfunction ϕ and $|\Psi_s(\mathbf{r}_0)|^2 \propto e^{-2\kappa(R+d)}$, where d is the tip–sample separation measured from the tip apex center of radius R.

In Equation (2.23) the density of states of the sample D_{sample} is not explicitly taken into account. It also enters the tunneling current in the same manner as D_{tip} [150–152]:

$$I_{tunnel} \propto \int_{E_F}^{E_F + eU_{bias}} D_{sample}(E - eU_{bias}) D_{tip}(r_{tip}, E) \mathrm{d}E \tag{2.24}$$

Here r_{tip} is the position of the spherical tip apex center.

From the above equations the essential parameters determining the tunneling current become obvious:

$$I_{tunnel} \propto U_{bias} \cdot D_{sample} \cdot D_{tip} \cdot e^{-d} \tag{2.25}$$

The tunneling current depends linearly on the bias voltage U_{bias} but exponentially on the tip–sample distance d, making it very sensitive to changes in the tunneling gap width. Both, the local densities of states of sample D_{sample} and tip D_{tip} enter the expression for I_{tunnel}. This makes the tunneling current not only depend on the topography, but adds sensitivity for the electronic structure of the sample surface and STM tip.

2.2.2 Operation principle

In STM experiments, the STM tip is moved ("scanned") linewise over the sample surface by a three axis piezo actuator (see Figure 2.6). The three voltages (U_x, U_y, U_z) determining the deflexion of the piezo actuator and the tunneling current are recorded for a certain number of equidistant points in each line. From these measured values a map of

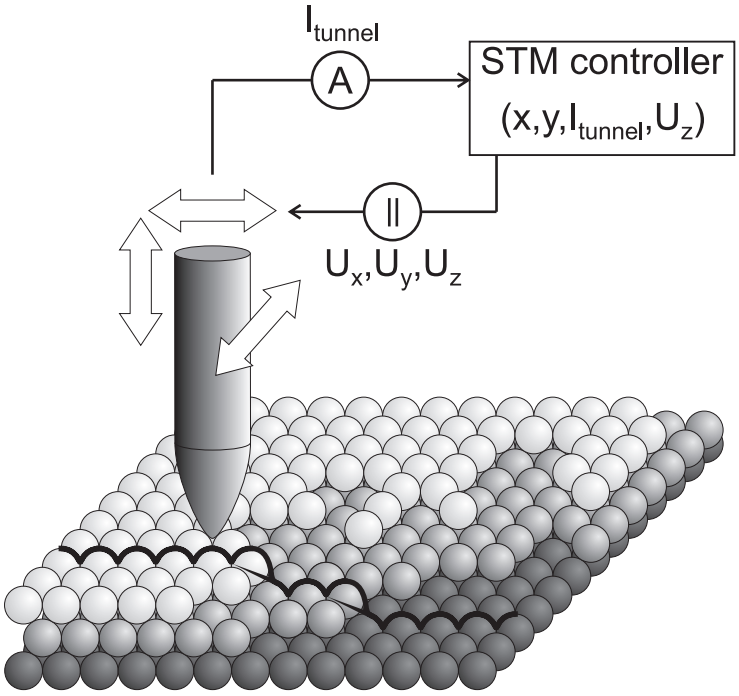

Figure 2.6: Illustration of the STM working principle. The STM tip in tunneling contact is moved linewise over the surface (x-y plane), while recording the tunneling current and the voltages U_x, U_y, U_z determining the STM tip position. From this information an reals space "image" of the surface can be generated.

the surface can be generated. There are two operation modes of a STM, each one offering different advantages or drawbacks.

Constant height mode

In constant height mode the tip is approached, until a certain tunneling current I_0 is established. Then the piezo axis perpendicular to the sample surface is kept at this deflexion and the surface scanned "in parallel" to the surface by the STM tip (see Figure 2.7). In the resulting plane of acquired data points, a certain current value is attributed to each point (pixel in the STM image). From this current map, information on the electronic structure of the surface can be obtained or a height profile of the scanned surface can be generated by comparing the individual current values to I_0. When operating a STM in constant height mode, the investigated surface topology should not alter much in height and the tilt of the surface plane with respect to the scanning plane should be minimised, since a structure on the surface higher than the tip–sample distance at I_0 or an intersection of the scanning plane and the surface cause a crash irreversibly damaging the STM tip.

Constant current mode

In constant current mode, the tip is approached, until the desired tunneling current I_0 is reached. A feedback loop is engaged, maintaining the tunneling current at I_0 by controlling the piezo axis perpendicular to the sample surface and, thus, the tip–sample distance. If a topological or electronic structure on the sample surface causes a deviation of the tunneling current from I_0, this is compensated by adjusting the deflexion of the piezo (see Figure 2.7). The piezo voltage, i.e. piezo deflexion, at each pixel is used to generate a topography image of the surface. The constant current mode is suited for imaging surfaces with large variations in height, as a properly working feedback loop avoids tip crashes into the sample surface.

2.2.3 STM in electrochemical environment

Scanning tunneling microscopy in the electrochemical environment is utilised for the characterisation of solid / liquid interfaces and for in-situ studies of nucleation and growth at electrode surfaces [44, 153–194], gaining topographical data of those processes [154, 155, 168, 171, 179, 195, 196].

The STM tip is introduced as an additional working electrode into the electrochemical cell. The working electrode potentials of the sample and the STM tip can be set independently from each other using a reference electrode and a counter electrode in the electrochemical cell. The bias voltage of the tunneling contact is given by the difference in the potentials of sample and STM tip.

The configuration of independent electrode potentials allows for individual and selective electrochemical manipulation of the two electrodes and electrochemical nanostruc-

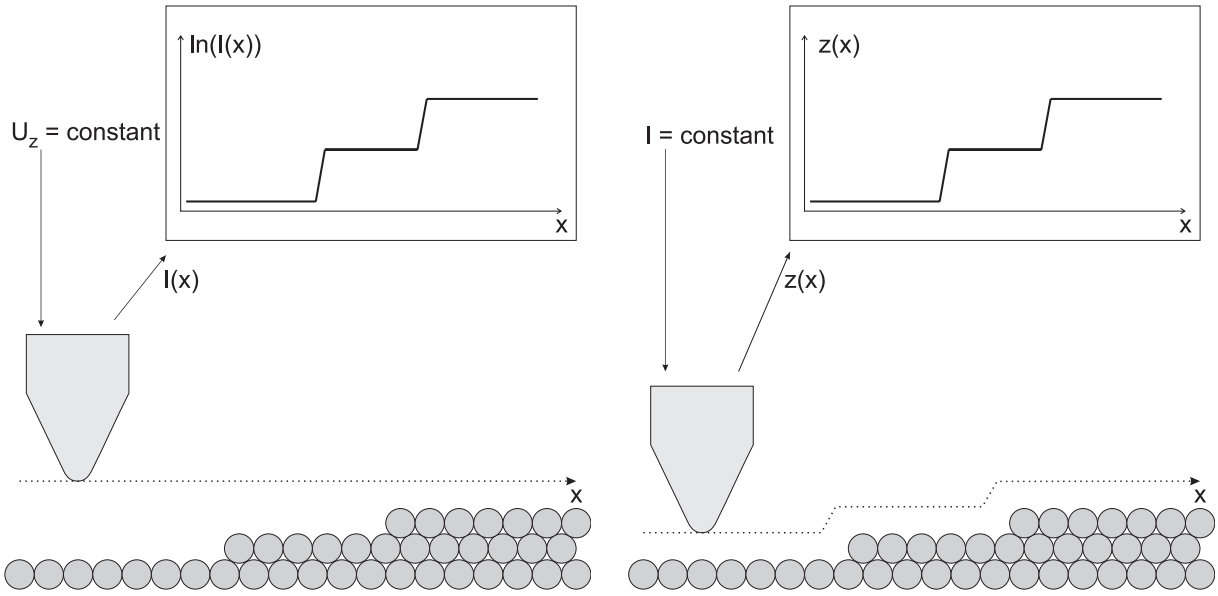

Figure 2.7: Illustration of the different operation modes of the STM. In constant height mode (left schematic), the initial deflexion of the STM tip is kept constant; a change in the tip–sample distance causes a corresponding change in the tunneling current, which is used for generating a current map of the sample surface. In constant current mode (right schematic) a change in the tunneling current is compensated by a change in the tip sample distance; from the corresponding change in height a surface map is generated

turing of the sample by the STM tip [23, 25, 30–32, 37, 197, 198]. Care has to be taken on selecting the potential range for the measurements, since for each electrolyte – working electrode system different working electrode potential dependent electrochemical reactions may occur, including processes capable of corrupting a working electrode.

At working electrode surfaces in an electrolytic environment (small) Faraday currents occur. At a STM tip these currents may be of the same order of magnitude as the desired tunneling current. Faraday currents are proportional to the surface area exposed to the electrolyte and, thus, can be minimised by reducing this area in an appropriate way, e.g. partially isolating the STM tip (see subsection 3.3.1).

Another aspect discriminating STM experiments in electrochemical environment and UHV is the finding of a reduced tunneling barrier height in electrochemical environment in comparison to UHV [160, 177, 199–202]. A detailed investigation of the tunneling barrier in an aqueous electrolyte revealed a modulation of the barrier height with the STM tip–sample separation [201, 202]. This finding was attributed to layers of water molecules fitting into the gap with increasing STM tip–sample separation, thus, modifying the tunneling barrier [201, 202]. The dependence of the tunneling current on the STM tip–sample separation, however, follows an exponential relation like in UHV experiments [47, 201, 202], as predicted by theory [200].

2.3 Semiconductors

Semiconductors, conductors and isolators are discriminated according to their electronic properties, which are determined by the respective electronic band structure. This band structure originates from the periodic lattice of atoms and the periodic potential these atoms represent for electrons: The energetic levels accessible for electrons bound to an isolated atom are discrete and associated with electron orbitals. Bringing initially isolated atoms closer to another, the orbitals of the different atoms begin to overlap and the energetic levels split into a band of new states. The more orbitals of different atoms overlap, the more and the energetically closer spaced levels are generated, which, due to the huge number of atoms in bulk solids, allows the approximation of continuous energy bands. The bands may be separated by (band)gaps, i.e. ranges on the energy scale, where due to a lack of states no electrons are present.

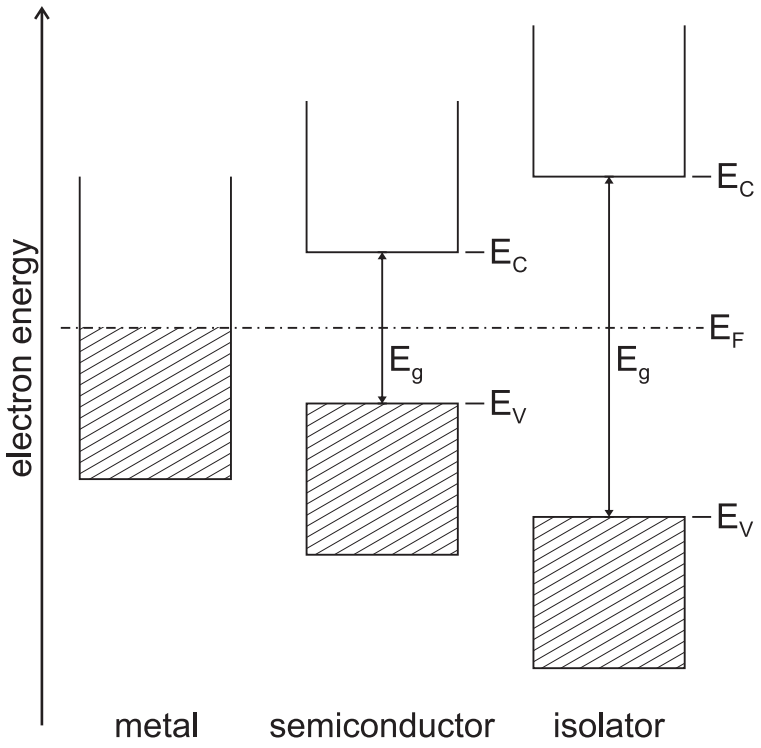

Figure 2.8: Schematic illustrating the different band structures of conductors (metal), semiconductors and isolators. In metals the Fermi level E_F sits within a band, while for semiconductors and isolators E_F is found in the band gap. The band gap of isolators is larger than that of semiconductors. E_C and E_V denote the conduction band minimum and valence band maximum, respectively.

In a solid state body having a band gap, the band containing electrons of highest energy is referred to as valence band, the energetically next higher, empty band is referred to as conduction band. In the electronic band structure only partially filled electronic bands contribute to the electric conductivity, because empty states for electrons within the band

are required for charge transfer.

The (energetic) level, up to which the electronic bands are filled, is the Fermi level E_F. As illustrated in Figure 2.8, in the case of a conductor, e.g., a metal, E_F sits within a band and, thus, next to E_F empty states are available, while in the case of a semiconductor or an insulator E_F sits in a (band) gap E_{gap} between two bands, i.e. the valence band is completely filled, while the conduction band is completely empty.

The width of the band gap is used to distinguish between isolators ($E_{gap} \gtrapprox 3\,eV$) and semiconductors ($E_{gap} \approx 1\,eV$) [112]. For $T \neq 0\,K$, due to the smearing of the Fermi distribution, in a semiconductor electrons are available, which have high enough energy to access the conduction band, i.e. to cross the band gap. As a result, conduction and valence band in the semiconductor become partially filled, which causes conductivity in the semi–conductor and allows electronic transport. In insulators E_{gap} is larger than in semiconductors and, thus, no (much less) electrons can access the conduction band and consequently the isolator has a very low conductivity.

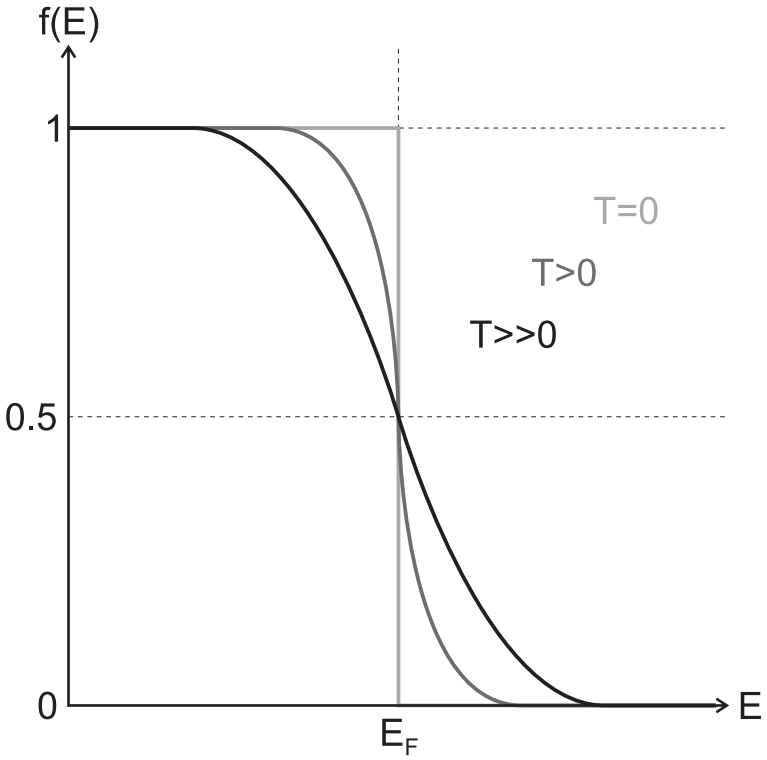

Figure 2.9: Schematic illustrating the occupation probability of states above the Fermi level E_F according to Fermi statistics. At $T = 0$ all levels up to E_F are occupied, levels above E_F are empty. For $T \neq 0$ there is a finite probability for electrons to occupy levels above E_F, while states below E_F become unoccupied.

2.3.1 Doping of semiconductors

The conductivity of semiconductors can be increased by increasing the charge carrier concentration from the intrinsic value (Si: $n_i \approx 1.5 \cdot 10^{10}\,cm^{-3}$ [123]) by adding charge carriers via doping [203, 204]. This is achieved by inserting a chemical element ("dopant") into the semiconductor lattice, that has a valency different from the semiconductor.

A dopant having a higher valency than the semiconductor makes additional electrons available in the semiconductor. In this case the dopant is referred to as donator and the semiconductor n-type. The level of the donator electrons typically sits slightly below the conduction band edge.

A dopant having lower valency than the semiconductor captures electrons and makes holes available in the semiconductor. In such a case, the dopant is referred to as acceptor and the semiconductor p-type. The level of the acceptor hole typically sits slightly above the valence band edge.

Doping of Si is typically achieved by adding P for n-type or B for p-type electronic properties (see schematic Figure 2.10).

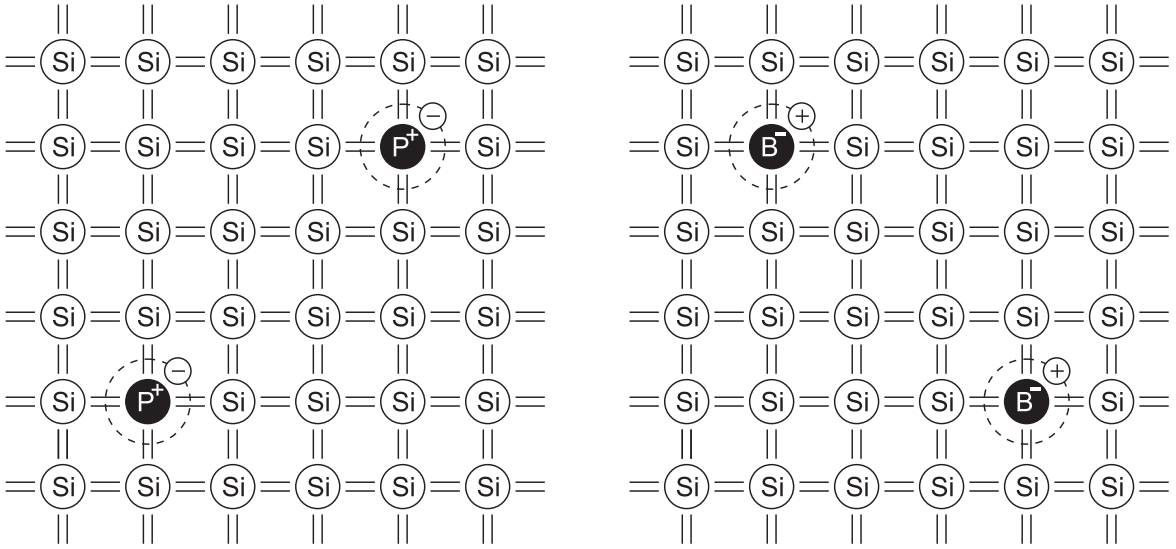

Figure 2.10: Introducing atoms of a different element ("dopant") into a semiconductor lattice makes additional charge carriers (electrons or holes) available in the semiconductor, due to the difference in valency of the semiconductor and dopant. The cases of P (electron donator, electrons) and B (electron acceptor, holes) for Si are illustrated here.

In doped semiconductors at $T = 0$ the Fermi level sits at the level of the dopants in the band gap, since those states hold the lowest energetic electrons. For $T > 0$ there is a shift of the Fermi level to higher energies due to thermal ionisation of dopants in the semiconductor.

At room temperature ($k_B T \approx 25\,meV$) impurity exhaustion is present in a semicon-

ductor containing low donors. The Fermi level and charge carrier density n are then given by Equation (2.26) and Equation (2.27).

$$n \approx N_D = \text{constant} \tag{2.26}$$

$$E_F \approx E_C - k_B T \ln\left(\frac{N_C}{N_D}\right) \tag{2.27}$$

$E_d = E_C - E_D$ is the energy of ionisation of the donor with respect to the conduction band edge. For Phosphorous in Silicon $E_d = 44\,\text{meV}$ [123, 203]. $N_C = 2.8 \cdot 10^{19}\,\text{cm}^{-3}$ is the effective density of states in the conduction band of Silicon [205].

2.3.2 Semiconductors in electrochemical environment

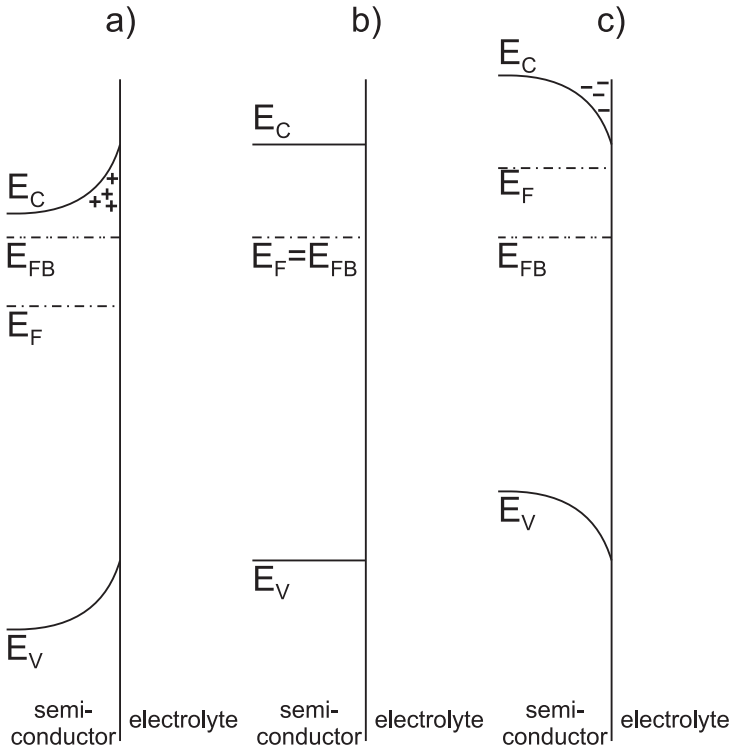

Figure 2.11: Band structure at a semiconductor surface in contact with an electrolyte. E_C, E_V, E_{FB}, and E_F denote conduction band edge, valence band edge, flatband potential and Fermi level, respectively. Plus and minus signs at the semiconductor / electrolyte interface represent excess positive and negative charge at the surface. In a) the surface is depleted of electrons (excess positive charge at the surface), the bands are bent upwards towards the interface. In b) the surface is at flatband conditions (no excess charge at the surface), there is no band bending. In c) electrons accumulate at the surface (excess negative charge), the bands are bent downwards towards the interface.

The charge carrier concentration in typical semiconductors is much lower than in a metal ($10^{23}\,\text{cm}^{-3}$) or in an electrolyte ($10^{20}\,\text{cm}^{-3}$ for a 1 M electrolyte) [199, 206–210].

Consequently, a semiconductor in contact to an aqueous electrolyte has properties similar to a semiconductor / metal contact, since the alignment of the electrochemical potentials of the semiconductor and the electrolyte in equilibrium causes electron depletion at the surface of a n-type semiconductor ("depletion zone" or "space charge region") and a corresponding modification of the band structure. Electron depletion is represented by an upward bending of the band edges of conductance and valence band in the electronic band structure of the semiconductor at the semiconductor / electrolyte interface, as illustrated in Figure 2.11. The modification of the band structure is referred to as "band bending". The relation between band bending and electron concentration is given by Equation (2.28) [108, 123, 124, 130, 145, 145, 210–212]

$$n_{surface} = n_{bulk} e^{\frac{-eU_{bb}}{k_B T}} \tag{2.28}$$

Here $n_{surface}$ is the density of electrons at the semiconductor surface, n_{bulk} is the density of electrons in the bulk and U_{bb} is the potential difference between the bulk and at the surface, due to band bending (see Figure 2.11). The position of the band edges at the semiconductor / electrolyte interface is fixed ("pinned") independently of the amount of band bending. This is due to the partitioning of the potential difference between bulk semiconductor and electrolyte across the double layer and across the space charge region, in which the potential drop across the Helmholtz layer is the smaller one and constant independently of the potential difference [209, 210, 212–214].

Applying a potential to the semiconductor electrode with respect to the electrolyte and, thus, shifting the Fermi level in the semiconductor, changes the band bending at the semiconductor / electrolyte interface. At appropriate potentials the electron depletion at the surface can be compensated or electron accumulation at the semiconductor surface can be established (band edges are bent downward, see Figure 2.11). The applied potential that exactly compensates electron depletion is referred to as "flatband potential" E_{FB}, because the band edges at this potential are flat, i.e. the band bending vanishes.

The flat band potential can be utilised to relate the working electrode potential to the semiconductor band structure: Since at the flatband potential the bands are flat throughout the semiconductor, the relative position of conduction band edge E_C and valence band edge E_V to the Fermi level E_F (which equals the working electrode potential E_{WE}) can be determined from the doping concentration of the semiconductor and its band gap (see Equation (2.27)).

The flatband potential can be determined from experiments by analysing the potential dependence of the space charge region capacitance C_{SC} at the semiconductor surface in deep electron depletion by a "Mott-Schottky-Plot" [106, 130, 205, 210, 215–225] , which is

based on the Mott-Schottky equation (Equation (2.29)).

$$\left(\frac{A}{C_{SC}}\right)^2 = \frac{2}{\epsilon\epsilon_0 N_D e}\left(E_{WE} - E_{FB} - k_B T\right) \tag{2.29}$$

In these plots (A / C^2) is plotted against E_{WE} the slope of this plot gives information on the bulk doping and relative permittivity [214, 218, 226–228], the intersection of the extrapolated data of the semiconductor in depletion with the abscissa is used to determine the value of E_{FB} [210, 229–232]. At the point of intersection C_{SC} becomes "infinite", which corresponds to width of the space charge region of "zero", i.e. flat band conditions.

The values $C_{SC}(E_{WE})$ can be determined from impedance measurements [209, 218, 233, 234] by a fitting procedure. In this procedure the impedance of an equivalent circuit representing semiconductor / electrolyte interface and space charge region is fitted to the experimentally determined data by varying the values of the components in this circuit. Appropriate equivalent circuits representing solid / liquid interface and the space charge region are shown in Figure 2.12.

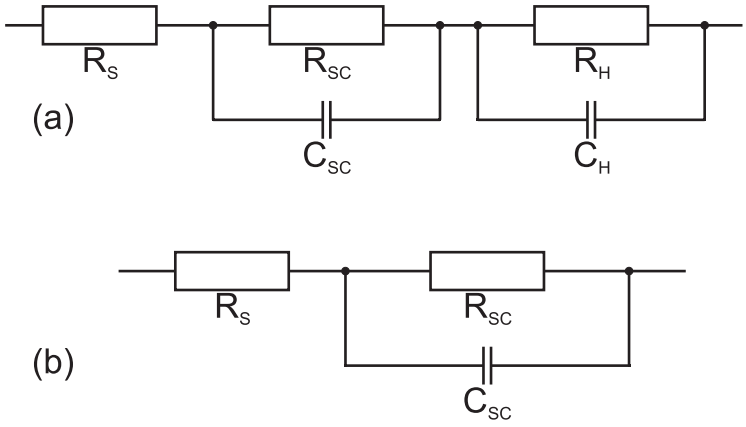

Figure 2.12: Equivalent circuits for the semiconductor / electrolyte interface employed for interpreting impedance measurements. While (a) includes the Helmholtz double layer (C_H and R_H), the circuit in (b) used for analysing Mott-Schottky plots only consists of the space charge region (C_{SC} and R_{SC}) and R_S which accounts for all ohmic potential drops in the measurements. The Helmholtz double layer may be omitted, since $C_H \gg C_{SC}$.

The circuit in Figure 2.12a consists of a parallel circuit of a resistor R_{SC} and a capacitor C_{SC}, which represent the space charge region, and in series the Helmholtz double layer capacitor C_H parallel to the corresponding resistor (R_H), while R_S accounts for all ohmic potential drops in the measurement. The capacitance of the space charge region is much smaller than that of the Helmholtz double layer, and, thus, dominates the impedance spectroscopy measurements, since $\mathcal{X}_C = (\omega C)^{-1}$. Therefore, the Helmholtz double layer circuit contribution can be omitted [145, 210, 219, 234–236] and the equivalent circuit in

Figure 2.12b can be employed for the treatment of the space charge region.

The width of the space charge region can be calculated from the capacitance of the space charge region by modeling it as a plate capacitor [112, 208, 209, 223]:

$$d = A\frac{\epsilon\epsilon_0}{C_{SC}} = \sqrt{\frac{2\epsilon\epsilon_0}{eN_D}\left(E_{\mathrm{WE}} - E_{\mathrm{FB}} - k_BT\right)} \tag{2.30}$$

2.3.3 Electrodeposition onto semiconductor electrodes

Due to the dependence of the surface charge on the semiconductor working electrode potential, different behaviour of electrodeposition is observed, depending on the relative position of the metal Nernst potential with respect to the band structure of the semiconductor. Different situations are illustrated in the schematic in Figure 2.13.

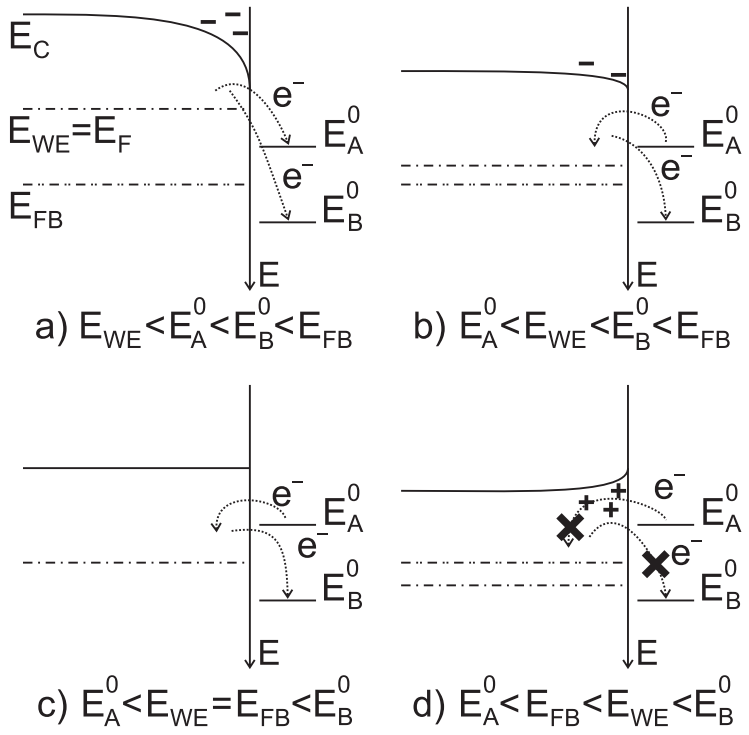

Figure 2.13: Illustration of metal electrodeposition and -dissolution onto and from semiconductor surfaces for two different metals with equilibrium potentials $E_A^0 < E_{FB}$ negative and $E_B^0 > E_{FB}$ positive of the flat band potential E_{FB}. In the band diagrams the space charge is indicate by plus (positive charge) and minus (negative charge) signs. In a) the working electrode potential $E_{WE} = E_F$, the flatband potential E_{FB}, and the conduction band edge E_C are labeled. a) For $E_{WE} < E_A^0 < E_B^0 < E_{FB}$ both metals are electrodeposited. b) For $E_A^0 < E_{WE} < E_B^0 < E_{FB}$ metal A is dissolved, while metal B is electrodeposited. c) At flatband conditions $E_A^0 < E_{WE} = E_{FB} < E_B^0$ metal A is dissolved, while metal B is electrodeposited. d) For $E_A^0 < E_{FB} < E_{WE} < E_B^0$ the potential barrier at the semiconductor / liquid interface inhibits charge transfer.

Equilibrium potential negative of flatband potential

A metal with a Nernst potential $E^0 < E_{FB}$ (E^0_A in Figure 2.13) can be electrodeposited at potentials $E_{WE} \leqq E^0$ (Figure 2.13a) and subsequently dissolved in the potential range $E_{FB} > E_{WE} > E^0$ (Figure 2.13b-c).

Equilibrium potential positive of flatband potential

A metal with a Nernst potential $E^0 > E_{FB}$ (E^0_B in Figure 2.13) is not electrodeposited at potentials $E_{WE} > E_{FB}$, due to electron depletion at the semiconductor surface (Figure 2.13d), but at potentials negative of the flat band potential ($E_{WE} < E_{FB} < E^0$) as shown schematically in Figure 2.13a-c. In the potential range $E_{WE} > E_{FB} > E^0$ a dissolution of electrodeposited metal at the surface is inhibited by the potential barrier at the semiconductor / electrolyte interface. The asymmetry of electrodeposition and -dissolution make the interface show rectifying behaviour.

2.3.4 Photoelectric effect

Charge carriers in semiconductors are not only generated by thermal excitation, but also photons with a sufficient energy $E_{photon} = h\nu \geq E_{gap}$ excite electrons from the valence band into the conduction band (photoelectric effect [123, 208, 223, 237]). While for the electrochemical behaviour of semiconductor surfaces at accumulation conditions the additional electrons play only a minor role, at depletion conditions the additional electrons can not be neglected with respect to electrochemical reactions [208, 238]. Consquently, to avoid uncontrolled electrochemical reactions, it is recommended to carry out all electrochemical experiments in the dark.

Chapter 3

Experimental details

In this chapter, at first, the experimental setup of the homebuilt scanning tunneling microscope operated in an electrochemical cell and the associated electric equipment used during the experiments in this thesis is presented.

The second part of this chapter introduces the experimental techniques employed for characterisation of the working electrodes in electrochemical environment.

In the last part of this chapter, the preparation of the working electrodes, i.e. STM tips and samples is described.

3.1 Experimental setup

The scanning tunneling microscope system operating in electrochemical environment, which was used for the experiments, is a homebuilt system combining commercially available components with parts developed in our group. A measurement chamber isolates the electrochemical cell together with the STM scanner from the environmental influences of the laboratory. The electronic equipment used for data acquisition and control of the experimental parameters is conveniently placed outside the chamber.

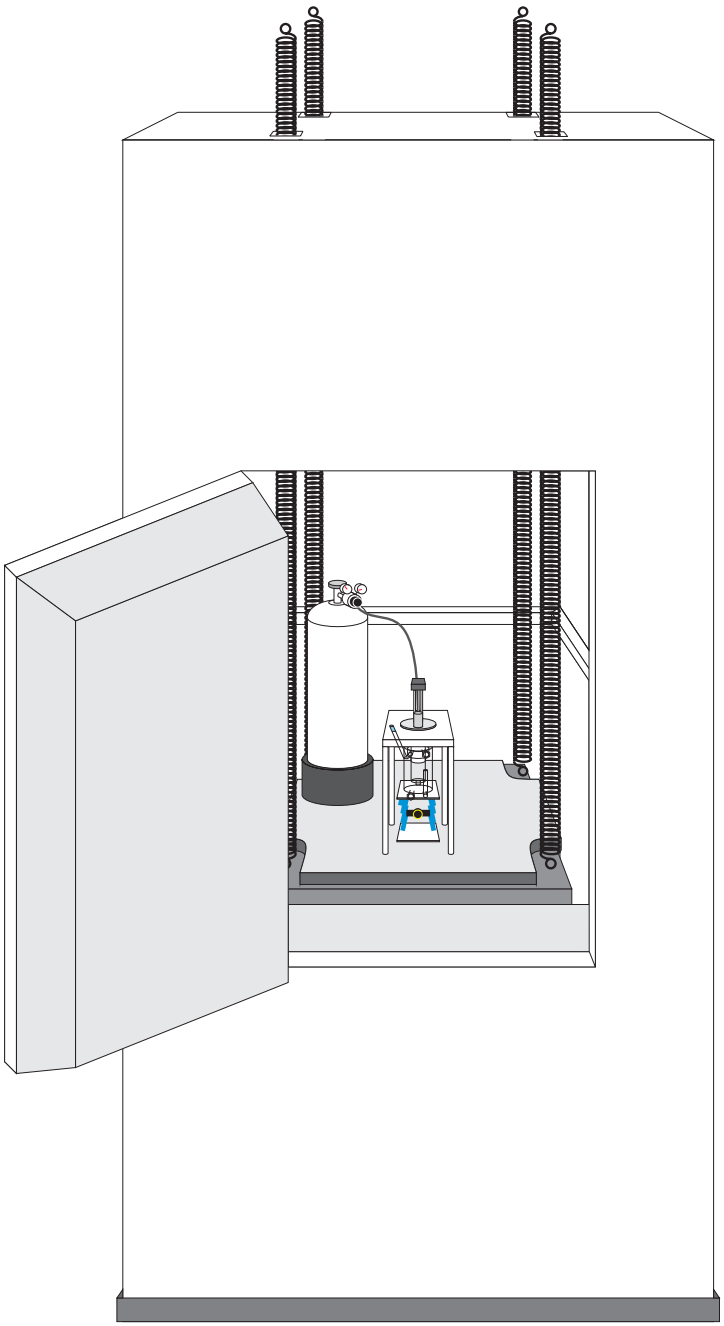

Figure 3.1: The experimental setup is suspended from the ceiling by springs and placed inside a chamber, which shields the setup against sounds, vibrations and light.

3.1.1 Measurement chamber

The scanning tunneling microscope has to be shielded against sounds and vibrations from the (laboratory) environment to allow for a stable tunneling contact [60,99,100,239]. The components for electrochemical measurements have to be placed in the dark, to avoid photoinduced electrochemical effects during the experiments [193,209–211,240–242]. Both conditions are fulfilled, by enclosing the experimental setup in a chamber (see Figure 3.1). This chamber consists of two boxes, a steel made one integrated into a wooden one. The steel made box shields electromagnetic radiation, the space between the two boxes filled with foamed plastic of 20 cm thickness for damping purposes. A door allows access to the experimental setup.

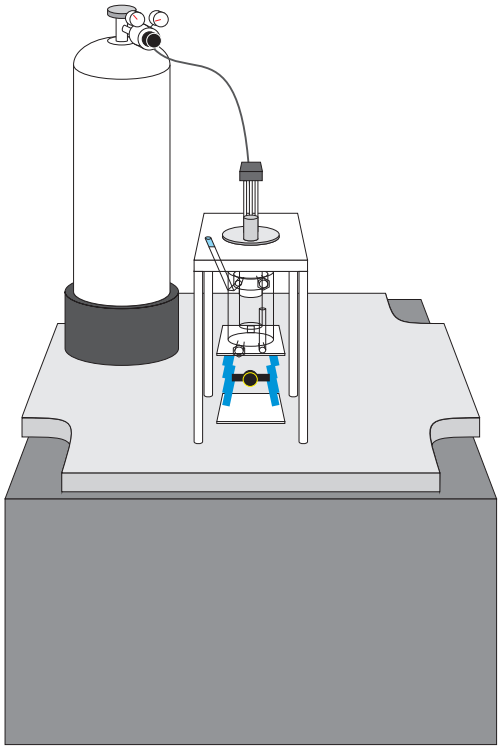

Figure 3.2: Experimental setup mounted on a concrete block. The electrochemical cell is placed underneath a fixture holding the assembly of sample holder and STM scanner. The cell provides a hermetically sealed electrochemical environment. The gas bottle allows for purging the electrolyte in the electrochemical cell with Ar gas.

The experimental setup is installed on a concrete block hovering within the metal box and, thus, isolated from vibrations from the floor (see Figure 3.1 and Figure 3.2). The concrete block is held by four spiral springs, which reach through the top of the chamber and are fixed on the ceiling of the laboratory. A support frame made from aluminum is fixed on the concrete block. It accepts the assembly of sample holder and STM scanner, while the electrochemical cell is put below the support frame onto a magnetic stirrer sitting on a lab boy. The latter arrangement allows a precise movement of the cell upwards

until the STM fixture with mounted sample holder is sitting tightly in the glass joint of the electrochemical cell, hermetically sealing the STM scanner / sample / electrolyte system against the environment. The setup allows for stirring of the solutions within the electrochemical cell, e.g. during removal of oxygen dissolved in the electrolyte from the electrochemical cell by purging with Argon 5.0. For this purpose a gas system, made of lightweight components, sits on the concrete block inside the box, thus, not short circuiting the vibrational isolation of the measuring setup.

Electrochemical cell

The electrochemical cell sketched in Figure 3.3 and Figure 3.4 evolved from the model developed in [243–245]. It is made of quartz glass, and consists of a main vessel and

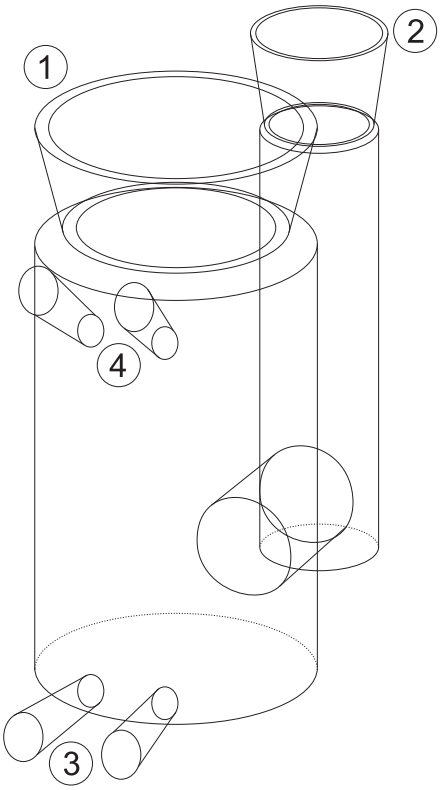

Figure 3.3: Sketch of the electrochemical cell utilised in the experiments. See text for details.

a support vessel interconnected by a small and big glass tube allowing the mixing of the electrolyte between the two vessels. The glass joint (1) of the main vessel receipts the fixture carrying sample holder and STM scanner, the glass joint (2) of the support vessel receipts the assembly for purging the electrolyte with Argon gas. One of the two glass joints (3) is used for connecting the platinum wire counter electrode and one of the glass joints (4) for connecting the Luggin capillary containing the reference electrode (Schott model B 3510, Calomel). The Luggin capillary is placed close to the sample

surface to minimise deviations of the electrode potential from its setpoint, due to the finite conductivity of the electrolyte. In contrast the counter electrode is placed at a long distance from the sample to generate a highest possible homogeneity in the current density, that the sample "sees". The counter electrode is separated from the main vessel by a frit, to avoid its eventual electroplating. The remaining joints of pairs (3) and (4) can be used for monitoring the tip of the STM by a camera (4) or are reserved (3), respectively.

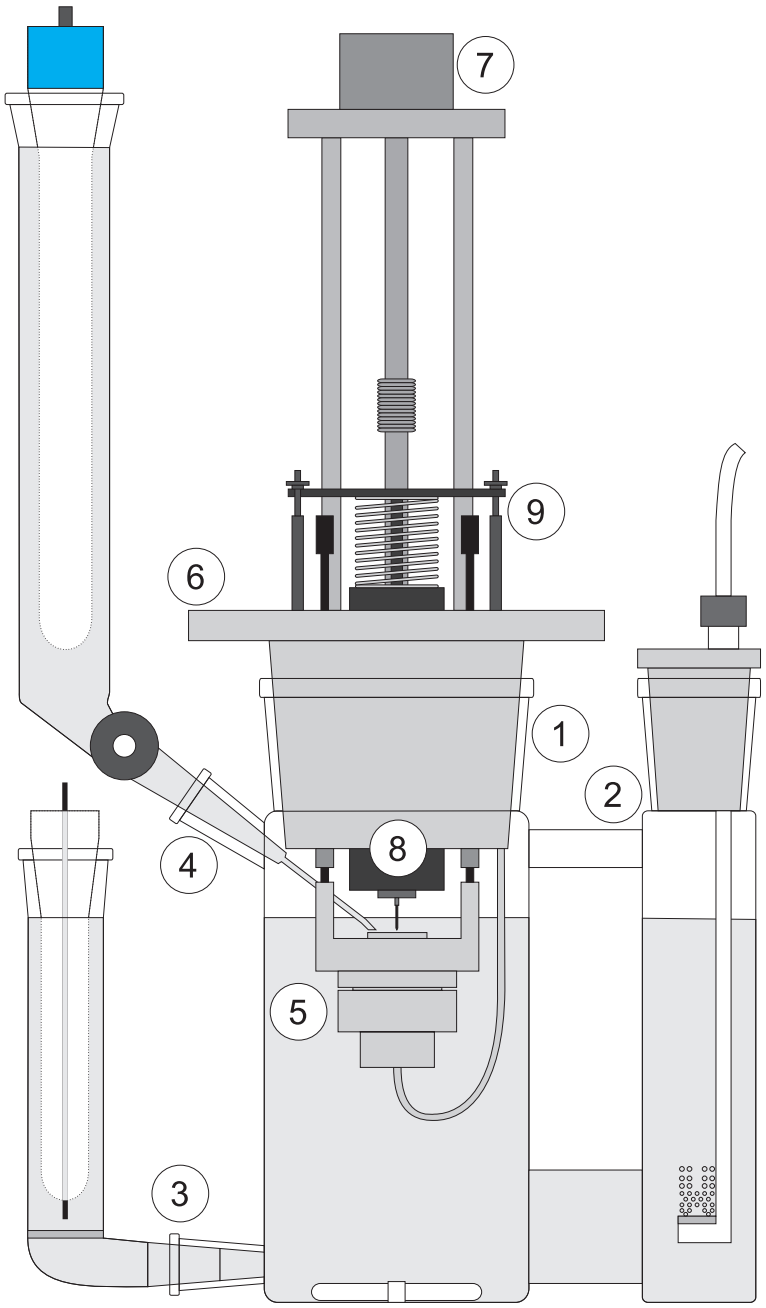

Figure 3.4: Sketch of the experimental setup used in combined STM and electrochemical experiments. See text for details.

Sample holder

The sample holder (5) is made of Teflon®, due to the inertness and low conductivity of this material and its resistance against contamination. It consists of two parts that are screwed together (see cross section in Figure 4.1), where into one part the sample is inserted while the other part houses a stamp connecting the sample to the bi-potentiostat on assembly. An aperture in the sample holder determines a defined area of the sample surface, which is exposed to the electrolyte. The sample surface outside this aperture is tightened to the electrolyte by a sealing lip on the screwed-in PCTFE receptacle in the case of a silicon sample and a Viton® O-ring of a different receptacle in case of a Au sample. The samples are pressed against the respective sealing by the spring of the contacting stamp.

The assembled sample holder is mounted at three points to a fixture by two bayonet couplings and one magnetic coupling. All three couplings are connected to the fixture (6) by fine pitch threads, that allow for coarse adjusting the distance between the sample (holder) and the tip of the STM. For an automated approach or retraction of the STM

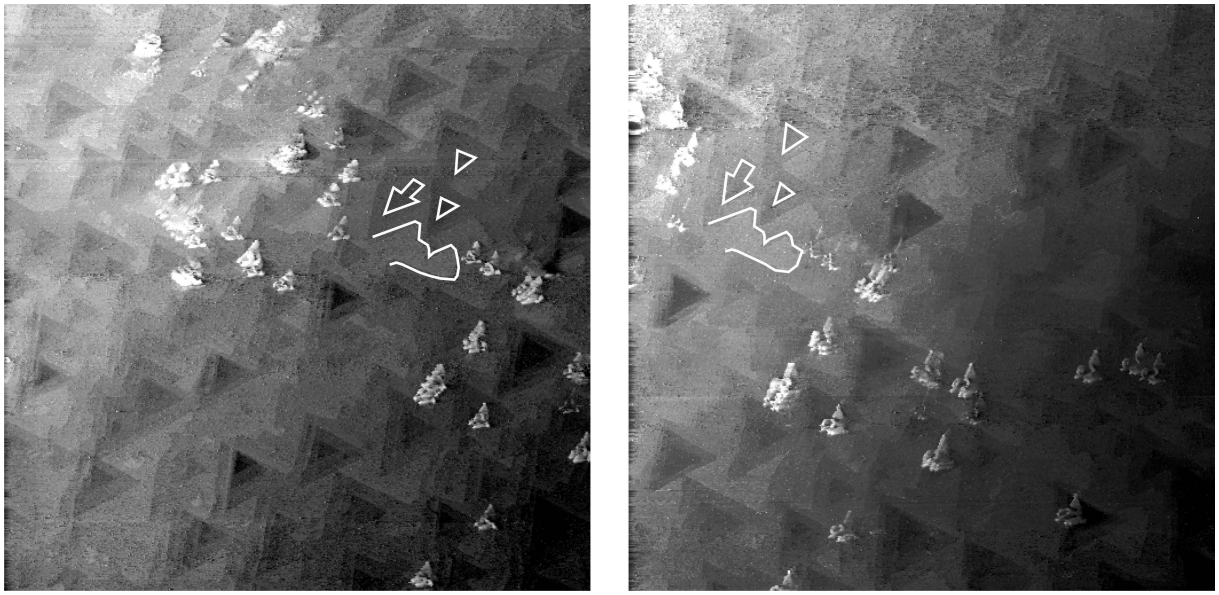

Figure 3.5: Two STM images ($3 \times 3\,\mu m$) of a n – Si (111):H surface illustrating the accuracy of the stepper motor based coarse height adjust of the STM tip. After the left image had been recorded, the STM tip was retracted and reapproached. Subsequently the right image was recorded. The white line markers in both images indicate the same structures on the n – Si (111):H surface. The displacement due to the reapproach is about $1.5\,\mu m$.

tip, a stepper motor (7) is available, which computer controlled drives the magnetic coupling. Retracting the STM tip and subsequently approaching it is achieved with a lateral accuracy of less than $2\,\mu m$ (see Figure 3.5). The fixture with mounted sample holder as a whole is put into the support frame (see Figure 3.2).

STM scanner

The housing of the STM scanner (8) is made of stainless steel, tightened by Viton® O-rings against the atmosphere in the electrochemical cell and contains the piezo ceramic for positioning the STM tip and the electronic part of the scanner. The piezo ceramic is a eight field tube element, sitting concentrically in the housing with one end of the tube being glued to the housing. Inside this tube sits the circuit board of the preamplifier, which gives a voltage signal proportional the tunneling current. In the experiments the STM scanner is is mounted to the fixture of the setup (6) and pressed against it by springs (9) to eliminate any clearance in between the two components.

3.1.2 Electronic equipment

A flowchart of parameters incorporated in the experiments is presented in the schematic in Figure 3.6. Details on the role of the related devices are given below.

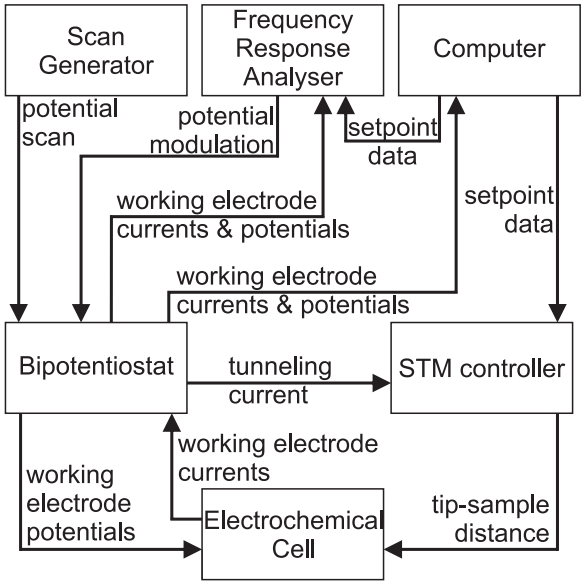

Figure 3.6: Flowchart of experimental parameters. The arrows indicate the direction of information flow, the text next to the arrows the information contents.

Electrochemical setup

The four electrode arrangement [163] used in the experiments is sketched in Figure 3.7. The working electrode potentials E_{WE} of both, sample (WE2) and STM tip (WE1) in the electrolyte were were set and controlled individually by a EC-Tec bi-potentiostat Model BP-700 with respect to the reference electrode (RE) involving the counter electrode (CE).

The BP-700 device makes electrode potentials and currents electronically available to a LabView program on a PC, which was used for recording cyclic voltammograms. The

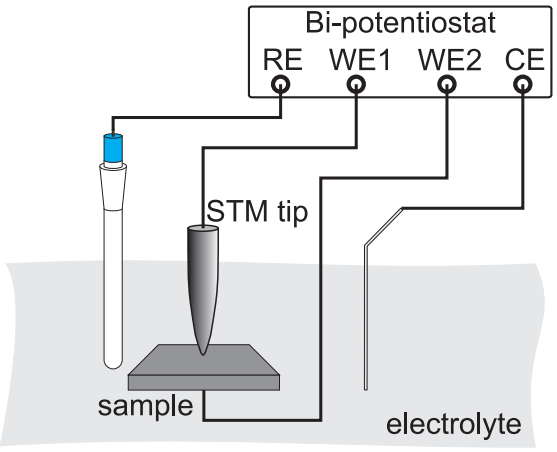

Figure 3.7: Schematic of the four electrode arrangement incorporated in the experiments.

tunneling current signal from the STM scanner is fed directly from the bi-potentiostat into the Nanoscope IIIA STM hardware as a $\pm 10\,\mathrm{V}$ signal.

The BP-700 allows the modification of the working electrode potentials by external devices as, e.g., an EC-Tec Bi-Scangenerator model SG-600, which was used for ramping the electrode potentials in cyclic voltammetry measurements and for adjusting them during nanostructuring routines.

For impedance measurements an impedance analyzer Model 1260 from Solartron was available. This device creates a periodic (sinusoidal) output voltage which is fed into the bi-potentiostat to modulate a working electrode potential. The electrode potential and current of the corresponding working electrode as measured by the bi-potentiostat are fed back into the analyzer. The analyzer generates the real and imaginary part of the complex impedance of the working electrode interface as function of frequency of the applied sinusoidal signal. For programming the analyzer the software ZPlot Version 3.3b was used, data analysis was done by ZView Version 3.3b, both from Scribner Associates Inc.

Scanning tunneling microscope

A Digital Instruments Nanoscope IIIA STM hardware in combination with the Nanoscope software 5.30r3sr3 installed on a PC running Microsoft Windows XP is incorporated for controlling the STM tip position relative to the sample and for obtaining STM images. Using the C/C++-like scripting language of the Nanoscope software the piezo of the STM Scanner could be addressed directly, allowing spatially manipulation of the tip relative to the sample, which was used in the experiments in Section 4.5.

3.2 Experimental techniques in electrochemistry

This section briefly introduces techniques employed for characterisation of sample surfaces in contact with aqueous electrolytes. Cyclic voltammetry is employed for studying electrodeposition and -dissolution processes at the surface of working electrodes. Impedance measurements are a suitable for investigating the electronic properties of the solid / liquid interface.

3.2.1 Cyclic voltammetry

In cyclic voltammetry the working electrode potential is ramped cyclic at a constant rate dE_{WE} / dt in between two potential values and at the same time the corresponding current is recorded. The potential values E_{WE} are plotted on the abscissa, the corresponding current density values $j(E_{WE})$ on the ordinate. From the $j(E_{WE})$ curve(s) electrochemical deposition or dissolution processes onto and from the working electrode surface can be identified. Some examples are illustrated in the schematic cyclic voltammogram in Figure 3.8 and the following text passages.

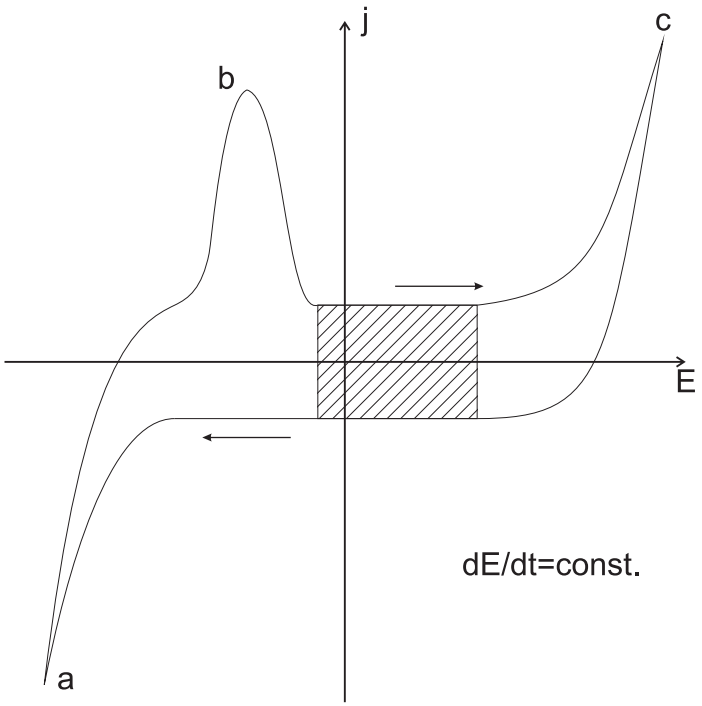

Figure 3.8: Schematic representation of a cyclic voltammogram. From the ruled area the capacitance of the Helmholtz layer may be determined. The increase in current density (a, b, c) is associated with different electrochemical processes at the sample surface.

A pair of cathodic *and* anodic current density (peaks a *and* b in Figure 3.8) centered at a working electrode potential indicate a redox system. In such a case a the areas under

the curves give the same amount of charge for reversible redox processes and the potential with no net current density determines the equilibrium potential of the redox system.

A cathodic or anodic current density *without* a corresponding current density of opposite sign indicates an irreversible process (peak a *without* b, peak c in Figure 3.8) – on the accessible potential and energy scales of the electrochemical experiment. Possible mechanisms involved at the working electrode surface are e.g. oxidation reactions, evolution of gas escaping from the electrolyte or energetic "asymmetries" like rectifying Schottky-contacts.

The capacitance of the Helmholtz layer can be obtained from a potential range in a cyclic voltammogram, where no electrochemical transfer processes occur (Figure 3.8, ruled area): When the working electrode potential is changed, the capacitance of the Helmholtz layer requires a charging current due to $\mathrm{Q} = \mathrm{C} \cdot \mathrm{U}$. At a constant ramping rate $\dot{\mathrm{E}} = \mathrm{dE/dt}$ the charge is given by $\mathrm{Q} = \mathrm{I} \cdot \mathrm{t} = \mathrm{j} \cdot \mathrm{A} \cdot \mathrm{t}$ and, thus, $\mathrm{C} = \mathrm{I}/\dot{\mathrm{E}} = (\mathrm{j} \cdot \mathrm{A})/\dot{\mathrm{E}}$. Typical values for the Helmholtz double layer capacitance for metal electrodes in aqueous electrolytes are in the order of $10\,\mu\mathrm{F\,cm^{-2}}$ [233, 246–257]. For n – Si (111):H the Helmholtz capacitance in aqueous electrolytes has been determined to lie in the range $(0.5 - 4)\,\mu\mathrm{F\,cm^{-2}}$, which is in the same order of magnitude as it was determined for other semiconductors. [212, 233, 234, 258–264]

3.2.2 Impedance measurements

In an electrochemical system a change in working electrode potential is accompanied by an electrical current. Response (current) and stimulus (potential change) characterise the interface and are related to the interface impedance $\mathcal{Z}$ of the working electrode. When the working electrode potential is modulated by a small sinusoidal alternating voltage of amplitude $\mathrm{U_{rms}}$[2], the current response amplitude is $\mathrm{I_{rms}}$ and the relative phase between $\mathrm{U_{rms}}$ and $\mathrm{I_{rms}}$ is $\varphi = \varphi_\mathrm{I} - \varphi_\mathrm{U}$, the surface impedance magnitude is given by Equation (3.1). A variation of the stimulus frequency reveals time constants in the response of the working electrode interface, which are represented by a change of φ.

$$|\mathcal{Z}| = \frac{U_{rms}}{I_{rms}} = \sqrt{\mathcal{R}^2 + \mathcal{X}^2} \tag{3.1}$$

Here $\mathcal{R}$ and $\mathcal{X}$ are the real and imaginary part of the (complex) impedance $\mathcal{Z}$ which are linked to each other by the relative phase φ (Equation (3.2)).

$$tan(\varphi) = \frac{\mathcal{X}}{\mathcal{R}} \tag{3.2}$$

[2] rms: - root mean square

In the complex notation the impedance $\mathcal{Z}$ is given by Equation (3.3)

$$\mathcal{Z} = \mathcal{R} + i\mathcal{X} \tag{3.3}$$

where $i = \sqrt{-1}$.

For a more detailed understanding of the interface, the interior of the "black box" impedance has to be revealed. This is achieved by modeling the impedance by an appropriate equivalent circuit based on common passive circuit elements. Since the electrical behaviour of those passive elements is well known, the (frequency dependent) behaviour of the equivalent circuit is accessible. By comparing the experimentally obtained impedance data to calculations based on the equivalent circuit, the values of the components in the equivalent circuit can be obtained.

This is illustrated in Figure 3.9 for the electrical circuit depicted in the upper part of the same figure. The values for the plot of $\mathcal{X}$ over $\mathcal{R}$ once have been obtained experimentally (full dots) and once have been obtained by calculations (open dots connected by lines). Next to some data points the frequency is noted at which they have been recorded.

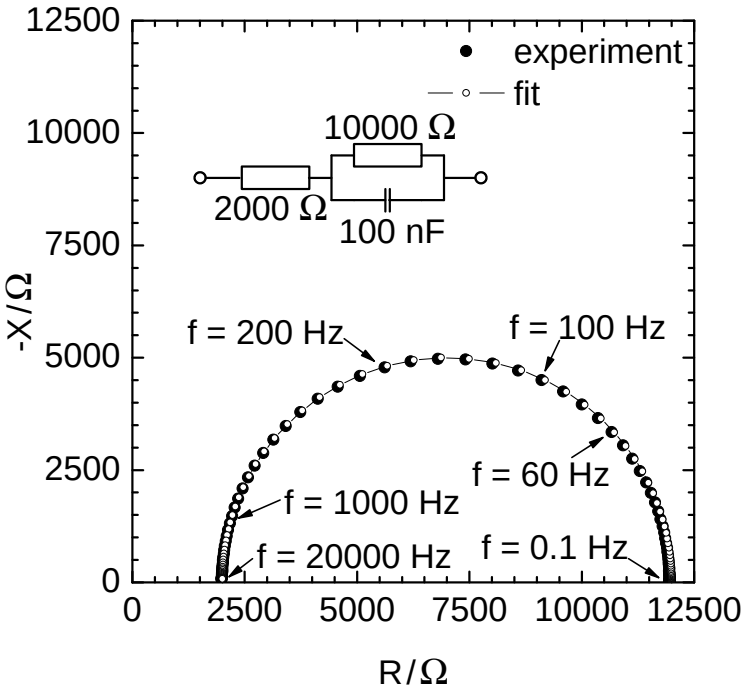

Figure 3.9: Plot of imaginary ($\mathcal{X}$) over real ($\mathcal{R}$) part of the complex impedance $\mathcal{Z}$ for the circuit depicted in the upper part of the figure. The frequency range under investigation was 0.1 to 20000 Hz, for some datapoints the corresponding frequencies are indicated in the plot.

From the plot several characteristics of the circuit can be easily identified:
At $\mathcal{R} = 2000\,\Omega$, $\mathcal{X} = 0$, $\mathrm{f} = 20000\,\mathrm{Hz}$ the $2000\,\Omega$ resistor dominates the circuit, since at high frequencies the capacitor short-circuits the $10000\,\Omega$ resistor.
At $\mathcal{R} = 12000\,\Omega$, $\mathcal{X} = 0$, $\mathrm{f} = 0.1\,\mathrm{Hz}$ the $2000\,\Omega$ and the $10000\,\Omega$ resistor in series dominate the circuit, since at low frequencies the capacitor can be neglected.
At $\mathcal{R} = 7000\,\Omega$, $\mathcal{X} = 5000\,\Omega$, the capacitor has the same impedance as the $10000\,\Omega$ resistor, thus, their equivalent is a resistor of $5000\,\Omega$, while the $2000\,\Omega$ resistor in series is unaffected.

The calculations are based on equations for the impedance of a resistor (Equation (3.4)) and a capacitor (Equation (3.5)), where $\omega = 2\pi\mathrm{f}$.

$$\mathcal{Z}_R = R \tag{3.4}$$

$$\mathcal{Z}_C = -\frac{i}{\omega C} = \frac{1}{i\omega C} \tag{3.5}$$

The impedance of the parallel circuit of the $10000\,\Omega$ resistor and the capacitor is given by

$$\begin{aligned}
\mathcal{Z}_{R/C} &= \left(\frac{1}{R_{10k}} + i\omega C\right)^{-1} = \left(\frac{1}{R_{10k}} + \frac{i\omega R_{10k} C}{R_{10k}}\right)^{-1} = \\
&= \frac{R_{10k}}{1 + i\omega R_{10k} C} = \\
&= \frac{R_{10k}\,(1 - i\omega R_{10k} C)}{1 + \omega^2 R_{10k}^2 C^2} = \\
&= \left[\frac{R_{10k}}{1 + \omega^2 R_{10k}^2 C^2}\right] + i\left[\frac{(-\omega R_{10k} C)}{1 + \omega^2 R_{10k}^2 C^2}\right]
\end{aligned} \tag{3.6}$$

Thus, the total impedance of the circuit in Figure 3.9 is given by combining Equation (3.6) and the $2000\,\Omega$ resistor.

$$\begin{aligned}
\mathcal{Z} &= \mathcal{Z}_R + \mathcal{Z}_{R/C} = \\
&= R_{2k} + \left(\frac{1}{R_{10k}} + i\omega C\right)^{-1} = \\
&= \left[R_{2k} + \frac{R_{10k}}{1 + \omega^2 R_{R/C}^2 C^2}\right] + i\left[\frac{-\omega R_{R/C}^2 C}{1 + \omega^2 R_{R/C}^2 C^2}\right] = \\
&= \mathcal{R} + i\mathcal{X}
\end{aligned} \tag{3.7}$$

3.3 Sample preparation

To ensure highest quality sample surfaces, samples are prepared only shortly before an experiment. In STM experiments in aqueous electrolytes at room temperature, other than in experiments in UHV environment and eventually at low temperatures, frequently changing the STM tips is unavoidable. For this reason, and because the same quality requirements as for the samples apply also to the STM tips, a batch of freshly prepared STM tips has to be available for each experiment. Electrochemical experiments are sensitive to contaminations and, thus, require highest possible purity of the electrochemical components in the setup. These aspects have to be borne in mind during sample preparation, to establish a reproducible and reliable basis for the experiments.

3.3.1 Preparation of STM tips

Etching of STM tips

The STM tips employed in the experiments were made from a gold wire having a diameter of 250 µm by an electrochemical etching technique. An overview of the etching setup is given in Figure 3.10. The setup is enclosed by a box made out of acryl glass standing

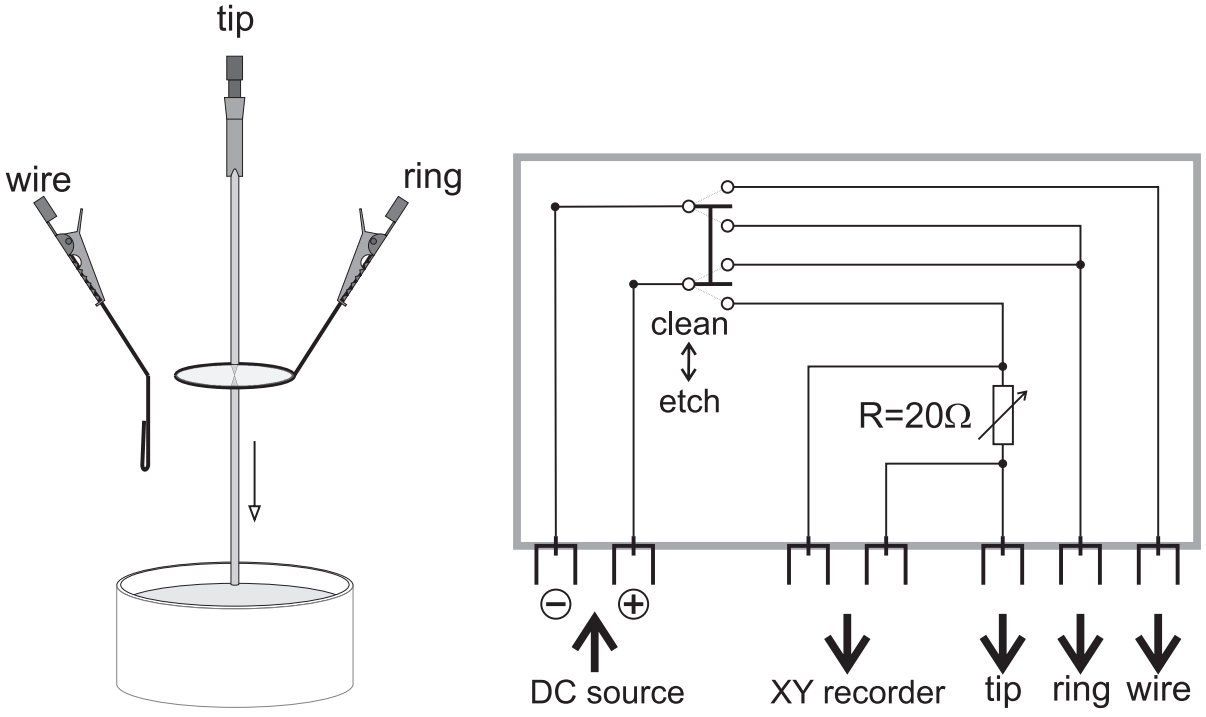

Figure 3.10: Left: Two electrode setup for etching STM tips from Au wire. Etching occurs at the contact surface of gold wire and HCl lamella. The electrodes (tip and ring) are connected to the DC Voltage supply by crocodile clamps. Right: Schematic of switching box employed for applying electrode potentials.

on top of a stack of foam rubber mats to isolate the etching procedure against vent and

mechanical vibrations. The potentials of the electrodes were controlled via a switching box (wiring diagram see Figure 3.10) connected to a Hewlett Packard E3615A DC Power supply. The tips are etched in a two electrode arrangement, with the gold wire being the anode. The cathode is a platinum wire of diameter 250 µm formed to a circle of diameter 10 mm. The gold wire is centered within this circle, to achieve symmetrical etching conditions.

The electrochemical etching occurs at the contact area of the Au wire and a lamella of hydrochloric acid of 32%,wt ("HCl") [202, 265–267] that is created within the platinum ring by dipping the ring into a small Teflon® beaker filled with HCl.

Only the part of the gold wire below the Pt ring is used as a STM tip, because when it is disconnected from the anode by dropping off, etching stops immediately and blunting of the tip apex by further etching is avoided. A specially designed Teflon® cup catches the dropping tip without contacting and, thus, damaging its apex. This cup is filled with tridistilled water, diluting the remaining acid on the tip after the drop off.

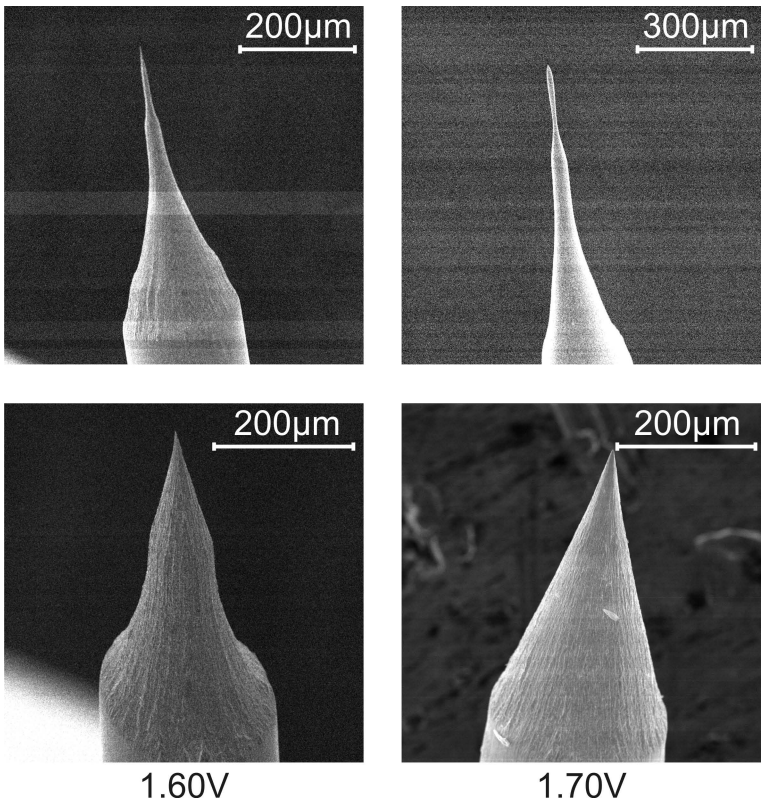

Figure 3.11: SEM images of four STM tips etched at 1.60 V (left column) and 1.70 V (right column), respectively.

After the tip had been etched, residues related to Au etching at the platinum ring were removed by immersing the ring in a Teflon® beaker filled with HCl and setting it as anode against the platinum wire cathode of diameter 250 µm at a DC voltage of 1.15 V for two minutes. The whole procedure was repeated for each STM tip.

Gold tips have been etched at a DC voltage of $U_{etch} = 1.65\,V$, since STM tips created at $1.60\,V \leqq U_{etch} \leqq 1.70\,V$ showed the best results regarding mechanical stability and imaging quality in STM experiments. In Figure 3.11 scanning electron microscope (SEM) images of STM tips etched in this potential range are shown. For lower voltages the surface of the tips showed many crystal facets which lead to multiple imaging of a surface, higher voltages gave long and tall tips that were mechanically not stable enough for STM imaging. These observations confirm the results obtained in [268].

Partial isolation of STM tips

To allow for operation of a STM in electrolytic environment, it is necessary to keep Faradic currents at STM tips immersed in an electrolyte smaller than the tunneling current through the STM tip, which is typically of the order of $(10^{-11} - 10^{-9})\,A$ [177, 193, 196, 245, 269–276].
Therefore, the STM tips were partially isolated with Apiezon W wax[3] [168, 177, 196, 269, 272, 274], as schematically shown in Figure 3.12, to reduce their surface area exposed to the electrolyte.

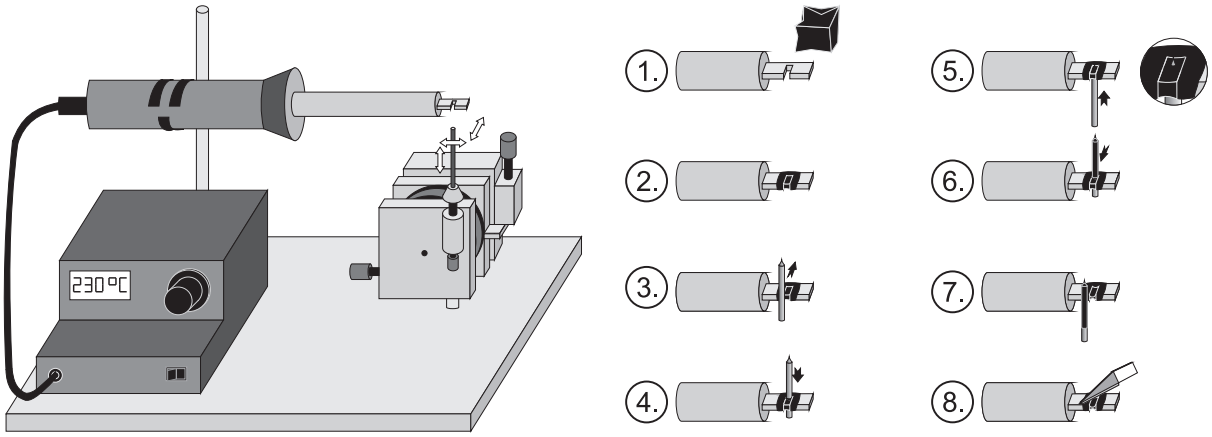

Figure 3.12: Left: Setup for partial isolation of the STM tips. The STM tip is moved by a manipulator within the wax molten by the soldering iron. Right: Procedure applied for partial isolation of the STM tips.

At a temperature of 230 °C the grove installed in the soldering tip is filled with wax. The blunt end of the gold tip is put into the stainless steel tube fixed to the multiple direction micrometer screw manipulator, that is used to move the tip inside the groove of the soldering tip. To coat the STM tip with wax, it is moved downwards, until only the apex of the tip remains uncovered by the wax and subsequently the direction is turned, resulting in a even wax coverage of the tip. The whole procedure is monitored by eye through a microscope. After the tip is removed from the apparatus, the soldering tip is

[3] M&I Materials Ltd., Hibernia Way, Trafford Park, Manchester M32 0ZD, United Kingdom

cleaned from the remaining wax by a scalpel. The wax covered STM tips were stored in a Teflon® holder, covered by tridistilled water, until they were used in STM experiments.

This isolation technique allows to reduce the faradic current though the STM tip to less than 10 pA in the experiments carried out during this thesis.

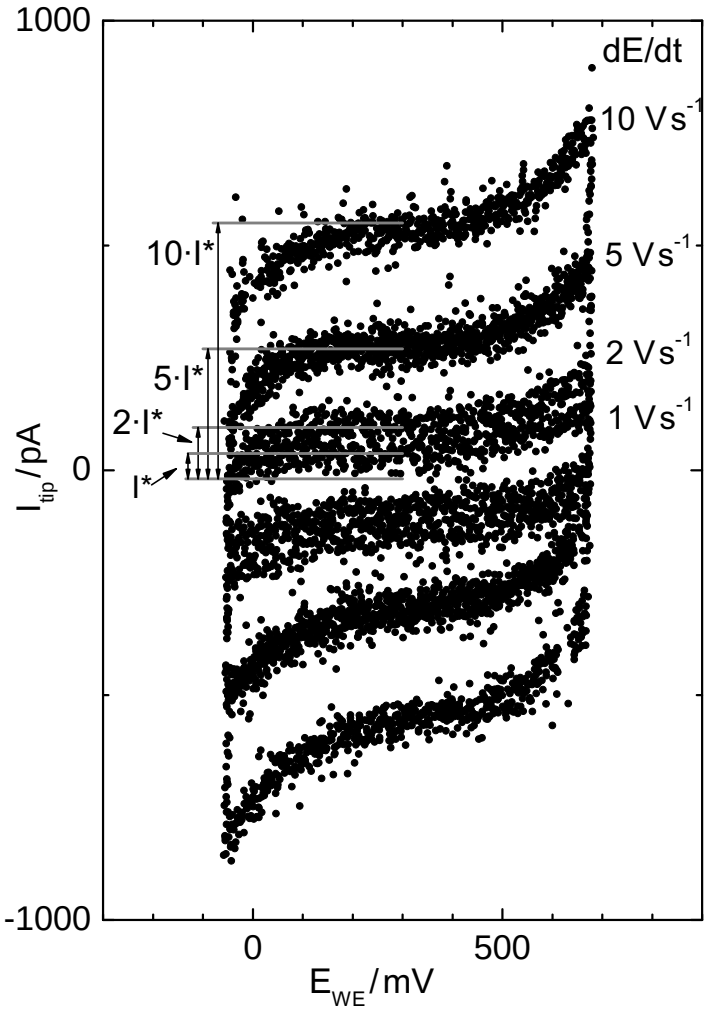

Figure 3.13: Cyclic voltammogram in the double layer potential range of a STM tip in 0.1 M H_2SO_4. Sweep rates were $dE/dt = 10\,V s^{-1}$, $dE/dt = 5\,V s^{-1}$, $dE/dt = 2\,V s^{-1}$, $dE/dt = 1\,V s^{-1}$. The grey lines indicate multiples of the current I* measured at $dE/dt = 1\,V s^{-1}$. From the current measured at a particular sweep rate the surface area exposed to the electrolyte can be determined.

In Figure 3.13 cyclic voltammetry measurements on a partially isolated STM tip are shown. The current is proportional to the potential sweep rate, as indicated in Figure 3.13 (multiples of I*). Cyclic voltammetry measurements of the STM tip allow the surface area exposed to the electrolyte to be calculated according to $C = (j \cdot A)/\dot{E} = I/\dot{E}$ (see section 3.2.1). From Figure 3.13 and a double layer capacitance $C_{dl}^{Au} = 25\,\mu C cm^{-2}$ [245] a surface area of $A_{tip} = 2.2 \cdot 10^{-6}\,cm^2$ is determined, which is within the range of values reported

in previous measurements in the literature [177, 245]: $10^{-4}\,\mathrm{cm}^{-2} < \mathrm{A_{tip}} < 2.2 \cdot 10^{-7}\,\mathrm{cm}^{-2}$.

STM tip performance on Au(111) surfaces

Au(111) surfaces were employed for testing the STM tips prepared in Section 3.3.1. No single crystals, but commercially available samples with (111) surface orientation fabricated by arrandee [4] were used. These samples consisted of a glass plate of $11 \times 11\,\mathrm{mm}^2$ with a intermediate layer of chromium and a top layer of gold on them. Their (111) surface after preparation can be compared in quality with massive single crystals [277].

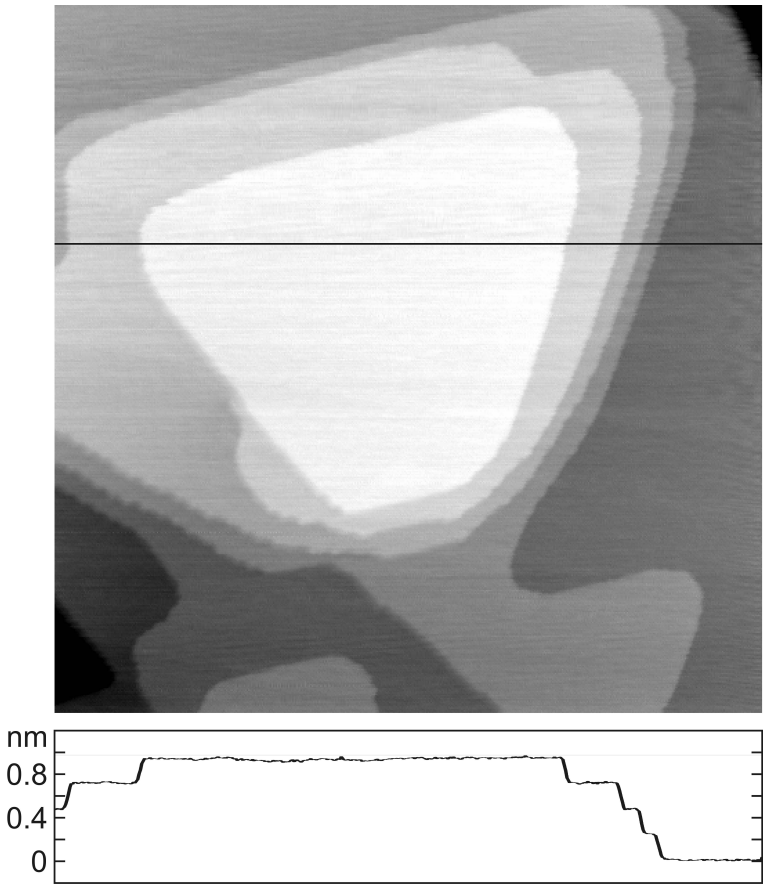

Figure 3.14: Typical STM image of a Au(111) surface after the annealing treatment (see text). In the linescan taken at the position of the solid line the equidistant spacing (height 0.24 nm) of terraces is clearly observed. Image size is 408 × 408 nm^2.

Before mounting the samples to the STM, they were flame annealed in a hydrogen flame to induce surface reconstruction [172, 254, 277–282]. Heating of the sample was regulated by adjusting the sample-flame distance by hand. The glowing colour was kept at a bright orange for two minutes with intermediate withdrawal of the sample from the flame to avoid a bending of the glass substrate by the heat from the flame. After annealing

[4] arrandee; Dr. Dirk Schröer; Schloßstraße 94; D-33824 Werther; Germany

the samples were stored below a glass cone under nitrogen atmosphere until they cooled down to room temperature.

By this treatment samples with broad terraces and a step height of 2.4 nm, typical for Au(111) surfaces [277, 278, 283, 284], were obtained (Figure 3.14). On those samples the reconstruction of the Au(111) surface [36, 172, 202, 245, 254, 277, 278, 280, 285–290] could be identified by STM imaging in experiments at ambient conditions and in electrolytic environment, illustrating the resolution achievable with some of the STM tips (Figure 3.15).

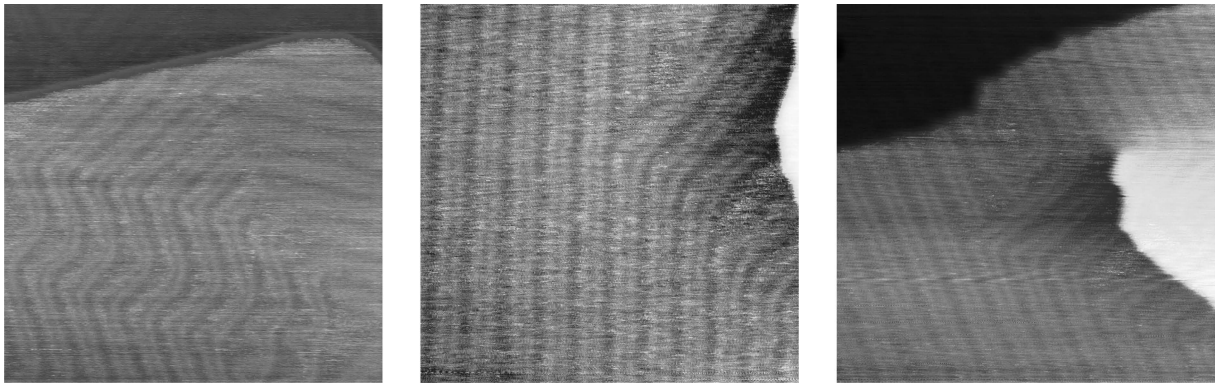

Figure 3.15: STM images of the reconstruction of the Au(111) surface after flame annealing the sample (see text) illustrating the imaging quality of the STM tips. Size of left image is $115 \times 115\,\mathrm{nm}^2$, middle and right image are $100 \times 100\,\mathrm{nm}^2$. Recorded at ambient conditions.

3.3.2 Preparation of n – Si (111):H surfaces

The Si samples in the experiments during this thesis were made from commercially available (Wacker Siltronics) n – Si (111) wafers fabricated in a floating zone process. The wafers are P-doped ($10^{15}\,\mathrm{cm}^{-3}$) with a conductivity of (1–10) Ωcm, and polished on one side to less than 0.1° misorientation.

From the "as delivered" wafers samples of size $11 \times 11\,\mathrm{mm}^2$ were cut by a glass cutter. The cuts were performed on the polished side of the wafer and aligned along the <110> orientation of the wafer [291] and perpendicular to this direction.

To obtain atomically flat, H-terminated n – Si (111) surfaces (n – Si (111):H), a wetchemical preparation procedure was employed, consisting of a precleaning step and the actual transformation of the Si sample surface into a n – Si (111):H surface. During this preparation procedure, the samples were only in contact with tools made of Teflon® and the chemicals.

The $11 \times 11\,\mathrm{mm}^2$ Si samples were mounted to a sample holder made of Teflon® with

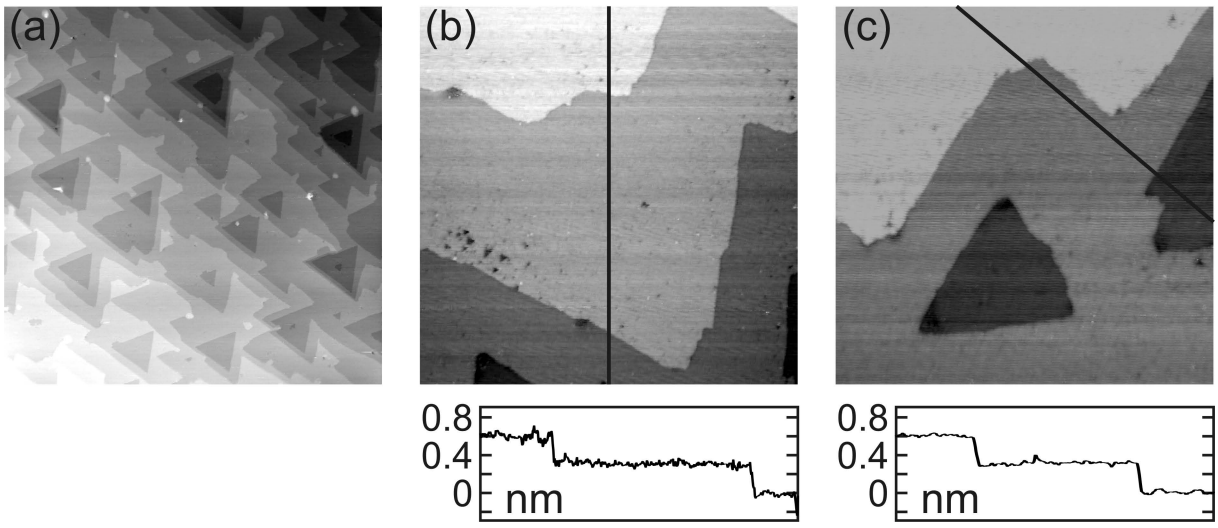

Figure 3.16: STM images of Si surfaces obtained after cleaning by acteon (5 min), ethanol (5 min) and triply distilled water (30 s), etching in NH_4F (6 min). The size is $3000 \times 3000\,nm^2$ for image (a) and $500 \times 500\,nm^2$ for (b) and (c). Imaging conditions were: (a) $E_{WE} = -20\,mV$, $E_{tip} = +680\,mV$ $I_{tunnel} = 50\,pA$; (b) $E_{WE} = -280\,mV$, $E_{tip} = +520\,mV$ $I_{tunnel} = 30\,pA$; (c) $E_{WE} = -20\,mV$, $E_{tip} = +680\,mV$ $I_{tunnel} = 30\,pA$. All images were recorded within electrochemical environment i.e. 0.1 M H_2SO_4. The lines in (b) and (c) indicate the position of the profiles depicted under the respective STM image. The step height of 3.1 Å for n – Si (111):H surfaces is outlined by bars in the profiles.

the polished (111) side directed downwards for handling during the wetchemical preparation procedure.

Precleaning of the sample started with putting the sample holder into a Teflon® beaker filled with acetone and putting the beaker into an ultrasonic bath for 5 minutes. In a next step, the acetone in the beaker was replaced by ethanol and ultrasonic cleaning continued for 5 minutes. Finally, the ethanol in the beaker was replaced by tridistilled water for a last ultrasonic cleaning step of 30 seconds. No RCA cleaning process [292–294] was applied, since it was not found to improve the sample surface quality any further. For the time, until the etching setup was prepared (approximately 2 minutes), the sample holder containing the sample was stored in another Teflon® beaker filled with tridistilled water.

The transformation of the precleaned Si samples into n – Si (111):H is achieved by etching the samples in a 40%,wt. solution of NH_4F. This etching step removes the thermal oxide from the sample surface [181, 186, 295–301] and saturates dangling Si bonds with hydrogen [36, 92, 93, 125, 181, 186, 193, 295, 296, 301–324]. Since NH_4F has a higher Si etch rate in the (111) plane than perpendicular to the (111) direction it preferentially attacks the step edges of Si(111) terraces [92, 181, 186, 193, 296, 304, 306, 308–310, 312–314, 316, 325, 326]. Due to this "step-flow etching" process, atomically flat (111) terraces emerge at the sample surface [36, 92, 95, 181, 186, 193, 296, 301, 303–308, 311–315, 317, 321, 327, 328] .

These terraces have a height of 0.31 nm and represent Si bilayer steps [166, 167, 182, 186, 193, 303, 304, 308, 310, 311, 315, 317, 322, 329–334], their width is determined by the miscut angle from the (111) plane.

For the etching step, the sample holder containing the sample was put in a Teflon® beaker filled with 30 ml of NH_4F for 6 min. The beaker was covered by a intransparent plastic cap during etching. After the etching step, the samples were removed from the sample holder by Teflon® tweezers. The surface of the n – Si (111):H samples is hydrophobic [125, 193, 295–297, 309, 320, 325, 335–337] and the surface becomes dry upon removal from the NH_4F. Drops, eventually remaining at the breaking edge of the samples were dipped off by a laboratory wipe, taking great care not to touch the surface. In a next step the n – Si (111):H samples were inserted into the sample holder of the experimental setup.

The samples obtained by the wetchemical etching show wide atomically flat terraces with step heights of 3.1 Å (Figure 3.16) which exhibit triangular shaped holes. The formation of such holes during etching has been attributed to oxygen in the etching solution [93, 304, 307, 312, 315, 317, 330, 332, 333, 338–340]. In our experiments, their emerging could not be suppressed by purging NH_4F with nitrogen or argon gas, which has been reported a suitable method in literature [93, 304, 312, 315, 317, 330, 332, 333, 338–340]. An

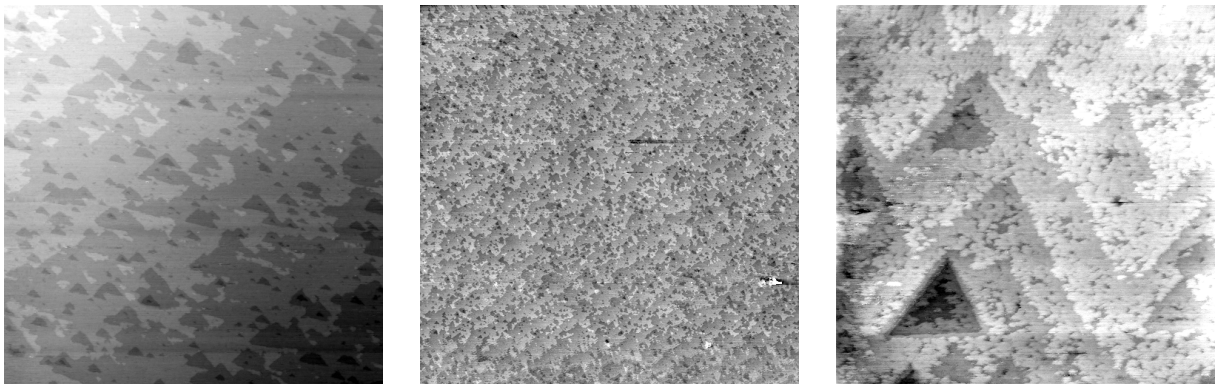

Figure 3.17: STM image of Si surfaces obtained after cleaning by acteon, ethanol and triply distilled water, etching in NH_4F and a subsequent 10 s dip in triply distilled water. The left and right image are $1000 \times 1000\,nm^2$ in size, the middle image $5000 \times 5000\,nm^2$, respectively. All images were recorded at ambient conditions, i.e. sample exposed to air. $E_{WE} = -40$ mV, $E_{tip} = +760$ mV, $I_{tunnel} = 100$ pA.

additional etching step in HF before the NH_4F treatment to remove oxide from the surface [296, 305, 325, 341] was not found to improve the sample quality any further regarding terrace width and creation of etching triangles [93, 304, 330] and, thus, omitted.

Extensively rinsing the Si sample under preparation in tridistilled water after the NH_4F etch resulted in a fraying of the (111) terraces on the sample surface (Figure 3.17).

Only for rinsing intervals below about half a second (dip inside water) such fraying

was not observed. Investigation of the underlying mechanism was not goal of this thesis and to avoid unnecessary degradation of the n – Si (111):H surface the water rinsing step was omitted.

Since the frayed n – Si (111):H surfaces were still hydrophobic and imaging by STM possible a oxidation of the sample surface is highly unlikely. A possible explanation of the observations may be an etching attack of water on the n – Si (111):H surface, as reported in the literature [342].

Great care has to be taken not to scratch the surface during handling of the Si samples, even "soft" Teflon® tools are capable of scratching the surface (see Figure 3.18). Those scratches can promote charge transfer processes [343] and cause unwanted or uncontrolled deposition of metal or other material from solution onto the surface [344–346].

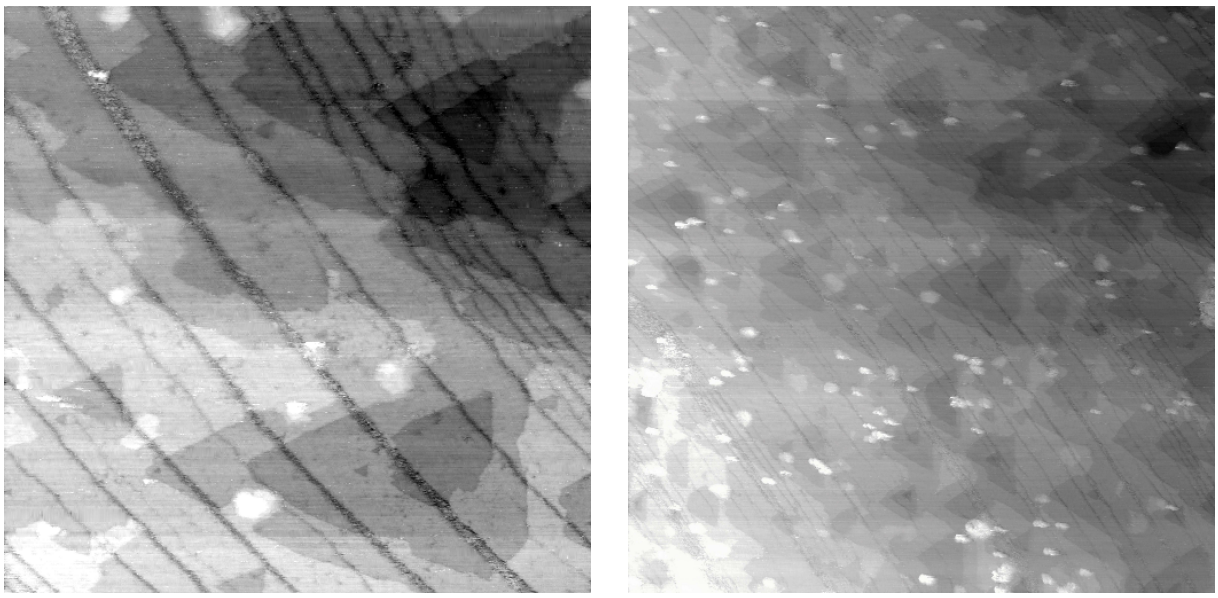

Figure 3.18: Two STM images showing scratches on the n – Si (111):H surface, which were accidentally generated by Teflon® tweezers during sample handling. $E_{WE} = -280\,mV$. $E_{tip} = +520\,mV$. $I_{tunnel} = 30\,pA$. Electrolyte: 0.1 M H_2SO_4. Image size is $1 \times 1\,\mu m^2$ and $3 \times 3\,\mu m^2$ for the left and right STM image, respectively.

Chapter 4

Experiments & results

This chapter gives a description of the experiments carried out during this thesis and presents the respective results.

The first section of this chapter treats the handling and proper installation of the experimental setup, which is common to all of the experiments presented here.

The second section of this chapter is concerned with the characterisation of the n – Si (111):H samples in the aqueous electrolyte 0.1 M H_2SO_4, which were employed in the experiments presented in the subsequent sections of this chapter. Electrically active "surface states" are found in the n – Si (111):H samples and related to hydrogen incorporated in the n – Si (111):H subsurface region.

The third section of this chapter presents a simulation study on the effect of the STM tip apex radius on the resolution obtained in STM images, focused in particular on the representation of nanometer sized structures in STM images. The results are employed in the analysis of STM images obtained within this thesis.

In the fourth section of this chapter the effect of the hydrogen related surface states on electrochemical charge transfer processes at electron depleted n – Si (111):H surfaces is investigated. Exemplarily, the system Cu / Cu^{2+} is employed, due to its Nernst potential positive of the flatband potential E_{FB}.

In the fifth section of this chapter the influence of electric fields on electrochemical charge transfer processes at n – Si (111):H surfaces under electron accumulation conditions is investigated using the system Co / Co^{2+}.

4.1 Preparation of experiments & preliminary considerations

To achieve significant and reproducible results from electrochemical experiments, highest purity of the incorporated substances and high precision instruments are required. Under appropriate experimental conditions, the cleanliness of an electrochemical environment is comparable to ultra high vacuum [244]. Accordingly, there is also a demand for highest cleanliness of the laboratory glassware and handling tools, since their contamination can easily annihilate all electrochemical preparation efforts.

To achieve the best possible cleanliness, the glass equipment and related accessories were stored in glass containers filled with Caro's acid [347, 348] (1 to 1 mixture of H_2O_2 and H_2SO_4) before and after the experiments. This acid decomposes and dissolves contaminants, in particular organic material. The equipment was washed most accurately by flowing triply distilled water before assembly and the beginning of the experiment. After finishing the experiments, the glass equipment was likewise washed, to avoid contamination of Caro's acid by residue from the experiments in the glass equipment, especially by metal ions. All handling of the glass equipment was carried out wearing Nitril gloves to further reduce sources for contaminants.

In all experiments the working electrodes were n – Si (111):H samples and gold STM tips prepared according to the procedures developed in section 3.3. The n – Si (111):H samples were contacted on the back side, which was not exposed to the electrolyte, by the copper stamp of the sample holder (Figure 4.1). An ohmic contact between copper stamp and n – Si (111):H was achieved by applying an GaIn eutectic to the stamp before assembly [208, 311, 322, 333, 334, 349–357].

The electrolyte always was 0.1 M H_2SO_4 made from ultrapure acid and triply distilled water. In all experiments the 0.1 M H_2SO_4 electrolyte inside the hermetically sealed electrochemical cell was purged with Argon 5.0 for at least 30 minutes before the n – Si (111):H sample and the STM tip attached to the STM piezo scanner were inserted into the electrolyte. By this purging procedure oxygen dissolved in the electrolyte could be removed to a sufficient extend for our experiments [225, 352, 353, 358, 359]. Without this Argon treatment, oxygen dissolved in the electrolyte would cause unwanted electrochemical reactions. During STM experiments, the Argon supply was shut down, since the vibrations from Argon bubbles and the magnetic stirrer make the formation of a stable tunneling contact impossible.

The samples were brought in contact with the electrolyte under potential control, i.e. connected to the bi-potentiostat and with the reference electrode and counter electrode already in contact to the electrolyte in the electrochemical cell, as illustrated by the

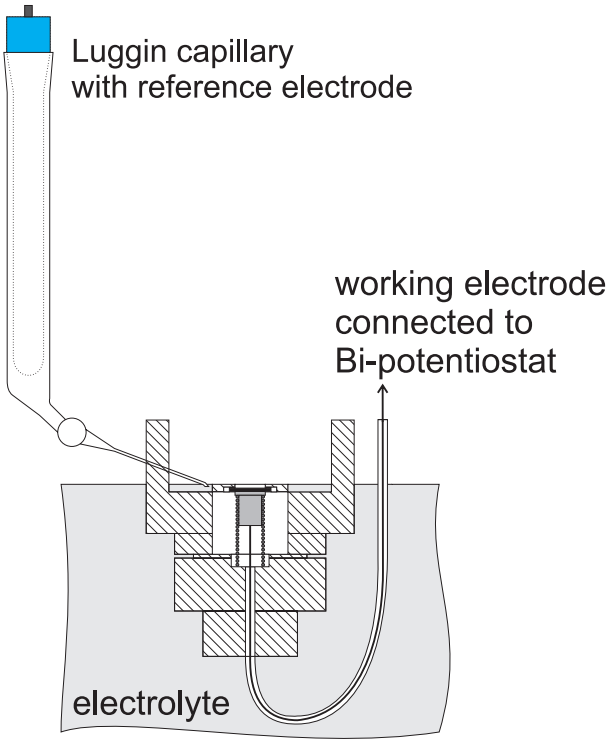

Figure 4.1: Insertion of the sample into the electrolyte under potential control. The schematic shows a cross section of the sample holder immersed in the electrolyte and a n – Si (111):H electrode contained in the sample holder. The Luggin capillary is placed as close to the n – Si (111):H sample surface as possible to minimise the potential drop within the electrolyte.

schematics Figure 4.1 and Figure 4.2.

Metal ions for electrochemical charge transfer reactions were introduced into the H_2SO_4 electrolyte by adding the sulfate salt (MSO_4, M: metal) of the desired metal. The required amount of salt was balanced and supplied into the electrolyte at a working electrode potential far positive of the Nernst potential E^0 of the corresponding metal redox couple M / M^{2+}.

All experiments were performed in the dark, i.e. in the closed measurement chamber, to avoid any photoinduced processes at the sample [360].

Impedance measurements were carried out using a sinusoidal potential modulation of $10\,mV_{rms}$ amplitude in the frequency range 0.1 to 3000 Hz.

The STM was operated in constant current mode in all of the experiments at a scanning speed of (0.5 – 1) Hz, i.e. (0.5 – 1) line scans per second.

The experiments in the present thesis have confirmed previous reports on the stability of n – Si (111):H surfaces, or H-terminated Si surfaces general, against oxidation in deaer-

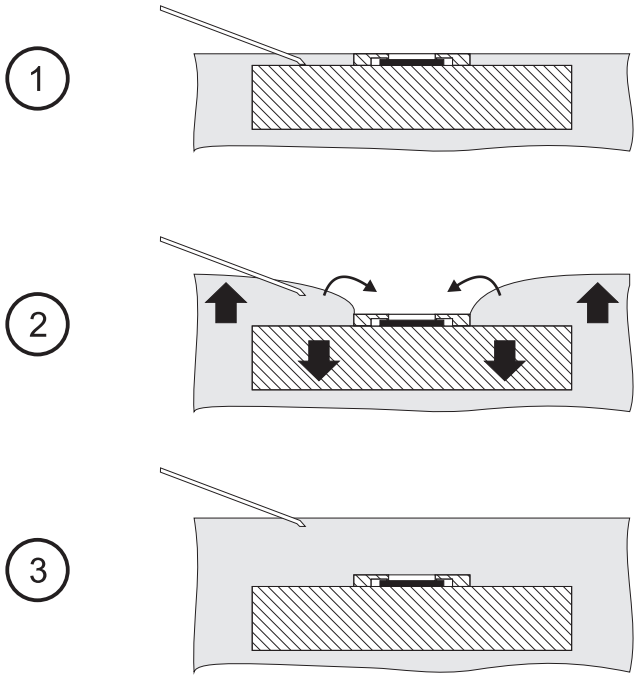

Figure 4.2: Contacting of the n – Si (111):H sample surface and the electrolyte. At first the reference electrode and counter electrode (not shown) are in contact with the electrolyte. Next, the electrochemical cell is raised with respect to the sample holder, which causes the level of electrolyte to raise also. The electrolyte covers the sample holder up to the elevation next to the sample surface. Finally the electrolyte spills and contacts the sample surface under potential control.

ated H_2SO_4 solutions [165, 311, 334, 354, 355, 361]: STM images obtained here show flat atomically flat n – Si (111):H terraces, which is not expected for oxide covered Si surfaces, but at least a strong degradation of STM image quality [305, 362], if imaging by STM is possible at all [295]. Furthermore, an oxide covered n – Si (111) surface immersed in an electrolyte can be identified from impedance measurements, where such a surface exhibits E_{WE} independent capacitance values [235]. This behaviour has not been observed in the present experiments.

4.2 Characterisation of n – Si (111):H aurfaces [5]

The n – Si (111):H surface in contact with 0.1 m H_2SO_4 was characterised by cyclic voltammetry and impedance spectroscopy in addition to the characterisation by STM in subsection 3.3.2. During these experiments no metal salts had been added to the electrolyte.

4.2.1 Oxygen dissolved in the electrolyte

In Figure 4.3 two cyclic voltammograms of a n – Si (111):H sample in 0.1 M H_2SO_4 electrolyte purged with Argon 5.0 are shown. The first scan (grey curve) was recorded after inserting the sample after about 15 minutes of purging, the second scan (black curve) was recorded after additional 20 minutes of purging. Going from positive to negative

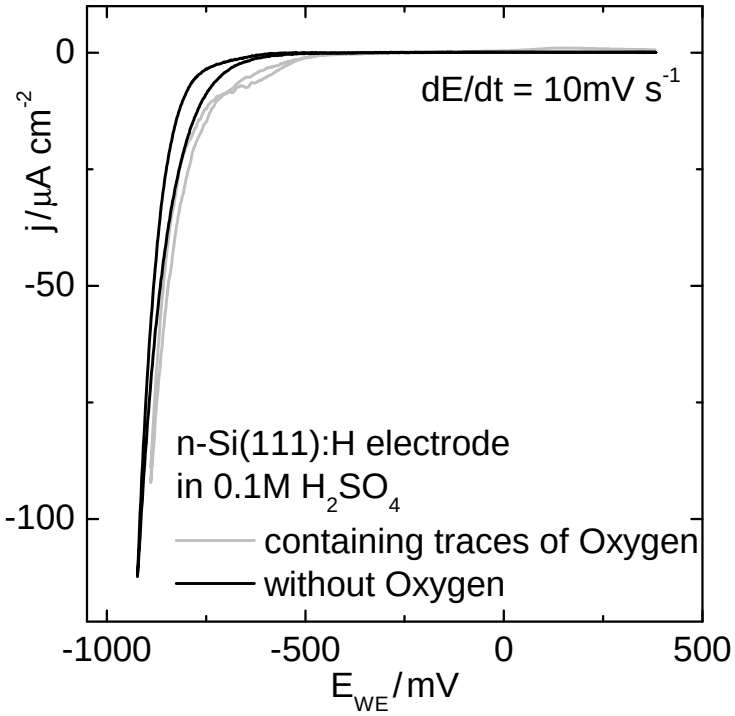

Figure 4.3: Cyclic voltammograms of a n – Si (111):H electrode in 0.1 M H_2SO_4. Traces of oxygen in the electrolyte (grey curve) cause an increase in the cathodic current density for potentials $E_{WE} \lessapprox 400\,mV$. Further purging of the electrolyte by Argon 5.0 expell the oxygen contamination and the feature in the cyclic voltammogram disappears (black curve).

working electrode potentials, in both cyclic voltammograms a steep increase of cathodic current density in the potential range $E_{WE} \lessapprox -750\,mV$ is obvious. It can be attributed to the hydrogen evolution reaction at the n – Si (111):H surface $2H^+ + 2e^- \rightarrow H_2 \uparrow$. In the

[5] Results presented in this section have been published in [i]

first potential scan (grey curve in Figure 4.3), however, there is already an increase in cathodic current density at approximately $E_{WE} = -400\,mV$. This feature can be attributed to traces of oxygen, which have still remained in the electrolyte [245, 363, 364] and are consumed according to $O_2 + 4H^+ + 4e^- \rightarrow H_2O$ or $O_2 + 2H^+ + 2e^- \rightarrow H2O2$ [365, 366]. Further purging of the electrolyte with Argon 5.0 (purity of 99.999%) expelled the oxygen contamination from the electrolyte and the corresponding feature in the cyclic voltammogram disappeared (black curve in Figure 4.3) [202, 245, 311, 363–365, 367, 368]. Thus, careful purging of the electrolyte with an inert gas is essential to obtain reliable data from cyclic voltammetry measurements, in particular when working with n – Si (111):H surfaces [369, 370].

4.2.2 Flatband potential of wet chemically etched n – Si (111):H samples

The flatband potential E_{FB} determines the transition of electron accumulation to electron depletion of n – Si (111):H surfaces, and vice versa, (see subsection 2.3.2). The availability of charge carriers at electrode surfaces, besides E_{WE}, determines metal electrodeposition and -dissolution onto and from these surface. Thus, for an overall interpretation of results from electrochemical experiments it is necessary to be aware of the value of E_{FB}. The flatband potential of the n – Si (111):H samples employed in this thesis was determined from impedance measurements on the n – Si (111):H samples exposed to the electrolyte 0.1 M H_2SO_4 in the potential range of deep electron depletion by applying the Mott-Schottky relation (see 2.3.2).

The n – Si (111):H samples were inserted into the deaerated electrolyte under potential control at $E_{WE} = -120\,mV < E_{FB}$.

The data from the impedance measurements at different values E_{WE} were fitted to the equivalent circuit depicted in Figure 4.4 in the software ZView 3.3b. In this circuit

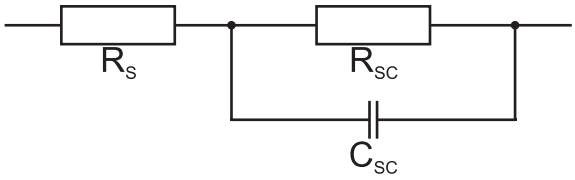

Figure 4.4: Equivalent circuit for extracting the space charge capacitance C_{SC} from the impedance measurements by a fitting procedure. The space charge region is represented by C_{SC} and R_{SC}, R_S accounts for ohmic potential drops in the measurement.

the space charge region at the n – Si (111):H surface is represented by the capacitance C_{SC} and the resistance R_{SC}, while the series resistance R_S accounts for ohmic potential drops

in the measurement. The electrochemical double layer capacitance can be safely omitted in this equivalent circuit since it is much larger than C_{SC} [208, 210, 218, 230].

In the potential range $E_{WE} \gtrapprox +300\,mV$ the capacitance C_{SC} (full circles in Figure 4.5), as obtained from the fit, follows the Mott-Schottky relation (Equation (2.29))

$$\left(\frac{A}{C_{SC}}\right)^2 = \frac{2}{\epsilon\epsilon_0 N_D e}\left(E_{WE} - E_{FB} - k_B T\right) \tag{2.29}$$

where A is the sample surface area under investigation and $k_B T \approx 25\,meV$ for $T = 300\,K$. C_{SC}^{-2} depends linearly on E_{WE} in this potential range, the slope of the Mott-Schottky plot

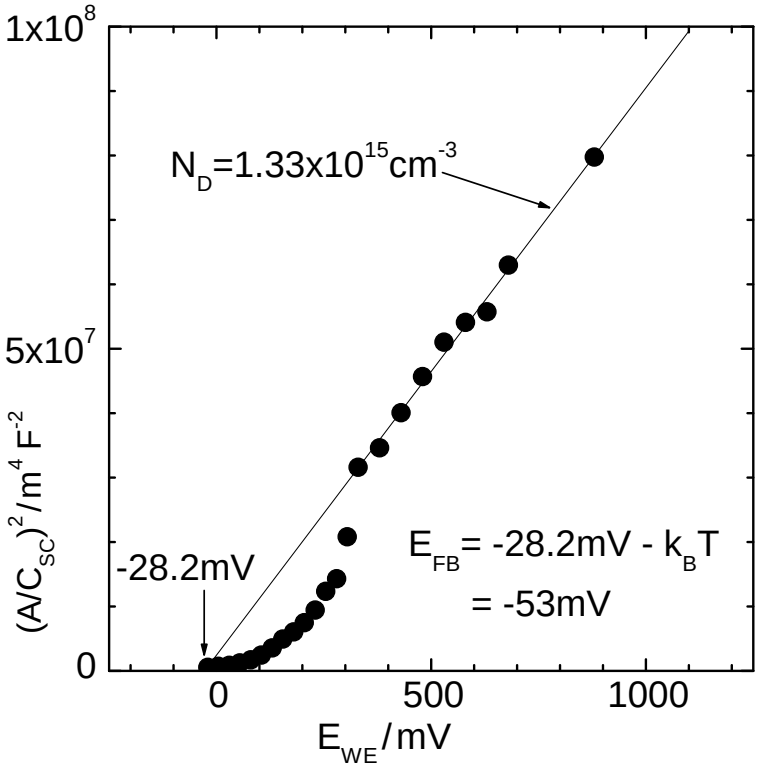

Figure 4.5: Mott-Schottky plot of the capacitance C_{SC}, as obtained by fitting the equivalent circuit shown as in Figure 4.4. The intersection of the extrapolation of C_{SC}^{-2} for $E_{WE} \geqq 330\,mV$ (solid line) and the abscissa results in a flatband potential $E_{FB} = -53\,mV$ of the n–Si(111):H samples. E_{WE} is quoted with respect to the SHE reference electrode.

(Figure 4.5) corresponds to a doping density $N_D = 1.33 \cdot 10^{15}\,cm^3$. This value is in good agreement with the manufacturer's specification of then n–Si(111) wafers investigated.

The extrapolation of C_{SC}^{-2} in Figure 4.5 intersects the abscissa at $E_{FB} + (k_B T/e)$, which gives a flatband potential $E_{FB} = -53\,mV$ for our substrates. This value of E_{FB} is consistent with reports in the literature, where values of $-150\,mV < E_{FB} < 0\,mV$ have been obtained for n–Si(111):H of $N_D \approx 10^{15}\,cm^3$ in contact with an electrolyte

of pH = 1 [225, 354, 355, 371]. An investigation of the pH dependence was not a goal in this thesis. The consistency of E_{FB} with previous results, obtained by impedance and microwave reflectivity measurements in HF solutions [371], shows in particular, that oxide free n – Si (111):H surfaces can be accomplished in Ar purged 0.1 M H_2SO_4.

In the potential range $E_{FB} < E_{WE} \lessapprox +300\,mV$ the space charge capacitance C_{SC}, as obtained from the fit to the impedance data using the equivalent circuit in Figure 4.4, becomes larger than the prediction for C_{SC} by the Mott-Schottky relation (Figure 4.5).

This deviation from the Mott-Schottky relation has been attributed in general to an additional, "surface state" related, capacitance in n – Si (111):H [218, 229, 230, 235, 371]. From a theoretical point of view, the n – Si (111):H surface should not exhibit surface states [372–374], and in experiments in ultra high vacuum (UHV) such states have not been observed [199, 375–378].

Further investigation of this surface state related capacitance is presented in subsection 4.2.3.

4.2.3 Surface states of wet chemically etched n – Si (111):H surfaces

As presented in subsection 4.2.2, the space charge capacitance C_{SC}, as obtained from the fit to the impedance data using the equivalent circuit in Figure 4.4, becomes larger than the prediction for C_{SC} by the Mott-Schottky relation in the potential range $E_{FB} < E_{WE} + 300\,mV$ (Figure 4.5). This deviation from the Mott-Schottky relation has been attributed in general to an additional, "surface state" related, capacitance in n – Si (111):H [218, 229, 230, 235, 371]. The total measured capacitance (Figure 4.5) has been identified by simultaneous microwave reflectance and impedance measurements as a superposition of space charge capacitance, which obeys the Mott-Schottky relation, and surface state related capacitance [371].

In the present experiments similar results of a superposition of space charge capacitance and surface state related capacitance are found, when fitting the impedance data with the revised equivalent circuit shown in Figure 4.6, which accounts for surface states by C_{SS} and R_{SS} in parallel to C_{SC} and R_{SC} [130, 218, 232, 350, 351, 379–381]. C_{SC} now accounts only for the space charge capacitance.

Since it follows the Mott-Schottky relation, we set C_{SC} in this potential range ($E_{WE} \lessapprox +300\,mV$) in accordance with the Mott-Schottky relation and fit then the equivalent circuit from Figure 4.6 to the impedance data. This fitting procedure improves the quality of the fit and results in values for C_{SS} as shown in Figure 4.7.

The spreading of C_{SS} over a potential range of 350 mV can be explained by several surface states of different energy levels contributing to C_{SS}. A monoenergetic surface state

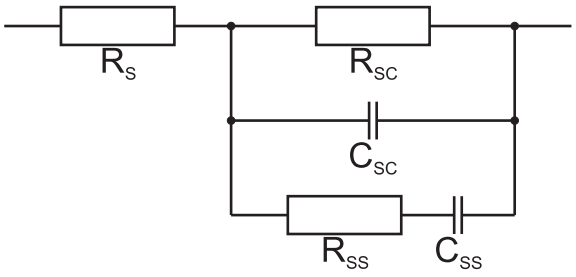

Figure 4.6: Circuit diagram employed for separating the capacitance of the surface states (C_{SS}) from the capacitance of the space charge region (C_{SC}). R_{SS} is the surface state resistance, R_{SC} the space charge resistance and R_S is the series resistance of the experimental setup to the sample.

is characterised by

$$C_{SS} = \frac{e^2}{4k_BT} N_{SS} \left[\frac{\cosh(E_{SS} - E_{WE})}{2k_BT} \right]^{-2} \tag{4.1}$$

with a full width at half maximum of $3.52 k_B T/e \approx 88\,\text{mV}$ at room temperature [382,383]. Thus, the broad distribution of C_{SS} in Figure 4.7 can be explained by a superposition of a minimum of three distinct surface states with a particular energy level each. This is shown in Figure 4.8: The thin lines represent the three surface states at $E^1_{SS} \approx +26\,\text{mV}$, $E^2_{SS} \approx +109\,\text{mV}$, and $E^3_{SS} \approx +212\,\text{mV}$ with respect to the SHE reference electrode.

The curves in Figure 4.8 are a best fit to the C_{SS} values. The potential dependence of C_{SS} (Figure 4.7) is reproducibly found in all investigated n – Si (111):H samples, although the magnitude of C_{SS} at a particular potential varies by about a factor of three. This suggests a similar distribution and occupation of the surface states in all investigated samples, but a variation in the density of surface states from sample to sample.

The position of these surface state levels with respect to the band edges of n – Si (111):H can be easily calculated at flatband conditions $E_{WE} = E_F = E_{FB}$. For flatband conditions and for complete donor exhaustion, the Fermi level E_F is approximately given by $E_F \approx E_C + k_B T \ln(N_C/N_D)/e = E_C + 245\,\text{mV}$, where N_C is the effective density of states in the conduction band [123, 208, 209, 214].

The conduction band edge E_C at flatband conditions can be determined from E_{FB} in Figure 4.5 to $E_C = -298\,\text{mV}$. The surface state levels relative to E_C then read $E^1_{SS} = E_C + 324\,\text{mV}$, $E^2_{SS} = E_C + 407\,\text{mV}$, and $E^3_{SS} = E_C + 510\,\text{mV}$. For convenience, these levels are given on a potential scale rather than an energy scale. Their positions in the bandgap of n – Si (111):H are indicated in the schematic in Figure 4.9 for the case of flatband conditions. They do not overlap with the conduction or valence band, which legitimates their surface state character.

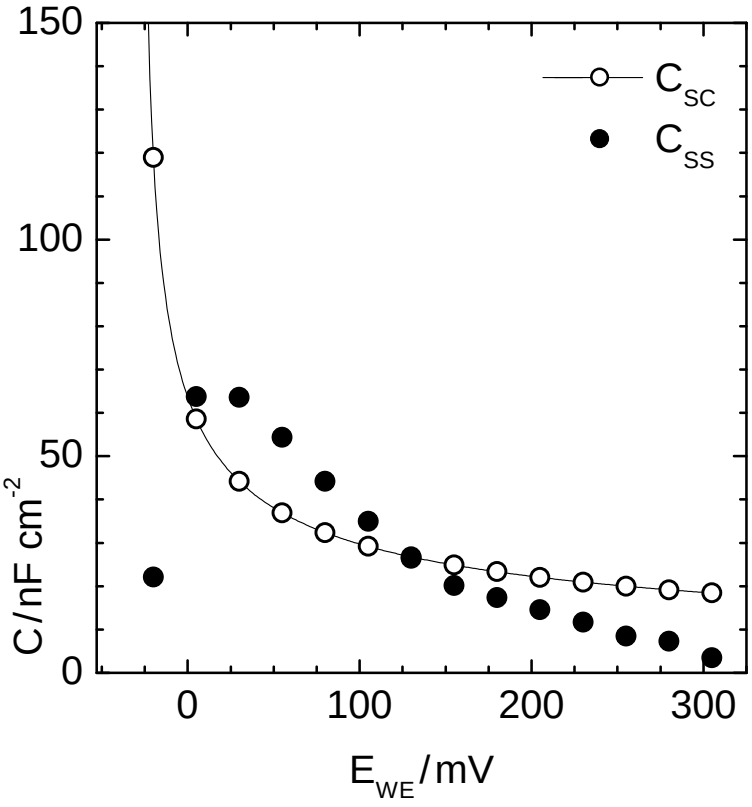

Figure 4.7: Surface state capacitance C_{SS}, as fitted to the impedance data using the equivalent circuit in Figure 4.6 (full circles). The open circles connected by a solid line represent the space charge capacitance C_{SC} according to the Mott-Schottky relation. E_{WE} is quoted with respect to the SHE reference electrode.

The observed surface states seem to be correlated to the wet chemical preparation procedure of H-terminated n – Si (111):H surfaces. This procedure not only creates H-terminated n – Si (111):H surfaces, but results also in a hydrogen diffusion into the subsurface region of n – Si (111):H [384–389].

It has been shown by experiments in UHV, that hydrogen in the subsurface region of n – Si (111) samples occupies interstitial positions in the Si lattice and neutralises dopant atoms by acting as oppositely doping species [385, 386, 388, 390–394]. Differently charged states of interstitial hydrogen, acting as donor or acceptor, are found in experiments carried out under UHV conditions by employing secondary mass ion spectroscopy, capacity-voltage measurements, deep level transient spectroscopy, infrared absorption measurements, reactivation of passivated dopants by minority charge carrier injection, or a combination of these techniques [391, 392, 395–402]. The corresponding energy levels associated with interstitial hydrogen have been reported to be located within the band gap of n – Si (111):H above midgap [391, 392, 395–401]. In experiments, which employ H^+ implantation for introducing hydrogen into the Si samples, besides the hydrogen related energy levels, a variety of energy levels associated with defects due to the implantation

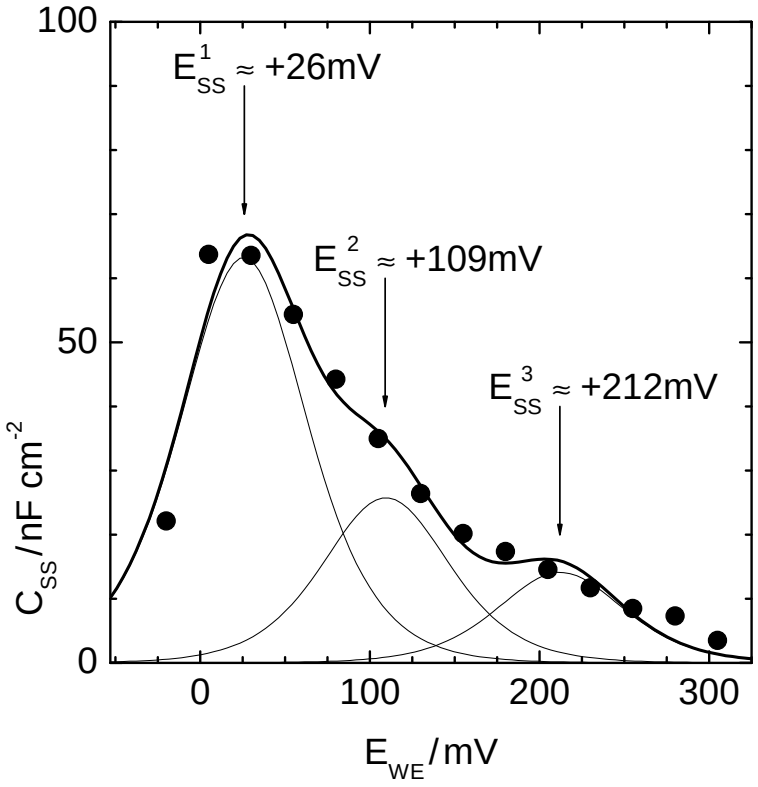

Figure 4.8: Representation of the measured surface state capacitance C_{SS} (filled circles) by three monoenergetic surface states E_{SS} (thin solid lines) and their superposition (thick solid line). E_{WE} is quoted with respect to the SHE reference electrode.

process are observed in the range from midgap up to the conduction band edge [401]. Such implantation defect related energy levels are not expected in the present wet chemically prepared n – Si (111):H samples.

When these previous findings of many references are compared with the present results, obtained by fitting only three distinct surface state levels to the impedance data, a nearly perfect agreement is found, although it is possible that there is a range of defect related states showing similar energy levels involved. The surface state levels E_{SS}, as derived from our measurements, are compared with the literature data in Table 4.1.

E_{SS} / mV	$(E_{SS} - E_C)$ / mV	$(E_H - E_C)$ / mV		
+26	+324	+320 [395,396,403],	+300 [401],	$\geqq$ +250 [397]
+109	+407	+450 [395,396,403],	+450 ±100 [392],	+390 [401]
+212	+510	+520 [398–400],	+510 [391]	

Table 4.1: Comparison of the surface state levels obtained in this publication (E_{SS}) with values from the literature for hydrogen induced states obtained from measurements, using different experimental techniques (E_H). Values in the left column are quoted with respect to the SHE reference electrode. Values in the middle and right column are given on a potential scale and correspond to energy values when multiplied with the electron charge.

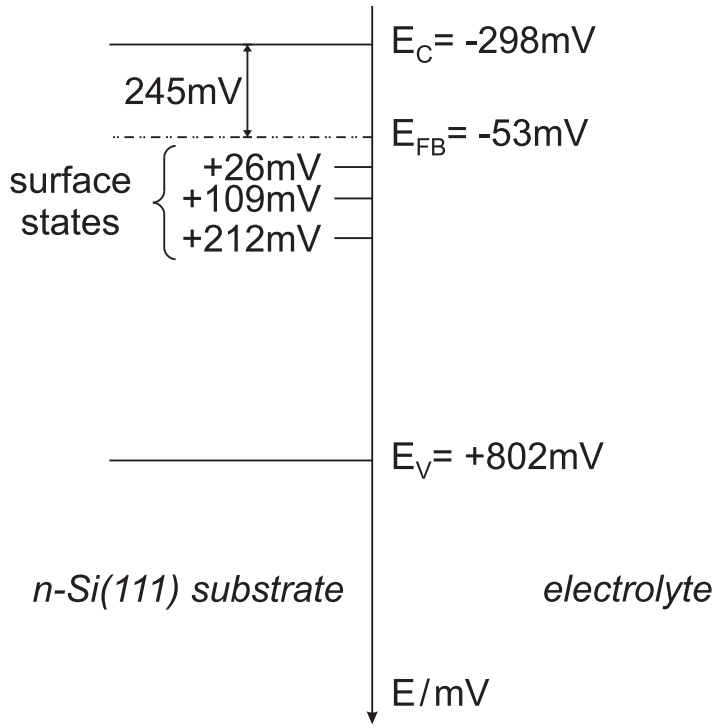

Figure 4.9: Energy scheme of n – Si (111):H under flatband conditions $E_{WE} = E_{FB} = -53\,mV$. E_C and E_V are the conduction band edge and the valence band edge, respectively. The surface state levels E_{SS} obtained from Figure 4.8 are indicated. E_{WE} is quoted with respect to the SHE reference electrode.

The deviation of the capacitance values in Figure 4.5 from the prediction for C_{SC} by the Mott-Schottky relation at potentials $E_{WE} \lessapprox +300\,mV$ occurs at a width of the space charge region [218] of $d_{SC} = \epsilon\epsilon_0(A/C_{SC}) \approx 600\,nm$ (see Figure 4.10).

This value for d_{SC} is in the same range as the hydrogen diffusion depth into the n – Si (111):H subsurface region, which has been reported to be several 100 nm up to 3 µm [386, 388, 391–393, 404]. This coincidence is another argument for hydrogen in the n – Si (111):H subsurface region being the origin of the observed surface states. While at potentials $E_{WE} \gtrapprox +300\,mV$ these surface states are located within the electron depleted space charge region and do not participate in charge transfer processes, at potentials $E_{WE} \lessapprox +300\,mV$ the width of the space charge region d_{SC} becomes similar or smaller than the hydrogen diffusion depth, which allows for a participation of these surface states in charge transfer processes.

Nevertheless, the expression "surface states" is maintained throughout this thesis for convenience and to avoid confusion, although these states could be also, more accurately, described as (subsurface) volume states extending to the surface.

The discussion so far assumes a constant doping density N_D in n – Si (111):H, and therefore an ideal Mott-Schottky behaviour of C_{SC}, which is modified by the additional

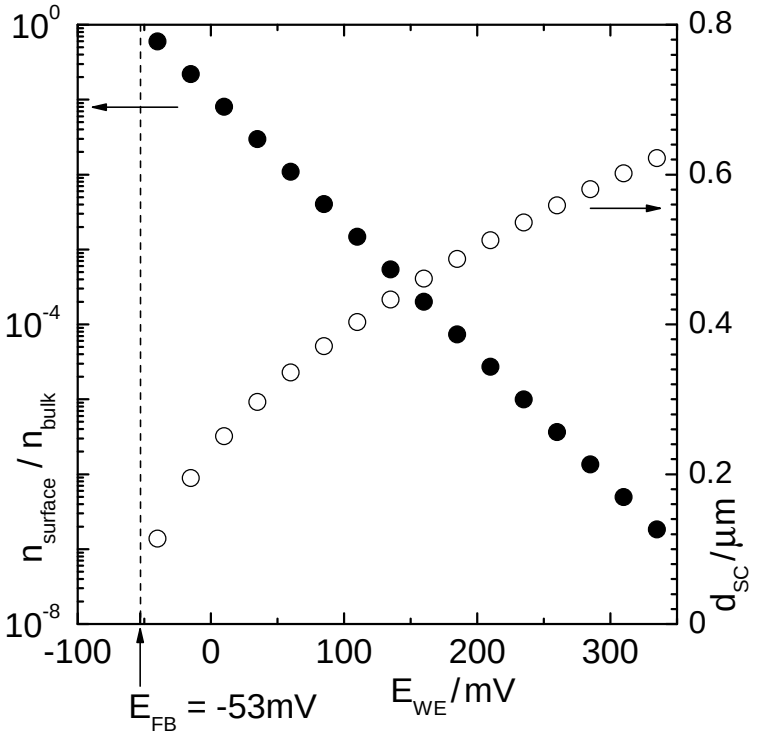

Figure 4.10: Calculated width of the space charge region d_{SC} (open circles) and surface electron concentration relative to the bulk value n_{surf}/n_{bulk} (filled circles) as function of working electrode potential E_{WE} applied to a n – Si (111):H sample. The flatband potential E_{FB} is indicated by a dashed vertical line.

capacitance C_{SS} originating from the surface states.

However, there is still another aspect to be mentioned: In photoemission measurements at the n – Si (111):H / UHV interface, which are sensitive to the actual electronic structure at the surface, hydrogen diffused into the subsurface region of n – Si (111):H has been found to result in a lowering of the Fermi level at the n – Si (111):H surface [405]. The explanation for this finding has been, that hydrogen in the n – Si (111):H subsurface region changes the doping density N_D [405].

The value $N_D = 1.33 \cdot 10^{15}\,cm^{-3}$ which we deduce from our measurements at $E_{WE} \gtrapprox +300\,mV$ represents the doping level at potential conditions with a broad electron depletion zone $d_{SC} \gtrapprox 600\,nm$ in accordance with the Mott-Schottky relation. Since surface states cannot participate in charge transfer at deep electron depletion conditions, i.e. broad depletion zones, this value is likely to be the bulk doping level of the n – Si (111) material, which does not reflect an eventual influence of subsurface hydrogen on the doping level. Therefore, it is questionable if the doping level in the subsurface region of n – Si (111):H ($d_{SC} \lessapprox 600\,nm$) can be determined from measurements of C_{SC} in the potential range $E_{WE} \gtrapprox +300\,mV$.

The area density N_{SS} of a monoenergetic surface state is derived from the maximum

of the C_{SS} distribution: $N_{SS} = 4k_BTC_{SS}^{max}/e^2$ [206, 218, 259, 379, 380, 383, 406, 407]. From Figure 4.7 the total area density of surface states is estimated to $(10^{10} - 10^{11})\,cm^{-2}$ in very good agreement with [371]. When we consider a hydrogen diffusion depth of the order of 1 µm [386, 388, 391–393, 404], this corresponds to a density of states of $(10^{14} - 10^{15})\,cm^{-3}$ in the n – Si (111):H subsurface region, suggesting that the term "subsurface volume states extending to the surface" would be more appropriate to classify these states. A significant influence of these states on the effective doping level in the subsurface region of n – Si (111):H may be reasonable in substrates whose doping level is of same order, as is the case for our n – Si (111):H samples.

In view of the photoemission results [405], the deviation of the space charge capacitance from the Mott-Schottky relation for $E_{WE} \lessapprox +300\,mV$ may be interpreted as a change in the effective doping level close to the n – Si (111):H surface due to dopant passivation by hydrogen.

The exposure of n – Si (111):H surfaces to fluorine containing etching chemicals like HF or NH_4F has been reported to result also in a diffusion of fluorine into the n – Si (111) lattice, giving rise to additional electronic levels [408, 409]. These should be "buried" in the valence band of Si [408] and not accessible in our experiments.

4.2.4 Conclusions

The results obtained in this section show, that the electronic structure at the n – Si (111):H surface is very complex, since hydrogen introduces electronically active states in the n – Si (111):H subsurface region. Three different states within the band gap of n – Si (111):H are identified at energy levels $E_{SS}^1 = E_C + 324\,mV$, $E_{SS}^2 = E_C + 407\,mV$, and $E_{SS}^3 = E_C + 510\,mV$, where E_C denotes the conduction band edge. These energy levels correspond to states originating from hydrogen in the subsurface region of n – Si (111):H, which have been measured previously under UHV conditions with different experimental techniques.

Due to their energetic position between midgap and conduction band edge of n – Si (111):H, they may participate in charge transfer processes in a potential range, where the n – Si (111):H surface is depleted of conduction band electrons. The density of these hydrogen-related states is of the order of $(10^{14} - 10^{15})\,cm^{-3}$. Consequently, a significant deviation of the effective doping level in the n – Si (111):H subsurface region may be expected in n – Si (111):H samples of comparable doping density N_D, with consequences for the Fermi level position at the n – Si (111):H surface. These aspects may be of particular importance in charge transfer processes at the nanoscale, where only small amounts of charge participate.

4.3 Correlation of image resolution with tip apex diameter in scanning tunneling microscopy on the nanoscale [6]

Scanning tunneling microscopy (STM) is a powerful tool for investigating surfaces, since it provides real-space images of surfaces with up to atomic resolution [46,64] and allows for manipulation of surfaces at theses scales [51,63]. STM is extremely sensitive on variations of the tip–sample distance (gap width) due to the exponential dependence of the tunneling current on the distance d between STM tip and sample:

$$I_{tunnel} \sim exp\left[-A \cdot \sqrt{\Phi} \cdot d\right] \tag{4.2}$$

with $A = 10.12\,(\mathrm{eV})^{-\frac{1}{2}}\mathrm{nm}^{-1}$ and the tunneling barrier Φ [99]. This exponential dependence of I_{tunnel} on the distance d leads to the common assumption that only one atom at the STM tip apex, which is closest to the sample surface, contributes to the tunneling current, and, thus, by default atomically resolved STM images are achievable.

However, such a situation is hardly achieved in experiments, particularly those carried out at ambient conditions, or at solid / liquid interfaces. STM tips are usually changed for each experiment, and experiments are performed at room temperature, where atomically sharp protrusions on the tip apex surface may not be stable. The actual tip apex radius in a particular experiment is usually unknown.

During imaging of atomically flat sample surfaces the influence of the tip apex radius is not immediately obvious since "only" the height contrast of a corrugated lattice plane decreases with increasing tip apex radius. However, the tip apex radius plays an important role for the achievable resolution when structures with finite extension perpendicular to the surface are imaged. This is often underestimated in the literature.

Abrupt vertical variations on surfaces, like step edges, are always imaged a few nanometers wide [24,36,98,179,361,410–412]. Nanoscale clusters with diameters below 10 nm are usually imaged without explicit atomic structure, and their height does not correlate to the number of atomic layers [26,31]. There are only very few examples in the literature, like a Co cluster on Au(111), where the layered structure and the single atomic planes of a cluster could be imaged [37]. The detailed analysis and reliable interpretation of nanoscale structures in STM images is a continuing and still unsolved problem.

The influence of the tip apex radius on the measured structure shape has been subject to a variety of investigations in the literature [413–427]. An estimate of the tip apex radius may be derived by applying statistical algorithms to STM images without detailed

[6] Results presented in this section have been published in [v]

knowledge of the individual structures [413–416]. Most of the approaches to deconvolute the tip influence are based on geometrical considerations, do not take into account the three-dimensional tip–sample geometry and / or do not account for the exponential dependence of the tunneling current on the gap width [414–425]. Unfortunately, most studies address characteristic length scales much larger than the length scale of interest in experiments at the nanoscale, as, e.g., in the investigation of clusters a few atoms in width and height. Finally, artificial structures of known structure shape have been imaged and the recorded image used for deconvolution of the tip shape, in order to apply this information subsequently to deconvolute an unknown structure shape in a different experiment, eventually using the same tip [419–425].

In this section, the influence of the tip apex radius on the gap width, on the lateral step edge width in STM images, and on the width and height of structures in STM images at the nanoscale is analysed, each time for a STM operated in constant current mode. Detailed calculations of a three-dimensional geometry taking into account the exponential current–distance dependence of a tunneling contact are employed. The results from the calculations are correlated to experimental observations. The term "apparent" width or height is used throughout this section instead of "measured", in order to indicate a calculated quantity.

The results show in particular, that finite STM tip apex radii increase the apparent width of a (nano)structure in STM images by a tip apex radius dependent offset. At a given structure size, this offset increases non linearly with increasing tip apex radius. Structures much smaller than the tip apex radius in addition appear reduced in height in STM images. This effect results in an additional nonlinear increase of the apparent structure width for small structures. Due to these effects, the resolution achievable in STM is severely limited by the STM tip apex radius.

The consequences are particularly substantial for structures sizes below 10 nm: The error between apparent structure size and actual structure size may be more than 1000%, when using tips of inappropriate tip apex radius, although the same blunt tips produce at the same time acceptable images of flat terraces. Therefore, STM images of nanoscale structures derived with different STM tips seem to be not comparable to each other unless the tip apex radius and its impact on the structure shape is known for each STM tip used.

However, the results indicate also, that the tip apex radius can be calculated from the measured shape of step edges in a STM image, and can be subsequently used to deconvolute the measured shape of nanostructures in the same STM image.

The principle of the calculations is sketched in Figure 4.11. The x-y plane is defined as the sample surface, the z-direction is along the tip axis, perpendicular to the sample surface. The apex of the STM tip is approximated as a half-sphere of radius r_{tip}, z_0 at

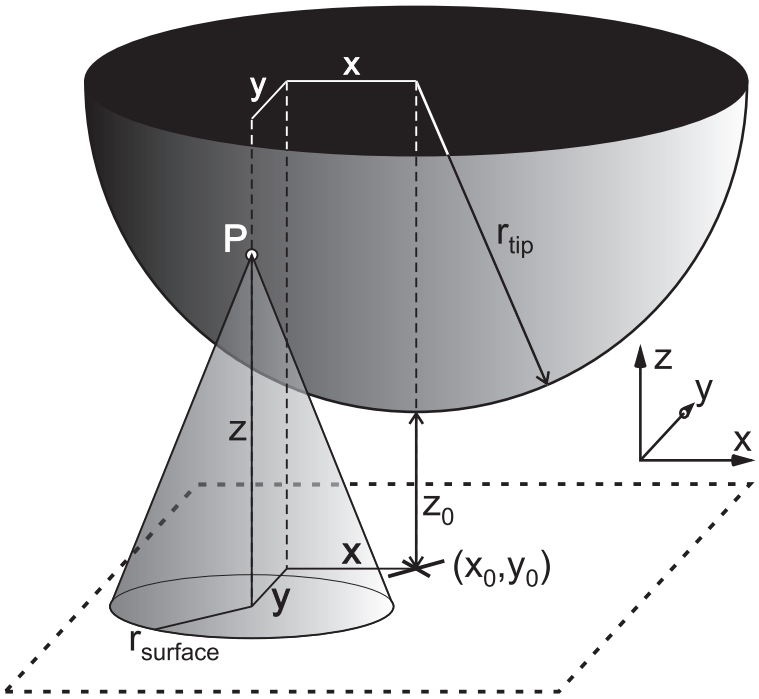

Figure 4.11: Geometry of the STM tip apex of radius r_{tip} used in the calculations. The point of the tip apex closest to the surface is given by z_0 at (x_0,y_0). A point P on the tip apex surface is has the coordinates by x, y, and z (x,y). The cone having a base of $r_{surface}$ indicates, that the tunneling current contribution of a point P to the total tunneling current is not only restricted to tunneling in perpendicular direction to the surface.

(x_0,y_0) determines the point of the tip apex closest to the sample surface, i.e. the width of the tunneling gap. The distance from the sample surface to any point P on the tip apex surface at the lateral position (x,y) is given by z (x,y), as shown in Figure 4.11.

The model applied in the calculations is based on continuous surfaces of sample and tip apex, although they exhibit a periodic atomic and, hence, electronic structure. This simplification is applicable in the calculations, since they average over lateral length scales of at least ten, or more, atomic distances. Atomic planes at the STM tip surface imply a discrete distance structure in the tunneling gap, but cannot be modeled realistically for a polycrystalline and, with respect to the crystallographic orientation, undefined tip apex.

The total tunneling current at the STM tip apex is obtained by integrating the current contribution of each point P on the tip apex surface over the whole tip apex surface (Figure 4.11). The current contribution of a single point P of the tip apex surface is obtained by integration of the tunneling current

$$I_{tunnel}(x,y) \sim exp\left[-A \cdot \sqrt{\Phi} \cdot \sqrt{z^2(x,y) + r^2_{surface}} \right] \tag{4.3}$$

over the whole sample surface ($0 \leqq r_{surface} \leqq \infty$) as schematically shown in Figure 4.11.

This appears to be necessary since the tunneling current is not restricted to the direction perpendicular to the sample surface.

The result of this twofold integration yields a measure for the tunneling current between the sample surface and the STM tip with an apex radius r_{tip}, separated by the gap width z_0.

The STM images shown for comparison with the calculations are unfiltered and have only been flattened to eliminate the surface curvature artifact in the original STM data.

(i) variation of gap width with r_{tip}:
The STM tip was placed above a flat sample surface.

First, the tunneling current for the smallest tip apex radius in our calculations, $r_{tip} = 5\,nm$, and a corresponding $z_0(r_{tip} = 5\,nm) = 0.8\,nm$ was calculated as the reference value $I^{flat}_{tunnel}(z_0(r_{tip} = 5\,nm), r_{tip} = 5\,nm)$. Next, the tunneling current was calculated for larger values of r_{tip}, and for each r_{tip} the gap width $z_0(r_{tip})$ was iteratively increased (so to speak, fitted), until the calculated value of $I^{flat}_{tunnel}(z_0(r_{tip}), r_{tip})$ corresponded to the reference value $I^{flat}_{tunnel}(z_0(r_{tip} = 5\,nm), r_{tip} = 5\,nm)$. The resulting dependence of the gap width $z_0(r_{tip})$ on the tip apex radius at constant current conditions is shown in Figure 4.12 (open squares).

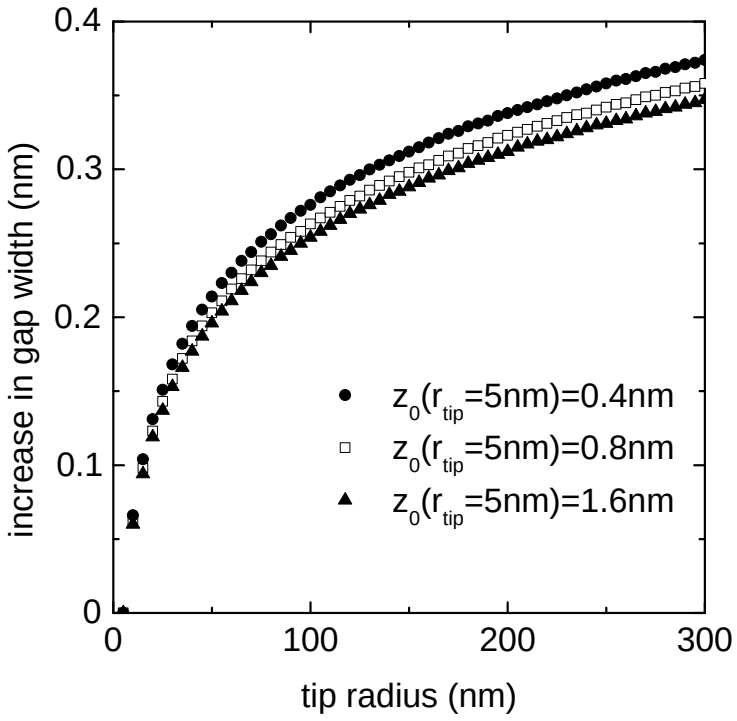

Figure 4.12: Increase of the gap width with increasing tip apex radius at constant current conditions for three different reference gap widths $z_0(r_{tip} = 5\,nm) = 0.4\,nm$, $0.8\,nm$, and $1.6\,nm$.

The above calculation was also performed for a smaller and a larger reference value $z_0(r_{tip} = 5\,nm)$ of the gap width in order to investigate the influence of the absolute gap width on the variation of the gap width with increasing r_{tip}. $z_0(r_{tip} = 5\,nm) = 0.4\,nm$ and $z_0(r_{tip} = 5\,nm) = 1.6\,nm$ were chosen, respectively. The resulting curves are shown in Figure 4.12 as filled circles ($z_0(r_{tip} = 5\,nm) = 0.4\,nm$) and filled triangles ($z_0(r_{tip} = 5\,nm) = 1.6\,nm$), respectively. Comparison of the curves for the three different values of $z_0(r_{tip})$ in Figure 4.12 shows, that the absolute value of $z_0(r_{tip} = 5\,nm)$ plays only a minor role for the increase of the gap width with increasing r_{tip}. The main contributor to the change in gap width is r_{tip}.

The calculations show, that the tunneling current $I^{flat}_{tunnel}(z_0, r_{tip})$ at constant gap width z_0 increases with increasing tip apex radius r_{tip}. This is a reasonable effect, since the geometrical cross section of the tunneling gap becomes larger with increasing r_{tip}. The effect is the more pronounced, the smaller the tip apex radius becomes (increase in slope in Figure 4.12 with decreasing r_{tip}). In an STM experiment, performed at constant current conditions, the feedback-loop of the STM will increase the gap width in such a situation, in order to maintain a constant tunneling current.

Consequently, STM experiments at the same constant current conditions, but with different STM tips are actually carried out at different gap widths. There may be a variation of up to $(0.2 - 0.3)\,nm$ in the gap width (Figure 4.12) depending on r_{tip} of the actually used STM tip, when considering typical tip apex radii of $(5 - 100)\,nm$ in STM experiments.

(ii) variation of apparent step edge width with r_{tip}:

The STM tip was again placed above a flat sample surface. When the STM tip moves across this surface and approaches a single step edge of height h from the lower side, the reduced gap width at the step edge causes an increase in tunneling current. A STM operated in constant current mode consequently reduces the measured tunneling current to the predefined tunneling current setpoint by increasing the gap width.

This situation was modeled by introducing a step of height $h = 0.31\,nm$, corresponding to a higher terrace with the n – Si (111) layer distance, in our simulations. A schematic of the geometry used for these calculations is shown in Figure 4.13.

First, the STM tip was placed on the lower terrace far away from the step edge at the reference gap width $z_0(r_{tip})$, to obtain $I^{flat}_{tunnel}(z_0(r_{tip}), r_{tip})$ for the flat surface. For this reference calculation a gap width $z_0(r_{tip} = 5\,nm) = 0.8\,nm$ was used, and for larger tip apex radii r_{tip} the particular value for $z_0(r_{tip})$ obeying the corresponding curve (open squares) in Figure 4.12, to account for the results of (i), i.e. the variation of $z_0(r_{tip})$ with r_{tip}. Initially, z'(r_{tip}), denoting the distance in between tip apex and lower terrace, was set equal to $z_0(r_{tip})$.

Next, the STM tip was moved in successive steps in direction towards the step edge.

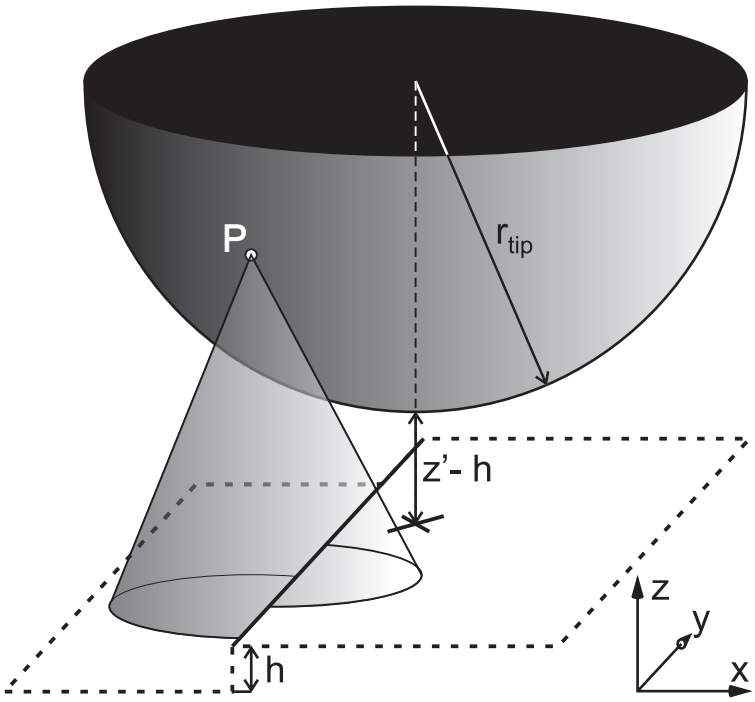

Figure 4.13: Geometry of the STM tip apex of radius r_{tip} used for calculating the apparent step width of a step edge having height h. The tip–sample separation z' is measured from the lower terrace. It is increased, until the tunneling current in the calculations matches the reference value of the tunneling current when the tip is completely positioned above the lower terrace.

Upon each step, $I^{step}_{tunnel}(z'(r_{tip}), r_{tip})$ was calculated and compared to $I^{flat}_{tunnel}(z_0(r_{tip}), r_{tip})$. The increasing contribution of the upper terrace to the tunneling current with the STM tip position closer to the step edge yields a larger $I^{step}_{tunnel}(z'(r_{tip}), r_{tip})$ in comparison to $I^{flat}_{tunnel}(z_0(r_{tip}), r_{tip})$. To equalise the two values, the gap width $z'(r_{tip})$ (see Figure 4.13) at this particular STM tip position was increased iteratively, until $I^{step}_{tunnel}(z'(r_{tip}), r_{tip}) = I^{flat}_{tunnel}(z_0(r_{tip}), r_{tip})$. Then, the STM tip was moved another step and the calculation repeated. This procedure was executed, until the STM tip was completely positioned above the higher terrace. The gap width on the higher terrace is then $z'(r_{tip}) = z_0(r_{tip}) + h$.

The calculated gap widths $z'(r_{tip})$ at particular positions relative to the step edge result in the apparent height profile of the step edge. This profile corresponds to the apparent width of a step edge as imaged in STM experiments by a STM tip with tip apex radius r_{tip}.

As an example the apparent step edge widths of a step edge on a n – Si (111) surface ($h = 0.31\,nm$), obtained for different r_{tip}, are shown in Figure 4.14. The broadening of the apparent step edge width increases with increasing tip apex radius r_{tip}. While the width of the step edge appears to be $(2-3)\,nm$ for $r_{tip} = 5\,nm$, the width appears to be $8\,nm$

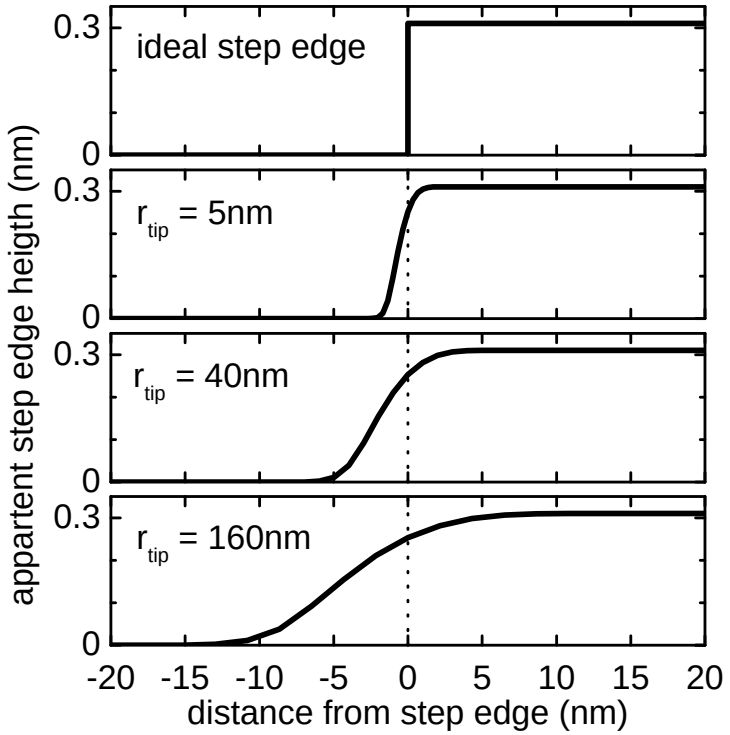

Figure 4.14: Ideal step edge and calculated shape of the step edge in STM images for different STM tip apex radii, using $z_0(r_{tip} = 5\,nm) = 0.8\,nm$ and constant current conditions.

and 16 nm for $r_{tip} = 40\,nm$ and $r_{tip} = 160\,nm$, respectively. The apparent width of a step edge in such a situation extends over 10 nm and is associated with a curvature of the flat terraces over a range of several nanometers.

(iii) variation of apparent dimensions of nanostructures with r_{tip}:
Following the procedure for a flat surface with a step edge in (ii), profiles of structures with same height of $h = 0.31\,nm$, but different width (1 nm, 5 nm, 8 nm, 40 nm) on the sample surface were calculated for different tip apex radii (5 nm, 40 nm, 160 nm). The results are shown in Figure 4.15a – d.

At sufficient width of the structure, there is no reduction of the apparent height in comparison to the actual structure height (Figure 4.15b–d). In the case of small structure widths (Figure 4.15a), the apparent height of structures is reduced in comparison to the actual structure height. This can be attributed to the background current from the flat sample surface surrounding the structure, which contributes to a larger extent to the tunneling current for small structures than for broad structures of same height. This effect becomes more pronounced for STM tips of large apex radius (Figure 4.15a – c), since such STM tips gather tunneling current from a larger area of the sample surface around the structure.

Secondly, with increasing tip apex radius r_{tip}, the width of the structures increases (Figure 4.15a–d). The r_{tip} dependent "broadening" corresponds to two times the value of the apparent step edge width as calculated in (ii), which adds up to the actual structure width.

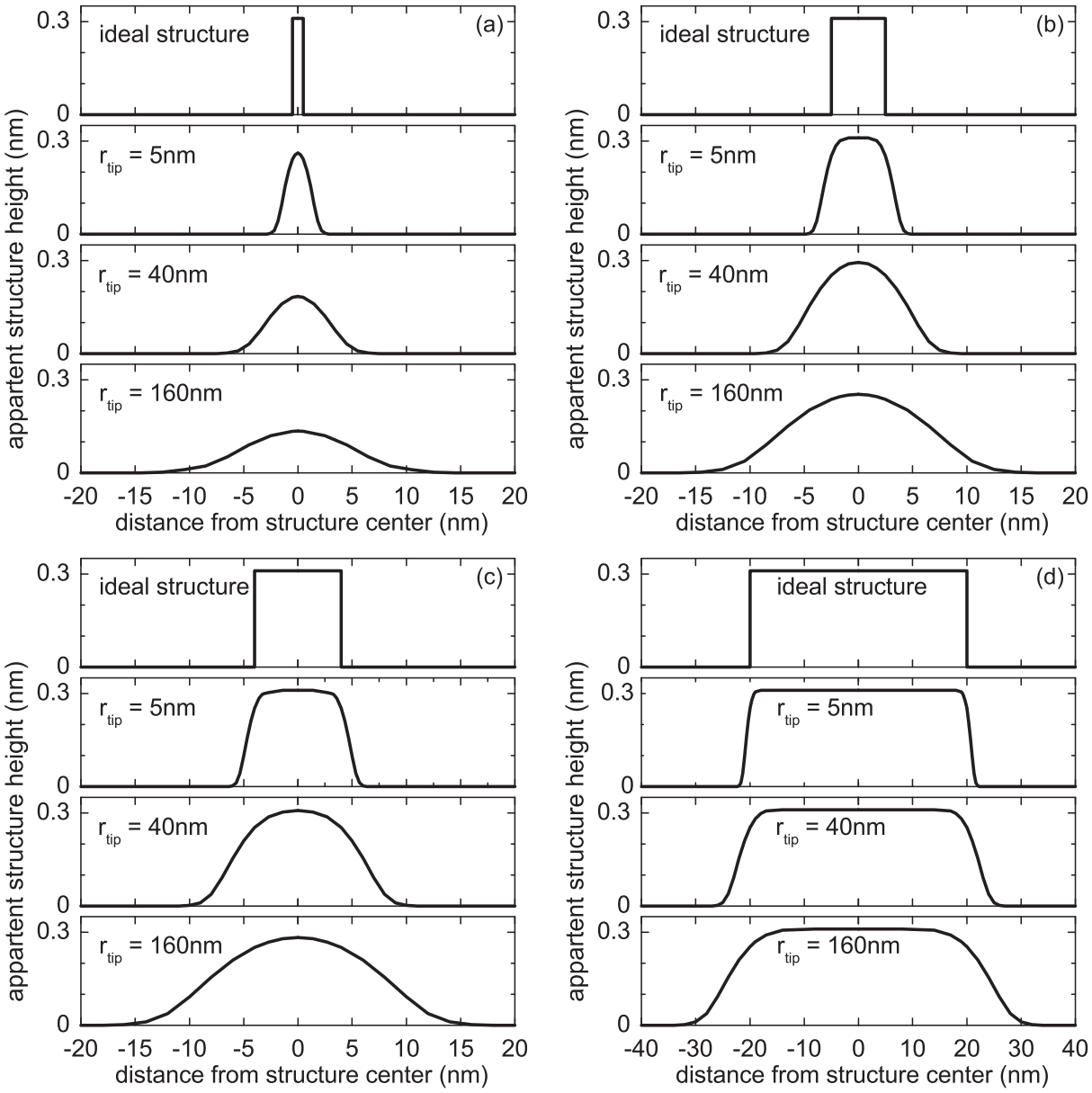

Figure 4.15: Ideal structures and calculated shape of the structures in STM images for different STM tip apex radii, using $z_0(r_{tip} = 5\,\text{nm}) = 0.8\,\text{nm}$ and constant current conditions. Structure widths are (a) 1 nm, (b) 5 nm, (c) 8 nm, (d) 40 nm.

The dependence of the apparent width (FWHM) of structures, as calculated in Figure 4.15a – d, on different STM tip apex radii is summarised in Figure 4.16. The case of an "ideal" STM tip, which exactly reproduces the actual structure, is represented by the diagonal solid straight line. A STM tip of finite radius gives an apparent structure width

larger than the "ideal" STM tip. The offset of two times the apparent width of a single step edge due to the finite tip apex radius r_{tip} is indicated by dashed lines in Figure 4.16.

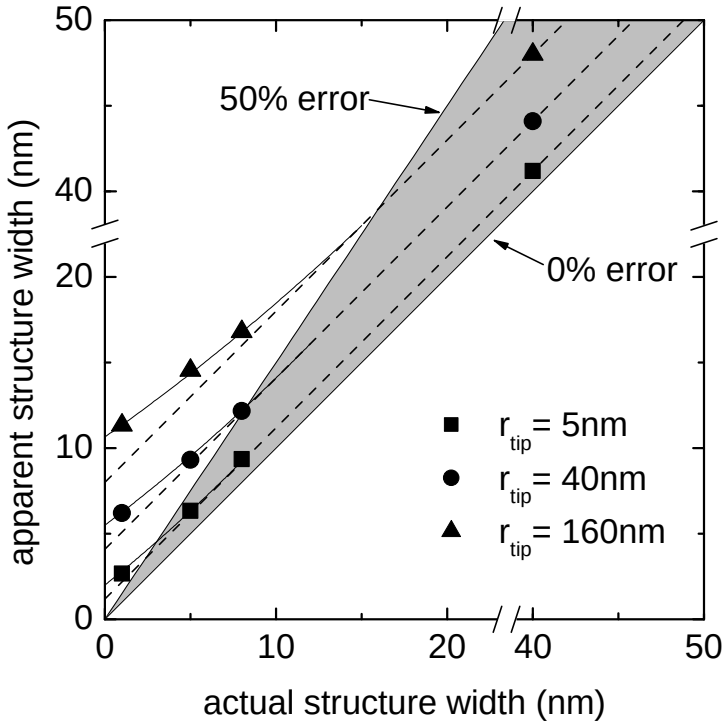

Figure 4.16: Comparison of actual and apparent structure widths (FWHM) as obtained from calculations using different values of r_{tip}. The diagonal straight solid line indicates the case of an "ideal" STM tip. Dashed lines indicate the offset added to the actual structure width in the case of broad structures, the solid lines at small structure widths show an additional nonlinearity, basically due to a decrease of the apparent structure height. Within the grey shaded area, the apparent structure width is within 50% error to the actual structure width.

In addition to the offset, there is a nonlinear increase in the apparent width of small structures, when they are imaged by tips of r_{tip} larger than the structure size (solid lines in Figure 4.16). This effect originates from the reduction of the apparent height and is the more pronounced the larger the reduction of apparent height becomes.

From Figure 4.16 the minimum achievable resolution in STM can be deduced from the intersection of the curves with the ordinate. It is obvious, that the resolution depends dramatically on the radius of the STM tip used.

Supposing an acceptable error between apparent and actual structure width of 50%, tip apex radii r_{tip} are required to be within the grey shaded area in Figure 4.16. Correspondingly, imaging of structures with actual widths of less than 10 nm makes high demands on the acceptable tip apex radius. The requirements are hard to achieve with current tip preparation procedures, even if they are highly sophisticated [196]. Electrochemical tip etching procedures without further processing ("sharpening") of the tips will not provide

the requirements according to the experience and investigations in the author's research group.

(iv) correlation of calculations with experiments:
In order to validate the calculations, a comparison of the results to experiments has been performed: The tip apex radius r_{tip} of a series of STM tips was determined at first by scanning electron microscopy (SEM), while subsequently the imaging capability of the same STM tips was analysed from STM images.

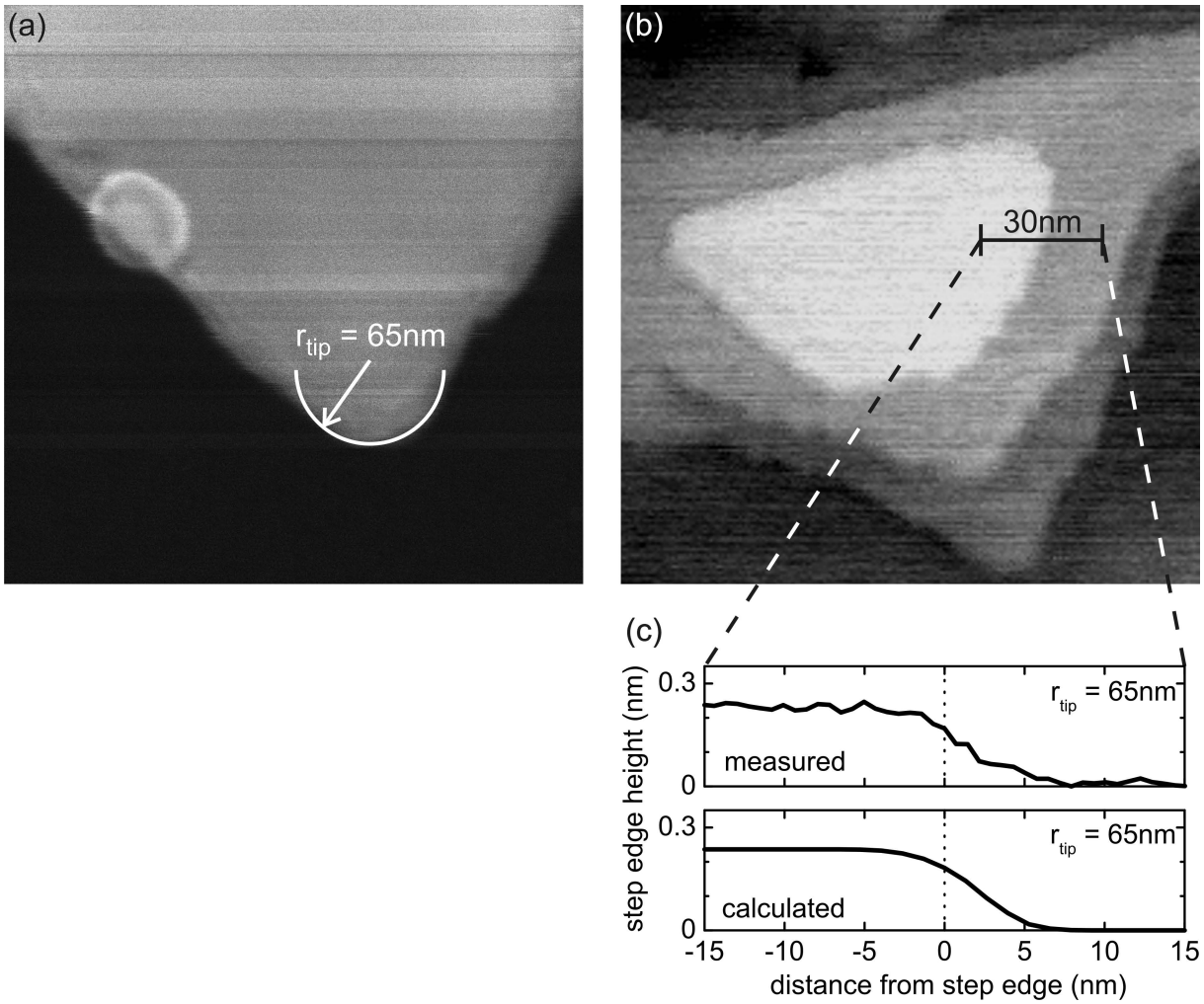

Figure 4.17: (a) Scanning electron microscope image of a STM tip with apex radius $r_{tip} = 65\,nm$. (b) Au(111) surface imaged at $I_{tunnel} = 30\,pA$ using the STM tip shown in (a). (c) Measured (black bar in (b)) and calculated step edge profile.

Exemplarily, the result for an etched Au STM tip is shown in Figure 4.17. The tip apex radius $r_{tip} = 65\,nm$ was determined from SEM (Figure 4.17a). The STM image of an Au (111) surface area imaged with this STM tip is shown in Figure 4.17b. Au(111) plateaus are observed, the image quality appears to be state of the art as frequently seen in the literature. The large value of $r_{tip} = 65\,nm$ has not been expected, when considering

the good quality of the STM image. From the upper line scan profile in Figure 4.17c (taken at the position of the black line in Figure 4.17b) a finite measured width of the step edge is obvious. The calculation of the apparent step edge width using $r_{tip} = 65\,nm$, which would be expected to be measured with this tip, is shown as the lower profile in Figure 4.17c. The coincidence of measured and calculated step edge profile in Figure 4.17c is nearly perfect.

Figure 4.17 demonstrates that the large tip apex radii which are assumed in the calculations are not at all unrealistic for STM experiments.

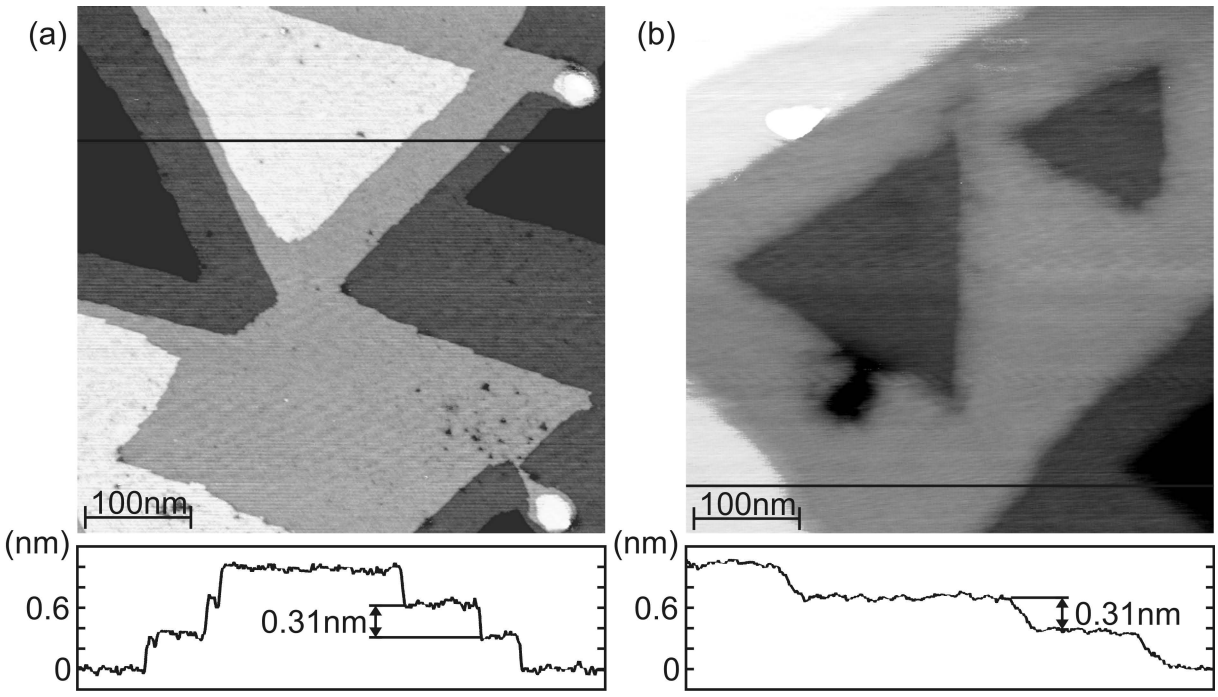

Figure 4.18: n – Si (111):H surfaces exhibiting step edges of 0.31 nm in height imaged by different STM tips at the same experimental conditions $U_{bias} = 700\,mV$ and $I_{tunnel} = 30\,pA$. From the line scans a larger apparent step edge width in STM image (b) is obvious. This broadening is due to the larger $r_{tip} = 300\,nm$ used in STM image (b) in comparison to $r_{tip} = 25\,nm$ in STM image (a).

When analysing "high quality" images as shown in Figure 4.18a, large tip apex radii are found as well. A tip apex radius $r_{tip} = 25\,nm$ is determined from the measured step edge width in Figure 4.18a. On the other hand tip apex radii of $r_{tip} = 300\,nm$ result in reasonable images as well, although this had not been expected at all (Figure 4.18b). The worse STM tip, i.e. the tip with larger r_{tip}, even shows a better STM image with respect to the ripple in the line scan on top of a terrace (Figure 4.18b), since it averages the tunneling current from a larger area.

The investigations point out, that the presence of flat terraces in STM images is not a reliable source for judging the STM tip quality, i.e. tip apex radius r_{tip}. Rather a detailed analysis of the apparent width of sharp vertical features as, e.g., step edges is required.

An experimental determination of the actual tip apex radius r_{tip}, as performed in the presented experiments, is a cumbersome and time consuming task, but verifies, that the tip apex radius can be determined in STM experiments from comparison of a calculated step edge profile and the corresponding profile from the measurement.

(v) actual and apparent shape of nanoscale multilayer clusters:

So far, the study was focussed on features of one atomic layer in height. Metal clusters

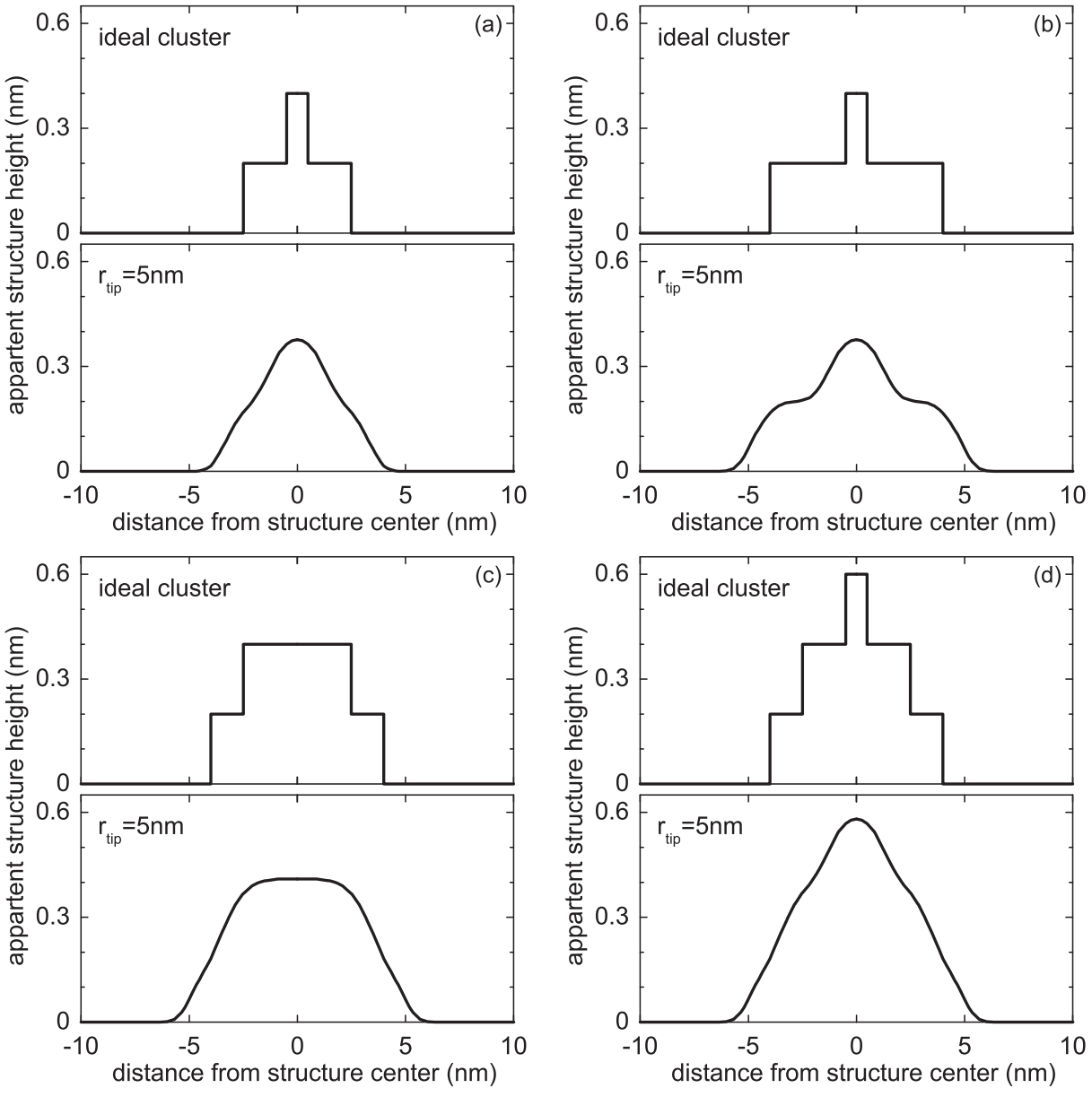

Figure 4.19: Ideal clusters and calculated shape of the clusters in STM images for tip apex radius $r_{tip} = 5\,nm$, using $z_0(r_{tip} = 5\,nm) = 0.8\,nm$ and constant current conditions. The clusters consist of 0.2 nm high layers with a width of (a) 5/1 nm, (b) 8/1 nm, (c) 8/5 nm, (d) 8/5/1 nm.

at the nanoscale usually exhibit heights of several monolayers. This situation is simulated

by a superposition of the calculations for individual layers (Figure 4.19). This procedure is applicable, as long as the step edges of the various layers in the cluster are separated by approximately two times the broadening of a single step edge. This is approximately 2 nm for a tip apex radius $r_{tip} = 5\,nm$. Various cluster configurations are shown in Figure 4.19 together with their apparent shape calculated using a tip apex radius $r_{tip} = 5\,nm$ and $z_0(r_{tip} = 5\,nm) = 0.8\,nm$.

The cluster in Figure 4.19a consists of a base layer of 5 nm width and a 1 nm wide top layer. Its apparent shape does hardly exhibit the steps of its actual shape, the cluster appears broadened and reduced in height.

A cluster with a broader base layer of 8 nm, keeping the 1 nm wide top layer is shown in Figure 4.19b. The apparent cluster shape implies a step shape of the actual cluster, but also shows significant broadening of the base and top layer and a reduced cluster height in comparison to the actual cluster shape.

Keeping the base width of the cluster at 8 nm and increasing the top layer to 5 nm results in an apparent cluster shape, which barely reproduces the stepped shape of the actual cluster and is broadened in comparison to the actual cluster shape (Figure 4.19c). The apparent height of the cluster reproduces the actual cluster height.

Adding a third layer of 1 nm width to the cluster from Figure 4.19c gives the cluster in Figure 4.19d. Again, the apparent shape does hardly reproduce the step shape of the actual cluster. Each layer of the cluster appears broadened and the cluster height reduced in comparison to the actual cluster shape.

The analysis of the clusters in Figure 4.19 shows, that clusters of sizes below 10 nm can hardly be imaged accurately in STM experiments, even using STM tips of radius $r_{tip} = 5\,nm$. Detailed features like step edges are barely reproduced and are not expected to be resolved in actual STM experiments. Although flat terraces and step edges can be imaged with very good resolution by a tip of radius $r_{tip} = 5\,nm$ (Figure 4.14 and Figure 4.15), and STM images with $r_{tip} = 25\,nm$ appear to be of "high quality" (Figure 4.18a), the imaging of clusters implies much higher requirements to the STM tip apex radius.

Conclusion

Three-dimensional calculations taking into account the electronic interaction across a tunneling contact demonstrate severe limitations of the achievable resolution in STM experiments caused by a finite STM tip apex radius.

The width of nanoscale structures on a sample surface deviates from the actual structure width by a tip apex radius dependent offset, which increases nonlinearly with increasing tip apex radius. In addition to the offset, the apparent width of small structures is further increased, and their height reduced, when they are imaged with tips of radii larger than the actual structure size.

These effects have dramatic consequences when structures with finite vertical height, e.g., nanoscale clusters of several atomic layers in height, are imaged. The clusters appear significantly broadened in STM images, their actual height is not accurately reproduced and their layered structure can hardly be resolved using tips of inappropriately large radius. Maintaining the error in the apparent size of structures extending a few nanometers in comparison to their actual size below 50% demands for STM tip apex radii of approximately the actual structure size, as a rule of thumb, while for structures of larger size the requirements in the tip apex radii become less stringent.

The results obtained can be exploited to determine STM tip apex radii from known structures as, e.g., step edges in STM images. This information can then be used to deconvolute the measured shape of unknown structures in the same STM image, in order to reconstruct their actual shape. Despite the possibility to deconvolute STM tip effects and actual structure shapes in STM images, the calculations line out, that for meaningful STM experiments on nanoscale structures tips with radii of several nanometers and their reproducible preparation are mandatory.

4.4 Charge transfer processes via surface states at electron depleted n – Si (111):H surfaces probed by electrochemical deposition and dissolution of Cu [7]

n – Si (111):H surfaces exposed to aqueous electrolytes are utilised in studies on the initial stages of metal electrodeposition [36, 37, 190, 311, 334, 354, 363, 428] or as substrate for other applications in various fields of research and technology. Charge transfer processes at the n – Si (111):H surface are determined by the band gap, doping level and working electrode potential, which result either in electron depletion or electron accumulation conditions at the n – Si (111):H surface. Surface states in n – Si (111):H are known (see section 4.2.3), their role in charge transfer processes at the solid / liquid interface is still vague, when the corresponding literature is reviewed [36, 37, 190, 225, 311, 334, 354, 363, 428, 429]. A major origin for these surface states seems to be hydrogen, incorporated in the n – Si (111):H subsurface region (see section 4.2.3). The associated energy levels are positive of the flatband potential E_{FB}, i.e. in a potential range, where the n – Si (111):H surface is depleted of electrons (see section 4.2.3). The density of these states in the n – Si (111):H subsurface region is $(10^{14} - 10^{15})\,cm^{-3}$ (see section 4.2.3) and compares to typical doping densities of $10^{15}\,cm^{-3}$ of n – Si (111):H samples utilised frequently in charge transfer experiments or applications at solid / liquid interfaces.

These surface states in n – Si (111):H actually participate in charge transfer processes at working electrode potentials positive of the n – Si (111):H flatband potential E_{FB}, as it is shown in this section of the present thesis. As an example, the Cu / Cu^{2+} system was chosen, where electrodeposition onto and dissolution from electron depleted n – Si (111):H surfaces in the potential range $E_{WE} > E_{FB}$ is observed. The amount of transferred charge is small, but, nevertheless, substantial on the nanoscale.

To assure the quality of the n – Si (111):H surfaces used in the studies on electrochemical charge transfer processes, at first STM images of the n – Si (111):H surfaces in metal ion free 0.1 M H_2SO_4 were recorded, with the electrode potential adjusted between $E_{WE} = -280\,mV$ and $E_{WE} = +280\,mV$ at a bias voltage $U_{bias} = E_{tip} - E_{WE} = +600\,mV$. The n – Si (111):H surfaces show potential independent clean terraces and a small surface roughness, as shown exemplarily in Figure 4.20. In a next step, the substrate potential has been adjusted to $E_{WE} = +430\,mV$, i.e. far positive of the flatband potential $E_{FB} = -53\,mV$ and the STM tip was set at a potential $E_{tip} = +1030\,mV$, keeping $U_{bias} = +600\,mV$. The bias voltage was maintained constant at $U_{bias} = +600\,mV$ during

[7] Results presented in this section have been published in [ii]

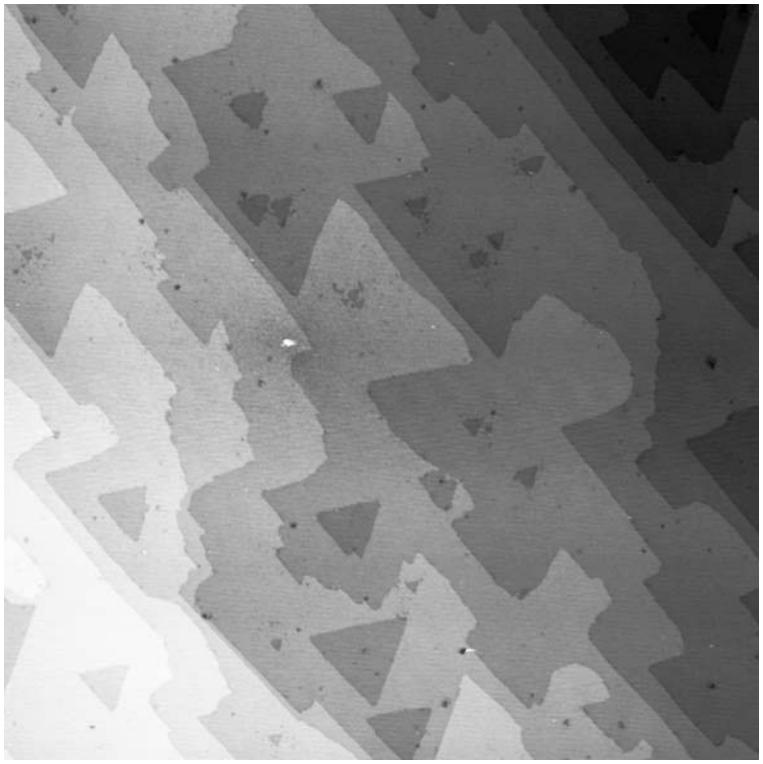

Figure 4.20: Freshly prepared n – Si (111):H surface imaged by STM in a 0.1 M H_2SO_4 electrolyte without Cu^{2+} ions. ewe = −280 mV, E_{tip} = +520 mV, I_{tip} = 30 pA. Image size is 1000 nm × 1000 nm.

all measurements and all substrate potential variations, unless explicitly denoted. In the next step, $CuSO_4$ was added to the electrolyte resulting in a 100 mM Cu^{2+} solution. The $CuSO_4$ used was either of p.a. (BDH Prolabo) or 99.995% metals basis (Sigma-Aldrich) quality. There was no difference in the electrochemical behaviour of the two qualities noticed.

The initial down-scan of E_{WE} on a freshly prepared n – Si (111):H surface in Figure 4.21a shows a steep increase in cathodic current density at working electrode potentials $E_{WE} < E_{FB}$. In this potential range the n – Si (111):H surface is under electron accumulation conditions. The semi-logarithmic plot of the current-potential curve in Figure 4.21b (black filled circles) shows a slope of approximately 60 mV per decade of current density. According to the relation of the Tafel slope $B = (2.3\,R\,T/\alpha\,F\,n) = (118/n)$ mV [104], the measured slope indicates a charge transfer process with two electrons (n = 2) involved, as expected for the reaction $Cu^{2+} + 2e^- \rightarrow Cu$, i.e. electrodeposition of Cu from the solution. The steeper increase of the current density below $E_{WE} \approx -100$ mV can be attributed to hydrogen evolution on electrodeposited Cu in parallel to the ongoing Cu electrodeposition. The potential independent current density due to double layer charging at clean n – Si (111):H surfaces in a Cu^{2+} free electrolyte is shown as grey filled circles

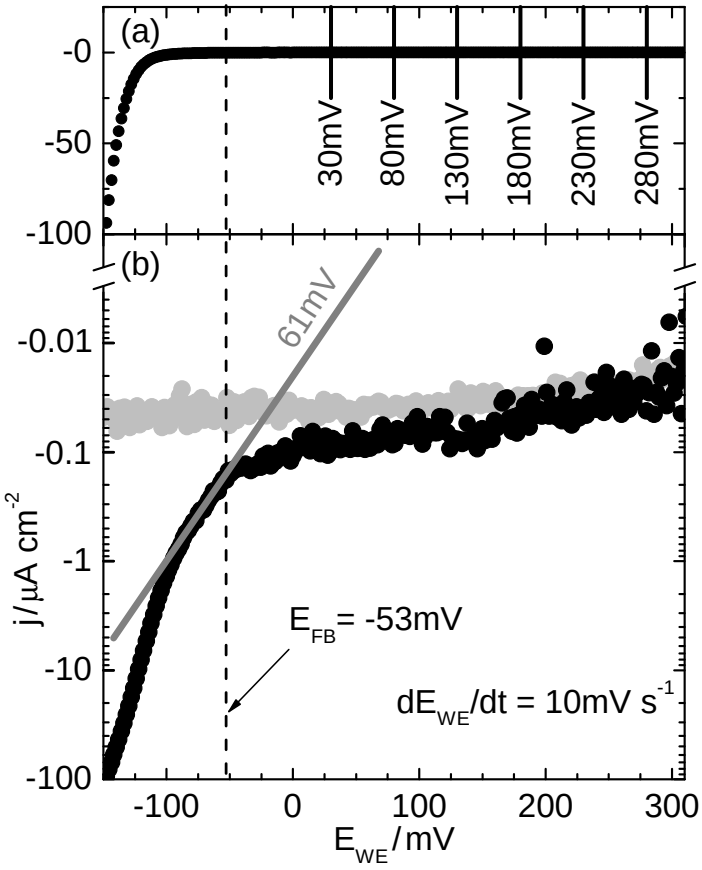

Figure 4.21: Current–potential curve (black filled circles) of Cu deposition onto a freshly prepared n – Si (111):H surface for decreasing E_{WE}, shown on a linear (a) and semi-logarithmic scale (b). The grey line in (b) indicates the slope of approximately 60 mV per decade of current density of the electrochemical Cu deposition. The grey filled circles in (b) show the current–potential curve of n – Si (111):H in a metal ion free 0.1 M H_2SO_4 electrolyte, representing the double layer charging current. The dashed line indicates the flatband potential E_{FB}. The vertical solid lines and potential values in (a) indicate the particular values of E_{WE} where the STM images shown in Figure 4.23 were taken.

in Figure 4.21b. Substracting this charging current from the total current in Figure 4.21b (black filled circles) allows extraction of the Cu electrodeposition current density shown in Figure 4.22. The Tafel slope is slightly changed and now 56 mV per decade of current density, nevertheless compatible with a two electron transfer process $Cu^{2+} + 2e^- \rightarrow Cu$.

The slope of approximately 60 mV per decade of current density would be also compatible to the forward current density limitation of a Schottky barrier, which is given by $j \sim (\exp(eU/k_BT) - 1)$ [205]. This interpretation might apply on the first view, supposed that small Cu clusters form a Schottky interface to n – Si (111). However, the increase in current density below $E_{WE} \approx -100$ mV (Figure 4.21b and Figure 4.22), which is assigned to hydrogen evolution in parallel to the Cu electrodeposition, is not compatible with this interpretation. Also, current densities obtained from current–voltage measurements at nanoscale diodes on n – Si (111) under electrochemical conditions [98] result in a

Schottky barrier limited current density, which is several orders of magnitude larger than the current density shown in Figure 4.21b and Figure 4.22. Therefore, the slope of approximately 60 mV per decade of current density observed in the experiments is unlikely to represent a Schottky barrier limited current density. The electrochemical interpretation of the slopes at working electrode potentials negative of the flatband potential E_{FB} (Figure 4.21b and Figure 4.22) seems to be more appropriate to the experiments, and is in accordance to previous reports in the literature on the electrodeposition behaviour of Cu on n – Si (111):H [311,334,354,355,363,429].

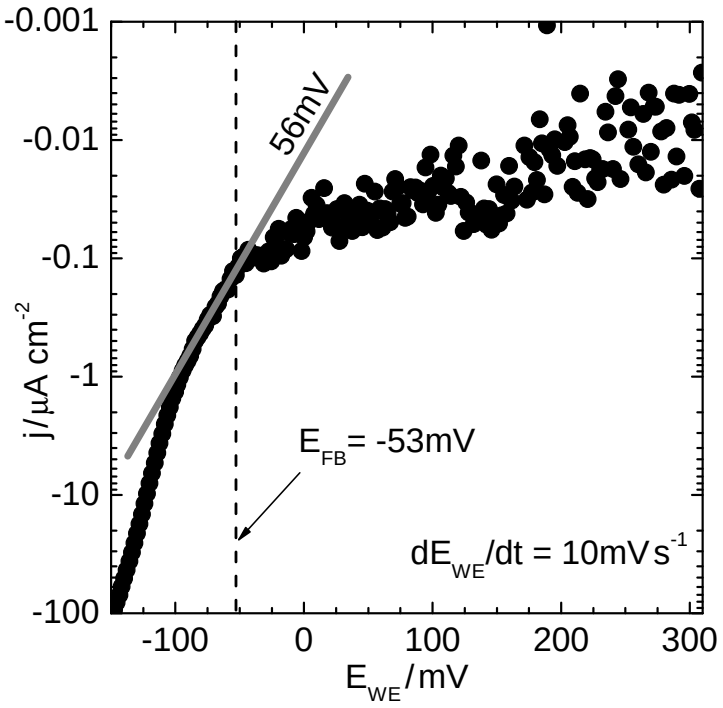

Figure 4.22: Current density related to Cu deposition upon substraction of the double layer charging current density (grey filled circles in Figure 4.21b) from the total current density (black filled circles in Figure 4.21b). The grey line indicates the slope of 56 mV per decade of current density of the electrochemical Cu deposition. The dashed line indicates the flatband potential E_{FB}.

At potentials $E_{WE} > E_{FB}$, i.e. at electron depletion conditions at the n – Si (111):H surface, a substantial current density is observed (Figure 4.21b, black filled circles and Figure 4.22), although a much steeper decrease of the current density with E_{WE} than approximately 60 mV per decade of current density had been expected due to the electron depletion at the n – Si (111):H surface in the potential range $E_{WE} > E_{FB}$.

The characterisation of the n – Si (111):H surface by STM at $E_{WE} > E_{FB}$, where a clean surface had been expected, is summarised in Figure 4.23. This sequence of images has been taken at the electrode potentials indicated in Figure 4.21a. A clean n – Si (111):H

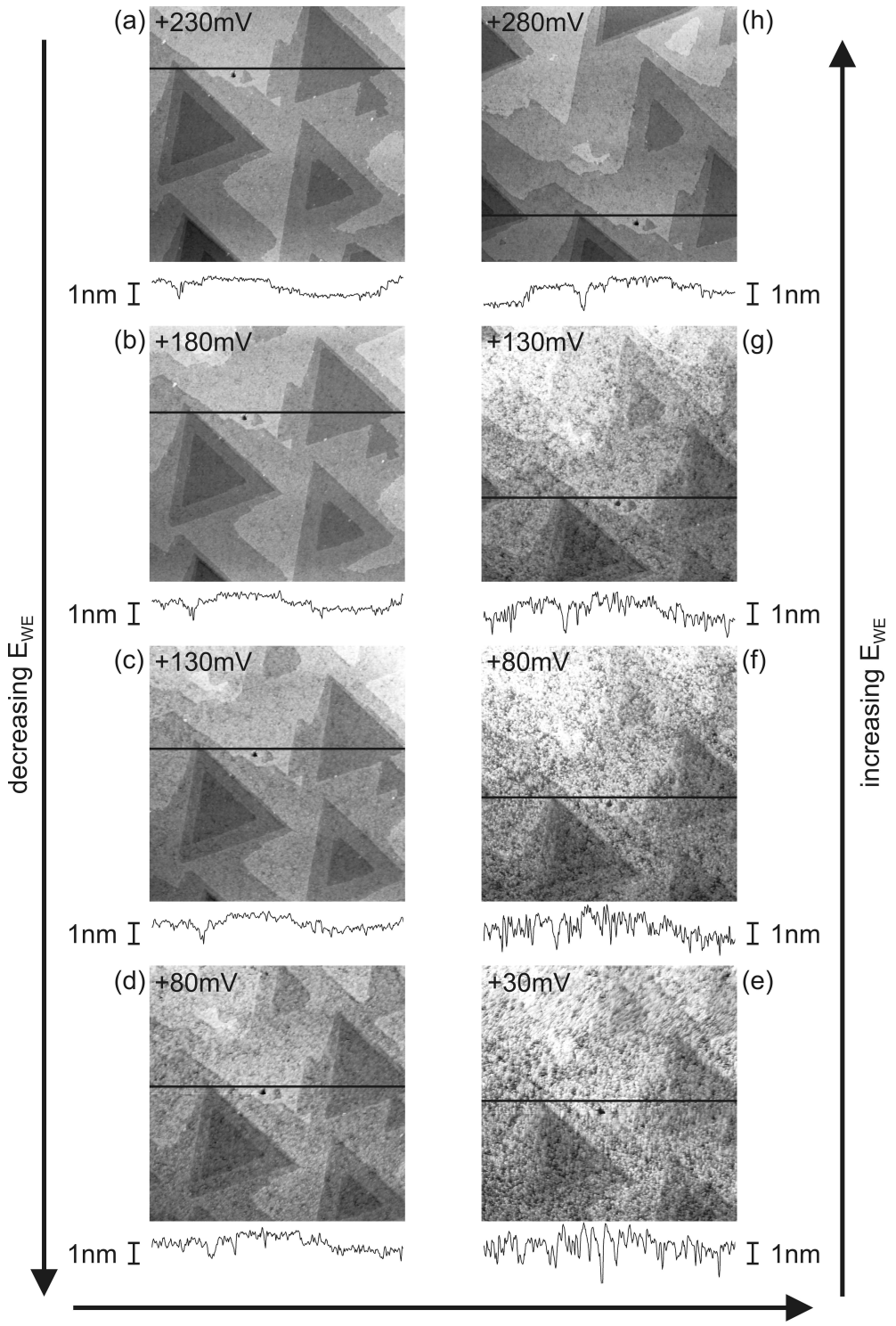

Figure 4.23: Eight subsequent STM images of Cu clusters emerging on the n – Si (111):H surface in contact with a 100 mM Cu^{2+} solution in the potential regime $E_{WE} > E_{FB}$. In each STM image the black line indicates the same position on the sample. At this position the line scans depicted below the corresponding STM image have been taken. The grey scales of the images are not directly comparable to each other due to the flattening of the STM images. The particular working electrode potential E_{WE} is indicated in each image. The bias voltage for all images was $U_{bias} = E_{tip} - E_{WE} = +600\,mV$, $I_{tip} = 30\,pA$. Image size is $1000\,nm \times 1000\,nm$.

surface is only observed at the most positive working electrode potentials of +230 mV and +280 mV. When decreasing the working electrode potential E_{WE} from +230 mV (Figure 4.23a) to +30 mV (Figure 4.23e), nucleation and growth of Cu clusters on the n – Si (111):H surface is observed. The subsequent increase of the working electrode potential from $E_{WE} = +30$ mV (Figure 4.23e) to $E_{WE} = +280$ mV (Figure 4.23h) results in a complete dissolution of the Cu coverage. The n – Si (111):H surface after complete dissolution of the Cu clusters (Figure 4.23h) appears to be as clean as before Cu deposition at the beginning of the sequence (Figure 4.23a), when comparing the smooth line scan before Cu deposition with the likewise smooth line scan upon Cu dissolution.

The observed coverage of the n – Si (111):H surface can be attributed to deposited Cu, since STM images taken in a Cu^{2+} free electrolyte at the same experimental conditions and same working electrode potentials E_{WE} as in Figure 4.23 do not show a potential dependent coverage of any kind, but clean atomically flat n – Si (111):H terraces as those depicted in Figure 4.20 or Figure 4.23a.

There are two prominent aspects in the STM images of Figure 4.23: First, Cu is deposited in a working electrode potential range, where deposition had not been expected in view of the literature [334, 354, 363] and where the n – Si (111):H surface is depleted from electrons [371] (see also section 4.2.3). Second, Cu already deposited onto the n – Si (111):H surface is dissolved, when the working electrode potential is increased. We observe a reversible deposition / dissolution behaviour of Cu.

Since this is an unexpected behaviour, the Cu electrodeposition onto n – Si (111):H under depletion conditions was verified independently of STM experiments by impedance measurements of the n – Si (111):H surface in the presence of Cu^{2+} ions in the electrolyte. The interface was modeled by the equivalent circuit shown as inset in Figure 4.24, and the various parameters simultaneously fitted to the impedance data, using the same procedure as reported in section 4.2.

The surface state capacitance C_{SS} of n – Si (111):H in the case of a Cu^{2+} free electrolyte is represented by open circles in Figure 4.24. It is consistent with the behaviour reported for the surface state capacitance in previous experiments (see section 4.2 and [371]) and proofs, when considering the results obtained in HF solutions [371], that the present n – Si (111):H surfaces are oxide free in Ar purged 0.1 M H_2SO_4 in the investigated potential range. In the case of a Cu^{2+} containing electrolyte (filled circles in Figure 4.24) C_{SS} is increased by a factor of approximately three. Five measurements for both cases have been averaged to get a better statistical significance. The range of these five measurements is indicated by the error bars in Figure 4.24. While in a Cu^{2+} free electrolyte $C_{SS}(E_{WE})$ shows a maximum around $E_{WE} \approx +25$ mV and drops down to zero at potentials negative

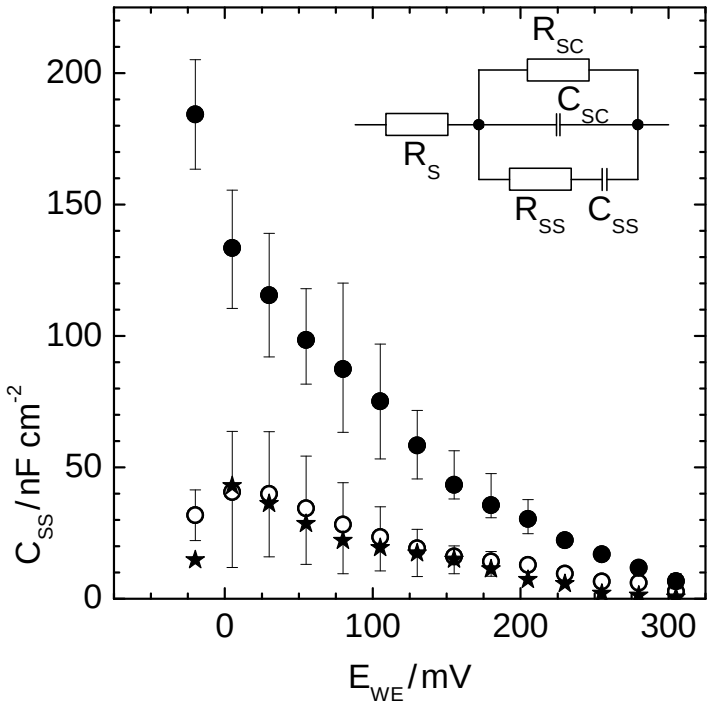

Figure 4.24: Surface state capacitance C_{SS} extracted from impedance measurements for a metal ion free electrolyte (open circles), for 100 mM Cu^{2+} electrolyte (filled circles), and for 10 mM Co^{2+} electrolyte (stars) utilising the depicted equivalent circuit for modeling the n – Si (111):H surface including surface states in contact with the electrolyte. Five measurements have been averaged for better statistical significance, the error bars indicate the range of these measurements. C_{SC}, R_{SC} and C_{SS}, R_{SS} are the capacitance and resistance associated with the space charge region and the surface states, respectively. The resistance R_S accounts for all other ohmic potential drops in the measurement. The electrochemical double layer capacitance can be omitted in the fitting procedure, since it is much larger than C_{SC} and C_{SS}, respectively.

of $E_{WE} \approx +25$ mV, the $C_{SS}(E_{WE})$ values in a Cu^{2+} containing electrolyte are continuously increasing with more negative values E_{WE}. The C_{SS} values for up- and down-scan of E_{WE} are nearly identical and lie within the error bars in Figure 4.24, pointing out the reversibility of the observed effect with respect to E_{WE}.

In order to counter check, whether the change in C_{SS} in the presence of Cu^{2+} correlates only to ionic species at the solid / liquid interfaces or indeed to Cu deposition on the n – Si (111):H surface, C_{SS} was determined also in a Cu^{2+} free electrolyte, but in the presence of Co^{2+} (Figure 4.24, stars). Co is not electrodeposited in the potential range investigated in our experiments and, consequently, C_{SS} obtained for a Co^{2+} containing electrolyte (Figure 4.24, stars) is identical to C_{SS} obtained for a metal ion free electrolyte (Figure 4.24, open circles). STM images of n – Si (111):H surfaces in a Co^{2+} containing electrolyte taken in the same E_{WE} potential range confirm also a Co free and clean

n – Si (111):H surface as for a metal ion free electrolyte (Figure 4.20).

An increase of $C_{SS}(E_{WE})$ either represents an increase in the density of surface states (increased charging current density), or is attributed to a deposition / dissolution current density – the response of the system to the sinusoidal modulation of E_{WE} during the impedance measurements. There is neither hydrogen evolution on n – Si (111):H in this particular potential range, which could result in a hydrogen diffusion into n – Si (111):H and a corresponding increase of the density of surface states, nor an influence of ionic species in the electrolyte as, e.g., Co^{2+} ions without actual deposition, i.e. charge transfer, onto n – Si (111):H.

Therefore, considering in addition the observations in the STM images in Figure 4.23, the totally different behaviour of C_{SS} in a Cu^{2+} containing electrolyte in comparison to a Cu^{2+} free electrolyte or a Co^{2+} containing electrolyte can be attributed to the deposition / dissolution of Cu onto / from the n – Si (111):H surface.

Deposition of Cu onto n – Si (111):H surfaces at $E_{WE} > E_{FB}$ requires a charge transfer of electrons from the n – Si (111) bulk to the electron depleted n – Si (111):H surface. This can be established either through the space charge region and / or by the involvement of surface states.

At a semiconductor / electrolyte interface, the current density associated with cathodic charge transfer is characterised by

$$j^{-}(E_{WE}) \sim e \cdot k_0 \cdot n_{surface}(E_{WE})$$

where e is the elementary charge, k_0 is the rate constant, and $n_{surface}$ is the electron concentration at the electrode surface [105]. In particular, $j^{-}(E_{WE})$ is proportional to $n_{surface}$, which – in contrast to metal electrodes – in semiconductor electrodes varies with E_{WE} as

$$n_{surface} = n_{bulk} \cdot \exp\left(-\frac{E_{WE} - E_{FB}}{k_B T}\right)$$

due to electron depletion at the surface, associated with the space charge region at working electrode potentials $E_{WE} > E_{FB}$ [205]: The density of electrons $n_{surface}$ decreases with more positive values of E_{WE}.

For the present n – Si (111):H samples $n_{bulk} \approx 10^{15}\,cm^{-3}$ for complete donor exhaustion and, thus, $n_{surface} \approx 2 \cdot 10^{13}\,cm^{-3}$ for $E_{WE} = +50\,mV$, $n_{surface} \approx 2 \cdot 10^{12}\,cm^{-3}$ for $E_{WE} = +100\,mV$, and $n_{surface} \approx 4 \cdot 10^{10}\,cm^{-3}$ for $E_{WE} = +200\,mV$.

The dependence of the surface electron concentration $n_{surface}$ on E_{WE} modifies charge transfer processes associated with the surface electron concentration in the potential range $E_{WE} > E_{FB}$ by an additional factor $n_{surface}/n_{bulk} = \exp(-(E_{WE} - E_{FB})/k_B T) \ll 1$.

As a consequence, in the potential range $E_{WE} > E_{FB}$ of the current–potential curve

(Figure 4.21b, black filled circles) a decrease in current density with a slope much smaller than approximately 60 mV per decade of current density (slope for $E_{WE} < E_{FB}$) would have been expected. The actually observed low decrease of the current density with increasing E_{WE} in the potential range $E_{WE} > E_{FB}$ (Figure 4.21b and Figure 4.22) proofs significant charge transfer originating from a different mechanism than charge transfer through the space charge region.

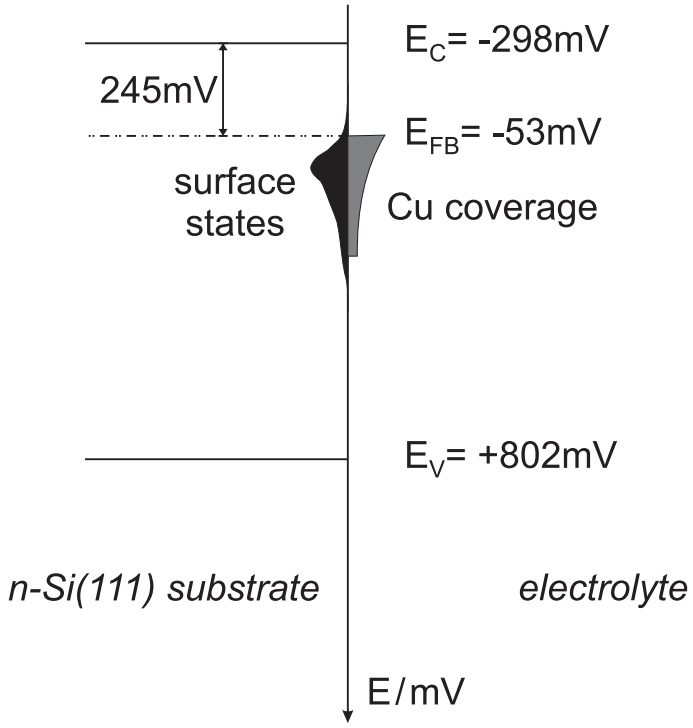

Figure 4.25: Schematic for $E_{WE} = E_{FB} = -53\,mV$ illustrating the position of surface states with respect to the conduction (E_C) and valence band edge (E_V). The surface states (black colour) allow charge transfer in a potential range $E_F = E_{WE} > E_{FB}$. The potential range where a Cu coverage on the n – Si (111):H surface was observed is indicated in grey colour.

It has been previously found, that our samples exhibit surface states extending from the surface up to several hundred nm into the bulk of n – Si (111):H with an associated density of $(10^{14} - 10^{15})\,cm^{-3}$ in the subsurface region (see section 4.2). These states are electronically active in the potential range $E_{FB} < E_{WE} < E_{FB} + 350\,mV$ (see schematic in Figure 4.25), their density is several orders of magnitude larger than the electron density $n_{surface}$ at the n – Si (111):H surface in this working electrode potential range (see section 4.2). As soon, as the Fermi level of n – Si (111):H is set within the potential range of the surface states, electron transfer from the n – Si (111) bulk to the n – Si (111):H surface is dominated by these states rather, than by the space charge region and its low surface electron density $n_{surface}$. Since the surface states extend beyond the space charge

region at the n – Si (111):H surface into the n – Si (111) bulk (see section 4.2), they bypass the inhibition of charge transfer at electron depleted n – Si (111):H surfaces, explaining the initial stages of Cu nucleation and growth being observed at much more positive potentials than E_{FB}.

There may be a discrepancy deduced from the small amount of charge transferred (Figure 4.21b, black filled circles and Figure 4.22) and the rough morphology of the STM images (Figure 4.23e, f), which could be misinterpreted as a much larger coverage. Although the STM images suggest a considerable Cu coverage, the actual coverage is of the order of 1% of a monolayer, which is in good agreement to the transferred charge determined from the current–potential curve (Figure 4.22) [430–432]. This overestimation in the STM images is due to the limited resolution achievable in STM experiments, when nanostructures or clusters of less than 10 nm diameter are imaged. They appear in general as broad features with reduced height in STM images, as has been investigated in detail in section 4.3.

The second aspect of Figure 4.23, Cu dissolution upon an increase of E_{WE} in the potential range $E_{FB} < E_{WE}$, is also in contrast to previous findings in the literature [334, 354,355,429]. There, it was argued, that a Schottky barrier formed between substrate and Cu inhibits Cu dissolution [311,354,429]. However, such an explanation hardly applies to the present experiments: The amount of charge transferred and the corresponding currents in the potential range $E_{WE} > E_{FB}$ are orders of magnitude smaller than the reverse current at room temperature leaking through a Cu / n – Si Schottky barrier with approximately 600 mV barrier height [205, 311, 429, 433]. There are previous STM experiments on Cu electrodeposition on n – Si (111):H [361] showing also that a Cu dissolution current of the order of $1\,\mu A\,cm^{-2}$ is actually observed. This current density would be compatible with a barrier height of approximately 700 mV in the thermionic emission model [205, 433] assuming this anodic dissolution current is determined by the Schottky barrier reverse current at room temperature.

The actual barrier height for nanometer sized Schottky junctions is quite unknown and may be different from the value of bulk junctions [98,434,435]. Regardless of 600 mV or 700 mV barrier height, the current density of less than $0.2\,\mu A\,cm^{-2}$ involved in the experiments at $E_{WE} > E_{FB}$ (Figure 4.21b, black filled circles and Figure 4.22) is well below the reverse current density of a Cu / n – Si Schottky barrier at room temperature. This explains the observed reversibility of Cu deposition and dissolution.

As can be seen from Figure 4.23, the Cu coverage depends on E_{WE} as a consequence of the deposition or dissolution when changing E_{WE} to more negative or positive potential values: The Cu clusters appear to be in an electrochemical equilibrium at a particular value of E_{WE} which corresponds to the Fermi level E_F of the substrate. There are no

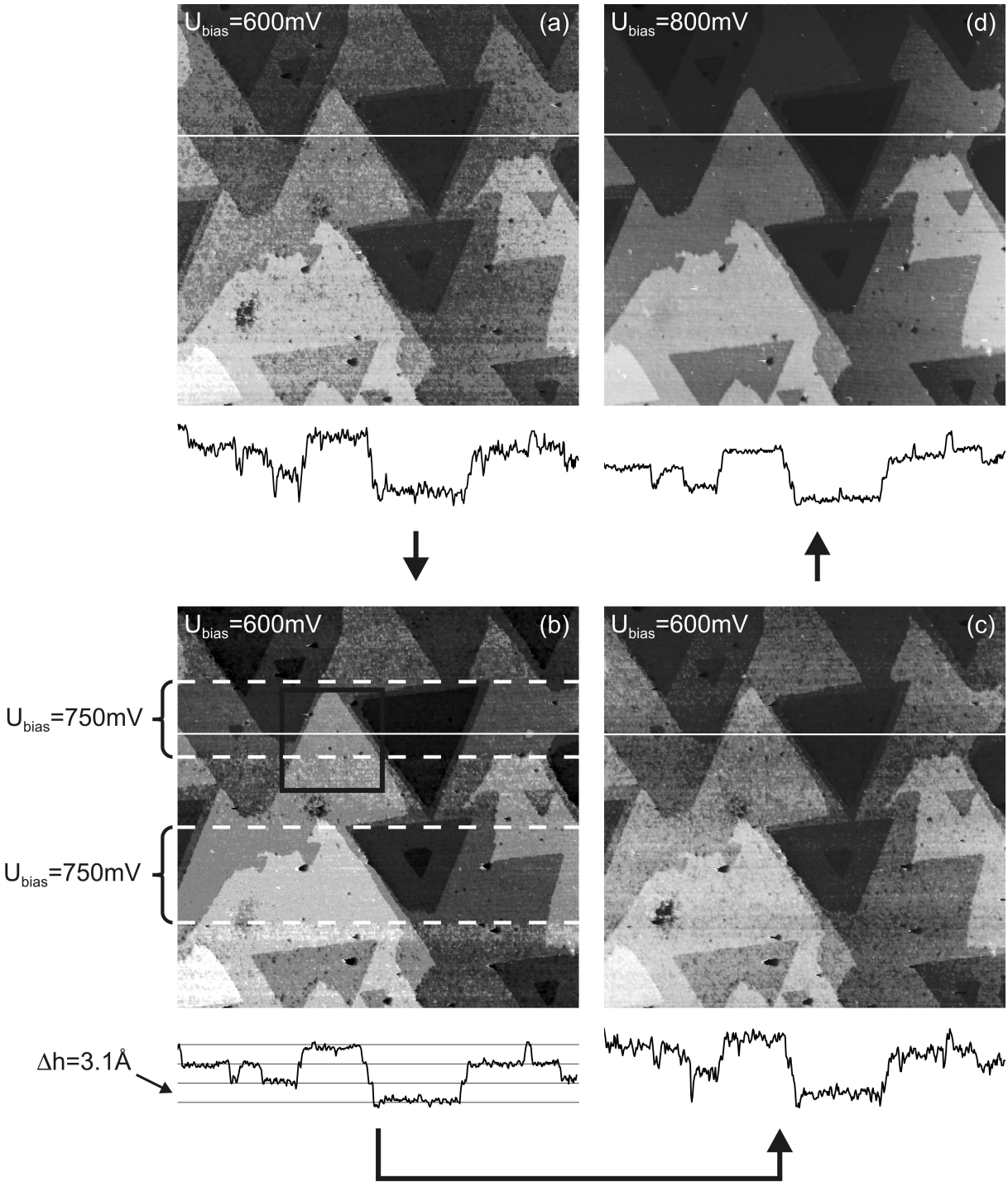

Figure 4.26: STM images showing the influence of the bias voltage U_{bias} on the deposition and dissolution of Cu clusters on n – Si (111):H in a 100 mM Cu^{2+} solution. Cu clusters dissolve underneath the STM tip upon increasing U_{bias} to 750 mV and 800 mV and are re-deposited upon lowering U_{bias} back to 600 mV. The black square in image (b) indicates the area shown in more detail in Figure 4.27. The line scans (same height scale) are taken at the same position in each image (white solid lines in the images). The size of the clusters is too small as to allow for a correct imaging of their height. In the line scan in (b) the individual steps of the n – Si (111):H surface with their typical step height $\Delta h = 3.1$ Å are outlined exemplarily. $I_{tip} = 30$ pA, $E_{WE} = +130$ mV. Image size is 1000 nm × 1000 nm.

dissolution or deposition phenomena observed, as long as the electrode potential is kept constant.

The electrochemical equilibrium of the Cu clusters with the Cu^{2+} solution can be probed by changing the Cu^{2+} concentration in the electrolyte. It is known, that a positively charged STM tip changes locally the Cu^{2+} ion concentration in the region around the tunneling gap [33, 190, 311, 354, 363, 436–438]. When the bias voltage is increased, and, thus, the STM tip more positive, it repels the positively charged Cu^{2+} ions to a larger extent from the tunneling gap region. The resulting local depletion of Cu^{2+} ions in the electrolyte shifts the electrochemical equilibrium of (Cu on the n – Si (111):H surface) / (Cu^{2+} in the electrolyte), and results in a dissolution of Cu underneath the STM tip. A subsequent decrease of the bias voltage results in the opposite effect.

The STM images in Figure 4.26 and Figure 4.27 show exactly this effect at a Cu covered n – Si (111):H surface at $E_{WE} = +130\,mV$ and different values of the bias voltage. At $U_{bias} = 600\,mV$ (Figure 4.26a) the n – Si (111):H surface is covered with Cu. Upon increasing U_{bias} by 150 mV during the next STM scan two times (scan lines enclosed by brackets in Figure 4.26b), the n – Si (111):H surface appears clean and without Cu coverage when scanned at increased U_{bias}. In Figure 4.27, a detail of the STM image of Figure 4.26b is shown, illustrating the sharp transition from a Cu covered to a clean n – Si (111):H surface upon changing U_{bias}. The bias induced dissolution of Cu is reversible, as can be observed in Figure 4.26c, where the bias voltage was restored to $U_{bias} = 600\,mV$ during the complete STM scan, and the surface is again covered with Cu. Upon increasing U_{bias} to 800 mV and scanning the same area of the n – Si (111):H surface again, there is no indication of Cu on the n – Si (111):H surface (Figure 4.26d).

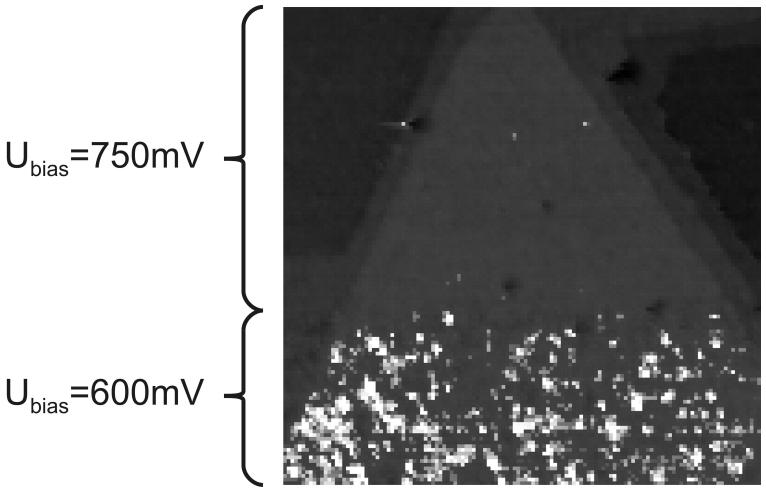

Figure 4.27: Detail of the STM image in Figure 4.26b. The sharp transition from a Cu cluster covered to an uncovered surface upon an increase of U_{bias} can be clearly observed. The grey scale is chosen different from the one in Figure 4.26, to highlight the Cu clusters on the surface. $I_{tip} = 30\,pA$, $E_{WE} = +130\,mV$. Image size is 250 nm × 250 nm.

The electrochemical equilibrium of the Cu clusters can further be deduced from a detailed analysis of the Cu coverage in the STM images of Figure 4.23. The apparent cluster size (FWHM) in equilibrium at particular values of E_{WE}, as measured with STM, is shown in Figure 4.28. Decreasing or increasing E_{WE} reversibly increases or decreases the size of the Cu clusters. Although their actual size is likely to be smaller than the measured apparent size due to the limited resolution of STM caused by finite STM tip apex radii (see section 4.3), Figure 4.28 still represents the principal size dependence of the clusters on the electrode potential E_{WE}.

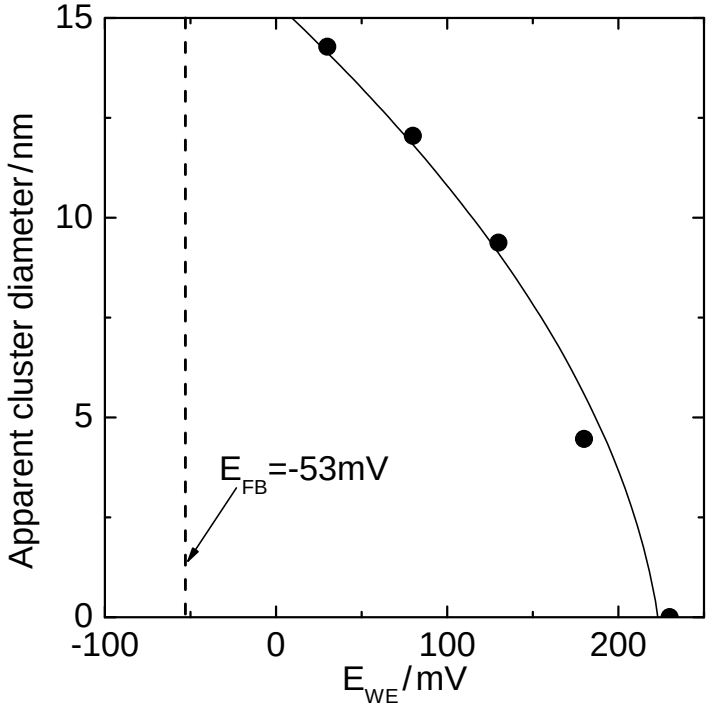

Figure 4.28: Apparent Cu cluster size for different working electrode potentials E_{WE}, as determined from the STM images in Figure 4.23. The line is a guide to the eye.

The decisive quantity for the electrochemical equilibrium of the clusters is E_{WE}, or the Fermi level of the substrate E_F, respectively. The positive STM tip may modify the band edges at the n – Si (111):H surface, bending them down to the Fermi level E_F, as reported previously [375], but does not change E_F. A previously reported compensation of the n – Si dopant concentration by the subsurface hydrogen may result in a variation of E_F in the subsurface region [405], but is speculative and not necessarily required to explain our results.

There are previous reports of stable Cu clusters in electrochemical environment [439, 440]. Their stability at a particular electrode potential has been found to be determined by the balance of increasing surface energy of a growing cluster and the electrochemical energy [439, 440]. The formation of step edges in the growing cluster requires a formation

energy, which is supplied by a decrease of E_{WE}. The same argument holds vice versa for dissolution during an increase of E_{WE}. This mechanism results in an electrochemical equilibrium of the clusters and may also apply to our findings.

The observed stability of the clusters may not be explained by anion adsorption [441] or a nucleation overpotential [111], since such phenomena would still allow for an ongoing electrodeposition at constant E_{WE}, once metal has been deposited onto the surface.

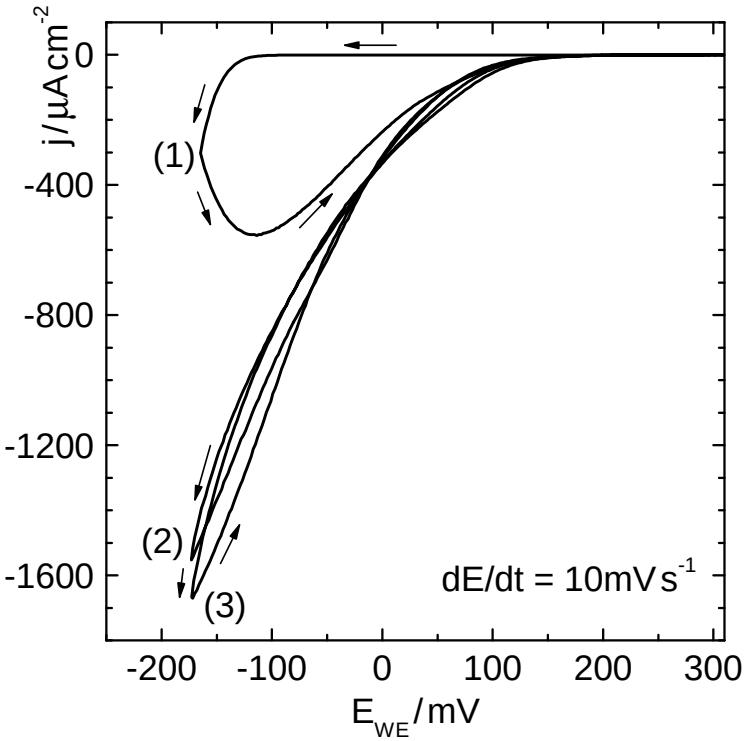

Figure 4.29: Cyclic voltammogram of Cu deposition onto a freshly prepared n – Si (111):H surface. Arrows indicate the scanning direction of E_{WE}. During the first cycle (1) the initially bare n – Si (111):H surface becomes entirely covered by Cu. As a consequence, in subsequent cycles (2) and (3) the onset of Cu deposition is shifted towards $E^0_{Cu\,/\,Cu^{2+}}$, positive of E_{FB}. With increasing Cu coverage, the electrochemical behaviour of the sample becomes similar to a Cu bulk electrode.

A further aspect important for the stability of the clusters is Cu interdiffusion into Si and silicide formation, which has been reported to occur for Cu evaporated onto Si in UHV experiments [442–447]. This process would be reasonable to occur also for electrodeposited Cu. However, a suppression of Cu diffusion into Si has been reported for the H-terminated n – Si (111):H surface [447], and there is no inhibition of Cu dissolution due to a silicide formation observed in our experiments.

The Cu clusters represent low dimensional systems, which are known to deviate in their properties from bulk electrodes [38]. Our experiments are a nice example for such systems, since the observation of Cu clusters and the control of their size by E_{WE} is re-

stricted to very small Cu coverages. As soon, as E_{WE} approaches the flatband potential, the n – Si (111):H surface becomes completely covered with Cu and starts to behave similar to a Cu bulk electrode in electrodeposition experiments, as shown in Figure 4.29.

Conclusions

STM, impedance measurements, and current–potential measurements in the potential range $E_{FB} < E_{WE}$ demonstrate nucleation / growth and dissolution of Cu onto and from electron depleted n – Si (111):H surfaces in contact with an aqueous electrolyte, depending on the actual electrode potential. The Cu clusters appear in this potential range to be in an electrochemical equilibrium with the Cu^{2+} solution. The observed charge transfer processes in the electron depletion regime of n – Si (111):H are mediated by surface states with energy levels in the band gap of n – Si (111):H, whose density is several orders of magnitude larger than the n – Si (111):H surface electron density in the investigated potential range $E_{FB} < E_{WE}$.

The observation of Cu clusters on n – Si (111):H surfaces at electron depletion conditions emphasises the role, surface states may play in electrochemical charge transfer reactions. This is of great importance on the nanoscale, where charge transfer is small compared to macroscopic scales.

4.5 Electrochemical Nanostructuring of n – Si (111):H surfaces by STM Probe Induced Electric Field Effects [8]

The role of electric and magnetic fields in electrodeposition, or charge transfer processes in general, has been rarely investigated. Whereas magnetic fields act preferably on the ionic transport in the electrolyte [448–451], electric fields are screened on nanometer length scales as a consequence of the solid / liquid interface. On the other hand, electric fields should be important only in systems which show a certain polarisability. This is the case for adsorbate structures, molecule layers, or semiconducting surfaces rather than for metal surfaces. At a solid / liquid and at nanoscale dimensions, it is very difficult to apply an electric field in a defined way and there is no possibility to measure the electric field. In the present experiments this task was accomplished in a STM setup, which allows to apply the required electric fields at the sample surface in the tunneling gap.

In such a configuration, the electric field is specified by the bias voltage applied between STM tip and sample surface and the separation of those electrodes (tunneling gap width). The gap width in STM experiments carried out in constant current mode is controlled by the tunneling current setpoint and the tunneling contact cross section, which is determined by the STM tip apex radius (see section 4.3). The STM tip apex radius varies from STM tip to STM tip and therefore from experiment to experiment at the solid / liquid interface. Normally, this is an unwanted effect – here, it is exploited in order to realise a variety of gap widths, which would be difficult to achieve with other methods.

In the present experiments the actual STM tip radius is determined in each STM image from the widths of n – Si (111) step edges on our n – Si (111):H samples following the results presented in section 4.3. The in–situ determination of the STM tip apex radii is a great advantage and increases the reliability of the results.

In this section of the present thesis the effects of electric fields on Co electrodeposition onto n – Si (111):H are studied in detail. It is found that the overpotential required for Co electrodeposition breaks down when a critical electric field is applied. Regarding the terminating H–Si bond at n – Si (111):H surfaces, which is known to inhibit reactions of Co with n – Si (111):H, this suggests, that a particular polarisation is required to allow for Co electrodeposition onto n – Si (111):H.

The inhibition of Co electrodeposition by the H-termination on the one hand, and the localisation of an electric field to the area of the tunneling gap and the corresponding local breakdown of the required overpotential for Co electrodeposition on the other hand,

[8] Results presented in this section have been published in [iii, v]

allow for an electrochemical "writing" process of Co onto n – Si (111):H surfaces by moving the STM tip across the surface at appropriate experimental conditions. We exploit this electrochemical "writing" process in this paper to investigate the influence of electric field on the electrodeposition of Co in more detail.

The n – Si (111):H samples were inserted into a 0.1 M H_2SO_4 electrolyte under potential control at $E_{WE} = -280\,mV$ after dissolved oxygen had been removed from the electrolyte by purging it with Ar 5.0 gas. The gold tip mounted to the STM scanner was inserted into the electrolyte at a potential $E_{tip} = +520\,mV$. Before $CoSO_4$ was added to the electrolyte, the working electrode potential was set to $E_{WE} = -20\,mV$, far more positive than the Nernst potential of a 10 mM Co / Co^{2+} solution $E^0_{Co\,/\,Co^{2+}} = -340\,mV$ and slightly more positive of the flatband potential of our n – Si (111):H samples $E_{FB} = -53\,mV$ as determined in subsection 4.2.2. At those conditions the n – Si (111):H surface was imaged to assure its quality. After $CoSO_4$ was added to achieve a 10 mM Co^{2+} concentration in the electrolyte, a STM scan of the surface was made to check for any contamination of the n – Si (111):H surface eventually introduced during adding the $CoSO_4$ and to again verify its quality. All experiments were performed in the dark, in order to avoid photoinduced electrochemical processes.

The STM was operated in constant current mode for the experiments.

Before the influence of electric fields on Co electrodeposition was investigated, as a reference, the Co electrodeposition onto n – Si (111):H was characterised by cyclic voltammetry, without an additional field applied to the n – Si (111):H surface. The initial scan of the electrode potential E_{WE} of a n – Si (111):H sample in contact with 0.1 M H_2SO_4 containing 10 mM Co^{2+} is shown in Figure 4.30. There is a steep increase in cathodic current density observed in the down-scan for $E_{WE} \lessapprox -590\,mV$. Upon initial electrodeposition of Co onto the bare n – Si (111):H surface, the deposition overpotential breaks down and the current density curve in the subsequent upward scan of E_{WE} is shifted to more positive potential values E_{WE}.

In the upward scan of E_{WE} only a small peak in current density positive of $E_{WE} \approx -250\,mV$ is observed in the logarithmic representation of the cyclic voltammogram in Figure 4.30. In view of the large amount of charge transferred in the downward scan of E_{WE} in comparison to the small amount of charge associated with this peak, the electrodeposition of Co onto n – Si (111):H can be considered basically irreversible, in accordance with previous reports of such charge mismatch in the Co electrodeposition and -dissolution branch in cyclic voltammetry experiments [452–454]. The inhibition of electrochemical Co dissolution upon Co electrodeposition can be explained by the formation of Co-silicide, a process which has been widely studied at bare and H-terminated

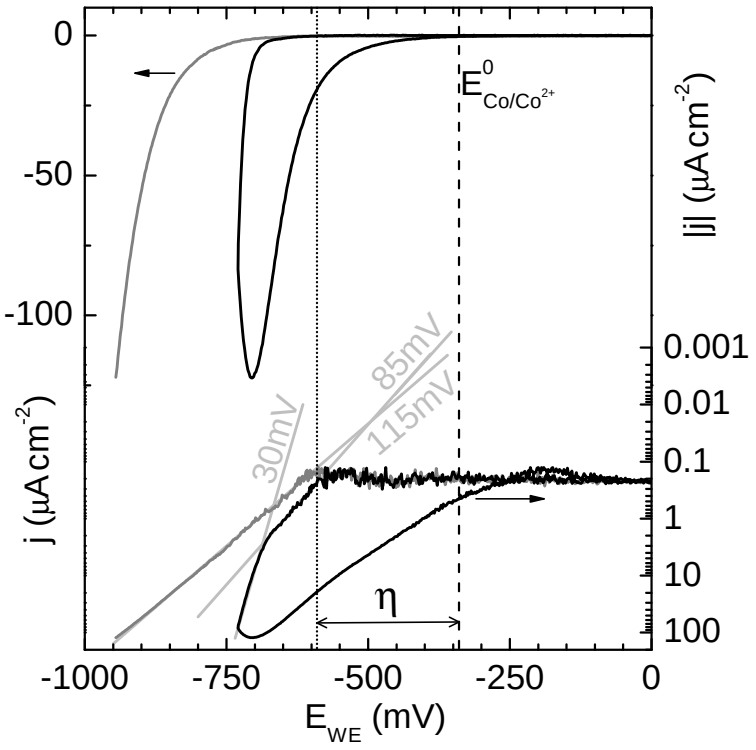

Figure 4.30: Current–potential curve of the initial down scan of a n – Si (111):H working electrode in 0.1 M H_2SO_4 (grey curves) and in 0.1 M H_2SO_4 containing 10 mM $CoSO_4$ on a linear (left axis) and logarithmic (right axis) scale. The current density in the Co^{2+} free electrolyte is due to hydrogen evolution at the n – Si (111):H surface. An overpotential $\eta \approx 250\,\text{mV}$ with respect to $E^0_{Co\,/\,Co^{2+}}$ (dashed vertical line) is required to initiate Co electrodeposition. The different slopes of in the logarithmic plot (115 mV, 85 mV and 30 mV per decade of current variation) indicate hydrogen evolution on n – Si (111):H in a Co^{2+} free electrolyte, Co electrodeposition and hydrogen evolution in parallel to Co electrodeposition, respectively. Potentials are quoted with respect to the SHE reference electrode.

silicon surfaces [329, 455–467], but whose investigation has not been goal of this study. The simultaneous formation of a Schottky barrier at the Si / Co interface cannot account for the observed inhibition of Co dissolution, because the reverse current at room temperature leaking through a Co / n – Si Schottky barrier with approximately (600 – 700) mV barrier height [468, 469], according to the thermionic emission model [205, 433], is orders of magnitude larger than the currents in our experiments and, thus, are no limitation for an eventual Co dissolution process.

The Tafel-plot of the black curve in the lower part of Figure 4.30 suggests two different chemical reactions with the different slopes in $j(E_{WE})$ (light grey lines in Figure 4.30 with 30 mV and 85 mV per decade of current density). To determine the origin of these different slopes, at first the contribution of the hydrogen evolution reaction (dark grey curve) at the bare n – Si (111):H surface is subtracted from the black curve, supposing that

hydrogen evolution reaction on and Co electrodeposition onto the bare n–Si(111):H surface are independent processes. The hydrogen evolution curve (grey curve) was recorded using the same sample as for recording the Co electrodeposition (black curve), but before $CoSO_4$ was added to the electrolyte. The result of the substraction is shown in Figure 4.31 as light grey curve, which corresponds to the current due to the presence of Co^{2+} in the electrolyte. From the light grey curve in Figure 4.31 now the onset of Co electrodeposition can be determined to $E_{WE} \approx -590\,mV$, corresponding to an overpotential $\eta = E_{WE} - E^0_{Co\,/\,Co^{2+}} \approx -250\,mV$. Since Co is know to catalyse hydrogen evolution [470], there may be a contribution from hydrogen evolution also included. However, there need to be Co nuclei on the surface also in this case. At $E_{WE} \approx -675\,mV$ the slope in the current density related to Co (black and light grey curve in Figure 4.31) changes. This may indicate progressive nucleation of Co on the n–Si(111):H surface, after, at more positive potentials E_{WE}, a seed layer of Co was electrodeposited. Also the upward scan of E_{WE} indicates such a nucleation behaviour, due to its hysteretic behaviour with a substantially increased current density in the upward scan. The slopes of 30 mV per decade of current density and 85 mV per decade of current density may therefore be attributed to Co electrodeposition and hydrogen evolution in parallel to Co electrodeposition.

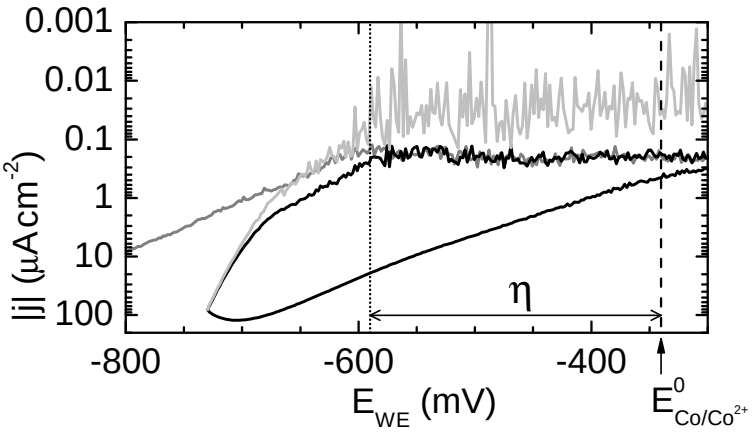

Figure 4.31: Detail of Figure 4.30: Current–potential curves on a logarithmic scale representing hydrogen evolution on n–Si(111):H in a Co^{2+} free electrolyte (grey curve), Co electrodeposition onto n–Si(111):H (black curve) and Co electrodeposition onto n–Si(111):H after substraction of the contribution due to hydrogen evolution on the bare n–Si(111):H surface (light grey curve). Potentials are quoted with respect to the SHE reference electrode

Both reactions (hydrogen evolution and Co electrodeposition) require a substantial overpotential at the n–Si(111):H surface. From the dark grey curve in Figure 4.31 the onset of hydrogen evolution on the bare n–Si(111):H surface is determined at the same E_{WE} value as the onset of Co electrodeposition. Since the onset of both reactions coincides at $E_{WE} \approx -590\,mV$, it seems to be likely, that at this potential the activation barrier

inhibiting the reactions is vanishing. Origin for this inhibition it the H-termination of the n – Si (111):H surface. Its polarisation at the n – Si (111):H / electrolyte interface weakens the H –Si bonds at the n – Si (111):H surface, which is sufficient at $E_{WE} \approx -590\,mV$ to overcome the activation barrier and to allow for hydrogen evolution and, in the presence of Co^{2+}, Co electrodeposition.

These results are in line with findings of a weak interaction of metals with H-terminated Si surfaces, which is well known for electrochemical environment [37,38,190,197,311,428] as well as for surfaces in vacuum [329, 471–473]. The proposed mechanism seems a reasonable explanation for the overpotential required for Co electrodeposition, which has already been reported previously [452–454], although its origin remained unclear.

An electrochemical nanostructuring routine making use of the stimulation of Co electrodeposition by an electric field at the n – Si (111):H surface was used as a probe for investigating the detailed relation between electric field and electric field induced Co electrodeposition.

Nanostructures created by the routine were imaged by the STM in constant current mode. During STM imaging of the n – Si (111):H surface, the potential of the n – Si (111):H substrates was set to $E^{I}_{WE} > E^{0}_{Co\,/\,Co^{2+}}$, i.e. in a potential range positive of the $Co\,/\,Co^{2+}$ Nernst potential, where Co is not electrodeposited onto n – Si (111):H. The STM tip potential during imaging was set to $E^{I}_{tip} > E^{I}_{WE}$, which results in a bias voltage $U_{bias} = E^{I}_{tip} - E^{I}_{WE}$. Co is not electrodeposited at $E^{I}_{WE} > E^{0}_{Co\,/\,Co^{2+}}$, and, neither is electrodeposited Co dissolved from the n – Si (111):H electrode surface at $E^{I}_{WE} > E^{0}_{Co\,/\,Co^{2+}}$ (see Figure 4.30). This effect is exploited for imaging the Co nanostructures by STM at potentials positive of $E^{0}_{Co\,/\,Co^{2+}}$.

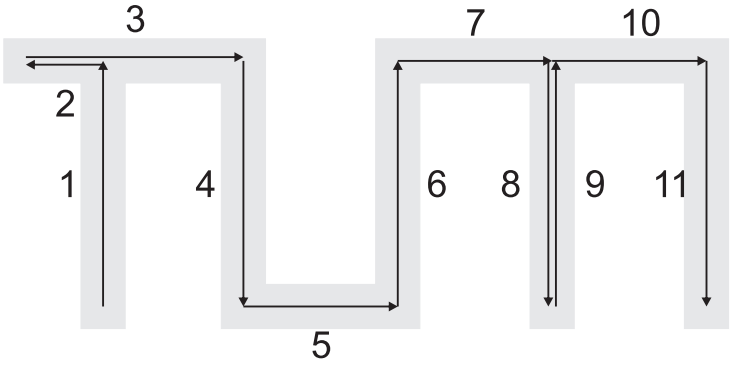

Figure 4.32: Scheme illustrating the path for “writing” the nanostructure “TUM” onto n – Si (111):H surfaces.

For the creation of nanostructures, the operation mode of the STM was altered, following a certain procedure: At first, the x-y scanning of the STM tip across the n – Si (111):H surface is stopped. Next, the working electrode potentials of the n – Si (111):H substrate

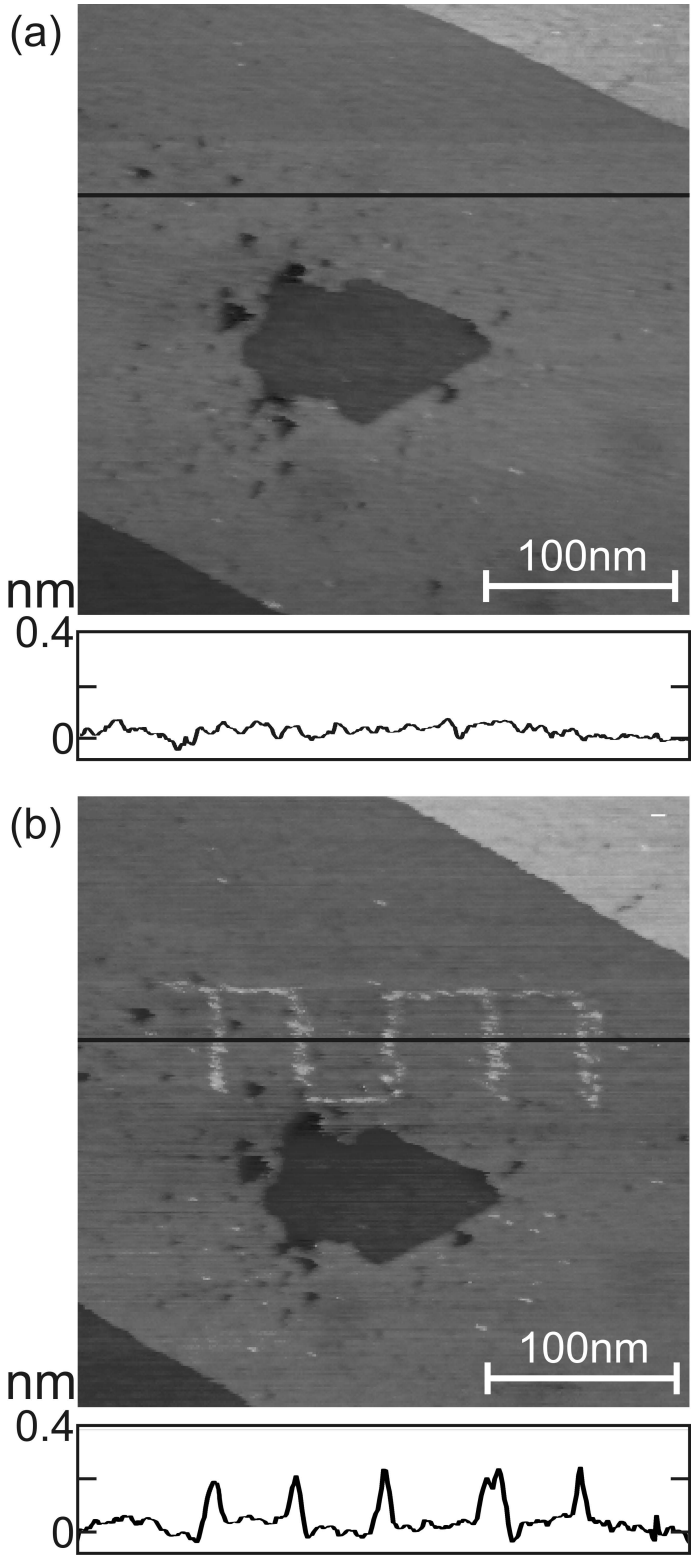

Figure 4.33: STM images showing the n–Si(111):H surface before (a) and after (b) application of the nanostructuring routine ($I_{tip} = 30\,pA$, $U_{bias} = 700\,mV$) on a n–Si(111):H terrace. The line scans below the STM images were taken at the position indicated by the black horizontal line in the respective STM image.

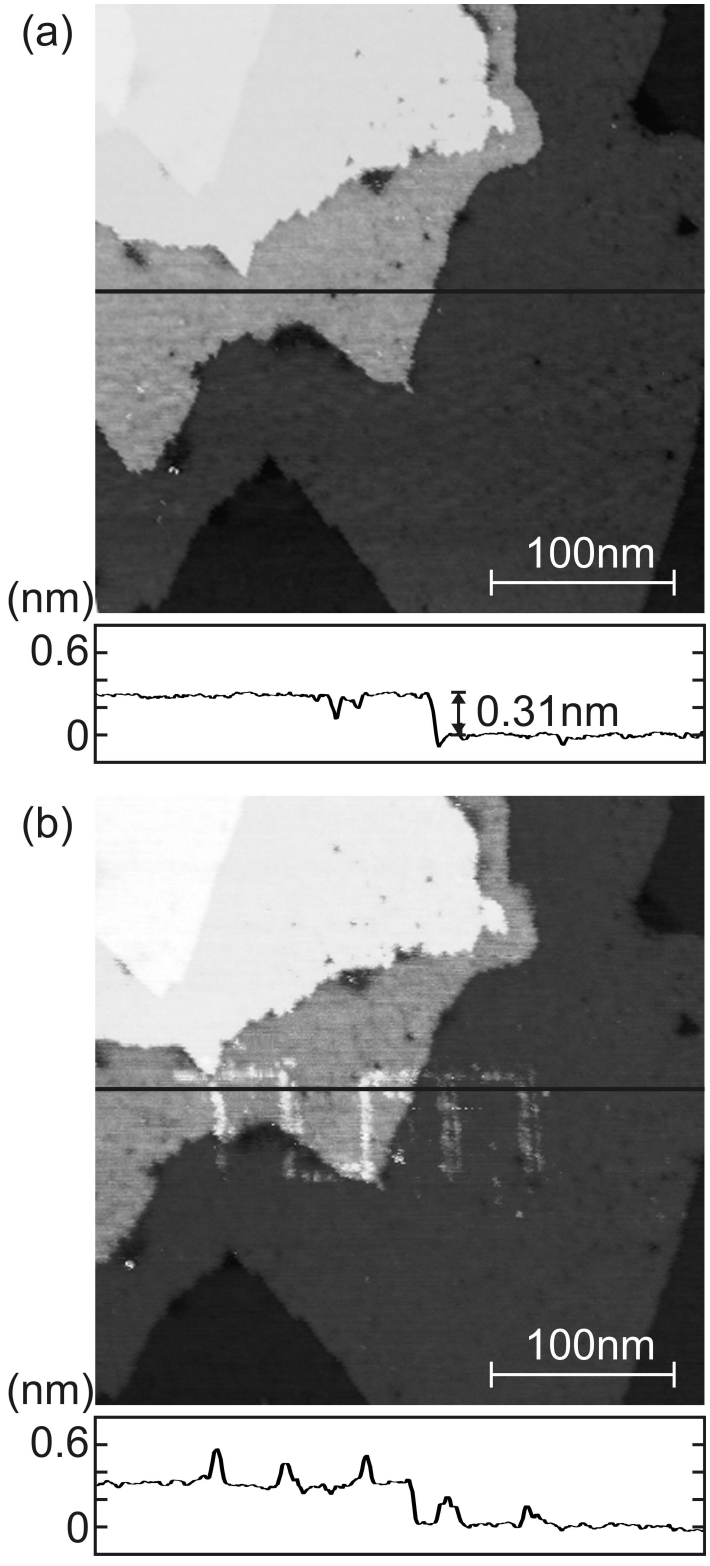

Figure 4.34: STM images showing the n – Si (111):H surface before (a) and after (b) application of the nanostructuring routine ($I_{tip} = 30\,pA$, $U_{bias} = 600\,mV$). The nanostructure has been created across a n – Si (111):H step edge. The line scans below the STM images were taken at the position indicated by the black horizontal line in the respective STM image. The typical step height for n – Si (111):H surfaces of 0.31 nm can be clearly determined.

and the STM tip are changed simultaneously from E^{I}_{WE} and E^{I}_{tip} to E^{W}_{WE} and E^{W}_{tip}, respectively, while keeping $U_{bias} = E^{I}_{tip} - E^{I}_{WE} = E^{W}_{tip} - E^{W}_{WE}$ constant. The potential of the substrate is set to $E^{W}_{WE} > -590\,mV$, i.e. in a potential range, where E^{W}_{WE} is not negative enough to attain the required overpotential η of about 250 mV for Co deposition onto n–Si(111):H (Figure 4.30). Now the STM tip is moved along a predefined x-y path across the surface. At the end of the path the working electrode potentials are reset to E^{I}_{WE} and E^{I}_{tip}. Finally, the x-y scanning motion is continued in the usual manner. Whether the nanostructuring of the surface was successful now was determined from the observation of the programmed pattern on the n–Si(111):H surface.

A modification of the n–Si(111):H surface by the electrochemical nanostructuring procedure was only observed using a Co^{2+} containing electrolyte. The n–Si(111):H surface was not altered when using the very same experimental parameters and conditions in a Co^{2+} free electrolyte. Therefore, the nanostructuring of n–Si(111):H surfaces in our experiments can be attributed to local Co electrodeposition, rather than to tip–sample interactions as, e.g., scratching the surface or tip material transfer to the surface.

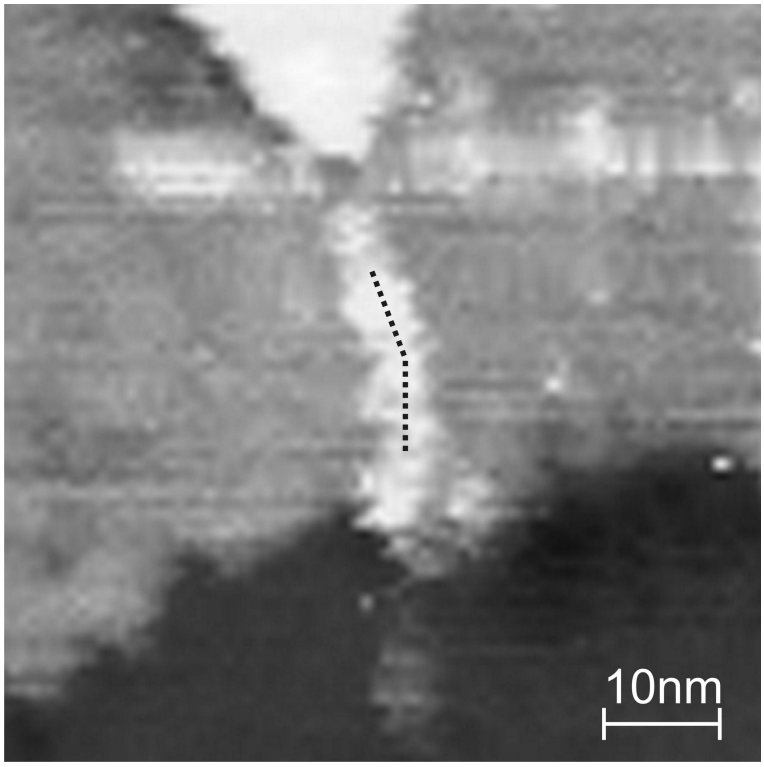

Figure 4.35: Enlarged detail of Figure 4.34 illustrating the deflection of the electrochemically grown Co line from the vertical path of the STM tip due to the influence of the upper protrusion on the electric field distribution in the tunneling gap. The dotted line is a guide to the eye. This feature demonstrates also the lateral length scale of the tip–sample interaction of approximately 20 nm.

Results of the nanostructuring routine are shown in Figure 4.33 and Figure 4.34, where as an example pattern (see Figure 4.32) the logo "TUM" for Technische Universität München was "written" onto the n – Si (111):H surface. Since I_{tunnel} is kept constant by the STM feedback loop during the nanostructuring procedure, "writing" across step edges of the n – Si (111):H surface is possible, regardless of the actual n – Si (111):H surface topography (Figure 4.34). The structures appear (5 – 8) nm in width, about (0.2 – 0.3) nm in height, and indicate a sufficient electric field for a modification of the n – Si (111):H surface by localised electrodeposition ("writing") in the experiment.

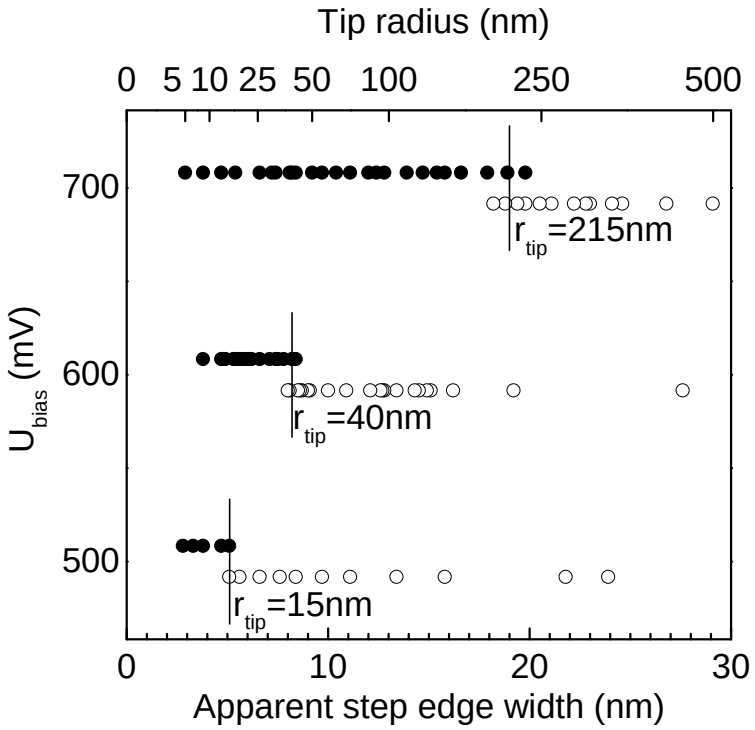

Figure 4.36: Successful nanostructuring was only achieved for tip apex radii below a critical radius (filled circles), while larger tip apex radii were not suitable (empty circles). The STM tip apex radii determine tunneling gap width and the electric field at the n – Si (111):H surface and, thus, whether nanostructures can be created on n – Si (111):H surfaces. The critical tip apex radius allowing for nanostructuring increases with increasing bias voltage. The tip radii were determined from the apparent n – Si (111):H step edge width in STM images (shown as a second abscissa) according to the relation shown in Figure 4.37.

In these experiments, several indications towards an electric field effect are observed: The upper part of the vertical line of "T" in "TUM" is deflected from the vertical direction towards the protrusion at the upper n – Si (111):H step edge, as shown in detail in Figure 4.35. This deflection occurs on top of the n – Si (111):H terrace, is independent of the lower n – Si (111):H step edge, and is caused by the change in the electric field distribution underneath the STM tip due to the protrusion at the upper step edge. Second, sometimes double lines are found, as can be seen for example in Figure 4.34 (letter "M"),

well separated by a few nm, although the STM image does not show any indication for a double tip. Nevertheless, this feature may be caused by a second protrusion on the STM tip further away from the sample surface than the main tip. While its contribution to the tunneling current vanishes during imaging due to the exponential dependence of I_{tunnel} on z, it represents a second source for high electric field during "writing", since the electric field E(z) directly underneath a protrusion or the main tip apex varies with z^{-1}.

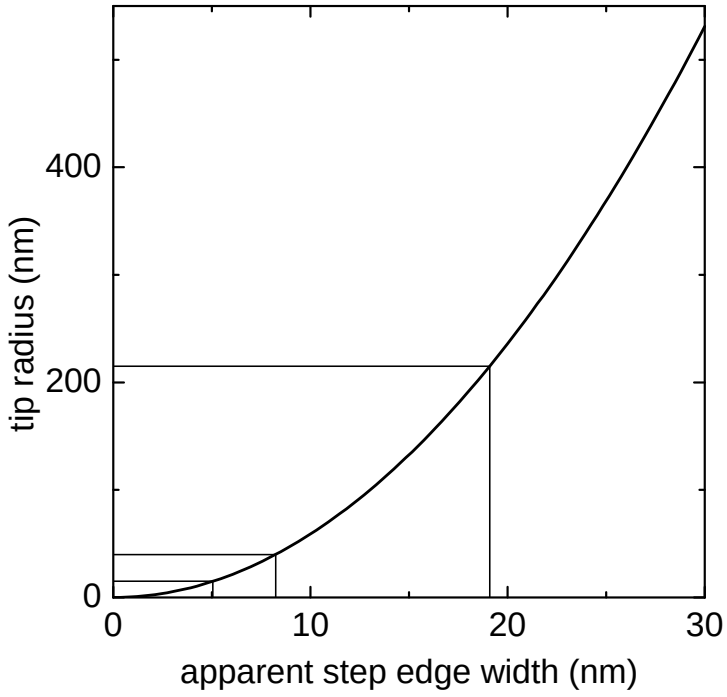

Figure 4.37: Calculated tip radii r_{tip} for experimentally determined apparent step edge widths.

"Writing" could not be achieved with every STM tip. When a "blunt" STM tip has been replaced in-situ by a "sharp" one, and the remaining experimental parameters and sample left unchanged (which is possible with the electrochemical cell used), subsequently "writing" could be achieved. When a "blunt" tip was used, which did not allow for "writing" at $U_{bias} = 600\,mV$, and subsequently U_{bias} increased to 700 mV, "writing" could also be achieved. When a "blunt" tip was used, which did not allow for "writing" at a certain U_{bias}, and subsequently U_{bias} was increased, "writing" could also be achieved.

From the evaluation of many experiments at bias voltages of $U_{bias} = 500\,mV$, $U_{bias} = 600\,mV$, and $U_{bias} = 700\,mV$ a correlation of the "quality" (in terms of resolution) of STM images and "writing" onto n–Si(111):H surfaces is found: "writing" is solely possible at experimental conditions, where the measured width of the n–Si(111):H step edges, as shown by the line scan in Figure 4.34, is smaller than 5 nm in the case of $U_{bias} = 500\,mV$, 8 nm in the case of $U_{bias} = 600\,mV$, and 19 nm in the case of $U_{bias} = 700\,mV$ (Figure 4.36).

"Writing" onto n – Si (111):H requires a STM tip with a particular apex radius r_{tip} depending on the bias voltage U_{bias}. A sharp transition from the "writing" (filled circles) to the "writing not possible" (empty circles) regime in observed in Figure 4.36.

Employing the results from section 4.3, the apparent width of a step edge on a n – Si (111):H surface in a STM image can be related to the apex radius of the tip used for acquiring a STM image, as illustrated in Figure 4.37. For convenience, this information is also included as a second abscissa in Figure 4.36.

The STM tip apex radius determines the electric field distribution at the n – Si (111):H surface on the one hand by its geometry, and on the other hand by its influence on the effective tunneling contact cross section, which in turn, in STM experiments carried out at constant current conditions affects the tunneling contact gap width (see section 4.3). Considering these aspects, a calculation of the electric field distribution at the n – Si (111):H surface for the "critical" tip apex radii r_{tip} determined in Figure 4.36 at the respective bias voltage U_{bias} was performed using the simulation program SIMION 8.1 [474] and the tunneling contact geometry applied in section 4.3.

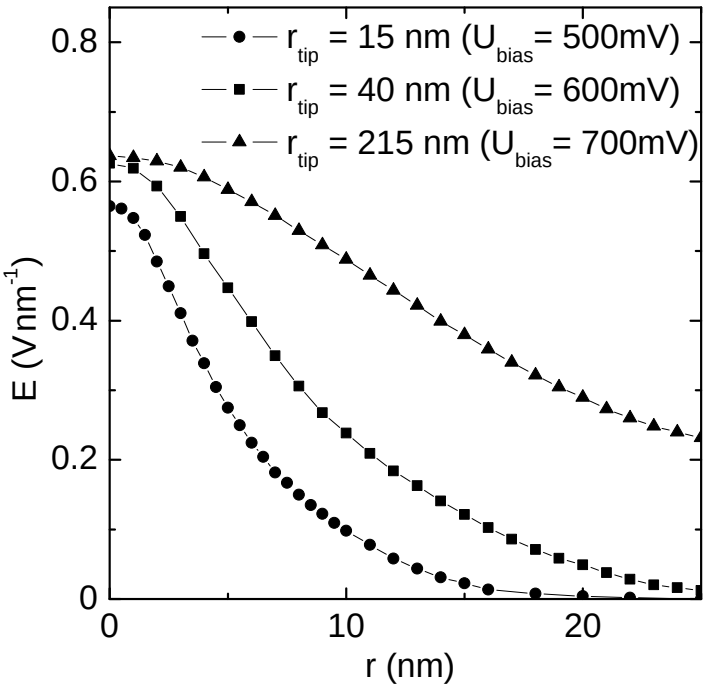

Figure 4.38: Simulation of radial electric field distributions for $U_{bias} = 500\,mV$, $U_{bias} = 600\,mV$, and $U_{bias} = 700\,mV$ at the respective critical tip apex radii $r_{tip} = 15\,nm$, $r_{tip} = 40\,nm$ and $r_{tip} = 215\,nm$, as determined from Figure 4.36

.

In Figure 4.38 the electric field distributions at the n – Si (111):H surface for the critical STM tip radii r_{tip} and the corresponding bias voltages U_{bias}, as determined in Figure 4.36, are shown. The electric field distributions E(r) almost coincide at $r = 0$ (STM tip axis)

for $U_{bias} = 600\,mV$ (0.62 V/nm) and $U_{bias} = 700\,mV$ (0.64 V/nm). For $U_{bias} = 500\,mV$ a maximum in electric field of 0.57 V/nm is obtained, deviating slightly from the values determined for the other bias voltages.

The variation of the tunneling gap width with U_{bias} due to $I_{tunnel} \propto U_{bias}$ was not explicitly included in the calculations. However, taking this effect into account, the maximum field at $U_{bias} = 500\,mV$ increases and the maximum field at $U_{bias} = 700\,mV$ decreases by approximately 3%, choosing $U_{bias} = 600\,mV$ as reference. As a consequence, the maximum field values coincide almost perfectly: 0.6 V/nm at $U_{bias} = 500\,mV$ and 0.62 V/nm at $U_{bias} = 600\,mV$ and $U_{bias} = 700\,mV$, respectively.

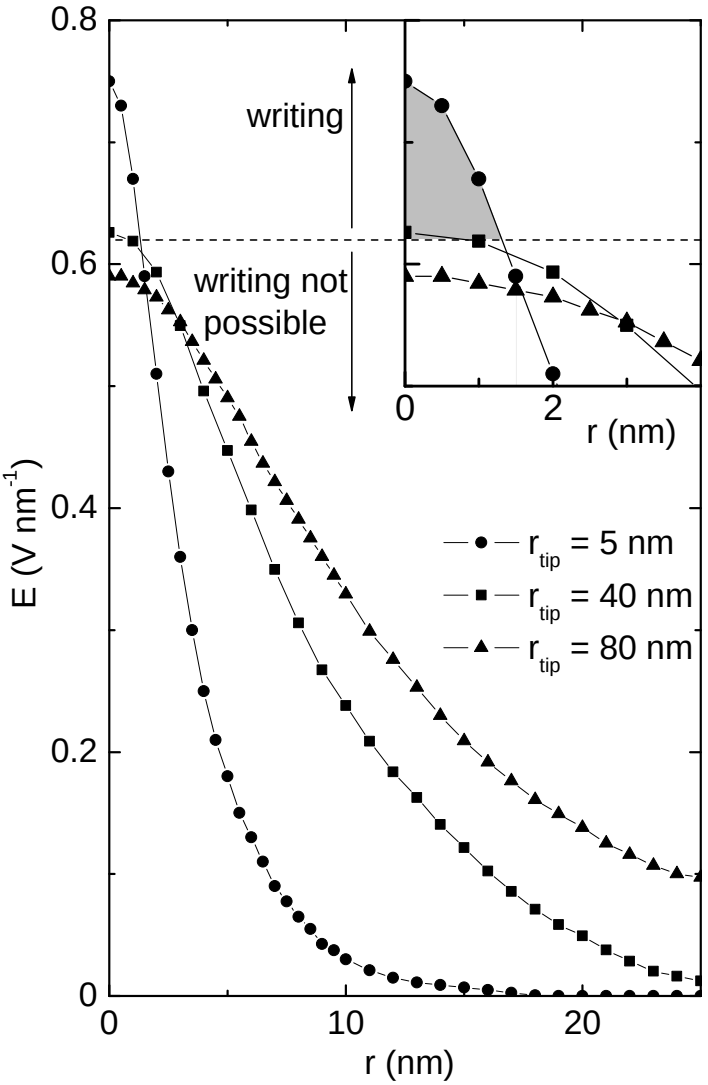

Figure 4.39: Simulation of the radial distribution of the electric field at the n–Si(111):H surface for various tip radii r_{tip} by SIMION 8.1. The STM tip axis is at r = 0. The inset shows the curves on a magnified radial scale. The grey shade indicates the range, where the critical field $E_{critical}$ is exceeded.

A significant variation of the structure width with the tip apex radius is not observed. This is illustrated in Figure 4.39 by the simulation of the field distribution at the n – Si (111):H surface for different tip radii and a bias voltage $U_{bias} = 600\,mV$. As can be seen from the inset in Figure 4.39, the radial range where the curves for $r_{tip} = 40\,nm$ and $r_{tip} = 5\,nm$ exceed the critical electric field $E_{critical} = 0.62\,V/nm$ is nearly identical. Supposed there is an uncertainty in $E_{critical}$, variations in the structure width are expected to be of the order of 1 nm, which is below the finite resolution, which can be achieved in STM experiments.

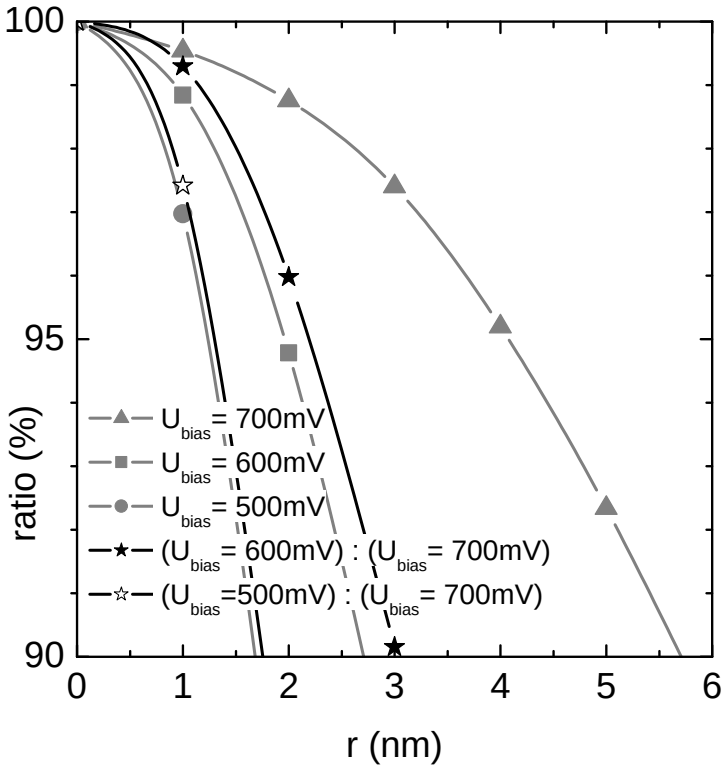

Figure 4.40: Renormalised electric field distributions at the n – Si (111):H surface for three bias voltages ($U_{bias} = 500\,mV$, $U_{bias} = 600\,mV$, $U_{bias} = 700\,mV$) at the corresponding critical tip radii r_{tip}. Ratios of $(U_{bias} = 600\,mV) : (U_{bias} = 700\,mV)$ (filled stars) and $(U_{bias} = 500\,mV) : (U_{bias} = 700\,mV)$ (open stars) illustrate the relative radial decrease in electric field at the n – Si (111):H surface.

The critical field allowing for localised electrodeposition and the relation of its distribution to the observed nanostructure size is analysed from Figure 4.40. This figure shows the field distributions for $U_{bias} = 500\,mV$ (grey filled circles), $U_{bias} = 600\,mV$ (grey filled squares), and $U_{bias} = 700\,mV$ (grey filled triangles) renormalised to their respective value at $r = 0$. From Figure 4.40 it becomes obvious, that the smaller the bias voltages, the steeper the decrease in electric field with radial distance from the STM tip axis ($r = 0$). This is easily explained by the fact, that with decreasing U_{bias} also the corresponding critical STM tip radius decreases (Figure 4.36). According to Figure 4.40, the Co width

of nanostructures obtained at different bias voltages (and correspondingly with different tip radius) should differ by up to a factor of three. Considering, that these critical tip apex radii represent the largest tip radii suitable for the creation of nanostructures at this particular bias voltage (Figure 4.36), a even larger difference in structure width should be observed. However, these differences cannot be observed experimentally, since even they are too small for a reasonably detailed imaging by the limited resolution of STM, which causes structures a few nanometer in size to appear of larger size in STM images (see section 4.3).

Summarising the analysis of Figure 4.36, Figure 4.38, and Figure 4.40, an electric field at the n – Si (111):H surface of approximately 0.6 V/nm allows for localised Co electrodeposition. In general, electric fields of the order of (0.1 – 1) V/nm are known to polarise H – Si bonds [475–478], resulting in a modification of their chemical characteristics and lowering the H – Si dissociation energy [479–482], which favours Co electrodeposition by lowering the corresponding activation barrier. This effect is consistent with the deposition overpotential η (Figure 4.30), which corresponds also to an effective polarisation of H – Si bonds, required to initiate Co electrodeposition onto n – Si (111):H. The (localised) application of an electric field makes Co electrodeposition accessible in a potential range, where electrodeposition is not observed in "conventional" electrodeposition experiments.

The mechanism behind the electric field induced Co electrodeposition is different from the electron injection based H-desorption mechanisms via inelastic scattering or multiple vibrational excitations in UHV [378, 473, 483–487]. While in those experiments bonds are broken by electrons of several eV in energy, the bias voltages in the present experiments ranging from 500 mV to 700 mV are not sufficient for such processes. In addition, the polarity of U_{bias} (tip positive of sample) in the present experiments does not allow for electron injection into the sample.

In the hitherto part of this section the electric field allowing electric field induced Co electrodeposition has been determined. The following part of the paper addresses the electrochemical aspects of this electrodeposition process.

Localised Co electrodeposition onto the n – Si (111):H surfaces by the nanostructuring routine is achieved, as soon as the critical field at the n – Si (111):H surface is exceeded. The nanostructuring routine was used to electrodeposit Co onto n – Si (111):H at different potentials E^W_{WE} and bias voltages U_{bias}. Each filled circle in Figure 4.41 represents a value of E^W_{WE} at corresponding U_{bias}, where Co was electrodeposited onto n – Si (111):H by the nanostructuring routine. In the potential range positive of these measurements, indicated by open bars in Figure 4.41, no Co electrodeposition can be achieved by applying the nanostructuring routine. The black bars in Figure 4.41 indicate the potential range, where bulk electrodeposition at the position of the STM tip destroyed the STM tip during the

nanostructuring routine.

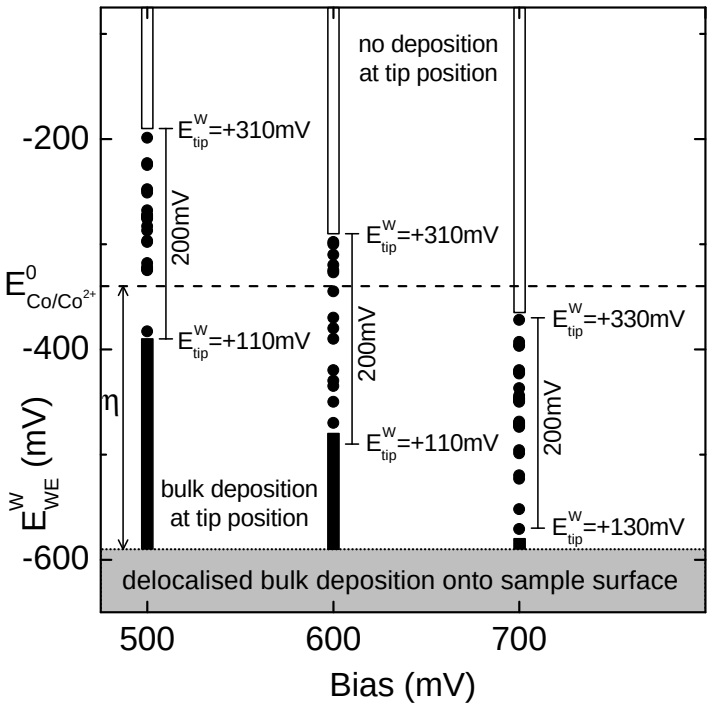

Figure 4.41: Working electrode potentials E^W_{WE} (filled circles) for successful field induced electrodeposition different bias voltages ($U_{bias} = 500\,mV$, $U_{bias} = 600\,mV$, $U_{bias} = 700\,mV$). Open bars indicate the potential ranges, where no field induced electrodeposition could be achieved, filled bars indicate the potential range of bulk electrodeposition at the position of the STM tip. The grey shaded area indicates bulk electrodeposition onto the sample surface. Potentials are quoted with respect to the SHE reference electrode.

These three regimes shift to more negative potentials E_{WE} with increasing bias voltage. In all of the experiments the electric field at the n – Si (111):H surface exceeds the critical field: a STM tip which did allow for localised electrodeposition in a first experiment, did not achieve localised electrodeposition in the regime of the open bars, but in a third experiment in the regime of the filled circles it succeed doing so. The effect shifting the regimes is not related to the electric field, but of electrochemical nature.

A positive STM tip repels positive metal ions, which results in a reduction of the metal ion concentration next to the STM tip and due to the resulting metal ion depletion is not sufficient anymore to allow for metal electrodeposition [33, 190, 311, 354, 363, 436, 437].

It can be concluded, that the potential of the positive STM tip determines the Co^{2+} concentration in its periphery and, thus, the three regimes in Figure 4.41 can be attributed to a high Co^{2+} concentration while the potential of the tip set $E^W_{tip} \lessapprox +110\,mV$ (bulk electrodeposition at tip position), a medium Co^{2+} concentration while the potential of the tip set $+310 \gtrapprox E^W_{tip} \gtrapprox +110\,mV$ (nanostructuring regime), and a low Co^{2+} concentration while the potential of the tip set $E^W_{tip} \gtrapprox +310\,mV$ (no deposition at tip position). A

schematic illustrating respective potential ranges for E^W_{WE} and E^W_{tip} in the 200 mV wide potential window of the nanostructuring regime at the different bias voltages is shown in Figure 4.42. Experiments performed at a bias voltage of $U_{bias} = 800\,mV$ confirm the tendency of the above measurements. However, in these experiments the regime of low Co^{2+} concentration extended down to $E_{WE} = -590\,mV$ and the regimes of medium and high Co^{2+} concentration did coincide with the bulk electrodeposition of Co.

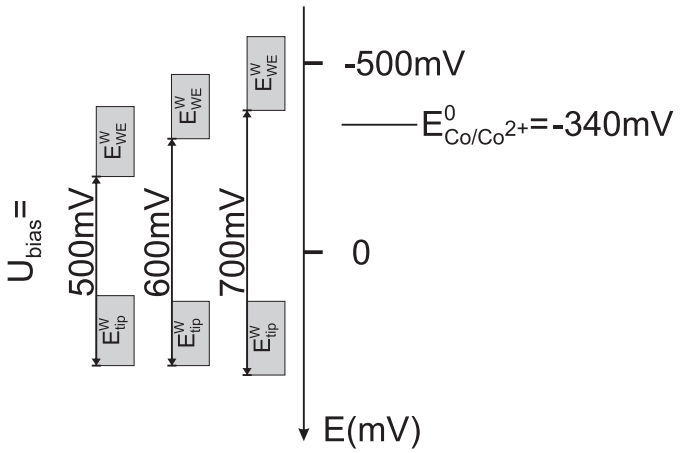

Figure 4.42: Schematic illustrating the shift of the E^W_{WE} potential range windows for successful application of the nanostructuring routine with U_{bias}. The corresponding potential range of E_{tip} is independent of U_{bias}.

Finally, it becomes obvious from Figure 4.41, that electric field induced Co electrodeposition is achieved at n–Si(111):H working electrode potentials positive of the onset of bulk Co electrodeposition as determined in Figure 4.30, i.e. positive of $E_{WE} = -590\,mV$. The electric field at the n–Si(111):H surface locally cancels the inhibition of electrodeposition by polarising the H–Si bonds, which is otherwise achieved by a polarisation of the solid / liquid interface at potentials negative of $E_{WE} = -590\,mV$. It is even more remarkable, however, that electric field induced Co electrodeposition is accomplished at $E^W_{WE} > E^0_{Co\,/\,Co^{2+}}$. Such an effect is usually expected only for strongly interacting systems in electrochemical metal on metal deposition experiments [24,111,488–491], whereas n–Si(111):H surfaces only interact weakly with metal ions [37,38,190,197,311,428]. This finding of electric field induced metal deposition at potentials positive of the $E^0_{Co\,/\,Co^{2+}}$ Nernst potential indicates a substantial change in the properties of the n–Si(111):H surface by an electric field, which has not been easily foreseen.

Conclusions

The influence of an electric field in a STM tunneling contact on Co electrodeposition onto n–Si(111):H surfaces has been investigated. The electric field distribution at the n–Si(111):H surface has been determined from simulations of the STM tunneling con-

tact including as parameters bias voltage as well as tip apex radius and gap width as-derived from STM images recorded at the solid / liquid interface. Above an electric field of 0.6 V/nm at the n – Si (111):H surface (localised) Co electrodeposition at the lateral position of the STM tip is observed in a potential range, where without this applied electric field Co electrodeposition is inhibited. This effect is explained by a modification of the H – Si bonds at the n – Si (111):H surface by the electric field in the tunneling gap, which lowers the activation barrier for the reaction of Co and the surface. This underlying mechanism is consistent with the observation of overpotentials in electrodeposition experiments of Co onto n – Si (111):H, which corresponds, likewise, to a polarisation of the solid / liquid interface. The application of an electric field even allows for (localised) electrodeposition at n – Si (111):H electrode potentials positive of the Co / Co^{2+} Nernset potential, thus significantly changing the properties of the otherwise weakly interacting n – Si (111):H electrode. Besides the enhancing effect of the electric field on Co electrodeposition, the electrostatic interaction of a positive STM tip and the Co^{2+} ions is found to retard Co electrodeposition, shifting it to more negative electrode potentials, or inhibit it at all. The present investigations show, that nanoscale electrodeposition at n – Si (111):H surfaces is significantly altered by electric field and electrostatic effects. Those effects are expected not to be limited to particularly n – Si (111):H surfaces, but also to be applicable to other solid / liquid interfaces. They may allow tuning electrodeposition processes at the nanoscale and in particular be useful tools in view of electrochemical nanostructuring.

Chapter 5

Summary and Outlook

H-terminated n – Si (111) surfaces (n – Si (111):H) in contact with an aqueous electrolyte (deaerated 0.1 M H_2SO_4) have been investigated by scanning tunneling microscopy (STM), impedance measurements and cyclic voltammetry in view of charge transfer processes at the solid / liquid interface, focussing on processes involving small amounts of charge.

Impedance measurements have shown, that the electronic structure at the n – Si (111):H surface is very complex. Hydrogen interdiffused up to several hundred nanometer into the n – Si (111):H subsurface region introduces electronically active states above midgap in the n – Si (111):H band gap, which were identified at $E^1_{SS} = E_C + 324\,mV$, $E^2_{SS} = E_C + 407\,mV$, and $E^3_{SS} = E_C + 510\,mV$. The states participate in charge transfer processes in a potential range, where the n – Si (111):H surface is depleted of conduction band electrons. The density of these states is of the order of $(10^{14} - 10^{15})\,cm^{-3}$, comparable to the doping density ($N_D \approx 10^{15}\,cm^{-3}$) of the n – Si (111):H samples. Consequently, a significant deviation of the effective doping level in the n – Si (111):H subsurface region may be expected. These aspects may be of particular importance in charge transfer processes at the nanoscale, where only small amounts of charge participate.

The hydrogen related states allow for the electrodeposition of Cu in a potential range positive of the flatband potential, where the n – Si (111):H surface is depleted of electrons and, thus, no charge transfer is expected. In this situation the states mediate the charge transfer, since their density is orders of magnitude larger than the electron concentration in the space charge region at the n – Si (111):H surface. On the electron depleted n – Si (111):H surfaces nucleation / growth and dissolution of Cu clusters depending on the actual electrode potential was observed. At each electrode potential in this potential range the Cu clusters appear to be in an electrochemical equilibrium with the Cu^{2+} solution.

In the investigations on electrochemical charge transfer processes at the nanoscale, the influence of the radius of a spherical tip apex on the achievable resolution in STM experiments was considered. Calculations taking into account the three-dimensional geometry

and the exponential current–distance dependence of a tunneling contact in a scanning tunneling microscope point out, that, when using STM tips of finite radii, nanoscale structures and, in particular, nanoscale clusters of some atomic layers in height appear broadened and eventually reduced in height in STM images in comparison to their actual size. These effects increase nonlinearly with increasing tip radius. Maintaining the error in the apparent size of nanoscale structure in STM images in comparison to their actual cluster size below 50% requires STM tips having radii of approximately the actual structure size. Exploiting the results from the calculations allows to determine the radii of tips in scanning tunneling experiments from n – Si (111):H step edges by comparing experimentally determined and calculated scan line profiles of the structures.

An electric field generated by a well characterised STM tunneling contact at the n – Si (111):H surface was found to locally promote the electrodeposition of Co, if the field exceeded approximately 0.6 V/nm. Electrodeposition was observed in a potential range, where without applied electric field no Co is electrodeposited. The effect was attributed to a modification of H – Si bonds at the n – Si (111):H surface by the field, similar to the polarisation of the solid / liquid interface by an overpotential in electrodeposition experiments. A positive STM tip was found to shift the localised field induced Co electrodeposition to more negative n – Si (111):H working electrode potentials. The localised electrodeposition underneath the STM tip in tunneling contact with the n – Si (111):H surface has been used for creating complex nanoscale structures on the n – Si (111):H surface by moving the STM tip in tunneling contact over the surface along an arbitrary path.

The results of this illustrate the complexity of electrochemical charge transfer at the nanoscale. The participation of the electronically active states in n – Si (111):H in charge transfer processes at the solid / liquid interface as, e.g., electrodeposition processes of metals, points out the relevance of (electronically) well characterised electrodes for a meaningful interpretation of experimental results.

The observed equilibrium of Cu clusters on the n – Si (111):H surface and the Cu^{2+} solution may find some interesting applications in the generation of large arrays of small metal clusters, which can be used in studies of catalytic properties of materials or as a basis for sensor devices. The potential dependent cluster size may help tuning of these systems. Other metals or metal / electrolyte combinations following the observed deposition / dissolution behaviour would open a large playground for further research on cluster covered, i.e. surface enlarged systems.

Such systems can be also generated using field induced localised electrodeposition (electrochemical “writing”). This mechanism has been shown to be suitable for generating complex structures on surfaces in a continuous process, which is an advance in comparison to previous techniques generating discrete low dimensional systems or uni-

formly distributed cluster arrays. In particular, it may be used for generating nanometer sized wires on n – Si (111):H surfaces. The mechanism based on a modification of the H-termination at the n – Si (111):H surface should not be limited exclusively to the usage of metals, but also work in combination with (organic) molecules. This would offer a possibility to selectively decorate n – Si (111):H surfaces with, e.g, functionalised or tailored molecules, while the remaining surface is still H-terminated. Further on, the influence of the terminating species on the creation of nanostructures should be investigated, e.g. by using halogenide terminated n – Si (111) surfaces. Eventually, the "writing" process could also be used to modify non-Si surfaces terminated by hydrogen (e.g. hydrogen terminated diamond) or other species to generate "active" patterns on those surfaces.

Considering these prospects and the results of the present thesis, future research on the "well known" n – Si (111):H surfaces in contact with an electrolyte or similar contacts will without much doubt reveal further unexpected phenomena, but also contribute to a more detailed understanding of solid / liquid interfaces.

Bibliography

[1] Nasser Kanani. *Electroplating – Basic Principles, Processes and Practice.* Elsevier, 2004.

[2] Daniel C. Edelstein, P.C. Andricacos, B. Agarwala, C. Carnell, D. Chung, E. Cooney III, W. Cote, P. Locke, S. Luce, C. Megivern, R. Wachnik, and E. Walton. *Electrochemical Processing in ULSI Fabrication and Semiconductor / Metal Deposition II*, volume 99-9 of *Proceedings of the International Symposium.* The Electrochemical Society, Inc., Pennington, 1999.

[3] D. Chung, J. Korejwa, E. Walton, and P. Locke. Introduction of copper electroplating into a manufacturing fabricator. In *Advanced Semiconductor Manufacturing Conference and Workshop, 1999 IEEE/SEMI*, pages 282–289, 1999.

[4] Panos C. Andricacos. Copper On-Chip Interconnections. *The Electrochemical Society Interface*, **8**(1):32–37, 1999.

[5] Tapan Gupta. *Copper Interconnect Technology.* Springer-Verlag New York, 2009.

[6] Christoph Steinbrüchel and Barry L. Chin. *Copper Interconnect Technology.* The International Society for Optical Engineering, 2001.

[7] Gordon E. Moore. Cramming more components onto integrated circuits. *Electronics*, **38**(8):114–117, 1965.

[8] Gordon E. Moore. Progress In Digital Integrated Electronics. In *International Electron Devices Meeting, IEEE, 1975 (Intel Corporation Reprint)*, pages 11–13, 1975.

[9] Gordon E. Moore. Lithography and the Future of Moore's Law. In *Conference Proceedings of the Society of Photo-Optical Instrumentation Engineers Vol. 2437 (Intel Corporation Reprint)*, 1995.

[10] Vivek Bakshi, editor. *EUV Lithography.* Society of Photo-Optical Instrumentation Engineers and John Wiley & Sons, Inc., 2009.

[11] Bruno LaFontaine, Yunfei Deng, Ryoung-Han Kim, Harry J. Levinson, Sarah McGowan, Uzodinna Okoroanyanwu, Rolf Seltmann, Cyrus Tabery, Anna Tchikoulaeva, Tom Wallow, Obert Wood, John Arnold, Don Canaperi, Matthew Colburn, Kurt Kimmel, Chiew-Seng Koay, Erin Mclellan, Dave Medeiros, Satyavolu Papa Rao, Karen Petrillo, Yunpeng Yin, Hiroyuki Mizuno, Sander Bouten, Michael Crouse, Andre van Dijk, Youri van Dommelen, Judy Galloway, Sang-In Han, Bart Kessels, Brian Lee, Sjoerd Lok, Brian Niekrewicz, Bill Pierson, Robert Routh, Emil Schmit-Weaver, Kevin Cummings, and James Word. The use of EUV lithography to produce demonstration devices. *Conference Proceedings of the Society of Photo-Optical Instrumentation Engineers*, **6921**:69210P, 2008.

[12] A.N. Broers, A.C.F. Hoole, and J.M. Ryan. Electron beam lithography – Resolution limits. *Microelectronic Engineering*, **32**(1–4):131–142, 1996.

[13] Paul Petric, Chris Bevis, Alan Brodie, Allen Carroll, Anthony Cheung, Luca Grella, Mark McCord, Henry Percy, Keith Standiford, and Marek Zywno. REBL Nanowriter: Reflective Electron Beam Lithography. *Conference Proceedings of the Society of Photo-Optical Instrumentation Engineers*, **7271**:727107, 2009.

[14] Huigao Duan, Vitor R. Manfrinato, Joel K. W. Yang, Donald Winston, Bryan M. Cord, and Karl K. Berggren. Metrology for electron-beam lithography and resist contrast at the sub-10 nm scale. *Journal of Vacuum Science & Technology B: Microelectronics and Nanometer Structures*, **28**(6):C6H11–C6H17, 2010.

[15] A. Heuberger. X-ray lithography. *Journal of Vacuum Science & Technology B: Microelectronics and Nanometer Structures*, **6**(1):107–121, 1988.

[16] Jerome P. Silverman. X-ray lithography: Status, challenges, and outlook for 0.13 μm. *Papers from the 41st international conference on electron, ion, and photon beam technology and nanofabrication*, **15**(6):2117–2124, 1997.

[17] J.E.E. Baglin. Ion beam nanoscale fabrication and lithography – A review. *Applied Surface Science*, **258**(9):4103–4111, 2012.

[18] D. Winston, B.M. Cord, B. Ming, D.C. Bell, W.F. DiNatale, L.A. Stern, A.E. Vladar, M.T. Postek, M.K. Mondol, J.K.W. Yang, and K.K. Berggren. Scanning-helium-ion-beam lithography with hydrogen silsesquioxane resist. *Journal of Vacuum Science & Technology B: Microelectronics and Nanometer Structures*, **27**(6):2702–2706, 2009.

[19] Andrew L. Schmitt, Jeremy M. Higgins, Jeannine R. Szczech, and Song Jin. Synthesis and applications of metal silicide nanowires. *Journal of Materials Chemistry*, **20**(2):223–235, 2010.

[20] S.L. Cheng, Y.P. Wei, and C.H. Chung. Synthesis of cobalt metal nanowire arrays and the interfacial reactions of cobalt nanowires on (001)Si. In *Nanoelectronics Conference (INEC), 2011 IEEE 4th International*, pages 1–2, june 2011.

[21] B. Tavel, T. Skotnicki, G. Pares, N. Carriere, M. Rivoire, F. Leverd, C. Julien, J. Torres, and R. Pantel. Totally silicided ($CoSi_2$) polysilicon: a novel approach to very low-resistive gate ($\sim 2\Omega / \square$) without metal CMP nor etching. In *Electron Devices Meeting, 2001. IEDM '01. Technical Digest. International*, pages 37.5.1–37.5.4, 2001.

[22] W.P. Maszara. Fully Silicided Metal Gates for High-Performance CMOS Technology: A Review. *Journal of The Electrochemical Society*, **152**(7):G550–G555, 2005.

[23] D.M. Kolb, R. Ullmann, and T. Will. Nanofabrication of Small Copper Clusters on Gold(111) Electrodes by a Scanning Tunneling Microscope. *Science*, **275**(5303):1097–1099, 1997.

[24] D.M. Kolb, R. Ullmann, and J.C. Ziegler. Electrochemical nanostructuring. *Electrochimica Acta*, **43**(19–20):2751–2760, 1998.

[25] D.M. Kolb and F.C. Simeone. Electrochemical nanostructuring with an STM: A status report. *Electrochimica Acta*, **50**(15):2989–2996, 2005.

[26] D.M. Kolb R. Ullmann, T. Will. Nanostructuring of Electrode Surfaces by Tip-Induced Metal Deposition. *Berichte der Bunsengesellschaft für Physikalische Chemie*, **99**:1414–1420, 1995.

[27] G.E. Engelmann, J.C. Ziegler, and D.M. Kolb. Nanofabrication of Small Palladium Clusters on Au(111) Electrodes with a Scanning Tunnelling Microscope. *Journal of The Electrochemical Society*, **145**(3):L33–L35, 1998.

[28] D.M. Kolb and M.A. Schneeweiss. Scanning Tunneling Microscopy for Metal Deposition Studies. *The Electrochemical Society Interface*, **3**(1):26–30, 1999.

[29] D.M. Kolb, G.E. Engelmann, and J.C. Ziegler. Nanoscale decoration of electrode surfaces with an STM. *Solid State Ionics*, **131**(1–2):69–78, 2000.

[30] Dieter M. Kolb. Electrochemical Surface Science. *Angewandte Chemie International Edition*, **40**(7):1162–1181, 2001.

[31] R. Ullmann, T. Will, and D.M. Kolb. Nanoscale decoration of Au(111) electrodes with Cu clusters by an STM. *Chemical Physics Letters*, **209**(3):238–242, 1993.

[32] W. Schindler, D. Hofmann, and J. Kirschner. Localized Electrodeposition Using a Scanning Tunneling Microscope Tip as a Nanoelectrode. *Journal of The Electrochemical Society*, **148**(2):C124–C130, 2001.

[33] J.C. Ziegler, G.E. Engelmann, and D.M. Kolb. Tip-induced Formation of Nanometer-Sized Metal Clusters. *Zeitschrift für Physikalische Chemie*, **208**:151–166, Februar 1999.

[34] D. Hofmann, W. Schindler, and J. Kirschner. Electrodeposition of nanoscale magnetic structures. *Applied Physics Letters*, **73**(22):3279–3281, 1998.

[35] Friedrich Temps, Dieter M. Kolb, John S. McCaskill, Eckart Rühl, Hans Wolfgang Spiess, Klaus Christmann, Gerhard Findenegg, and Frank-Gerrit Klärner und Arne E. Wigger. Physikalische Chemie 1994. *Nachrichten aus Chemie, Technik und Laboratorium*, **43**:195–214, 1995.

[36] M. Hugelmann, P. Hugelmann, W.J. Lorenz, and W. Schindler. Nanoelectrochemistry and nanophysics at electrochemical interfaces. *Surface Science*, **597**(1–3):156–172, 2005.

[37] W. Schindler, P. Hugelmann, M. Hugelmann, and F.X. Kärtner. Localized electrochemical nucleation and growth of low-dimensional metal structures. *Journal of Electroanalytical Chemistry*, **522**(1):49–57, 2002.

[38] W.J. Lorenz, G. Staikov, W. Schindler, and W. Wiesbeck. The Role of Low-Dimensional Systems in Electrochemical Phase Formation and Dissolution Processes. *Journal of The Electrochemical Society*, **149**(12):K47–K59, 2002.

[39] Enrique Herrero, Lisa J. Buller, and Héctor D. Abruña. Underpotential Deposition at Single Crystal Surfaces of Au, Pt, Ag and Other Materials. *Chemical Reviews*, **101**(7):1897–1930, 2001.

[40] D.M. Kolb and F.C. Simeone. Nanostructure formation at the solid/liquid interface. *Current Opinion in Solid State and Materials Science*, **9**(1–2):91–97, 2005.

[41] Toshinori Hachiya and Kingo Itaya. In situ scanning tunneling microscopy of underpotential deposition in aqueous solution III. Silver adlayers on Au(111). *Ultramicroscopy*, **42–44, Part 1**:445–452, 1992.

[42] W. Obretenov, U. Schmidt, W.J. Lorenz, G. Staikov, E. Budevski, D. Carnal, U. Müller, H. Siegenthaler, and E. Schmidt. Underpotential Deposition and Electrocrystallization of Metals An Atomic View by Scanning Tunneling Microscopy. *Journal of The Electrochemical Society*, **140**(3):692–703, 1993.

[43] Knud Gentz and Klaus Wandelt. Electrochemical Scanning Tunneling Microscopy. *CHIMIA International Journal for Chemistry*, **66**(1):44–51, 2012.

[44] Kingo Itaya. In situ scanning tunneling microscopy in electrolyte solutions. *Progress in Surface Science*, **58**(3):121–247, 1998.

[45] A.M. Bittner, J. Wintterlin, and G. Ertl. Strain relief during metal-on-metal electrodeposition: a scanning tunneling microscopy study of copper growth on Pt(100). *Surface Science*, **376**(1–3):267–278, 1997.

[46] G. Binnig and H. Rohrer. Scanning tunneling microscopy. *Helvetica Physica Acta*, **55**(6):726–735, 1982.

[47] G. Binnig, H. Rohrer, Ch. Gerber, and E. Weibel. Tunneling through a controllable vacuum gap. *Applied Physics Letters*, **40**(2):178–180, 1982.

[48] G. Binnig, H. Rohrer, Ch. Gerber, and E. Weibel. Surface Studies by Scanning Tunneling Microscopy. *Physical Review Letters*, **49**:57–61, Jul 1982.

[49] R. Wiesendanger. Contributions of scanning probe microscopy and spectroscopy to the investigation and fabrication of nanometer-scale structures. *Journal of Vacuum Science & Technology B: Microelectronics and Nanometer Structures*, **12**(2):515–529, 1994.

[50] Ampere A. Tseng, Andrea Notargiacomo, and T.P. Chen. Nanofabrication by scanning probe microscope lithography: A review. *Journal of Vacuum Science & Technology B: Microelectronics and Nanometer Structures*, **23**(3):877–894, 2005.

[51] Saw-Wai Hla. Scanning tunneling microscopy single atom/molecule manipulation and its application to nanoscience and technology. *Journal of Vacuum Science & Technology B: Microelectronics and Nanometer Structures*, **23**(4):1351–1360, 2005.

[52] Richard J. Colton. Nanoscale measurements and manipulation. *Journal of Vacuum Science & Technology B: Microelectronics and Nanometer Structures*, **22**(4):1609–1635, 2004.

[53] Sébastien Gauthier. Atomic and molecular manipulations of individual adsorbates by STM. *Applied Surface Science*, **164**(1–4):84–90, 2000.

[54] R. Wiesendanger. Fabrication of nanometer structures using STM. *Applied Surface Science*, **54**:271–277, 1992.

[55] M.R. Castell. *Scanning Tunneling Microscopy of Surfaces and Nanostructures*. The Royal Society of Chemistry, 2007. Chapter 3.

[56] Joseph A. Stroscio and D.M. Eigler. Atomic and Molecular Manipulation with the Scanning Tunneling Microscope. *Science*, **254**(5036):1319–1326, 1991.

[57] L.J. Whitman, Joseph A. Stroscio, R.A. Dragoset, and R.J. Celotta. Manipulation of Adsorbed Atoms and Creation of New Structures on Room-Temperature Surfaces with a Scanning Tunneling Microscope. *Science*, **251**(4998):1206–1210, 1991.

[58] R.S. Becker, J.A. Golovchenko, and B.S. Swartzentruber. Atomic-scale surface modifications using a tunnelling microscope. *Nature*, **325**:419–421, 1987.

[59] J.E. Demuth, R.J. Hamers, R.M. Tromp, and M.E. Welland. A scanning tunneling microscope for surface science studies. *IBM Journal of Research and Development*, **30**(4):396–402, July 1986.

[60] G. Binnig and H. Rohrer. Scanning tunneling microscopy. *IBM Journal of Research and Development*, **30**(4):355–369, July 1986.

[61] G. Binnig, H. Rohrer, Ch. Gerber, and E. Weibel. (111) facets as the origin of reconstructed Au(110) surfaces. *Surface Science Letters*, **131**(1):L379–L384, 1983.

[62] G. Binnig and H. Rohrer. Scanning tunneling microscopy. *Surface Science*, **126**(1–3):236–244, 1983.

[63] D.M. Eigler and E.K. Schweizer. Positioning single atoms with a scanning tunnelling microscope. *Nature*, **344**:524–526, 1990.

[64] Y. Kuk and P.J. Silverman. Scanning tunneling microscope instrumentation. *Review of Scientific Instruments*, **60**(2):165–180, 1989.

[65] H.J. Güntherodt and R. Wiesendanger, editors. *Scanning Tunneling Microscopy I*, volume 20 of *Springer Series in Surface Science*. Springer Verlag Berlin Heidelberg, 1992.

[66] L. Oberbeck, N.J. Curson, T. Hallam, M.Y. Simmons, and R.G. Clark. STM imaging of buried P atoms in hydrogen-terminated Si for the fabrication of a Si:P quantum computer. *Thin Solid Films*, **464–465**:23–27, 2004.

[67] Liuyan Zhao, Rui He, Kwang Taeg Rim, Theanne Schiros, Keun Soo Kim, Hui Zhou, Christopher Gutiérrez, S. P. Chockalingam, Carlos J. Arguello, Lucia Pálová, Dennis Nordlund, Mark S. Hybertsen, David R. Reichman, Tony F. Heinz, Philip Kim, Aron Pinczuk, George W. Flynn, and Abhay N. Pasupathy. Visualizing Individual Nitrogen Dopants in Monolayer Graphene. *Science*, **333**(6045):999–1003, 2011.

[68] Toshio Sakurai, Y. Hasegawa, T. Hashizume, I. Kamiya, T. Ide, I. Sumita, H.W. Pickering, and S. Hyodo. Atomic hydrogen chemisorption on the Si(111) 7×7 surface. *Journal of Vacuum Science & Technology A: Vacuum, Surfaces, and Films*, **8**(1):259–261, 1990.

[69] T. Hashizume, S. Heike, M.I. Lutwyche, S. Watanabe, and Y. Wada. Atom structures on the Si(100) surface. *Surface Science*, **386**(1–3):161–165, 1997.

[70] H.F. Hess. Scanning tunneling spectroscopy of vortices in a superconductor. *Physica C: Superconductivity*, **185–189, Part 1**:259–263, 1991.

[71] R. Berthe, U. Hartmann, and C. Heiden. Influence of a transport current on the Abrikosov flux lattice observed with a low-temperature scanning tunneling microscope. *Ultramicroscopy*, **42–44, Part 1**:696–698, 1992.

[72] H.F. Hess, R.B. Robinson, R.C. Dynes, J.M. Valles, and J.V. Waszczak. Scanning-Tunneling-Microscope Observation of the Abrikosov Flux Lattice and the Density of States near and inside a Fluxoid. *Physical Review Letters*, **62**:214–216, Jan 1989.

[73] Ch. Renner, A.D. Kent, Ph. Niedermann, Ø. Fischer, and F. Lévy. Scanning tunneling spectroscopy of a vortex core from the clean to the dirty limit. *Physical Review Letters*, **67**:1650–1652, Sep 1991.

[74] R. Berthe, U. Hartmann, and C. Heiden. Scanning tunneling microscopy of the Abrikosov flux lattice with ferromagnetic probes. *Applied Physics Letters*, **57**(22):2351–2353, 1990.

[75] Ch. Renner, A.D. Kent, Ph. Niedermann, Ø. Fischer, and F. Lévy. Scanning tunneling spectroscopy of the Abrikosov flux lattice from the clean toward the dirty limit. *Ultramicroscopy*, **42–44, Part 1**:699–704, 1992.

[76] H.F. Hess, R.B. Robinson, and J.V. Waszczak. Vortex-core structure observed with a scanning tunneling microscope. *Physical Review Letters*, **64**:2711–2714, May 1990.

[77] H.F. Hess, R.B. Robinson, and J.V. Waszczak. STM spectroscopy of vortex cores and the flux lattice. *Physica B: Condensed Matter*, **169**(1–4):422–431, 1991.

[78] M.F. Crommie, C.P. Lutz, and D.M. Eigler. Confinement of Electrons to Quantum Corrals on a Metal Surface. *Science*, **262**(5131):218–220, 1993.

[79] M.F. Crommie, C.P. Lutz, D.M. Eigler, and E.J. Heller. Waves on a metal surface and quantum corrals. *Surface Review and Letters*, **2**(1):127–137, 1995.

[80] H.C. Manoharan, C.P. Lutz, and D.M. Eigler. Quantum mirages formed by coherent projection of electronic structure. *Nature*, **403**:512–515, 2000.

[81] Phaedon Avouris. Probing the Wave Properties of Electrons and Manipulating Atoms at Surfaces with the Scanning Tunneling Microscope. *Accounts of Chemical Research*, **27**(6):159–165, 1994.

[82] M.F. Crommie, C.P. Lutz, and D.M. Eigler. Imaging standing waves in a two-dimensional electron gas. *Nature*, **363**:524–527, 1993.

[83] Y. Hasegawa and Ph. Avouris. Direct observation of standing wave formation at surface steps using scanning tunneling spectroscopy. *Physical Review Letters*, **71**:1071–1074, Aug 1993.

[84] G. Binnig, H. Rohrer, Ch. Gerber, and E. Weibel. 7×7 Reconstruction on Si(111) Resolved in Real Space. *Physical Review Letters*, **50**:120–123, Jan 1983.

[85] O. Enea. Local probe microscopies and their applications to semiconducting materials. *Coordination Chemistry Reviews*, **125**(1–2):213–240, 1993.

[86] S.A. Wolf, D.D. Awschalom, R.A. Buhrman, J.M. Daughton, S. von Molnár, M.L. Roukes, A.Y. Chtchelkanova, and D.M. Treger. Spintronics: A Spin-Based Electronics Vision for the Future. *Science*, **294**(5546):1488–1495, 2001.

[87] J.F. Gregg, I. Petej, E. Jouguelet, and C. Dennis. Spin electronics – a review. *Journal of Physics D: Applied Physics*, **35**(18):R121–R155, 2002.

[88] J.S. Tsay, Y.D. Yao, K.C. Wang, W.C. Cheng, and C.S. Yang. Magnetic properties of ultrathin cobalt films grown on Ge(111) and Si(111) substrates. *Journal of Applied Physics*, **91**(10):8766–8768, 2002.

[89] J.S. Tsay, C.S. Yang, Y. Liou, and Y.D. Yao. Magnetic properties of ultrathin Co films on Si(111) and $CoSi_2$ surfaces. *Journal of Applied Physics*, **85**(8):4967–4969, 1999.

[90] H.W. Chang, J.S. Tsay, Y.C. Hung, F.T. Yuan, W.Y. Chan, W.B. Su, C.S. Chang, and Y.D. Yao. Magnetic properties and microstructure of ultrathin Co/Si(111) films. *Journal of Applied Physics*, **101**(9):09D124, 2007.

[91] J.S. Tsay, T.Y. Fu, M.H. Lin, C.S. Yang, and Y.D. Yao. Microscopic interfacial structures and magnetic properties of ultrathin Co/Si(111) films. *Applied Physics Letters*, **88**(10):102506, 2006.

[92] P. Jakob and Y.J. Chabal. Chemical etching of vicinal Si(111): Dependence of the surface structure and the hydrogen termination on the pH of the etching solutions. *The Journal of Chemical Physics*, **95**(4):2897–2909, 1991.

[93] Philippe Allongue, Catherine Henry de Villeneuve, Sylvie Morin, Rabah Boukherroub, and Danial D.M. Wayner. The preparation of flat H-Si(111) surfaces in 40% NH_4F revisited. *Electrochimica Acta*, **45**(28):4591–4598, 2000.

[94] Toshio Sakurai and H. D. Hagstrum. Chemisorption of atomic hydrogen on the silicon (111) 7×7 surface. *Physical Review B*, **12**:5349–5354, Dec 1975.

[95] D. Barredo, F. Calleja, A.E. Weeks, P. Nieto, J.J. Hinarejos, G. Laurent, A.L. Vazquez de Parga, D.A. MacLaren, D. Farías, W. Allison, and R. Miranda. Si(111)-H(1×1): A mirror for atoms characterized by AFM, STM, He and H_2 diffraction. *Surface Science*, **601**(1):24–29, 2007.

[96] Peter C. Searson. volume 4 of *Advances in Electrochemical Science and Engineering*. VCH Verlagsgesellschaft mbH, Weinheim, 1995.

[97] W. Schindler, M. Hugelmann, and Ph. Hugelmann. In situ scanning probe spectroscopy at nanoscale solid/liquid interfaces. *Electrochimica Acta*, **50**(15):3077–3083, 2005.

[98] M. Hugelmann and W. Schindler. Schottky diode characteristics of electrodeposited Au/n-Si(111) nanocontacts. *Applied Physics Letters*, **85**(16):3608–3610, 2004.

[99] Claus Hamann and Michael Hietschold. *Raster-Tunnel-Mikroskopie*. Akademie Verlag GmbH, Berlin, 1991.

[100] Ernst Meyer, Hans Josef Hug, and Roland Bennewitz. *Scanning Probe Microscopy - The Lab on a Tip*. Springer Berlin / Heidelberg, 2004.

[101] C. Julian Chen. *Introduction to Scanning Tunneling Microscopy, Second Edition*, volume 64 of *Monographs on the Physics and Chemistry of Meterials*. Oxford University Press, 2008.

[102] Sergei N. Magonov and Myung-Hwan Whangbo. *Surface Analysis with STM and AFM*. VC, 1996.

[103] W.N. Unertl and M.E. Kordesch. *Handbook of Surface Science*, volume 1 – Physical Structure of *Handbook of Surface Science*. North-Holland, 1996. Chapter 8 Direct imaging and geometrical methods.

[104] Carl H. Haman and Wolf Vielstich. *Elektrochemie, 4. vollständig überarbeitete und aktualisierte Auflage*. Wiley-VCH, Weinheim, 2005.

[105] Rüdiger Memming. *Semiconductor Electrochemistry*. Wiley-VCH, Weinheim, 2001.

[106] Stanley Roy Morrison. *Electrochemistry at Semiconductor and Oxidized Metal Electrodes*. Plenum Press, New York, 1980.

[107] Ashok K. Vijh. *Electrochemistry of Metals and Semiconductors*. Monographs in Electroanalytical Chemistry and Electrochemistry. Marcell Dekker, Inc., New York, 1973.

[108] Hans Rickert. *Electrochemistry of Solids – An Introduction*, volume 7 of *Inorganic Chemistry Concepts*. Springer-Verlag Berlin, Heidelberg, 1982.

[109] R. Greef, R. Peat, L.M. Peter, D. Pletcher, and J. Robinson. *Instrumental Methods in Electrochemistry*. Ellis Horwood series in Physical Chemistry. Southampton Electrochemistry Group/ Ellis Horwood Limited, 1985.

[110] Jerry Goodisman. *Electrochemistry: Theoretical Foundations*. John Wiley & Sons, Inc., 1987.

[111] E. Budevski, G. Staikov, and W.J. Lorenz. *Electrochemical Phase Formation and Growth*. VCH Verlagsgesellschaft mbH, Weinheim, 1996.

[112] R.J. Dwayne Miller, George L. McLendon, Arthur J. Nozik, Wolfgang Schmickler, and Frank Willig. *Surface Electron Transfer Processes.* VCH Publishers, Inc., 1995.

[113] Eliezer Gileadi. *Physical Electrochemistry – Fundamentals, Techniques and Applications.* Wiley-VCH, Weinheim, 2011.

[114] Roger Parsons. volume 1 of *Advances in Electrochemistry and Electrochemical Engineering.* Interscience Publishers, New York, London, 1961.

[115] M. Fleischmann and H.R. Thirsk. volume 3 of *Advances in Electrochemistry and Electrochemical Engineering.* Interscience Publishers, New York, London, 1963.

[116] Allen J. Bard and Larry R. Faulkner. *Electrochemical Methods – Fundamentals and Applications, 2^{nd} edition.* Wiley, New York, 2001.

[117] W. Göpel, J. Hesse, and J.N. Zemel, editors. *Chemical and Biochemical Sensors, Part 1*, volume 2 of *Sensors - A comprehensive Survey.* VCH, Weinheim, 1991.

[118] Norio Sato. *Electrochemistry at Metal and Semiconductor Electrodes.* Elsevier B.V., 1998.

[119] Jürgen Heinze. Cyclovoltammetrie – die „Spektroskopie" des Elektrochemikers. *Angewandte Chemie*, **96**(11):823–916, 1084.

[120] D. Wahl. Eine Kleine Geschichte der Elektrochemie – Teil 1. *Galvanotechnik*, **96**(7):1600–1610, 2005.

[121] D. Wahl. Eine Kleine Geschichte der Elektrochemie – Teil 2. *Galvanotechnik*, **96**(8):1820–1828, 2005.

[122] P.J. Gellings and H.J.W. Brouwmeester, editors. *The CRC Handbook of Solid State Electrochemistry.* CRC Press, Inc., 1997.

[123] Harald Ibach and Hand Lüth. *Festkörperphysik – Einführung in die Grundlagen, 4. Auflage.* Springer Verlag, Berlin, 1995.

[124] Siegfried Hunklinger. *Festkörperphysik, 2. verbesserte Auflage.* Oldenbourg Wissenschaftsverlag, München, 2009.

[125] Winfried Mönch. *Semiconductor Surfaces and Interfaces, Third Edition*, volume 26 of *Springer Series in Surface Science.* Springer Berlin / Heidelberg, 2001.

[126] Wolfgang Schmickler and Elizabeth Santos. *Interfacial Electrochemistry, Second Edition.* Springer Verlag, Berlin, 2010.

[127] S. Roy Morrison. *The Chemical Physics of Surfaces, Second Edition.* Plenum Press, New York, 1990.

[128] A. Many, Y. Goldstein, and N.B. Grover. *Semiconductor Surfaces.* North Holland Publishing Company, Amsterdam, 1965.

[129] John O'M. Bockris and Shahed U.M. Khan, editors. *Surface Electrochemistry – A Molecular Level Approach.* Plenum Press, New York, 1993.

[130] H. Gerischer. volume 1 of *Advances in Electrochemistry and Electrochemical Engineering.* Interscience Publishers, New York, London, 1961.

[131] Andrew Hamnett. *Electrode Kinetics: Reactions*, volume 27 of *Comprehensive Chemical Kinetics.* Elsevier, 1988. Chapter 2: Semiconductor Electrochemistry.

[132] Allen J. Bard, Roger Parsons, and Joseph Jordan, editors. *Standard Potentials in Aqueous Solution.* International Union of Pure and Applied Chemistry, 1985.

[133] Marvin S. Antelman. *The Encyclopedia of Chemical Electrode Potentials.* Plenum Press, New York, 1982.

[134] Marcel Pourbaix, editor. *Atlas of Electrochemical Equilibria in Aqueous Solutions, 2. engl. edition.* National Association of Corrosion Engineers, 1974.

[135] Chris G. Van de Walle and J. Neugebauer. Universal alignment of hydrogen levels in semiconductors, insulators and solutions. *Nature*, **423**:626–628, 2003.

[136] F. Lohmann. Fermi-Niveau und Flachbandpotential von Molekülkristallen aromatischer Kohlenwasserstoffe. *Zeitschrift für Naturforschung A*, **22a**:843–844, 1967.

[137] Hermann Helmholtz. Studien über elektrische Grenzschichten. *Annalen der Physik und Chemie, Neue Folge*, **7**:337–382, 1879.

[138] David Leonard Chapman. A contribution to the theory of electrocapillarity. *Philosophical Magazine Series 6*, **25**:475–481, 1913.

[139] Louis Georges Gouy. Sur la constitution de la charge electrique a la surface d'un electrolyte. *Journal de Physique Théorique et Appliquée, Quatrieme Serie*, **9**:457–468, 1910.

[140] Louis Georges Gouy. Sur la fonction électrocapillaire. *Annales de Physique*, **7**:129–184, 1917.

[141] M. Gouy. Sur la fonction électrocapillaire. *Annales de Chimie et Physique, Huitième Série*, **8**:291–363, 1906.

[142] Otto Stern. Zur Theorie der elektrolytischen Doppelschicht. *Zeitschrift für Elektrochemie*, **30**:508, 1924.

[143] J. Lyklema. The measurement and interpretation of electric potentials from a physico-chemical point of view. *Medical and Biological Engineering and Computing*, **2**:265–280, 1964.

[144] H. Gerischer, D.M. Kolb, and J.K. Sass. The study of solid surfaces by electrochemical methods. *Advances in Physics*, **27**(3):437–498, 1978.

[145] P.J. Boddy. The structure of the semiconductor-electrolyte interface. *Journal of Electroanalytical Chemistry (1959)*, **10**(3):199–244, 1965.

[146] Gerd Binnig and Heinrich Rohrer. Scanning Tunneling Microscopy – from Birth to Adolescence (Nobel Lecture). *Angewandte Chemie International Edition in English*, **26**(7):606–614, 1987.

[147] G. Binnig and H. Rohrer. Surface imaging by scanning tunneling microscopy. *Ultramicroscopy*, **11**(2–3):157–160, 1983.

[148] J. Bardeen. Tunnelling from a Many-Particle Point of View. *Physical Review Letters*, **6**:57–59, Jan 1961.

[149] J. Tersoff and D. R. Hamann. Theory of the scanning tunneling microscope. *Physical Review B*, **31**:805–813, Jan 1985.

[150] N.D. Lang. Spectroscopy of single atoms in the scanning tunneling microscope. *Physical Review B*, **34**:5947–5950, Oct 1986.

[151] R.J. Hamers. Atomic-Resolution Surface Spectroscopy with the Scanning Tunneling Microscope. *Annual Review of Physical Chemistry*, **40**(1):531–559, 1989.

[152] T.E. Feuchtwang, P.H. Cutler, and N.M. Miskovsky. A theory of vacuum tunneling microscopy. *Physics Letters A*, **99**(4):167–171, 1983.

[153] N.J. Tao, C.Z. Li, and H.X. He. Scanning tunneling microscopy applications in electrochemistry – beyond imaging. *Journal of Electroanalytical Chemistry*, **492**(2):81–93, 2000.

[154] Richard Sonnenfeld and Paul K. Hansma. Atomic-Resolution Microscopy in Water. *Science*, **232**(4747):211–213, 1986.

[155] Hsue Yang Liu, Fu Ren F. Fan, Charles W. Lin, and Allen J. Bard. Scanning electrochemical and tunneling ultramicroelectrode microscope for high-resolution examination of electrode surfaces in solution. *Journal of the American Chemical Society*, **108**(13):3838–3839, 1986.

[156] J. Schneir, R. Sonnenfeld, P.K. Hansma, and J. Tersoff. Tunneling microscopy study of the graphite surface in air and water. *Physical Review B*, **34**:4979–4984, Oct 1986.

[157] B. Drake, R. Sonnenfeld, J. Schneir, and P.K. Hansma. Scanning tunneling microscopy of processes at liquid-solid interfaces. *Surface Science*, **181**(1–2):92–97, 1987.

[158] Richard Sonnenfeld, J. Schneir, B. Drake, P.K. Hansma, and D.E. Aspnes. Semiconductor topography in aqueous environments: Tunneling microscopy of chemomechanically polished (001)GaAs. *Applied Physics Letters*, **50**(24):1742–1744, 1987.

[159] Ovadia Lev, Fu-Ren Fan, and Allen J. Bard. The Application of Scanning Tunneling Microscopy to In Situ Studies of Nickel Electrodes under Potential Control. *Journal of The Electrochemical Society*, **135**(3):783–784, 1988.

[160] P. Lustenberger, H. Rohrer, R. Christoph, and H. Siegenthaler. Scanning tunneling microscopy at potential controlled electrode surfaces in electrolytic environment. *Journal of Electroanalytical Chemistry and Interfacial Electrochemistry*, **243**(1):225–235, 1988.

[161] Kingo Itaya, Shizuo Sugawara, and Katsutoshi Higaki. In situ scanning tunneling microscopy for platinum surfaces in aqueous solutions. *The Journal of Physical Chemistry*, **92**(23):6714–6718, 1988.

[162] Kingo Itaya and Shizuo Sugawara. Scanning Tunneling Microscopy with Atomic Resolution in Aqueous Solutions. *Chemistry Letters*, **16**(10):1927–1930, 1987.

[163] Kingo Itaya and Eisuke Tomita. Scanning tunneling microscope for electrochemistry – a new concept for the in situ scanning tunneling microscope in electrolyte solutions. *Surface Science*, **201**(3):L507–L512, 1988.

[164] Kingo Itaya, Katsutoshi Higaki, and Shizuo Sugawara. In-Situ Scanning Tunneling Microscopy of Platinum Electrode in Sulfuric Acid. *Chemistry Letters*, **17**(3):421–424, 1988.

[165] R. Houbertz, U. Memmert, and R. J. Behm. Atomic step resolution in scanning tunneling microscope imaging of H_2SO_4 covered Si(100) surfaces. *Applied Physics Letters*, **58**(10):1027–1029, 1991.

[166] Philippe Allongue, Harald Brune, and Heinz Gerischer. In situ STM observations of the etching of n-Si(111) in NaOH solutions. *Surface Science*, **275**(3):414–423, 1992.

[167] P. Allongue, V. Costa-Kieling, and H. Gerischer. Etching of Silicon in NaOH Solutions (I). *Journal of The Electrochemical Society*, **140**(4):1009–1018, 1993.

[168] Nikola Batina, Torsten Will, and Dieter M. Kolb. Study of the initial stages of copper deposition by in situ scanning tunnelling microscopy. *Faraday Discussions*, **94**:93–106, 1992.

[169] Willy Obretenov, Ute Schmidt, Wolfgang J. Lorenz, Georg Staikov, Evgeni Budevski, Didier Carnal, Ulrich Muller, Hans Siegenthaler, and Eberhard Schmidt. Underpotential deposition and electrocrystallization of metals: an in situ scanning tunnelling microscopy study with lateral atomic resolution. *Faraday Discussions*, **94**:107–116, 1992.

[170] Naohiko Kimizuka and Kingo Itaya. In situ scanning tunnelling microscopy of underpotential deposition: silver adlayers on Pt(111) in sulfuric acid solutions. *Faraday Discussions*, **94**:117–126, 1992.

[171] O.M. Magnussen, J. Hotlos, G. Beitel, D.M. Kolb, and R.J. Behm. Atomic structure of ordered copper adlayers on single-crystalline gold electrodes. *Journal of Vacuum Science & Technology B*, **9**(2):969–975, 1991.

[172] D.M. Kolb. Reconstruction phenomena at metal-electrolyte interfaces. *Progress in Surface Science*, **51**(2):109–173, 1996.

[173] Shueh-Lin Yau, Fu-Ren F. Fan, and Allen J. Bard. In Situ STM Imaging of Silicon(111) in HF under Potential Control. *Journal of The Electrochemical Society*, **139**(10):2825–2829, 1992.

[174] Wenjie Li, Jorma A. Virtanen, and Reginald M. Penner. A nanometer-scale galvanic cell. *The Journal of Physical Chemistry*, **96**(16):6529–6532, 1992.

[175] Richard Sonnenfeld and Bruce C. Schardt. Tunneling microscopy in an electrochemical cell: Images of Ag plating. *Applied Physics Letters*, **49**(18):1172–1174, 1986.

[176] R.T. Pötzschke, C.A. Gervasi, S. Vinzelberg, G. Staikov, and W.J. Lorenz. Nanoscale studies of Ag electrodeposition on HOPG (0001). *Electrochimica Acta*, **40**(10):1469–1474, 1995.

[177] J. Wiechers, T. Twomey, D.M. Kolb, and R.J. Behm. An in-situ scanning tunneling microscopy study of au (111) with atomic scale resolution. *Journal of Electroanalytical Chemistry and Interfacial Electrochemistry*, **248**(2):451–460, 1988.

[178] I. Otsuka and T. Iwasaki. STM imaging of noble metal electrodes in solution under potentiostatic control. *Journal of Microscopy*, **152**(1):289–297, 1988.

[179] R.J. Nichols, O.M. Magnussen, J. Hotlos, T. Twomey, R.J. Behm, and D.M. Kolb. An in-situ STM study of potential-induced changes in the surface topography of Au(100) electrodes. *Journal of Electroanalytical Chemistry and Interfacial Electrochemistry*, **290**(1–2):21–31, 1990.

[180] K. Itaya, R. Sugawara, Y. Morita, and H. Tokumoto. Atomic resolution images of H-terminated Si(111) surfaces in aqueous solutions. *Applied Physics Letters*, **60**(20):2534–2536, 1992.

[181] Sang-Eun Bae, Mi-Kyung Oh, Nam-Ki Min, Se-Hwan Paek, Suk-In Hong, and Chi-Woo J. Lee. Preparation of Atomically Flat Si(111)-H Surfaces in Aqueous Ammonium Fluoride Solutions Investigated by Using Electrochemical, *In Situ* EC-STM and ATR-FTIR Spectroscopic Methods. *Bulletin of the Korean Chemical Society*, **25**(12):1822–1828, 2004.

[182] Sang-Eun Bae, Jung-Hyun Yoon, Chi-Woo J. Lee, and Il Cheol Jeon. In situ EC-STM studies of n-Si(111):H in 40% NH4F solution at pH 10. *Electrochimica Acta*, **53**(21):6178–6183, 2008.

[183] J. Tang, M. Petri, L.A. Kibler, and D.M. Kolb. Pd deposition onto Au(111) electrodes from sulphuric acid solution. *Electrochimica Acta*, **51**(1):125–132, 2005.

[184] D.M. Kolb, R.J. Randler, R.I. Wielgosz, and J.C. Ziegler. The Initial Stages of Metal Deposition on Metal and Semiconductor Electrodes Studied by In Situ STM. *MRS Proceedings*, **451**:19–30, 1996.

[185] Xiaoyin Xiao, Michael Nielinger, and Helmut Baltruschat. Local and global electrochemical nanostructuring of Pt and Au single crystal electrodes. *Electrochimica Acta*, **48**(20–22):3093–3105, 2003. Electrochemistry in Molecular and Microscopic Dimensions.

[186] Sang-Eun Bae, Jung-Hyun Yoon, and Chi-Woo J. Lee. Etching of n-Si(111) in 40% NH_4F Solution Investigated by OCP, In Situ EC-STM, and ATR-FTIR Spectroscopic Methods. *The Journal of Physical Chemistry C*, **112**(5):1533–1538, 2008.

[187] O.M. Magnussen A. Lachenwitzer, S. Morin and R.J. Behm. In situ STM study of electrodeposition and anodic dissolution of Ni on Ag(111). *Physical Chemistry Chemical Physics*, **3**:3351–3363, 2001.

[188] M. Schweizer and D.M. Kolb. First observation of an ordered sulfate adlayer on Ag single crystal electrodes. *Surface Science*, **544**(1):93–102, 2003.

[189] S.G. García, D.R. Salinas, and G. Staikov. Underpotential deposition of Cd on Ag(111): an in situ STM study. *Surface Science*, **576**(1-3):9–18, 2005.

[190] J.C. Ziegler, R.I. Wielgosz, and D.M. Kolb. Pb deposition on n-Si(111) electrodes. *Electrochimica Acta*, **45**(4–5):827–833, 1999.

[191] Andrew A. Gewirth and Brian K. Niece. Electrochemical Applications of in Situ Scanning Probe Microscopy. *Chemical Reviews*, **97**(4):1129–1162, 1997.

[192] D.M. Kolb. Structure studies of metal electrodes by in-situ scanning tunneling microscopy. *Electrochimica Acta*, **45**(15–16):2387–2402, 2000.

[193] Kazutoshi Kaji, Shueh-Lin Yau, and Kingo Itaya. Atomic scale etching processes of n-Si(111) in NH_4F solutions: In situ scanning tunneling microscopy. *Journal of Applied Physics*, **78**(9):5727–5733, 1995.

[194] S.M. Lindsay. Atomic Resolution Microscopy at the Solid-Liquid Interface. *Current Separations*, **17**:17–24, 1998.

[195] O. M. Magnussen, J. Hotlos, R. J. Nichols, D. M. Kolb, and R. J. Behm. Atomic structure of Cu adlayers on Au(100) and Au(111) electrodes observed by *in situ* scanning tunneling microscopy. *Physical Review Letters*, **64**:2929–2932, Jun 1990.

[196] Philipp Hugelmann, Martin Hugelmann, and Werner Schindler. Electrochemical nanoelectrodes for advanced investigations of nanostructures. *Journal of Electroanalytical Chemistry*, **612**(1):131–139, 2008.

[197] R.T. Pötzschke, G. Staikov, W.J. Lorenz, and W. Wiesbeck. Electrochemical Nanostructuring of n-Si(111) Single-Crystal Faces. *Journal of The Electrochemical Society*, **146**(1):141–149, 1999.

[198] W. Schindler, D. Hofmann, and J. Kirschner. Nanoscale electrodeposition: A new route to magnetic nanostructures? *Journal of Applied Physics*, **87**(9):7007–7009, 2000.

[199] Phillippe Allongue. volume 4 of *Advances in Electrochemical Science and Engineering*. VCH Verlagsgesellschaft mbH, Weinheim, 1995.

[200] Wolfgang Schmickler and Douglas Henderson. A model for the scanning tunneling microscope operating in an electrolyte solution. *Journal of Electroanalytical Chemistry and Interfacial Electrochemistry*, **290**(1–2):283–291, 1990.

[201] Martin Hugelmann and Werner Schindler. Tunnel barrier height oscillations at the solid/liquid interface. *Surface Science*, **541**(1–3):L643–L648, 2003.

[202] Martin Hugelmann and Werner Schindler. In Situ Distance Tunneling Spectroscopy at Au(111)/0.02 M $HClO_4$. *Journal of The Electrochemical Society*, **151**(3):E97–E101, 2004.

[203] S.M. Sze and J.C. Irvin. Resistivity, mobility and impurity levels in GaAs, Ge, and Si at 300°K. *Solid-State Electronics*, **11**(6):599–602, 1968.

[204] Y.M. Liu W.R. Thurber, R.L. Mattis and J.J. Filliben. *The Relationship Between Resistivity and Dopant Density for Phosphorus- and Boron-Doped Silicon*. NBS Special Publication 400-64. National Bureau of Standards, Washington, DC, 1981.

[205] S.M. Sze and Kwok K. Ng. *Physics of Semiconductor Devices*. John Wiley & sons, Inc., 2007.

[206] Heinz Gerischer. volume IXA/ Electrochemistry of *Physical Chemistry - An Advanced Treatise*. Academic Press, Inc., New York/ London, 1970.

[207] Henry Eyring, Douglas Henderson, and Wilhelm Jost, editors. volume IXA/ Electrochemistry of *Physical Chemistry - An Advanced Treatise*. Academic Press, Inc., New York/ London, 1970.

[208] Harry O. Finklea, editor. *Semiconductor Electrodes*, volume 55 of *Studies in Physical and Theoretical Chemistry*. Elsevier Science Publishers B.V., Amsterdam, 1988.

[209] Arthur J. Nozik and Rüdiger Memming. Physical Chemistry of Semiconductor–Liquid Interfaces. *The Journal of Physical Chemistry*, **100**(31):13061–13078, 1996.

[210] J.-N. Chazalviel. Impedance studies at semiconductor electrodes: classical and more exotic techniques. *Electrochimica Acta*, **35**(10):1545–1552, 1990.

[211] R. Memming and G. Schwandt. Potential and Charge Distribution at Semiconductor-electrolyte Interfaces. *Angewandte Chemie International Edition in English*, **6**(10):851–861, 1967.

[212] Arun Natarajan, Gerko Oskam, and Peter C. Searson. The Potential Distribution at the Semiconductor/Solution Interface. *The Journal of Physical Chemistry B*, **102**(40):7793–7799, 1998.

[213] R. Memming and G. Schwandt. Potential distribution and formation of surface states at the silicon-electrolyte interface. *Surface Science*, **5**(1):97 – 110, 1966.

[214] W.P. Gomes and F. Cardon. On the Electrochemical Behaviour of the Hexacyonferrate Redox System at Different Semiconductor Electrodes. *Zeitschrift für Physikalische Chemie Neue Folge*, **86**:330–334, 1973.

[215] Walter Schottky. Vereinfachte und erweiterte Theorie der Randschichtgleichrichter. *Zeitschrift für Physik*, **118**:539–592, 1942.

[216] Walter Schottky. Zur Halbleitertheorie der Sperrschicht- und Spitzengleichrichtung. *Zeitschrift für Physik*, **113**:367–414, 1939.

[217] N. F. Mott. The Theory of Crystal Rectifiers. *Proceedings of the Royal Society of London. Series A. Mathematical and Physical Sciences*, **171**(944):27–38, 1939.

[218] W.P. Gomes and F. Cardon. Electron energy levels in semiconductor electrochemistry. *Progress in Surface Science*, **12**(2):155–215, 1982.

[219] F. Cardon and W.P. Gomes. On the determination of the flat-band potential of a semiconductor in contact with a metal or an electrolyte from the Mott-Schottky plot. *Journal of Physics D: Applied Physics*, **11**(4):L63–L67, 1978.

[220] T. Freund and S. Roy Morrison. Mechanism of cathodic processes on the semiconductor zinc oxide. *Surface Science*, **9**(1):119–132, 1968.

[221] J.F. Dewald. The Charge and Potential Distributions at the Zinc Oxide Electrode. *The Bell System Technical Journal*, **39**:615–639, May 1960.

[222] J.F. Dewald. The charge distribution at the zinc oxide-electrolyte interface. *Journal of Physics and Chemistry of Solids*, **14**(0):155–161, 1960.

[223] Karl H. Hauffe. *Electrochemistry – The Past Thirty and the Next Thirty Years*. Plenum Press, New York, 1977.

[224] G. Nagasubramanian, B.L. Wheeler, and A.J. Bard. Semiconductor Electrodes: XLIX. Evidence for Fermi Level Pinning and Surface-State Distributions from Impedance Measurements in Acetonitrile Solutions with Various Redox Couples. *Journal of The Electrochemical Society*, **130**(8):1680–1688, 1983.

[225] J.-N. Chazalviel. Schottky barrier height and reverse current of the n-Si–electrolyte junction. *Surface Science*, **88**(1):204–220, 1979.

[226] Walter C. Johnson and Peter T. Panousis. The Influence of Debye Length on the C–V Measurements of Doping Profiles. *IEEE Transactions on Electron Devices*, **18**:965–973, 1971.

[227] Geula Dagan, Wu-Mian Shen, and Micha Tomkiewicz. Passivation of Permalloy Thin Films. *Journal of The Electrochemical Society*, **139**(7):1855–1861, 1992.

[228] J.A. Bardwell, N. Draper, and P. Schmuki. Growth and characterization of anodic oxides on Si(100) formed in 0.1 M hydrochloric acid. *Journal of Applied Physics*, **79**(11):8761–8769, 1996.

[229] Eduardo C. Muñoz, Ricardo S. Schrebler, Paula K. Cury, Claudio A. Suárez, Ricardo A. Córdova, Carlos H. Gómez, Ricardo E. Marotti, and Enrique A. Dalchiele. The Influence of Poly(ethylene oxide) and Illumination on the Copper Electrodeposition Process onto n-Si(100). *The Journal of Physical Chemistry B*, **110**(42):21109–21117, 2006.

[230] Micha Tomkiewicz. The Potential Distribution at the TiO_2 Aqueous Electrolyte Interface. *Journal of The Electrochemical Society*, **126**(9):1505–1510, 1979.

[231] M.J. Madou, B.H. Loo, K.W. Frese, and S. Roy Morrison. Bulk and surface characterization of the silicon electrode. *Surface Science*, **108**(1):135–152, 1981.

[232] S. Ottow, G.S. Popkirov, and H. Föll. Determination of flat-band potentials of silicon electrodes in HF by means of ac resistance measurements. *Journal of Electroanalytical Chemistry*, **455**(1–2):29–37, 1998.

[233] John A. Turner. Energetics of the semiconductor-electrolyte interface. *Journal of Chemical Education*, **60**(4):327–329, 1983.

[234] Arun Natarajan, Gerko Oskam, and Peter C. Searson. Characterization of silicon surfaces in HF solution using microwave reflectivity. *Journal of Applied Physics*, **83**(4):2112–2120, 1998.

[235] Chunxin Ji, Gerko Oskam, and Peter C. Searson. Electrodeposition of Copper on Silicon from Sulfate Solution. *Journal of The Electrochemical Society*, **148**(11):C746–C752, 2001.

[236] R. De Gryse, W.P. Gomes, F. Cardon, and J. Vennik. On the Interpretation of Mott-Schottky Plots Determined at Semiconductor/Electrolyte Systems. *Journal of The Electrochemical Society*, **122**(5):711–712, 1975.

[237] I. Runge and R. Sewig. Über den inneren Photoeffekt in kristallinen Halbleitern. *Zeitschrift für Physik*, **62**:726–729, 1930.

[238] R.L. Smith and S.D. Collins. Porous silicon formation mechanisms. *Journal of Applied Physics*, **71**(8):R1–R22, 1992.

[239] Dieter W. Pohl. Some design criteria in scanning tunneling microscopy. *IBM Journal of Research and Development*, **30**(4):417–427, July 1986.

[240] Carl A. Koval and Jason N. Howard. Electron transfer at semiconductor electrode-liquid electrolyte interfaces. *Chemical Reviews*, **92**(3):411–433, 1992.

[241] H. Gerischer. The impact of semiconductors on the concepts of electrochemistry. *Electrochimica Acta*, **35**(11–12):1677–1699, 1990.

[242] S. Yoshihara, K. Endo, E. Sato, and J. O'M. Bockris. STM study of photoelectrochemical plating on p-type silicon electrodes. *Journal of Electroanalytical Chemistry*, **372**(1–2):91–94, 1994.

[243] W. Schindler and J. Kirschner. New electrochemical cell for in situ tunneling microscopy, cyclovoltammetry, and optical measurements. *Review of Scientific Instruments*, **67**(10):3578–3582, 1996.

[244] W. Schindler and J. Kirschner. Ultrathin magnetic films: Electrochemistry versus molecular-beam epitaxy. *Physical Review B*, **55**:R1989–R1996, Jan 1997.

[245] Philipp Hugelmann and Werner Schindler. In-situ Voltage Tunneling Spectroscopy at Electrochemical Interfaces. *The Journal of Physical Chemistry B*, **109**(13):6262–6267, 2005.

[246] T. Vitanov, A. Popov, and E.S. Sevastyanov. Electrical double layer on (111) and (100) faces of silver single crystals in solutions containing ClO_4^- and F^-. *Journal of Electroanalytical Chemistry and Interfacial Electrochemistry*, **142**(1–2):289–297, 1982.

[247] Rolf Schuster, Viola Kirchner, Philippe Allongue, and Gerhard Ertl. Electrochemical Micromachining. *Science*, **289**(5476):98–101, 2000.

[248] Georges and Valette. Double layer on silver single crystal electrodes in contact with electrolytes having anions which are slightly specifically adsorbed: Part III. The (111) face. *Journal of Electroanalytical Chemistry and Interfacial Electrochemistry*, **269**(1):191–203, 1989.

[249] Marie Anne Schneeweiss and Dieter Kolb. Das Rastertunnelmikroskop in der Elektrochemie. *Chemie in unserer Zeit*, **34**(2):72–83, 2000.

[250] T. Pajkossy and D.M. Kolb. Double layer capacitance of Pt(111) single crystal electrodes. *Electrochimica Acta*, **46**(20–21):3063–3071, 2001.

[251] G.E. Engelmann and D.M. Kolb. Tunnel spectroscopy of tip-generated copper clusters on Au(111). *Electrochimica Acta*, **48**(20–22):2897–2901, 2003.

[252] D.M. Kolb. An atomistic view of electrochemistry. *Surface Science*, **500**(1–3):722–740, 2002.

[253] J.-N. Chazalviel. Introduction to the session on liquid-solid interfaces. *Journal of Electron Spectroscopy and Related Phenomena*, **54–55**:1183–1184, 1990.

[254] Marc Petri, Dieter M. Kolb, Ulrich Memmert, and Heinrich Meyer. Adsorption of mercaptopropionic acid onto Au(111): Part I. Adlayer formation, structure and electrochemistry. *Electrochimica Acta*, **49**(1):175–182, 2003.

[255] Christopher M.A. Brett and Ana Maria Oliveira Brett. *Electrochemistry – Principles, Methods, and Applications*. Oxford University Press, 1993.

[256] A.K. Shukla, S. Sampath, and K. Vijayamohanan. Electrochemical supercapacitors: Energy storage beyond batteries. *Current Science*, **79**(12):1656–1661, December 2000.

[257] R. Kötz and M. Carlen. Principles and applications of electrochemical capacitors. *Electrochimica Acta*, **45**(15–16):2483–2498, 2000.

[258] J.-N. Chazalviel. Electrochemical Transfer via Surface States: A New Formulation for the Semiconductor/Electrolyte Interface. *Journal of The Electrochemical Society*, **129**(5):963–969, 1982.

[259] Peter M. Hoffmann, Gerko Oskam, and Peter C. Searson. Analysis of the impedance response due to surface states at the semiconductor/solution interface. *Journal of Applied Physics*, **83**(8):4309–4323, 1998.

[260] Xiaomin Bin, Trevor K. Mischki, Chaoyang Fan, Gregory P. Lopinski, and Danial D.M. Wayner. Electrochemical Characterization of Si(111) Modified with Linear and Branched Alkyl Chains. *The Journal of Physical Chemistry C*, **111**(36):13547–13553, 2007.

[261] G. Oskam, J.C. Schmidt, and P.C. Searson. Electrical Properties of n-Type (111) Si in Aqueous $K_4Fe(CN)_6$ Solution (II). *Journal of The Electrochemical Society*, **143**(8):2538–2543, 1996.

[262] J. Schefold. Impedance and intensity modulated photocurrent spectroscopy as complementary differential methods in photoelectrochemistry. *Journal of Electroanalytical Chemistry*, **341**(1–2):111–136, 1992.

[263] A.R. de Wit, D. Vanmaekelbergh, and J.J. Kelly. A Study of the Photoanodic Dissolution of CdS with Electrical and Opto-electrical Impedance Spectroscopy. *Journal of The Electrochemical Society*, **139**(9):2508–2513, 1992.

[264] A. Fujishima, A. Sakamoto, and K. Honda. Flatband potential of TiO_2 semiconductor electrode. *Seisan Kenkyu*, **21**(7):450–452, 1969.

[265] Guoguang Qian, Swatilekha Saha, and K. M. Lewis. Note: A simple, convenient, and reliable method to prepare gold scanning tunneling microscope tips. *Review of Scientific Instruments*, **81**(1):016110, 2010.

[266] Bin Ren, Gennaro Picardi, and Bruno Pettinger. Preparation of gold tips suitable for tip-enhanced Raman spectroscopy and light emission by electrochemical etching. *Review of Scientific Instruments*, **75**(4):837–841, 2004.

[267] H.J. Mamin, P.H. Guethner, and D. Rugar. Atomic emission from a gold scanning-tunneling-microscope tip. *Physical Review Letters*, **65**:2418–2421, Nov 1990.

[268] Philipp Hugelmann. *Elektrochemische Herstellung und Charakterisierung von Nanostrukturen – Entwicklung ultrascharfer STM-Spitzen als Nanoelektroden*. PhD thesis, Universtität Karlsruhe, 2004.

[269] M. Giesen, R. Randler, S. Baier, H. Ibach, and D.M. Kolb. Step dynamics on Cu (100) and Ag (111) electrodes in an aqueous electrolyte. *Electrochimica Acta*, **45**(4–5):527–536, 1999.

[270] Claudia E. Bach, Richard J. Nichols, Heinrich Meyer, and Jürgen O. Besenhard. An electropainting method for coating STM tips for electrochemical measurements. *Surface and Coatings Technology*, **67**(3):139–144, 1994.

[271] Albert Schulte. STM tips for in-situ scanning tunneling microscopy in aqueous solutions prepared using electrophoretic deposition of paint. *SPIE Conference Proceedings*, **3512**(1):353–357, 1998.

[272] L.A. Nagahara, T. Thundat, and S.M. Lindsay. Preparation and characterization of STM tips for electrochemical studies. *Review of Scientific Instruments*, **60**(10):3128–3130, 1989.

[273] Andrew A. Gewirth, Derek H. Craston, and Allen J. Bard. Fabrication and characterization of microtips for in situ scanning tunneling microscopy. *Journal of Electroanalytical Chemistry and Interfacial Electrochemistry*, **261**(3):477–482, 1989.

[274] E. Abelev, N. Sezin, and Y. Ein-Eli. An alternative isolation of tungsten tips for a scanning tunneling microscope. *Review of Scientific Instruments*, **76**(10):106105, 2005.

[275] Z.W. Tian, X.D. Zhuo, J.Q. Mu, J.H. Ye, Z.D. Fen, B.W. Mao, C.L. Bai, and C.D. Dai. A new electrochemical scanning tunneling microscope. *Ultramicroscopy*, **42–44**(1):460–463, 1992.

[276] T. Hashizume, I. Kamiya, Y. Hasegawa, N. Sano, T. Sakurai, and H.W. Pickering. A role of tip geometry on STM images. *Journal of Microscopy*, **152**:347–354, November 1988.

[277] D.M. Kolb. *Nanoscale Probes of the Solid/Liquid Interface*, volume 288 of *NATO ASI Series E: Applied Sciences*. Kluwer Academic Publishers, Dordrecht, 1995.

[278] J.V. Barth, H. Brune, G. Ertl, and R.J. Behm. Scanning tunneling microscopy observations on the reconstructed Au(111) surface: Atomic structure, long-range superstructure, rotational domains, and surface defects. *Physical Review B*, **42**:9307–9318, Nov 1990.

[279] Gabor Nagy and Thomas Wandlowski. Adlayer Structures Probed by Distance Tunnelling Spectroscopy for $Au(111)/H_2SO_4 + Cu^{2+}$. *Zeitschrift für Physikalische Chemie*, **217**:587–606, 2003.

[280] D.M. Kolb and J. Schneider. Surface reconstruction in electrochemistry: Au(100)-(5×20), Au(111)-(1×23) and Au(110)-(1×2). *Electrochimica Acta*, **31**(8):929–936, 1986.

[281] N. Batina, A.S. Dakkouri, and D.M. Kolb. The surface structure of flame-annealed Au(100) in aqueous solution: An STM study. *Journal of Electroanalytical Chemistry*, **370**(1–2):87–94, 1994.

[282] Philippe Allongue and Fouad Maroun. Self-ordered electrochemical growth on single-crystal electrode surfaces. *Journal of Physics: Condensed Matter*, **18**(13):S97–S114, 2006.

[283] Toshihiro Kondo, Jun Morita, Kazuya Hanaoka, Satoru Takakusagi, Kazuhisa Tamura, Masamitu Takahasi, Jun'ichiro Mizuki, and Kohei Uosaki. Structure of Au(111) and Au(100) Single-Crystal Electrode Surfaces at Various Potentials in Sulfuric Acid Solution Determined by In Situ Surface X-ray Scattering. *The Journal of Physical Chemistry C*, **111**(35):13197–13204, 2007.

[284] W. Haiss, D. Lackey, J. K. Sass, and K. H. Besocke. Atomic resolution scanning tunneling microscopy images of Au(111) surfaces in air and polar organic solvents. *The Journal of Chemical Physics*, **95**(3):2193–2196, 1991.

[285] J.V. Barth, R. Schuster, R.J. Behm, and G. Ertl. The system K/Au(111): adsorption and surface restructuring. *Surface Science*, **348**(3):280–286, 1996.

[286] J.V. Barth, R.J. Behm, and G. Ertl. Adsorption, surface restructuring and alloy formation in the Na/Au(111) system. *Surface Science*, **341**(1-2):62–91, 1995.

[287] J.V. Barth, R.J. Behm, and G. Ertl. Mesoscopic structural transformations of the Au(111) surface induced by alkali metal adsorption. *Surface Science Letters*, **302**(3):L319–L324, 1994.

[288] Kunio and Takayanagi. High resolution surface study by In-situ UHV transmission electron microscopy. *Ultramicroscopy*, **8**(1–2):145–161, 1982.

[289] A. Gundel, L. Cagnon, C. Gomes, A. Morrone, J. Schmidt, and P. Allongue. In-situ magnetic measurements of electrodeposited ultrathin Co, Ni and Fe/Au(111) layers. *Physical Chemistry Chemical Physics*, **3**:3330–3335, 2001.

[290] Philippe Allongue, Fouad Maroun, Hugo F. Jurca, Nicolas Tournerie, Gregory Savidand, and Robert Cortès. Magnetism of electrodeposited ultrathin layers: Challenges and opportunities. *Surface Science*, **603**(10–12):1831–1840, 2009.

[291] W. Göpel, J. Hesse, and J.N. Zemel, editors. *Fundamentals and General Aspects*, volume 1 of *Sensors - A comprehensive Survey*. VCH, Weinheim, 1989.

[292] Werner Kern. The Evolution of Silicon Wafer Cleaning Technology. *Journal of The Electrochemical Society*, **137**(6):1887–1892, 1990.

[293] Werner Kern and David A. Puotinen. Cleaning Solutions Based on Hydrogen Peroxide for use in Silicon Semiconductior Technology. *RCA Review*, **31**:187–206, 1970.

[294] W. Kern, editor. *Handbook of Semiconductor Wafer Cleaning Technology – Science, Technology, and Applications*. William Andrew Publishing/ Noyes, 1993.

[295] Gregor S. Hsiao, Jorma A. Virtanen, and Reginald M. Penner. Scanning tunneling microscopy investigations of the Si(111) topography produced by etching in 40% NH_4F: Observation of an optimum etch duration. *Applied Physics Letters*, **63**(8):1119–1121, 1993.

[296] G.J. Pietsch. Hydrogen on Si: Ubiquitous surface termination after wet-chemical processing. *Applied Physics A: Materials Science & Processing*, **60**:347–363, 1995.

[297] H. Angermann, W. Henrion, A. Röseler, and M. Rebien. Wet-chemical passivation of Si(111)- and Si(100)-substrates. *Materials Science and Engineering: B*, **73**(1–3):178–183, 2000.

[298] M. Lublow and H.J. Lewerenz. Real-time monitoring of SiO2/Si(111) interlayer etching by Brewster-angle reflectometry. *Surface Science*, **602**(9):1677–1687, 2008.

[299] M. Lublow, T. Stempel, A. G. Muñoz K. Skorupska and, M. Kanis, and H. J. Lewerenz. Morphological and chemical optimization of ex situ NH4F (40%) conditioned Si(111)-(1×1):H. *Applied Physics Letters*, **93**:062112, 2008.

[300] Hiroki Kato, Takumi Taoka, Susumu Nishikata, Gen Sazaki, Taro Yamada, Ryszard Czajka, Andrzej Wawro, Kazuo Nakajima, Atsuo Kasuya, and Shozo Suto. Preparation of an Ultraclean and Atomically Controlled Hydrogen-Terminated Si(111)-(1×1) Surface Revealed by High Resolution Electron Energy Loss Spectroscopy, Atomic Force Microscopy, and Scanning Tunneling Microscopy: Aqueous NH_4F Etching Process of Si(111). *Japanese Journal of Applied Physics*, **46**(9A):5701–5705, 2007.

[301] John J. Boland. Scanning tunnelling microscopy of the interaction of hydrogen with silicon surfaces. *Advances in Physics*, **42**(2):129–171, 1993.

[302] G.S. Higashi, Y.J. Chabal, G.W. Trucks, and Krishnan Raghavachari. Ideal hydrogen termination of the Si (111) surface. *Applied Physics Letters*, **56**(7):656–658, 1990.

[303] G. S. Higashi, R. S. Becker, Y. J. Chabal, and A. J. Becker. Comparison of Si(111) surfaces prepared using aqueous solutions of NH_4F versus HF. *Applied Physics Letters*, **58**(15):1656–1658, 1991.

[304] Christopher P. Wade and Christopher E. D. Chidsey. Etch-pit initiation by dissolved oxygen on terraces of H-Si(111). *Applied Physics Letters*, **71**(12):1679–1681, 1997.

[305] U. Neuwald, H.E. Hessel, A. Feltz, U. Memmert, and R.J. Behm. Initial stages of native oxide growth on hydrogen passivated Si(111) surfaces studied by scanning tunneling microscopy. *Applied Physics Letters*, **60**(11):1307–1309, 1992.

[306] K. Eng, R.N. McFarland, and B.E. Kane. High mobility two-dimensional electron system on hydrogen-passivated silicon(111) surfaces. *Applied Physics Letters*, **87**(5):052106, 2005.

[307] M.L. Munford, R Cortes, and P Allongue. The preparation of ideally ordered flat H-Si(111) surfaces. *Sensors and Materials*, **13**:259–269, 2001.

[308] Sang-Eun Bae, Jung-Hyun Yoon, and Chi-Woo J. Lee. Slow etching of triangular pits on atomically flat monohydride terminated Si(111) surface in 40% NH_4F solution. *Surface Science*, **602**(6):1185–1190, 2008.

[309] Theresa A. Newton, Yi-Chiau Huang, Lori A. Lepak, and Melissa A. Hines. The site-specific reactivity of isopropanol in aqueous silicon etching: Controlling morphology with surface chemistry. *The Journal of Chemical Physics*, **111**(20):9125–9128, 1999.

[310] H.E. Hessel, A. Feltz, M. Reiter, U. Memmert, and R.J. Behm. Step-flow mechanism versus pit corrosion: scanning-tunneling microscopy observations on wet etching of Si(111) by HF solutions. *Chemical Physics Letters*, **186**(2–3):275–280, 1991.

[311] J.C. Ziegler, A. Reitzle, O. Bunk, J. Zegenhagen, and D.M. Kolb. Metal deposition on n-Si(111):H electrodes. *Electrochimica Acta*, **45**(28):4599–4605, 2000.

[312] Melissa A. Hines. The picture tells the story: using surface morphology to probe chemical etching reactions. *International Reviews in Physical Chemistry*, **20**(4):645–672, 2001.

[313] J.H. Ye, T.H. Bok, J.S. Pan, Sam F.Y. Li, and J.Y. Lin. Dynamics of Hydrides on Hydrogen-Terminated Silicon (111)-(1×1) Surface. *The Journal of Physical Chemistry B*, **103**(28):5820–5825, 1999.

[314] Hui Zhou, Joseph Fu, and Richard M. Silver. Time-Resolved Kinetic Monte-Carlo Simulation Study on Si (111) Etching. *The Journal of Physical Chemistry C*, **111**(9):3566–3574, 2007.

[315] Joseph Fu, Hui Zhou, John Kramar, Richard Silver, and Satoshi Gonda. Dependence of morphology on miscut angle for Si(111) etched in NH_4F. *Applied Physics Letters*, **82**(18):3014–3016, 2003.

[316] Atsushi Ando, Kazushi Miki, Kazuhiko Matsumoto, Tetsuo Shimizu, Yukinori Morita, and Hiroshi Tokumoto. Surface Observation and Modification of Si Substrate in NH_4F and H_2SO_4 Solutions. *Japanese Journal of Applied Physics*, **35**(Part 1, No. 2B):1064–1068, 1996.

[317] Sang-Eun Bae, Jong-Soon Lee, In-Churl Lee, Moon-Bong Song, and Chi-Woo J. Lee. Behavior of Hydrogen-Terminated Si(111) Surface in Oxygen-Dissolved NH_4F Solution with or without Cu(II) Ions. *Bulletin of the Korean Chemical Society*, **26**(11):1891–1894, 2005.

[318] Satoru Watanabe. Chemical structure and surface phonons associated with H on Si. *The Journal of Chemical Physics*, **108**(14):5965–5974, 1998.

[319] Tatsuhiro Yasaka, Kozo Kanda, Kenichi Sawara, Seiichi Miyazaki, and Masataka Hirose. Chemical Stability of HF-Treated Si(111) Surfaces. *Japanese Journal of Applied Physics*, **30**(Part 1, No. 12B):3567–3569, 1991.

[320] Satoru Watanabe, Kei Horiuchi, and Takashi Ito. Atomic Step Structure on Vicinal H/Si(111) Surface Formed by Hot Water Immersion. *Japanese Journal of Applied Physics*, **32**(8):3420–3425, 1993.

[321] T. Yasuda and D. E. Aspnes. Optical-standard surfaces of single-crystal silicon for calibrating ellipsometers and reflectometers. *Applied Optics*, **33**(31):7435–7438, Nov 1994.

[322] P. Allongue, V. Kieling, and H. Gerischer. Etching mechanism and atomic structure of H-Si(111) surfaces prepared in NH_4F. *Electrochimica Acta*, **40**(10):1353–1360, 1995.

[323] G.W. Trucks, Krishnan Raghavachari, G.S. Higashi, and Y.J. Chabal. Mechanism of HF etching of silicon surfaces: A theoretical understanding of hydrogen passivation. *Physical Review Letters*, **65**(4):504–507, Jul 1990.

[324] J.E. Mejía, Bernardo S. Mendoza, M. Palummo, G. Onida, R. Del Sole, S. Bergfeld, and W. Daum. Surface second-harmonic generation from Si(111)(1×1) Theory versus experiment. *Physical Review B*, **66**:195329, Nov 2002.

[325] G.J. Pietsch, U. Kohler, and M. Henzler. Anisotropic etching versus interaction of atomic steps: Scanning tunneling microscopy observations on HF/NH_4F-treated Si(111). *Journal of Applied Physics*, **73**(10):4797–4807, 1993.

[326] R.E. Oosterbroek, J.W. Berenschot, H.V. Jansen, A.J. Nijdam, G. Pandraud, A. van den Berg, and M.C. Elwenspoek. Etching methodologies in ⟨111⟩-oriented silicon wafers. *Microelectromechanical Systems, Journal of*, **9**(3):390 –398, sept. 2000.

[327] M. Lublow and H.J. Lewerenz. Combined AFM and Brewster-angle analysis of gradually etched ultrathin SiO_2 - Comparison with SRPES results. *Surface Science*, **601**(7):1693–1700, 2007.

[328] Hiroshi Tokumoto, Kazushi Miki, Hiroshi Murakami, Naotake Morita, Hiroshi Bando, Akira Sakai, Shigeru Wakiyama, Masatoshi Ono, and Koji Kajimura. Imaging of hydrogen-induced Si(111) surface with the scanning tunnelling microscope. *Journal of Microscopy*, **152**(3):743–750, December 1988.

[329] M. Gruyters. Growth and structure of Fe, Co and Ni films on hydrogen-terminated Si(111) surfaces. *Surface Science*, **515**(1):53–60, 2002.

[330] Hirokazu Fukidome and Michio Matsumura. Effect of dissolved oxygen on etching process of Si(111)in 2.5% NH_3 solution. *Surface Science*, **463**(3):L649–L653, 2000.

[331] Norio Tokuda, Daisuke Hojo, Satoshi Yamasaki, Kazushi Miki, and Kikuo Yamabe. Selective Growth of Cu Nanowires on Si(111) Substrates. *Japanese Journal of Applied Physics*, **42**(Part 2, No. 10A):L1210–L1212, 2003.

[332] Takayuki Homma, Christopher P. Wade, and Christopher E. D. Chidsey. Nucleation of Trace Copper on the H–Si(111) Surface in Aqueous Fluoride Solutions. *The Journal of Physical Chemistry B*, **102**(41):7919–7923, 1998.

[333] M.L. Munford, F. Maroun, R. Cortès, P. Allongue, and A.A. Pasa. Electrochemical growth of gold on well-defined vicinal H–Si(111) surfaces studied by AFM and XRD. *Surface Science*, **537**(1–3):95–112, 2003.

[334] Chunxin Ji, Gerko Oskam, and Peter C. Searson. Electrochemical nucleation and growth of copper on Si(111). *Surface Science*, **492**(1–2):115–124, 2001.

[335] J.-N. Chazalviel, F. Maroun, and F. Ozanam. An Interface-Free-Energy Approach to Semiconductor Electrode Chemistry. *Journal of The Electrochemical Society*, **151**(2):E51–E55, 2004.

[336] Shen Ye, Taro Ichihara, and Kohei Uosaki. Attenuated total reflection Fourier transform infrared spectroscopy study of the adsorption of organic contaminants on a hydrogen-terminated Si(111) surface in air. *Applied Physics Letters*, **75**(11):1562–1564, 1999.

[337] Ç. Nuhoğlu, Ş. Aydoğan, and A. Türüt. The barrier height inhomogeneity in identically prepared Pb/p-type Si Schottky barrier diodes. *Semiconductor Science and Technology*, **18**(7):642–646, 2003.

[338] Hirokazu Fukidome and Michio Matsumura. Electrochemical study of atomically flattening process of silicon surface in 40% NH_4F solution. *Applied Surface Science*, **130–132**:146–150, 1998.

[339] Simon P. Garcia, Hailing Bao, and Melissa A. Hines. Understanding the pH dependence of silicon etching: the importance of dissolved oxygen in buffered HF etchants. *Surface Science*, **541**(1–3):252–261, 2003.

[340] A.J. Reddy, J.V. Chan, T.A. Burr, R. Mo, C.P. Wade, C.E.D. Chidsey, J. Michel, and L.C. Kimerling. Defect states at silicon surfaces. *Physica B: Condensed Matter*, **273–274**:468–472, 1999.

[341] H. Angermann, J. Rappich, I. Sieber, K. Hübener, and J. Hauschild. Smoothing and passivation of special Si(111) substrates: studied by SPV, PL, AFM and SEM measurements. *Analytical and Bioanalytical Chemistry*, **390**:1463–1470, 2008.

[342] G. J. Pietsch, U. Köhler, and M. Henzler. Direct observation of silicon surface etching by water with scanning tunneling microscopy. *Chemical Physics Letters*, **197**(4–5):346–351, 1992.

[343] Heinz Gerischer and Margot Lübke. The Electrochemical Behaviour of n-Type Silicon (111)-Surfaces in Fluoride Containing Aqueous Electrolytes. *Berichte der Bunsengesellschaft für Physikalische Chemie*, **91**:394–398, 1987.

[344] T. Nagai, A. Imanishi, and Y. Nakato. Scratch induced nano-wires acting as a macro-pattern for formation of well-ordered step structures on H-terminated Si(111) by chemical etching. *Applied Surface Science*, **237**(1–4):533–537, 2004.

[345] Y. Zhang, E. Balaur, and P. Schmuki. Potential influence on copper electrodeposition on scratched silicon surfaces. *Journal of Electroceramics*, **16**:65–70, 2006.

[346] A. Imanishi, T. Nagai, and Y. Nakato. Formation of Well-Ordered Step Structures on Si(111) by a Combination of Chemical Etching and Surface Scratching for Producing Macrosized Patterns. *The Journal of Physical Chemistry B*, **108**(1):21–23, 2004.

[347] H. Ahrle. Synthese und Formel der Caroschen Säure (Monosulfonpersäure). *Journal für Praktische Chemie*, **79**(1):129–164, 1909.

[348] Helmut Sitzmann. Carosche Säure. Thieme RÖMPP Online.

[349] H. Jungblut, J. Jakubowicz, S. Schweizer, and H.J. Lewerenz. Mechanism of initial structure formation on highly doped n-Si (111). *Journal of Electroanalytical Chemistry*, **527**(1–2):41–46, 2002.

[350] K. Chandrasekaran, R.C. Kainthla, and J.O'M. Bockris. An impedance study of the silicon – solution interface under illumination. *Electrochimica Acta*, **33**(3):327–336, 1988.

[351] K. Chandrasekaran, M. Weichold, F. Gutmann, and J.O'M. Bockris. On the equivalent circuit for the illuminated semiconductor electrolyte interface. *Electrochimica Acta*, **30**(7):961–963, 1985.

[352] S. D. Babenko, A. A. Balakai, A. G. Lavrushko, Yu. L. Moskvin, and S. N. Shamaev. Hydrogen Evolution Efficiency at Illuminated Silicon. *Russian Journal of Electrochemistry*, **40**:1205–1207, 2004.

[353] V. Bertagna, F. Rouelle, and M. Chemla. An improved electrochemical cell for the characterization of silicon/electrolyte interfaces. *Journal of Applied Electrochemistry*, **27**:1179–1183, 1997.

[354] A. Reitzle, F.U. Renner, T.L. Lee, J. Zegenhagen, and D.M. Kolb. Electrochemical growth of copper on well-defined n-Si(111):H surfaces. *Surface Science*, **576**(1–3):19–28, 2005.

[355] R. Krumm, B. Guel, C. Schmitz, and G. Staikov. Nucleation and growth in electrodeposition of metals on n-Si(111). *Electrochimica Acta*, **45**(20):3255–3262, 2000.

[356] Kenneth D. Legg, Arthur B. Ellis, Jeffrey M. Bolts, and Mark S. Wrighton. n-Type Si-based photoelectrochemical cell: New liquid junction photocell using a nonaqueous ferricenium/ferrocene electrolyte. *Proceedings of the National Academy of Sciences*, **74**(10):4116–4120, 1977.

[357] D. R. Lillington and W. G. Townsend. Effects of interfacial oxide layers on the performance of silicon Schottky-barrier solar cells. *Applied Physics Letters*, **28**(2):97–98, 1976.

[358] S. Rauscher, Th. Dittrich, M. Aggour, J. Rappich, H. Flietner, and H. J. Lewerenz. Reduced interface state density after photocurrent oscillations and electrochemical hydrogenation of n-Si(111): A surface photovoltage investigation. *Applied Physics Letters*, **66**(22):3018–3020, 1995.

[359] Cheng Fang, Eugen Foca, Sufan Xu, Jürgen Carstensen, and Helmut Föll. Deep Silicon Macropores Filled with Copper by Electrodeposition. *Journal of The Electrochemical Society*, **154**(1):D45–D49, 2007.

[360] Yukio H. Ogata, Katsutoshi Kobayashi, and Munekazu Motoyama. Electrochemical metal deposition on silicon. *Current Opinion in Solid State and Materials Science*, **10**(3–4):163–172, 2006.

[361] Sang-Ho An, Tae-Hyuk Lim, Young-Ho Kim, Sang-Eun Bae, Jung-Hyun Yoon, and Chi-Woo J. Lee. EC-STM studies on copper electrodeposition at n-Si(111):H electrodes. *Colloids and Surfaces A: Physicochemical and Engineering Aspects*, **313–314**:339–342, 2008.

[362] Masaaki Niwa, Hiroshi Iwasaki, and Shigehiko Hasegawa. Hydrogen terminated Si(100) surfaces studied by scanning tunneling microscopy, x-ray photon spectroscopy, and Auger electron spectroscopy. *Journal of Vacuum Science & Technology A: Vacuum, Surfaces, and Films*, **8**(1):266–269, 1990.

[363] T. Zambelli, M. L. Munford, F. Pillier, M.-C. Bernard, and P. Allongue. Cu Electroplating on H-Terminated n-Si(111): Properties and Structure of n-Si/Cu Junctions. *Journal of The Electrochemical Society*, **148**(9):C614–C619, 2001.

[364] Th. Koop, W. Schindler, A. Kazimirov, G. Scherb, J. Zegenhagen, Th. Schulz, R. Feidenhans'l, and J. Kirschner. Electrochemical cell for in situ x-ray diffraction under ultrapure conditions. *Review of Scientific Instruments*, **69**(4):1840–1843, 1998.

[365] K. Jüttner. Oxygen reduction electrocatalysis by underpotential deposited metal atoms at different single crystal faces of gold and silver. *Electrochimica Acta*, **29**(11):1597–1604, 1984.

[366] Chaojie Song and Jiujun Zhang. *PEM Fuel Cell Electrocatalysts and Catalyst Layers – Fundamentals and Applications*. Springer Verlag, Berlin, Heidelberg, 2008.

[367] A. Hamelin, S. Morin, J. Richer, and J. Lipkowski. Adsorption of pyridine on the (110) face of silver. *Journal of Electroanalytical Chemistry and Interfacial Electrochemistry*, **272**(1–2):241 – 252, 1989.

[368] G Brisard, N Bertrand, P.N Ross, and N.M. Marković. Oxygen reduction and hydrogen evolution–oxidation reactions on Cu(hkl) surfaces. *Journal of Electroanalytical Chemistry*, **480**(1–2):219–224, 2000.

[369] Valerie Bertagna, Christian Plougonven, François Rouelle, and Marius Chemla. p- and n-Type Silicon Electrochemical Properties in Dilute Hydrofluoric Acid Solutions. *Journal of The Electrochemical Society*, **143**(11):3532–3538, 1996.

[370] Hiroki Ogawa, Kenji Ishikawa, Miki T. Suzuki, Yuka Hayami, and Shuzo Fujimura. Effects of Dissolved Oxygen in HF Solution on Silicon Surface Morphology. *Japanese Journal of Applied Physics*, **34**(Part 1, No. 2B):732–736, 1995.

[371] G. Schlichthörl and L.M. Peter. Deconvolution of the Impedance of the Silicon/Electrolyte Interface by Potential-Modulated-Microwave Measurements. *Journal of The Electrochemical Society*, **141**(12):L171–L173, 1994.

[372] M. Schlüter and Marvin L. Cohen. Nature of conduction-band surface resonances for Si(111) surfaces with and without chemisorbed overlayers. *Physical Review B*, **17**:716–725, Jan 1978.

[373] Joel A. Appelbaum and D.R. Hamann. Self-Consistent Quantum Theory of Chemisorption: H on Si(111). *Physical Review Letters*, **34**:806–809, Mar 1975.

[374] I.B. Ortenburger, S. Ciraci, and I.P. Batra. A comparative study of the (111), (110) and (100) surfaces of silicon using the local density of states method applied to the bond orbital model. *Journal of Physics C: Solid State Physics*, **9**(22):4185–4201, 1976.

[375] M. McEllistrem, G. Haase, D. Chen, and R.J. Hamers. Electrostatic sample-tip interactions in the scanning tunneling microscope. *Physical Review Letters*, **70**:2471–2474, Apr 1993.

[376] H. Ibach and J.E. Rowe. Hydrogen adsorption and surface structures of silicon. *Surface Science*, **43**(2):481–492, 1974.

[377] J.E. Rowe, S.B. Christman, and H. Ibach. Photoemission Measurements of Step-Dependent Surface States on Cleaved Silicon (111). *Physical Review Letters*, **34**:874–877, Apr 1975.

[378] R. S. Becker, G. S. Higashi, Y. J. Chabal, and A. J. Becker. Atomic-scale conversion of clean Si(111):H-1×1 to Si(111)-2×1 by electron-stimulated desorption. *Physical Review Letters*, **65**(15):1917–1920, Oct 1990.

[379] Walter P. Gomes and Felix Cardon. Surface States at the Single Crystal Zinc Oxide/Electrolyte Interface. *Berichte der Bunsen Gesellschaft*, **74**:431–441, 1970.

[380] Gerko Oskam, Peter M. Hoffmann, John C. Schmidt, and Peter C. Searson. Energetics and Kinetics of Surface States at n-Type Silicon Surfaces in Aqueous Fluoride Solutions. *The Journal of Physical Chemistry*, **100**(5):1801–1806, 1996.

[381] G. Oskam, D. Vanmaekelbergh, and J.J. Kelly. The influence of electrodeposited gold on the properties of III–V semiconductor electrodes – part 2. A study of the impedance due to gold-related surface states at p-GaAs electrodes. *Electrochimica Acta*, **38**(2–3):301–306, 1993.

[382] Albert Goossens and Joop Schoonman. The impedance of surface recombination at illuminated semiconductor electrodes: A non-equilibrium approach. *Journal of Electroanalytical Chemistry and Interfacial Electrochemistry*, **289**(1–2):11–27, 1990.

[383] E.H. Nicollian and A. Goetzberger. The Si-SiO_2 Interface – Electrical Properties as Determined by the Metal-Insulator Silicon Conductance Technique. *The Bell System Technical Journal*, **XLVI**:1055–1133, August 1967.

[384] C.H. Seager, R.A. Anderson, and J.K.G. Panitz. The diffusion of hydrogen in silicon and mechanisms for "unintentional" hydrogenation during ion beam processing. *Journal of Materials Research*, **2**(1):96–106, 1987.

[385] Bhushan Sopori, Yi Zhang, and N. Ravindra. Silicon device processing in H-ambients: H-diffusion mechanisms and influence on electronic properties. *Journal of Electronic Materials*, **30**:1616–1627, 2001. 10.1007/s11664-001-0181-1.

[386] J.I. Pankove and N.M. Johnson, editors. *Hydrogen in Semiconductors*, volume 34 of *Semiconductors and Semimetals*. Academic Press, Inc., San Diego, 1991.

[387] Carleton H. Seager. *Hydrogen in Semiconductors*, volume 34 of *Semiconductors and Semimetals*. Academic Press, Inc., San Diego, 1991. Chapter 2.

[388] S.J. Pearton, J.W. Corbett, and M. Stavola. *Hydrogen in Crystalline Semiconductors*, volume 16 of *Springer Series in Materials Science*. Springer Berlin / Heidelberg, 1992. Chapter 11.

[389] A.J. Tavendale, A.A. Williams, and S.J. Pearton. Hydrogen Injection Into P-Type Silicon By Chemical Etching. In *MRS Proceedings*, volume 104, pages 285–290, 1987.

[390] Naoki Fukata, Shinichi Sasaki, Shuzo Fujimura, Hajime Haneda, and Kouichi Murakami. Hydrogen Passivation of Donors and Hydrogen States in Heavily Doped n-Type Silicon. *Japanese Journal of Applied Physics*, **35**(Part 1, No. 7):3937–3941, 1996.

[391] N.M. Johnson, F.A. Ponce, R.A. Street, and R.J. Nemanich. Defects in single-crystal silicon induced by hydrogenation. *Physical Review B*, **35**(8):4166–4169, Mar 1987.

[392] M. Capizzi and A. Mittiga. Hydrogen in crystalline silicon: A deep donor? *Applied Physics Letters*, **50**(14):918–920, 1987.

[393] N.M. Johnson, C. Herring, and D.J. Chadi. Interstitial hydrogen and neutralization of shallow-donor impurities in single-crystal silicon. *Physical Review Letters*, **56**(7):769–772, Feb 1986.

[394] P. C. Srivastava and U. P. Singh. Hydrogen in semiconductors. *Bulletin of Materials Science*, **19**:51–60, 1996.

[395] P. L'evêque, A. Hallén, B.G. Svensson, J. Wong-Leung, C. Jagadish, and V. Privitera. Identification of hydrogen related defects in proton implanted float-zone silicon. *The European Physical Journal Applied Physics*, **23**:5–9, July 2003.

[396] P. Lévêque, P. Pellegrino, A. Hallén, B.G. Svensson, and V. Privitera. Hydrogen-related defect centers in float-zone and epitaxial n-type proton implanted silicon. *Nuclear Instruments and Methods in Physics Research Section B: Beam Interactions with Materials and Atoms*, **174**(3):297–303, 2001.

[397] N.M. Johnson and C. Herring. Diffusion of negatively charged hydrogen in silicon. *Physical Review B*, **46**:15554–15557, Dec 1992.

[398] E.V. Monakhov and B.G. Svensson. Reversible room temperature interaction of impurities in Si. *Journal of Physics: Condensed Matter*, **17**(22):S2185–S2190, 2005.

[399] R. Rizk, P. de Mierry, D. Ballutaud, M. Aucouturier, and D. Mathiot. Hydrogen diffusion and passivation processes in p- and n-type crystalline silicon. *Physical Review B*, **44**(12):6141–6151, Sep 1991.

[400] D. Mathiot. Modeling of hydrogen diffusion in n - and p -type silicon. *Physical Review B*, **40**:5867–5870, Sep 1989.

[401] L. Palmetshofer and J. Reisinger. Defect levels in H^+-, D^+-, and He^+-bombarded silicon. *Journal of Applied Physics*, **72**(6):2167–2173, 1992.

[402] A.J. Tavendale, S.J. Pearton, and A.A. Williams. Evidence for the existence of a negatively charged hydrogen species in plasma-treated n-type Si. *Applied Physics Letters*, **56**(10):949–951, 1990.

[403] A. Hallén, B. U. R. Sundqvist, Z. Paska, B. G. Svensson, M. Rosling, and J. Tirén. Deep level transient spectroscopy analysis of fast ion tracks in silicon. *Journal of Applied Physics*, **67**(3):1266–1271, 1990.

[404] N.M. Johnson. Electric field dependence of hydrogen neutralization of shallow-acceptor impurities in single-crystal silicon. *Applied Physics Letters*, **47**(8):874–876, 1985.

[405] S. Miyazaki, J. Schäfer, J. Ristein, and L. Ley. Surface Fermi level position of hydrogen passivated Si(111) surfaces. *Applied Physics Letters*, **68**(9):1247–1249, 1996.

[406] Gerko Oskam, Peter M. Hoffmann, and Peter C. Searson. In Situ Measurements of Interface States at Silicon Surfaces in Fluoride Solutions. *Phys. Rev. Lett.*, **76**(9):1521–1524, Feb 1996.

[407] C. Barret, F. Chekir, and A. Vapaille. Study of metal-semiconductor interface states using Schottky capacitance spectroscopy. *Journal of Physics C: Solid State Physics*, **16**(12):2421–2438, 1983.

[408] Chris G. Van de Walle, F.R. McFeely, and S.T. Pantelides. Fluorine-silicon reactions and the etching of crystalline silicon. *Physical Review Letters*, **61**:1867–1870, Oct 1988.

[409] Satoru Watanabe and Mayumi Shigeno. Fluorine Adsorption and Etching on Si(111):SiH Surface during Immersion in HF Solution. *Japanese Journal of Applied Physics*, **31**(Part 1, No. 6A):1702–1708, 1992.

[410] C.L. Aravinda, B. Burger, and W. Freyland. Nanoscale electrodeposition of Al on n-Si(111):H from an ionic liquid. *Chemical Physics Letters*, **434**(4–6):271–275, 2007.

[411] F. Endres, S. Zein El Abedin, A. Y. Saad, E. M. Moustafa, N. Borissenko, W. E. Price, G. G. Wallace, D. R. MacFarlane, P. J. Newman, and A. Bund. On the electrodeposition of titanium in ionic liquids. *Physical Chemistry Chemical Physics*, **10**:2189–2199, 2008.

[412] R. Widmer and H. Siegenthaler. Nanostructuring experiments in the system Ag(111)/Pb2+. *Electrochemistry Communications*, **7**(4):421–426, 2005.

[413] J.S. Villarrubia. Scanned probe microscope tip characterization without calibrated tip characterizers. *Journal of Vacuum Science & Technology B: Microelectronics and Nanometer Structures*, **14**(2):1518–1521, 1996.

[414] Kirsten I. Schiffmann, Matthias Fryda, Günther Goerigk, Rolf Lauer, and Peter Hinze. Statistical methods for the correction of tip convolution effects in STM imaging of nanometer size particles in metalŮC: H films. *Ultramicroscopy*, **66**(3–4):183–192, 1996.

[415] K. I. Schiffmann, Matthias Fryda, Günther Goerigk, Rolf Lauer, and Peter Hinze. Correction of STM tip convolution effects in particle size and distance determination of metal-C:H films. *Fresenius' Journal of Analytical Chemistry*, **358**:341–344, 1997.

[416] P.M. Williams, K.M. Shakesheff, M.C. Davies, D.E. Jackson, C.J. Roberts, and S.J.B. Tendler. Blind reconstruction of scanning probe image data. *Journal of Vacuum Science & Technology B: Microelectronics and Nanometer Structures*, **14**(2):1557–1562, 1996.

[417] A.T. Winzer, C. Kraft, S. Bhushan, V. Stepanenko, and I. Tessmer. Correcting for AFM tip induced topography convolutions in proteinŮDNA samples. *Ultramicroscopy*, **121**:8–15, 2012.

[418] David Keller. Reconstruction of STM and AFM images distorted by finite-size tips. *Surface Science*, **253**(1–3):353–364, 1991.

[419] David J. Keller and Fransiska S. Franke. Envelope reconstruction of probe microscope images. *Surface Science*, **294**(3):409–419, 1993.

[420] Peter Markiewicz and M. Cynthia Goh. Atomic force microscope tip deconvolution using calibration arrays. *Review of Scientific Instruments*, **66**(5):3186–3190, 1995.

[421] Yasuhiko Harada, Hayato Sone, and Sumio Hosaka. Estimation of Three-Dimensional Atomic Force Microscope Tip Shape from Atomic Force Microscope Image for Accurate Measurement. *Japanese Journal of Applied Physics*, **47**(7):6186–6189, 2008.

[422] Masao Nagase, Hideo Namatsu, Kenji Kurihara, Kazumi Iwadate, and Katsumi Murase. Metrology of Atomic Force Microscopy for Si Nano-Structures. *Japanese Journal of Applied Physics*, **34**(Part 1, No. 6B):3382–3387, 1995.

[423] Kathryn A. Ramirez-Aguilar and Kathy L. Rowlen. Tip Characterization from AFM Images of Nanometric Spherical Particles. *Langmuir*, **14**(9):2562–2566, 1998.

[424] Hiroshi Itoh, Toshiyuki Fujimoto, and Shingo Ichimura. Tip characterizer for atomic force microscopy. *Review of Scientific Instruments*, **77**(10):103704, 2006.

[425] Hisataka Takenaka, Masatoshi Hatayama, Hisashi Ito, Tadayuki Ohchi, Akio Takano, Satoru Kurosawa, Hiroshi Itoh, and Shingo Ichimura. AFM Tip Characterizer fabricated by Si/SiO_2 multilayers. *e-Journal of Surface Science and Nanotechnology*, **9**:293–296, 2011.

[426] Y. Li and S. M. Lindsay. Polystyrene latex particles as a size calibration for the atomic force microscope. *Review of Scientific Instruments*, **62**(11):2630–2633, 1991.

[427] R. Zhang and D.G. Ivey. Preparation of sharp polycrystalline tungsten tips for scanning tunneling microscopy imaging. *Journal of Vacuum Science & Technology B: Microelectronics and Nanometer Structures*, **14**(1):1–10, 1996.

[428] B. Rashkova, B. Guel, R.T. Pötzschke, G. Staikov, and W.J. Lorenz. Electrodeposition of Pb on n-Si(111). *Electrochimica Acta*, **43**(19–20):3021–3028, 1998.

[429] G. Oskam, J.G. Long, A. Natarajan, and P.C. Searson. Electrochemical deposition of metals onto silicon. *Journal of Physics D: Applied Physics*, **31**(16):1927–1949, 1998.

[430] J. Zegenhagen, F.U. Renner, A. Reitzle, T.L. Lee, S. Warren, A. Stierle, H. Dosch, G. Scherb, B.O. Fimland, and D.M. Kolb. In situ X-ray analysis of solid/electrolyte interfaces: electrodeposition of Cu and Co on Si(1ă1ă1):H and GaAs(0ă0ă1) and corrosion of Cu_3Au(1ă1ă1). *Surface Science*, **573**(1):67–79, 2004.

[431] T. Yasue, T. Koshikawa, H. Tanaka, and I. Sumita. Initial stage of Cu growth on Si(111)7×7 surface studied by scanning tunneling microscopy. *Surface Science*, **287–288, Part 2**:1025–1029, 1993.

[432] Y.P. Zhang, L. Yang, Y.H. Lai, G.Q. Xu, and X.S. Wang. Formation of ordered two-dimensional nanostructures of Cu on the Si(111)-(7×7) surface. *Surface Science*, **531**(3):L378–L382, 2003.

[433] E.H. Rhoderick and R.H. Williams. *Metal–Semiconductor Contacts, Second Edition*, volume 19 of *Monographs in Electrical and Electronic Engineering*. Oxford University Press, 1988.

[434] H. Nienhaus, H. S. Bergh, B. Gergen, A. Majumdar, W. H. Weinberg, and E. W. McFarland. Ultrathin Cu films on Si(111): Schottky barrier formation and sensor applications. *Journal of Vacuum Science & Technology A: Vacuum, Surfaces, and Films*, **17**(4):1683–1687, 1999.

[435] Zhen Zhang and John T. Yates. Band Bending in Semiconductors: Chemical and Physical Consequences at Surfaces and Interfaces. *Chemical Reviews*, **112**(10):5520–5551, 2012.

[436] J.E.T. Andersen, G. Bech-Nielsen, P. Møller, and J.C. Reeve. Bulk copper electrodeposition on gold imaged by *in situ*STM: morphology and influence of tip potential. *Journal of Applied Electrochemistry*, **26**:161–170, 1996.

[437] U. Stimming, R. Vogel, D.M. Kolb, and T. Will. Metal deposition and dissolution monitored by *in situ* scanning tunneling microscopy. *Journal of Power Sources*, **43**:169–180, 1993.

[438] S.G. García, D.R. Salinas, C.E. Mayer, W.J. Lorenz, and G. Staikov. STM tip-induced local electrochemical dissolution of silver. *Electrochimica Acta*, **48**(9):1279–1285, 2003.

[439] X.H. Xia, R. Schuster, V. Kirchner, and G. Ertl. The growth of size-determined Cu clusters in nanometer holes on Au(111) due to a balance between surface and electrochemical energy. *Journal of Electroanalytical Chemistry*, **461**(1-2):102–109, 1999.

[440] R. Schuster, V. Kirchner, X.H. Xia, A.M. Bittner, and G. Ertl. Nanoscale Electrochemistry. *Physical Review Letters*, **80**:5599–5602, Jun 1998.

[441] Lian Guo and Peter C. Searson. Influence of anion on the kinetics of copper island growth. *Nanoscale*, **2**:2431–2435, 2010.

[442] J.A.Venables, G.D.T. Spiller, and M. Hanbucken. Nucleation and growth of thin films. *Reports on Progress in Physics*, **47**(4):399–459, 1984.

[443] Takehiko Nakahara, Shigeharu Ohkura, Fumiya Shoji, Teruo Hanawa, and Kenjiro Oura. RBS/channeling study on the annealing behavior of Cu thin films on Si(100) and (111) substrates. *Nuclear Instruments and Methods in Physics Research Section B: Beam Interactions with Materials and Atoms*, **45**(1–4):467–470, 1990.

[444] Stewart H. Corn, John L. Falconer, and A.W. Czanderna. The copper–silicon interface: Composition and interdiffusion. *Journal of Vacuum Science & Technology A: Vacuum, Surfaces, and Films*, **6**(3):1012–1016, 1988.

[445] Ryoya Ishigami, Junji Yuhara, and Kenji Morita. Thermal behavior of Cu films on the Si(111) surface in the monolayer regime. *Surface Science*, **315**(3):302–308, 1994.

[446] S.A. Chambers, G.A. Howell, T.R. Greenlee, and J.H. Weaver. Characterization of intermixing at metal-semiconductor interfaces by angle-resolved Auger-electron emission: Cu/Si(111)-7×7. *Physical Review B*, **31**:6402–6410, May 1985.

[447] B.G. Demczyk, R. Naik, G. Auner, C. Kota, and U. Rao. Growth of Cu films on hydrogen terminated Si(100) and Si(111) surfaces. *Journal of Applied Physics*, **75**(4):1956–1961, 1994.

[448] Adriana Ispas, Hisayoshi Matsushima, Andreas Bund, and Benedetto Bozzini. Nucleation and growth of thin nickel layers under the influence of a magnetic field. *Journal of Electroanalytical Chemistry*, **626**(1–2):174–182, 2009.

[449] Hisayoshi Matsushima, Adriana Ispas, Andreas Bund, and Benedetto Bozzini. Magnetic field effects on the initial stages of electrodeposition processes. *Journal of Electroanalytical Chemistry*, **615**(2):191–196, 2008.

[450] Andreas Bund and Adriana Ispas. Influence of a static magnetic field on nickel electrodeposition studied using an electrochemical quartz crystal microbalance, atomic force microscopy and vibrating sample magnetometry. *Journal of Electroanalytical Chemistry*, **575**(2):221–228, 2005.

[451] Hisayoshi Matsushima, Andreas Bund, Waldfried Plieth, Shiomi Kikuchi, and Yasuhiro Fukunaka. Copper electrodeposition in a magnetic field. *Electrochimica Acta*, **53**(1):161–166, 2007.

[452] M.L. Munford, M.L. Sartorelli, L. Seligman, and A.A. Pasa. Morphology and Magnetic Properties of Co Thin Films Electrodeposited on Si. *Journal of The Electrochemical Society*, **149**(5):C274–C279, 2002.

[453] Jong Duk Lee, Tae Hwan An, Hak Gi Noh, Sung Gon Kim, and Young R. Choi. Growth Kinetics and Properties of Thin Cobalt Films Electrodeposited on n-Si(100). *Japanese Journal of Applied Physics*, **49**(8):085802, 2010.

[454] Martin Hugelmann. *Erzeugung und Charakterisierung metallischer Nanostrukturen auf n – Si(111) : H Einkristalloberflächen*. PhD thesis, Universität Karlsruhe, 2004.

[455] Junghun Choi, Youngwoo Kim, Do Kyung Lim, Do Hwan Kim, and Sehun Kim. Subsurface Incorporation of Co Atoms into Si(100). *The Journal of Physical Chemistry C*, **115**(31):15467–15470, 2011.

[456] S.P. Dash, D. Goll, and H.D. Carstanjen. Subsurface enrichment of Co in Si (100) at initial stages of growth at room temperature: A study by high-resolution Rutherford backscattering. *Applied Physics Letters*, **90**(13):132109, 2007.

[457] I.I. Pronin, M.V. Gomoyunova, S.M. SolovŠev, O.Yu. Vilkov, and D.V. Vyalikh. Initial stages of the growth and magnetic properties of cobalt films on the Si(100)2×1 surface. *Physics of the Solid State*, **53**:616–621, 2011.

[458] G. W. Peng, A. C. H. Huan, E. S. Tok, and Y. P. Feng. Adsorption and diffusion of Co on the Si(001) surface. *Phys. Rev. B*, **74**:195335, Nov 2006.

[459] R. Flammini, F. Wiame, R. Belkhou, and A. Taleb-Ibrahimi. Co/Si(111) and Co/Si(111)–H interfaces: a comparative core-level photoemission study. *Applied Surface Science*, **233**(1–4):411–418, 2004.

[460] J.S. Pan, E.S. Tok, C.H.A. Huan, R.S. Liu, J.W. Chai, W.J. Ong, and K.C. Toh. Probing the behaviour of ultra thin Co layers on clean and hydrogen terminated Si(001) and Si(111) surfaces. *Surface Science*, **532–535**:639–644, 2003. <ce:title>Proceedings of the 7th International Conference on Nanometer-Scale Science and Technology and the 21st European Conference on Surface Science</ce:title>.

[461] M.G. Martin, J. Avila, M. Gruyters, C. Teodorescu, P. Dumas, Y.J. Chabal, and M.C. Asensio. Initial stage of the growth of Fe on Si(111)(1×1):H. *Applied Surface Science*, **123–124**:156–160, 1998. Proceedings of the Sixth International Conference on the Formation of Semiconductor Interfaces.

[462] Li Ma, Jianguang Wang, Jijun Zhao, and Guanghou Wang. Chemisorption of Co monolayer on H-passivated Si(111) surface: Comparison with clean Si(111) surface. *Chemical Physics Letters*, **414**(4–6):500–504, 2005.

[463] C.W.T. Bulle-Lieuwma. Epitaxial growth of CoSi2/Si structures. *Applied Surface Science*, **68**(1):1–18, 1993.

[464] F. Boscherini, J. J. Joyce, M. W. Ruckman, and J. H. Weaver. High-resolution photoemission study of Co/Si(111) interface formation. *Phys. Rev. B*, **35**:4216–4220, Mar 1987.

[465] J. Derrien. Structural and electronic properties of CoSi2 epitaxially grown on Si(111). *Surface Science*, **168**(1–3):171–183, 1986.

[466] L.J. Geerligs, Sven Rogge, Geroge Palasantzas, Burghard Ilge, Paul Scholte, and Jan de Nijs. NEXT: an Experimental Effort Towards Nanoelectronic Devices. *Journal of Surface Analysis*, **4**(2):204 – 208, January 1998.

[467] G. Palasantzas, B. Ilge, J. de Nijs, and L.J. Geerligs. Diffusion, nucleation and annealing of Co on the H-passivated Si(100) surface. *Surface Science*, **412-413**(0):509 – 517, 1998.

[468] G. J. van Gurp. Cobalt silicide layers on Si. II. Schottky barrier height and contact resistivity. *Journal of Applied Physics*, **46**(10):4308–4311, 1975.

[469] J.L. Tedesco, J.E. Rowe, and R.J. Nemanich. Conducting atomic force microscopy studies of nanoscale cobalt silicide Schottky barriers on Si(111) and Si(100). *Journal of Applied Physics*, **105**(8):083721, 2009.

[470] A. A. Pasa and W. Schwarzacher. Electrodeposition of Thin Films and Multilayers on Silicon. *physica status solidi (a)*, **173**(1):73–84, 1999.

[471] K. Ishida, Y. Miura, K. Hirose, S. Harada, and T. Narusawa. Epitaxial growth of CoSi2 on hydrogen-terminated Si(001). *Applied Physics Letters*, **82**(12):1842–1844, 2003.

[472] M. Copel and R. M. Tromp. Nucleation of Co silicide on H passivated Si(111). *Applied Physic Letters*, **65**(24):3102–3104, 1994.

[473] G. Palasantzas, B. Ilge, J. De Nijs, and L. J. Geerligs. Fabrication of Co/Si nanowires by ultrahigh-vacuum scanning tunneling microscopy on hydrogen-passivated Si(100) surfaces. *Journal of Applied Physics*, **85**(3):1907–1910, 1999.

[474] *http://www.simion.com, Scientific Instrument Services, Inc., USA.*

[475] H. J. Kreuzer and R. L. C. Wang. Physics and chemistry in high electric fields. *Philosophical Magazine Part B*, **69**(5):945–955, 1994.

[476] H.J. Kreuzer. *Surfac Science of Catalysis*, volume 482 of *ACS Symposium Series*. American Chemical Society, 1992.

[477] H.J. Kreuzer. *Chemistry and Physics of Solid Surfaces VIII*, volume 22 of *Springer Series in Surface Sciences*. Springer Verlag Berlin/ Heidelberg, 1990.

[478] H.J. Kreuzer. *Atomic and Nanometer-Scale Modification of Materials: Fundamentals and Applications*. Kluwer Academic Publishers, 1993.

[479] H.C. Akpati, P. Nordlander, L. Lou, and Ph. Avouris. The effects of an external electric field on the adatom-surface bond: H and Al adsorbed on Si(111). *Surface Science*, **372**(1–3):9–20, 1997.

[480] K. Stokbro. Electric field dependent structural and vibrational properties of the Si(100)-H(2x1) surface and its implications for STM induced hydrogen desorption. *Surface Science*, **429**(1-3):327 – 337, 1999.

[481] B.N.J. Persson and Ph. Avouris. The effects of the electric field in the STM on excitation localization. Implications for local bond breaking. *Chemical Physics Letters*, **242**(4–5):483–489, 1995.

[482] Ph. Avouris, R.E. Walkup, A.R. Rossi, H.C. Akpati, P. Nordlander, T.-C. Shen, G.C. Abeln, and J.W. Lyding. Breaking individual chemical bonds via STM-induced excitations. *Surface Science*, **363**(1–3):368–377, 1996. Dynamical Quantum Processes on Solid Surfaces.

[483] B. Ilge, G. Palasantzas, and L.J. Geerligs. Submonolayer growth of Co on H-passivated Si(100) surfaces and nanoscale metallization with Co on patterned H–Si(100). *Applied Surface Science*, **144–145**(0):543–547, 1999.

[484] G. Palasantzas, B. Ilge, S. Rogge, and L.J. Geerligs. Technology for nanoelectronic devices based on ultra-high vacuum scanning tunneling microscopy on the Si(100) surface. *Microelectronic Engineering*, **46**(1–4):133–136, 1999. International Conference on Micro- and Nanofabrication.

[485] J.W. Lyding, T.-C. Shen, J.S. Hubacek, J.R. Tucker, and G.C. Abeln. Nanoscale patterning and oxidation of H-passivated Si(100)-2×1 surfaces with an ultrahigh vacuum scanning tunneling microscope. *Applied Physic Letters*, **64**(15):2010–2012, 1994.

[486] E. T. Foley, A. F. Kam, J. W. Lyding, and Ph. Avouris. Cryogenic UHV-STM Study of Hydrogen and Deuterium Desorption from Si(100). *Phys. Rev. Lett.*, **80**:1336–1339, Feb 1998.

[487] T. C. Shen, C. Wang, G. C. Abeln, J. R. Tucker, J. W. Lyding, Ph. Avouris, and R. E. Walkup. Atomic-Scale Desorption Through Electronic and Vibrational Excitation Mechanisms. *Science*, **268**(5217):1590–1592, 1995.

[488] E. Leiva. Recent developments in the theory of metal upd. *Electrochimica Acta*, **41**(14):2185–2206, 1996.

[489] Ruxandra Vidu and Shigeta Hara. Surface alloying at the Cd | Au(100) interface in the upd region. Electrochemical studies and in situ EC-AFM observation. *Journal of Electroanalytical Chemistry*, **475**(2):171–180, 1999.

[490] S. Maupai, A.S. Dakkouri, and P. Schmuki. Tip-induced nanostructuring of alloy surfaces with an electrochemical scanning tunneling microscope. *Surface Science*, **597**(1–3):20–25, 2005.

[491] G. Staikov and W. J. Lorenz. Electrochemical 3D Metal Phase Formation on UPD Modified Foreign Substrates. *Zeitschrift für Physikalische Chemie*, **208**(1–2):17–42, 1999.

List of Publications

[i] Sebastian Jakob, Werner Schindler
Surface States of Wet Chemically Etched n – Si (111):H Surfaces
Electrochimica Acta, **88**, pages 659 – 663 (2013)

[ii] Sebastian Jakob, Werner Schindler
Charge Transfer Processes via Surface States at
Electron Depleted n – Si (111):H surfaces
Submitted

[iii] Sebastian Jakob, Werner Schindler
Electric Field Assisted Electrochemical "Writing"
of Co Nanostructures onto n – Si (111):H Surfaces
Surface Science, **612**, pages L1 – L4 (2013)

[iv] Sebastian Jakob, Werner Schindler
Impact of Electric Fields on the Co Electrodeposition
onto n – Si (111):H Surfaces
Submitted

[v] Sebastian Jakob, Werner Schindler
Correlation of Image Resolution with Tip Apex Diameter
in Scanning Tunneling Microscopy at the Nanoscale
Submitted

Acknowledgements

I would like to thank all the people who made this thesis possible.

At Technische Universität München, I would like to thank...

- Prof. Dr. Johannes V. Barth,
  for giving me the opportunity to do this thesis at E20.
- PD Dr. Werner Schindler,
  for supervising me during this thesis and for many fruitful discussions.
- Dr. Hartmut Schlichting,
  for his assistance in the SIMION electric field calculations.
- The Zentralinstitut für Medizintechnik (IMETUM),
  for providing their Solartron 1260 device for the experiments.
- everyone at E20
  and especially the people of office 222 – it was a great time with you.

In particular, I would like to thank my parents, for providing me the possibility of studying physics and for their ongoing support during this thesis.
Likewise, I would like to thank my girlfriend for supporting me during this thesis.